Model Order Reduction for Aeroelastic Analysis of Very Flexible Aircraft

by

Renato Rebouças de Medeiros

A dissertation submitted in partial fulfillment
of the requirements for the degree of
Doctor of Philosophy
(Aerospace Engineering)
in the University of Michigan
2019

Doctoral Committee:

Professor Carlos E. S. Cesnik, Chair
Professor Bogdan I. Epureanu
Assoc. Professor Krzysztof Fidkowski
Professor Peretz P. Friedmann

Renato Rebouças de Medeiros

renatorm@umich.edu

ORCID iD: 0000-0001-7185-9339

This dissertation is dedicated to my wife Patrícia and our awaited son Gabriel.

ACKNOWLEDGEMENTS

First and foremost, I would like to thank God for taking care of me and my family during these four intense years of the PhD.

I was not the only one working on this project. Since the beginning, I have been lucky to count on my wife Patrícia to share this challenge. I am so grateful for her support and company during this time. In the end, we received the gift of our son Gabriel.

I would like to say thanks to my parents Roosevelt and Rejane, my sister Rayanna and my grandmothers Célia and Leide for their love and attention along the way. My advisor Prof. Carlos E. S. Cesnik was a fundamental piece in this doctoral path. He introduced me to the academic world of scientific research and publications. I could learn a lot about critical thinking, problem-solving and writing strategies from his experience, and I am grateful for that. I also want to say thanks to him for all the guidance along this journey.

I acknowledge my other committee members Prof. Friedmann, Prof. Fidkowski and Prof. Epureanu for their inputs and for gladly evaluating my work, even when the dissertation was not complete.

This school is of a special kind, and the Aerospace Department is a big family. Thank you to Denise Phelps, our graduate coordinator, for her attention and care devoted to each student along 41 years of service.

To my research group at the university, the A^2SRL, a big thanks for all good moments, discussions and support during this time. This is a group where I could find many good friends for life. To each one of them, my deep gratitude for this great experience in the daily life along the PhD.

I would like to acknowledge our collaborators from external research groups, especially Markus Ritter from DLR, Olivia Stodieck from the University of Bristol, Ney Secco from the MDO Lab at the University of Michigan, and Dr. Etienne Coetzee from Airbus.

Finally, thank you to the Brazilian Air Force and to the Brazilian National Council of Scientific and Technological Development for believing in me and sending me to live this life-changing experience.

This work was sponsored by Airbus Americas, Inc., with Dr. David Hills as the project manager.

TABLE OF CONTENTS

LIST OF FIGURES

Figures

LIST OF TABLES

Tables

LIST OF APPENDICES

ABSTRACT

With increasing requirements for lower emissions and costs, next-generation transport aircraft are poised to deal with high-aspect-ratio wings. Long light-weight structures are naturally flexible, and this fact brings new challenges to the aeroelastic analysis. Time-domain simulation of these nonlinear systems is desirable to analyze their aeroelastic behavior over the flight envelope.

In the structural end, while simplified methods exist to model slender wings with equivalent nonlinear beams, essential details can only be captured with built-up finite element models. Unfortunately, these models are expensive and non-robust for extensive dynamic simulations. This dissertation builds upon previous efforts to develop nonlinear modal reduced-order models (ROMs). Through a series of nonlinear static solutions with large displacements as training data, stiffness terms and higher-order displacements are identified as functions of the modal degrees of freedom. A combination of linear modes and supplementary shapes called dual modes can accurately represent large displacements. A static condensation process allows the inclusion of dual modes in the equations of motion, keeping only the original degrees of freedom associated with the linear modes. Accounting for the inertia forces related to the dual modes is a significant contribution of this thesis to allow accurate simulations under large displacements. The developed nonlinear modal ROMs based on the newly-introduced Enhanced Implicit Condensation and Expansion (EnICE) process achieves computational time savings of orders of magnitude relative to the original 3D built-up finite element simulations.

The EnICE approach was integrated into the computational fluid dynamics code

CFL3D for high-fidelity aeroelastic analyses. This environment is later used as a source of reference data to build an aerodynamic ROM. This is based on (linear) convolution corrected by a (nonlinear) correction factor obtained from steady aerodynamic solutions. To reduce the number of steady aerodynamic solutions and speed up the process, the correction factors are obtained from the Method of Segments (MoS). Finally, the MoS evaluation process was modified from using local geometric angles of attack to local induced angles of attack, which improved the correlation of the aerodynamic ROM and the reference CFD solution particularly in transonic regime.

Among the contributions of this dissertation, the integration of the CFL3D code with a nonlinear modal solution represents a significant step towards the development of cost-effective high-fidelity analysis for geometrically nonlinear, very flexible structures. Due to the capability of the modeling approach to handle arbitrarily complex structural representations, it allows one to model realistic aircraft structures. Moreover, the modal-like nature of the nonlinear structural representation allows a direct modification of existing CFD-based aeroelastic analysis codes by enhancing its coupled structural model and creating a new enhanced framework for high-fidelity nonlinear analysis.

The aeroelastic solution arising from the two reduced-order models is capable of large displacement simulations, taking into account structural and aerodynamic nonlinearities. Employing a correction factor on top of a linear convolution from step responses proved to be a good strategy for the case of incompressible flow analyzed with large displacements and angles of attack. However, the errors were higher for a transonic case. At the end, significant reductions in simulation time were achieved by using the reduced order aeroelastic model when compared to the high-fidelity one. Accuracy may be increased in future investigations by adjusting the reference condition around which the correction factors are evaluated.

CHAPTER 1

Introduction

This chapter presents the motivation for the dissertation and introduces the structural and aerodynamic nonlinearities that can be addressed with reduced order models. The objectives and organization of the dissertation are explained at the end of the chapter.

1.1 Motivation

In the last 20 years, air traffic has more than doubled. With increasing globalization and overall economic growth, it is expected to continue on the same path for the next decades [4, 5]. However, the environmental impacts of aviation are important. Currently, 2% of all man-made carbon dioxide emissions are related to the aviation industry. Aligned with concerns of global warming and efficiency, plane makers and engine manufacturers have improved designs, keeping the growth of emissions to one-third of the passenger traffic growth [5]. In order to continue reducing costs and emissions, innovative designs have been studied.

One of the observed trends in design is the increased aspect-ratio of new aircraft. By decreasing the induced drag, longer wings bring higher flexibility. In such context, the aeroelastic analysis plays an important role in assuring safe operations over the flight envelope. Studies have pointed out that aeroelastic concerns may be limiting adoption of higher aspect-ratio wings for regional planes [6]. With the proposed

designs suggesting extended wings, such as the E-Thrust concept of Airbus and the Transonic Truss-Braced Wing of Boeing (Fig.1.1), demand for aeroelastic solutions that capture the geometrically nonlinear effects is expected to grow.

Source: Airbus Source: Boeing

Figure 1.1: Airbus and Boeing concepts showing general trend for high-aspect-ratio wings.

Not only commercial aviation requires expedited analysis for assessment of new flexible designs. High-Altitude Long Endurance (HALE) aircraft are increasingly pursued as alternative platforms for communications. These designs tend to have high-aspect-ratio wings as well. In 2003, after a mishap with the Helios experimental plane [7], it was clear the necessity of time-domain analysis to capture the nonlinear nature of the problem. More recently, structural problems involving the prototype Aquila from Facebook [8] again showed that the dynamics of high-aspect-ratio aircraft can be particularly challenging. With new developments in solar-powered airplanes for high-altitude missions, modeling the dynamic response of very flexible structures under different loads for control development will become more common. Examples of HALE aircraft are illustrated in Fig. 1.2.

To better understand its aeroelastic behavior, an experimental platform for aeroelastic tests was developed at the University of Michigan: the X-HALE [9, 10]. It was conceived as a family of experiments with increasing aspect ratio, keeping the chord at 0.2 m and varying the wingspan of 4, 6 or 8 m. Considering the 3 models, the

Figure 1.2: Examples of HALE aircraft.

aspect ratio ranges from 20 to 40. The prototypes of 4 and 6 m have been flown successfully, but coupling between the flight dynamics and the structural flexibility makes it challenging to fly. The 6-m model is shown in Fig. 1.3 during flight.

Figure 1.3: 6-m X-HALE experimental testbed during flight.

Often, finite-element beam models have been used to model the very flexible designs. Beam formulations based on displacement [11], strain [12] and intrinsic [13–16] formulations have been applied successfully to slender structures. They lead to accurate responses, particularly when the geometry of the cross section does not change significantly with the beam deformation.

There are situations where the beam model is not able to represent the dynamics of the structure properly. This is the case when local instability phenomena and Brazier effects [17] are significant, leading to section deformation and changing stiffness.

Modal analysis has been a standard aeroelastic tool used in industry. However, from the structural point of view, large deformations change the stiffness and the mass matrices in such a way that displacements can no longer be represented by a linear modal approach. Currently, time-domain solutions obtained with either nonlinear beam-based formulations (e.g., University of Michigan's UM/NAST solver [18]) or built-up nonlinear finite element models (e.g., AERO [19]) are used for the coupled aeroelastic-flight dynamics analysis when geometric nonlinearities are considered. While beam modeling may not be sufficient to capture complex structural details present in aircraft wings, built-up FEM may be too costly and lack numerical robustness for dynamic simulations.

In this context, a mid-fidelity methodology capable of representing details not captured by the beam formulations in a cost-effective way can be an alternative to expensive simulations involving buit-up FEM. A modal nonlinear reduced order model (ROM) based on the global finite element model (GFEM) fits into the tools that can possibly analyze large-displacement structures (Fig. 1.4). Starting from the detailed built-up FEM, the modal formulation does not require the estimation of equivalent beam properties.

Regarding the aerodynamic analysis, strip theory methods with tip correction are typically used to model high-aspect-ratio wings in low speed flight. However, conditions involving interaction between multiple surfaces and large deflections require 3-D methods [20]. Computational fluid dynamics (CFD) solutions using either Reynolds Averaged Navier Stokes (RANS) or Euler equations are commonly used in industry, especially for transonic flow analysis, but the cost may be prohibitive for extensive aeroelastic analysis. A method combining the accuracy of CFD solutions and the section-wise analysis of strip theory (Fig. 1.4) could be an adequate reduced order model for extensive simulations considering large deformations.

This work builds upon existing methodologies suitable for structural and aerody-

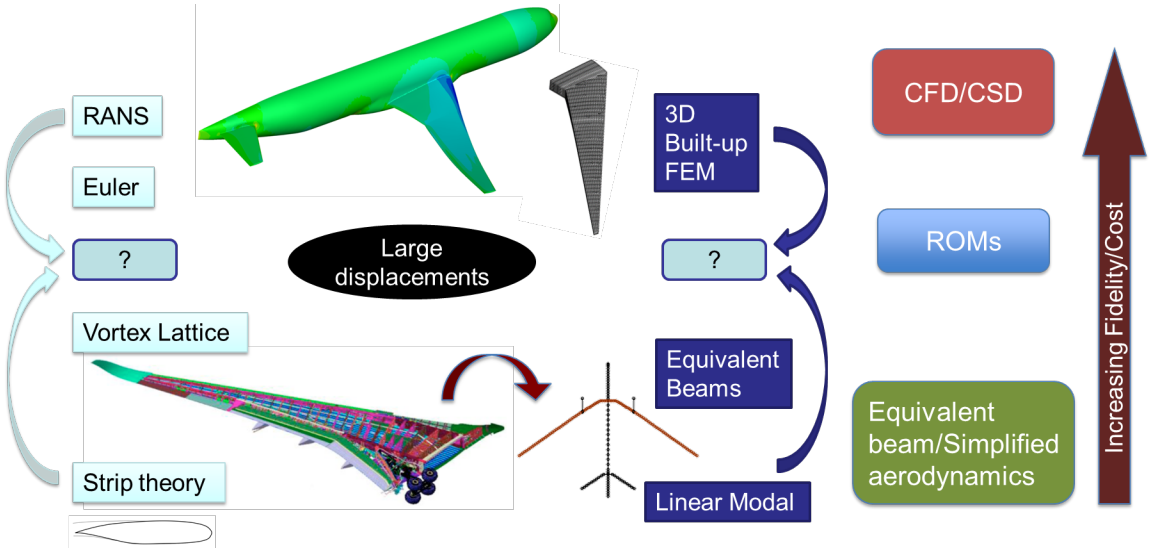

Figure 1.4: ROMs as mid-fidelity tools for analysis involving large displacements.

namic simulations of flexible aircraft. The ROM developed for the structural solution is based on identification of nonlinear terms from nonlinear static solutions obtained in different conditions of large displacements. Tip vertical motion can achieve 30% of the wing semi-span, for example. The displacements are represented by linear modes augmented with a base of additional shapes identified from the nonlinear static solutions. Methodologies existed before for this identification, but this work corrects the equations of motion and improves the nonlinear fitting quality.

The aerodynamic framework proposed is an extension of the model developed by Skujins and Cesnik called Method of Segments (MoS) [1, 21]. This approach divides the wing into segments and uses steady results from a single wing deformation condition to predict loads in different deformed states. This work introduces a calculation of effective angles of attack considering large displacements and rotations, as well as a lifting-line correction for induced angle of attack. A linear convolution predicts unsteady solutions, using step responses calculated from small modal deformations. A correction factor may be used to correct unsteady solutions for nonlinearities.

Combining the structural and aerodynamic ROMs, aeroelastic simulations with

reduced costs are possible.

1.2 Nonlinear Structural Analysis

1.2.1 Nonlinear Finite Element Solutions

Nonlinear structural problems can be solved routinely. Commercial FE solvers are capable of dealing with nonlinearities of different kinds, like nonlinear material properties, contact problems and large displacements. In general, updating the tangential stiffness matrix to satisfy new equilibrium conditions between internal and external forces is the main path for nonlinear solutions in FE codes [22]. Due to the extensive developments in nonlinear finite elements, these tools are an excellent starting point for development of nonlinear reduced order models.

In order to accommodate large displacements, a definition of conjugate strain and stresses that is invariant with rigid-body motion should be taken. Usually, the Green Lagrange strain and the Second Piola-Kirchhoff stress tensors are used. Either Total Lagrangian or Updated Lagrangian formulations [23] are employed by the FE codes to iteratively solve load increments. The differences between these approaches lies in the reference state for stress and strain computations, which is the initial configuration in the Total Lagrangian formulation and the current configuration for the Updated Lagrangian formulation. Pai [22] asserts that Total Lagrangian solutions are more accurate for highly flexible structures, avoiding error accumulation along the load increments and coordinate transformations. Solution procedures using Total Lagrangian approach are well developed in the literature for different element types using Green Lagrange strains and Second Piola-Kirchhoff stress [24]. However, those strain and stress measures are not geometrical, hence experimentally obtained material constants cannot be applied directly to them. Pai and Nayfeh [25] advocate for the use of Jaumann-Biot-Cauchy to improve solutions for highly flexible structures.

Large rotations require special treatment in the implementations of finite elements. Rotational degrees of freedom (DOFs) related to Euler angles and treated independently of translational DOFs may cause spurious strains due to inconsistency between the interpolation functions used for them and for the displacements [22]. For this reason, solutions using corotational approach [26, 27] are a good alternative, subtracting the rigid-body displacement and dealing with small rotations, which are vector quantities in a local element frame. As an alternative to Total Lagrangian and Updated Lagrangian solutions, the corotational approach has gained popularity [26].

1.2.2 Geometrical Nonlinearities

A structure modeled with constant stiffness and mass matrices is amenable to simpler linear solutions. However, as the structure is deformed stiffness and mass representations may change due to the assumed configuration. These effects are the nonlinearities, which can be caused by large displacements and/or rotations, nonlinear material properties or varying boundary conditions. This work is focused on geometrical nonlinearities, with all the examples considering linear material properties and non-contact problems. [1]

Geometrical nonlinearities arise from changes in configuration due to large displacements. A simple example to understand geometrical nonlinearities is an element with local coordinates, subjected to forces and rotated. Locally, the element has a stiffness matrix $\hat{K}$, that gives the force $\hat{f}$ after a generalized displacement $\hat{x}$ in the local frame, such as

$$\hat{K} = \frac{\partial \hat{f}}{\partial \hat{x}} \tag{1.1}$$

where $\frac{\partial \hat{f}}{\partial \hat{x}}$ is a square matrix where the i^{th} column is $\frac{\partial \hat{f}}{\partial \hat{x}_i}$.

[1] Note that the formulation developed in this dissertation could as well be applied to problems with material nonlinearities, after further developments.

A transformation leads from the local forces $\hat{f}$ to the global forces f through

$$f = \frac{\partial x}{\partial \hat{x}} \hat{f} = T_{gl} \hat{f} \tag{1.2}$$

where x are the generalized displacements in the global frame and T_{gl} is the transformation matrix from local to global frames.

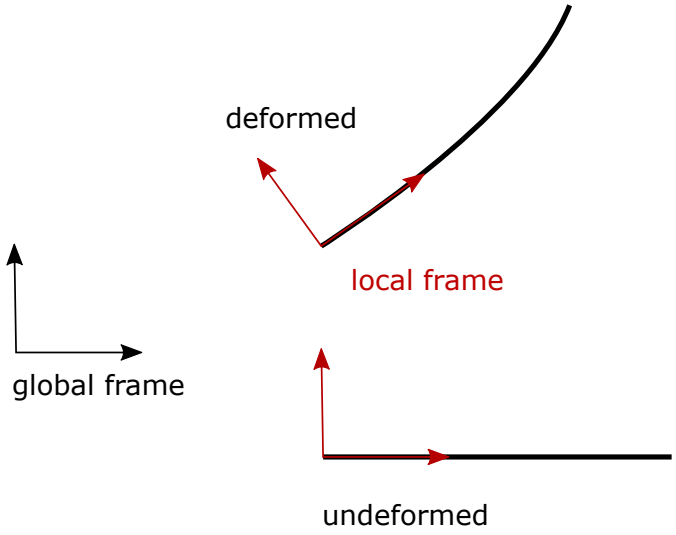

Figure 1.5: Global and local frames in undeformed and deformed configurations.

Figure 1.5 illustrates the local and global frames. In the global frame, the stiffness K is calculated from the derivative of generalized force f with respect to the generalized displacements x in the global frame, i.e.,

$$\begin{aligned} K &= \frac{\partial f}{\partial x} \\ &= \left[\frac{\partial T_{gl}}{\partial x} \hat{f}\right] + T_{gl} \frac{\partial \hat{f}}{\partial \hat{x}} \frac{\partial \hat{x}}{\partial x} \\ &= \underbrace{\left[\frac{\partial T_{gl}}{\partial x} \hat{f}\right]}_{\text{pre-loading effect}} + \underbrace{T_{gl} \hat{K} T_{gl}^T}_{\text{geometrical change effect}} \end{aligned} \tag{1.3}$$

where $\left[\frac{\partial T_{gl}}{\partial x} \hat{f}\right]$ is a matrix and its i^{th} column is $\frac{\partial T_{gl}}{\partial x_i} \hat{f}$.

Equation 1.3 shows that the stiffness as measured in the global frame changes due to two main effects. First, the internal forces on the deformed configuration may act stiffening or softening the structure, depending if it is extension or compression, respectively. This is the pre-loading effect. Second, the rotation of each element means that the global and local frames are not aligned after deformation. Vertical displacements that would be related to pure bending in the undeformed condition are associated to an axial component in the rotated condition. In total, the effect is a change in the global stiffness, if the formulation is based on displacements observed in the global frame.

Nonlinear vibration is a subject with extensive literature [28, 29]. The Duffing equation is generally used as a model to represent nonlinear oscillators. From these systems, interesting phenomena are observed, like jumps in the amplitude of frequency response and hysteresis, subharmonic and superharmonic resonances and even chaotic behavior. Perturbation methods [30] are used to solve weakly nonlinear problems, but problems of large displacements may not be amenable to such solutions [22].

1.2.3 Structural ROMs

In nonlinear structural dynamics, ROMs based on modal formulations from complete finite element configurations have been used extensively. Initially, these methodologies aimed at vibration problems for panels undergoing nonlinear displacements in the order of the magnitude of their thickness. Such problems arise in the context of large acoustic [31] and/or aerodynamic excitation and thermal loading, such as in components of launch vehicles or high-speed aircraft [32]. In this context, membrane stretching is coupled with transverse displacements in a quasi-static way. As large deflections develop, this coupling will usually lead to softening of the effective stiffness related to the transverse modes [33].

As demonstrated by Mignolet and Soize [34] through a Galerkin approach, ap-

proximations of the elastodynamic equations with a weak formulation using a set of basis functions lead to nonlinear quadratic and cubic terms for the stiffness. These terms can be obtained from the identification of the finite element static solutions. In fact, this was done by Shi and Mei [33], who proposed a time-domain modal formulation including the quadratic and cubic stiffness terms calculated from the complete FEM formulation. However, the nonlinear stiffness tensors for a complex model are not available from typical commercial finite element solvers.

In order to use the existing libraries of those commercial codes, indirect methods for estimation of modal nonlinear stiffness were proposed. Segalman and Dohrmann [35, 36]proposed the Method of Quadratic Components as a tool to analyze rotating flexible structures, using nonlinear static results for enhancing the description of displacements up to second order. Their work was devoted to cantilevered structures, where the large displacements are on the order of the beam length. Muravyov *et al.* [37] and later Muravyov and Rizzi [38] suggested the enforcement of displacements in the shapes of linear modes to recover the quadratic and cubic modal nonlinear stiffness terms using a sequence of nonliner static solutions. In the case of enformed displacements, the solutions are the forces needed to achieve those displacements. McEwan *et al.* [39] proposed a similar method for identification using loads in the shapes of linear modes and fitting the nonlinear stiffness coefficients. Later, Hollkamp and Gordon [40] improved the recovery of in-plane displacements by fitting them as static functions of the modal coordinates, leading to the Implicit Condensation and Expansion (ICE) method, which improved the kinematic description and simplified the recovery of stress.

Both the methods of identification, either using enforced displacements or imposing large forces, have led to well-identified ROMs (e.g., [41] and [42]). However, Kuether and Allen [43] investigated accuracy of both identification versions using nonlinear normal modes calculated with a continuation algorithm [44] and found that

the method of identification imposing forces and using static condensation of in-plane displacements is more accurate.

In-plane displacements may be treated as additional degrees of freedom with their own dynamics or may be condensed into the dynamics of the transverse large-amplitude displacements, assuming quasi-static dependence. For problems of shells constrained on all sides, the condensation makes sense because the inertia loads related to these in-plane displacements may be neglected. However, if this kinetic energy related to the in-plane displacements is important, then an independent dynamics may be beneficial, despite increasing the number of degrees-of-freedom. Mignolet and co-workers developed methods using this approach, including dual modes to represent the in-plane displacements effectively and identifying nonlinear stiffness coefficients [41, 45].

An important aspect of nonlinear ROMs is the selection of a basis for the description of displacements. Usually, the first linear modes are included due to their importance in the responses. However, the nonlinear displacements may be selected either from higher-frequency linear modes or from snapshots of representative solutions. This last option is more compact and effective in representing large displacements. In order to extract significant shapes to enhance the displacement description, proper orthogonal decomposition (POD) techniques are usually employed, leading to the additional basis of dual modes. Kim *et al.* [41] details a procedure for obtaining dual modes, along with methods for reducing the number of nonlinear stiffness terms to be identified, using symmetry and scale considerations. Alternative methods for basis selection exist to represent displacements, like methods using short-duration dynamic solutions and identification techniques, looking for shapes that contribute to both displacements and strain energy. The work of Przekop *et al.* [46] compares different methodologies for basis selection with identification. These approaches are suitable for experimental results. A recent development by Wang *et al.* [47] proposed

a method to analyze localized effects such as cracks by including an additional set of dual modes restricted to a detailed region of the model.

An extensive review of the approaches for nonlinear modal ROMs is presented by Mignolet *et al.* [48]. More recently, good results for static solutions of the modal nonlinear approach applied to cantilevered structures undergoing displacements on the order of the structure's length were presented in Kim *et al.* [49] and Wang *et al.* [45]. A nonlinear modal ROM based on fittings of potential energy and displacements was introduced by Ritter *et al.* [50] and later applied to static and dynamic simulations of a wing box [51] and a very flexible aircraft [20, 52], including flight dynamics and coupling with a vortex lattice solver. Medeiros *et al.* [53] included the kinetic energy of the nonlinear displacements and demonstrated dynamic solutions with a few degrees of freedom representing large displacements. This improved framework is used in this dissertation to represent the structural dynamics, and it is called the Enhanced Implicit Condensation and Expansion (EnICE) method.

For analysis of complex structures, it may be advantageous to integrate nonlinear ROMs of its different parts. Substructuring techniques have been developed to integrate ROMs. Kuether *et al.* used the ICE method and integrated the ROMs of two geometrically nonlinear plates [54]. This kind of development is important to allow effective use of nonlinear ROMs in the design environment. Interface reduction techniques have also been developed to allow integration of parts without increasing considerably the number of degrees of freedom of the assembled system [55, 56]. Another advantage of integration between nonlinear ROMs is the possibility to use mature multibody dynamics methods for analyses including large flexibility. In fact, aeroelastic frameworks have been successfully developed based on multibody dynamics [57, 58].

In terms of structural ROMs, the main contribution of this dissertation is the development of the first modal-based approach with static condensation including the

kinetic energy of nonlinear displacements in the dynamics. As indicated by Kuether *et al.* [43], static condensation may provide more accurate results. That is due to a decreased number of degrees-of-freedom and an identification that avoids reference solutions with enforced displacements. However, this method could be incaccurate for time-domain analyses involving large displacements. The inclusion of the kinetic energy of dual modes corrects the modal inertia loads. That correction may increase substantially the accuracy of time-domain simulations of slender structures.

1.3 Nonlinear Aerodynamics

Aerodynamic solutions present nonlinear effects due to compressibility effects, viscous influences, and large displacements. There are low and medium-fidelity solutions using strip theory, Vortex Lattice Method (VLM), Doublet Lattice Method (DLM) and panel methods, in both steady and unsteady versions. Additionally, for cases involving separation and dynamic stall, there are useful semi-empirical approaches such as the Leishman-Beddoes [59] and the ONERA [60] methods. In the computational fluid dynamics (CFD) realm, Reynolds Averaged Navier-Stokes (RANS) equations, while computationally expensive for time-domain analyses, provide a more accurate means of determining the loads.

This section provides an overview of nonlinear effects in aerodynamic simulations and review of output-based aerodynamic ROMs.

1.3.1 Nonlinearities in Aerodynamic Loads

In a review of nonlinear aeroelasticity applied to high-aspect-ratio wings, Afonso *et al.* [6] pointed four sources of nonlinearity related to aerodynamic loads: boundary layer effects, shocks, wake roll-up related to large displacements and geometric coupling between aerodynamic loads and deflections. The first two phenomena are

general for any aircraft flying in the supersonic or transonic regimes, with shock-/boundary layer interactions playing an important role on the aeroelastic response. The wake roll-up is usually related to leading-edge separation, and leads to lift force increase over thin and swept wings in the subsonic regime. The geometric coupling between aerodynamic loads and large displacements is specific to very flexible structures. This nonlinearity is related to follower forces and significant changes of aerodynamic interactions due to the large deflections.

1.3.2 Aerodynamic ROMs

Considering the nonlinear aerodynamic effects, ROMs have been developed to reduce computational costs and to allow extensive design and simulation investigations.

During the past 20 years, many techniques have been published for reduced order systems. A few literature reviews are available, such as Lucia *et al.* [61] and Taira *et al.* [62], as well as numerous conferences proceedings and books on the theme (e.g., [63–65]). Also, there are publications focused on the practical aspects of reduced order models, like sampling and interpolation, e.g., Forrester *et al.* [66].

The aerodynamic ROMs can be classified in output-based or projection-based. The first class refers to the ROM methods that use histories of outputs as reference data for new predictions. The second class comprises methods based on approximate solutions for the residue equations. The output-based ROMs are generally faster and more adequate for aeroelastic analyses, while the projection-based ROMs will involve more states in the solution, with the potential to obtain more accurate details of the pressure distribution. This review is focused on the output-based methods.

Even in the transonic regime, the aerodynamic solutions can be linearized around a given nonlinear state, given that no large deformations or variations of angle of attack occur about that point. For this reason, linear identification methods are extensively used for model reduction.

Linear identification methods can be applied to discrete-time state-space representations or frequency-domain analyses. For discrete systems, dynamic reference simulations serve as training data for the identification of the system dynamics.

State-space methods employ representations of dynamic systems with matrix relations between the inputs $\mathbf{u}$, the states $\mathbf{x}$, and the outputs $\mathbf{y}$. For discrete-time systems, such as discretized CFD simulations, these quantities are written at the time step k as

$$\mathbf{x}(k+1) = \mathbf{A}\mathbf{x}(k) + \mathbf{B}\mathbf{u}(k) \tag{1.4}$$

$$\mathbf{y}(k) = \mathbf{C}\mathbf{x}(k) + \mathbf{D}\mathbf{u}(k) \tag{1.5}$$

where $\mathbf{x}$ is a column vector with n terms representing the states, $\mathbf{A}$ is an $n \times n$ matrix that describes the dynamics of the system, and $\mathbf{B}$ is an $n \times m$ matrix representing the influence of the input $\mathbf{u}$ with m entries. $\mathbf{C}$ is the $p \times n$ matrix relating the output $\mathbf{y}$ and the states, while $\mathbf{D}$ is the $p \times m$ matrix relating the direct dependence of the outputs on the inputs.

The identification of the dynamic matrices may be performed around a nonlinear state. The identified system of Equations 1.4 and 1.5 is used then to predict the evolution of the system for a given input. Silva [67, 68] used this method for flutter predictions and root locus analysis with different transonic and supersonic configurations. Joint identification involving structural and aerodynamic states is possible. One of the methods used to identify the system representation matrices is the Eigensystem Realization Algorithm (ERA) [69]. Silva [70] also proposed a method for simultaneous excitation of different modes in a single dynamic simulation using Walsh functions, saving time for generation of model reference data.

Frequency-domain methods are an alternative for model reduction of linear sys-

tems. In this case, for aeroelastic analyses the focus is the estimation of generalized aerodynamic forces as function of the reduced frequency. The CFD reference simulations can be used for such task [71]. Special techniques to obtain smooth power spectral densities of the input signals and outputs may improve the results significantly [72].

In the nonlinear realm, techniques exist to deal with state-space representations, writing the dynamic and input influence matrices $\mathbf{A}$ and $\mathbf{B}$ as function of the states $\mathbf{x}$. Klock and Cesnik [73] proposed to use perturbations on the states to calculate the derivative $\dot{\mathbf{x}}$ using high-fidelity tools and use these results as samples for fitting. In this case, polynomials up to the sixth-order were used for fittings. This technique was applied for hypersonic vehicle simulation with reduction of computational costs around 15 times.

Among the methods for output-based aerodynamic ROMs, the Volterra series is a popular technique. It is based on the idea of convolution, which is valid for linear systems, but can be extended with higher-order kernels for nonlinear problems. The kernels of the Volterra functions are usually identified from CFD simulations using impulse or step responses at different amplitudes, but frequency-domain method can also be used. Raveh [74] noticed that identifications with step responses are less sensitive than analyses using impulse response. However, increasing the order of the kernels may lead to identification challenges, due to the many couplings in systems with multiple degrees of freedom. Balajewicz *et al.* and Balajewicz and Dowell [75] proposed methods to reduce the number of terms in the identification, improving the robustness of the models.

Since the identification of Volterra series with a large number of nonlinear terms may create accuracy issues, it was proposed by Raveh [74] that using a first-order Volterra series and adjusting the kernel according to the amplitude of the input could lead to better responses than increasing the order of the series. Later, this procedure

was generalized by Skujins and Cesnik [1, 76, 77]. The idea of correction factors for linear convolution was initially applied to hypersonic investigations, and later for varying Mach regimes. The basic approach is to use linear convolution to predict an unsteady aerodynamic output (lift, drag, generalized aerodynamic forces, etc.) and to correct it with a factor estimated from large, nonlinear static simulations. Different steady simulations can be run off-line to produce a surrogate for the correction factor. In the case of expensive simulations, the Method of Segments [1] can be used as a cheaper alternative to predict steady loads based on the local angle of attack.

More recently, methods using neural networks and Gaussian processes have been used to identify transient aerodynamic loads. Faller and Schreck [78] are among the first to use neural networks in unsteady fluid dynamics. They focused on rotorcraft aerodynamics, predicting pressure coefficients under large-amplitude motion. Marques and Anderson [79] used multi-layer functionals, which are temporal neural networks, for the prediction of unsteady aeroelastic loads. A particular shape of neural network was applied, called Finite Impulse Response (FIR). The choice of samples and network architecture was realized via a genetic algorithm and random search, which improved predictions for the two-dimensional pitching airfoil. Huang *et al.* [80] proposed to use a Wiener-type parallel cascade system. This system is interesting because the residue can be reduced successively using a series of Wiener-type elements, each one having a linear representation for the dynamic part followed by a static neural network to bring the nonlinearity. Using this approach, they could predict the flutter velocity and dynamic response of the Isogai wing [81] in the transonic regime. This approach of separating nonlinear steady contributions and linear unsteady ones resembles the aerodynamic method adopted in this dissertation.

The work of Winter and Breitsamter [82, 83] deserves a special mention for the applicability to transonic wings and complex aircraft configurations, like the Common Research Model (CRM). They perform identification using a few unsteady reference

simulations. A model is fitted to predict the aerodynamic outputs based on the previous history of outputs and inputs. For this fitting, Local Linear Neuro-Fuzzy models are employed. The training is specifically performed using the Local Linear Model Tree type of neural network. Using POD to represent the pressure distribution over the wing, good matching was observed between reference solutions and predictions over a range of reduced frequencies. The nonlinear fittings of neural networks may be improved using physical considerations for the selection of training inputs and delay states, as demonstrated by Wang *et al.* [84] using an error assessment.

POD is a tool largely used in output-based aerodynamic ROMs. In this case, it is used for compact representation of fields, like pressure coefficient distributions over wings. Usually, it is linked to surrogate model, like neural network or Gaussian process regression. Different variants of the POD exist to represent data sets with mixed quantities, like displacements and rotations. For linear systems, the balanced POD [85] scales the data to match the observability and controllability Grammians. This method has led to good results for unsteady aerodynamic ROMs [86,87]. Walton *et al.* [88] used POD for both field representation and temporal evolution. Using sets of reference solutions obtained with different excitation parameters, a POD was performed on the temporal evolution.

Other output-based ROM techniques that deserve mention are the Rational Function Approximations (RFAs). The RFA is a fitting function appropriate for the representation of unsteady generalized aerodynamic forces, from two-dimensional sections to complete configurations. Generally, the equations of motion for aeroelastic systems will include aerodynamic forces in the form of transcendental functions related to the convection phenomena. RFAs are used to approximate the Laplace transform of the transfer function between generalized aerodynamic displacements and loads. Then, the system is written in a state-space representation for time-domain simulations. Initial studies were focused on linear systems [89, 90]. However, the method can be

extended to nonlinear conditions, including effects of viscosity and compressibility via a model scheduling, adjusting the coefficients to different conditions of angle of attack, Mach number and reduced frequency. This methodology was proposed by Liu *et al.* [91, 92] and Friedmann [93], who used the RFA approach developed by Myrtle and Friedmann [94] and extended it with high-fidelity results and coefficients adapted to different conditions in the context of rotorcraft applications.

1.4 Objectives of this Dissertation

For the development of extensive time-domain simulations involving large displacements, it is imperative to employ nonlinear ROMs. Current structural modal solutions based on static condensation fail in conditions of large displacements due to the neglected kinetic energy of nonlinear components. This dissertation introduces a correction to the equations of motion, allowing accurate dynamic simulations with large displacements. On the structural side, the objective is to develop and verify the proposed formulation, applying it to model examples and built-up structures. For the aerodynamic analysis, the objective of this work is to extend the formulation of the Method of Segments developed by Skujins and Cesnik [1, 21, 76, 77] to nonlinear conditions involving large displacements and rotations. Considerations of flight mechanics are not included, even though the formulations developed are general and can be applied in the future for aeroelastic analyses of aircraft in free-flight.

Summarizing, the objectives of this dissertation are:

- To develop and implement a ROM formulation for modal-based nonlinear structural dynamics analyses involving large displacements;
- To demonstrate the aeroelastic analysis applicability of the structural ROM developed for built-up GFEM undegoing large-amplitude dynamic loading;

- To extend the Method of Segments for conditions of large wing deformations, implementing finite rotations for the segments and corrections for induced agle of attack;

- To demonstrate the aeroelastic analyses with the developed structural and aerodynamic ROMs applied to cantilevered wings.

1.5 Thesis Organization

Chapter 2 describes the formulation of the newly developed structural nonlinear modal ROM, the EnICE. In Chapter 3, the formulation of the Method of Segments is outlined. Chapter 4 describes the numerical implementation of the nonlinear ROMs, while Chapter 5 presents application of the ROMs to different structures. Finally, the conclusions and outlook of future research are presented in Chapter 6. Appendix A provides details about the parameters used in the ROM identifications and simulations, while Appendix B presents the data for the 16-m wing investigated in the results chapter. Appendix C presents an additional study where the EnICE was integrated to a CFD solver to investigate flutter onset for a high-aspect-ratio wing.

CHAPTER 2

Enhanced Implicit Condensation and Expansion Formulation

This chapter presents the formulation of the newly developed nonlinear structural model reduction method, called Enhanced Implicit Condensation and Expansion (EnICE). First, the Implicit Condensation and Expansion (ICE) formulation is presented as a starting point for the enhancement introduced in this dissertation. Then, assumptions and equations of motion (EOM) of the EnICE method are presented. The offline training process is explained in the second section, along with the required fittings of the nonlinear functions. After that, a fomulation for inclusion of fictitious loads arising from base motion in the context of EnICE is explained. Finally, there is a brief discussion about time integration methods to solve the resulting system of ordinary differential equations.

A schematic representation of the path followed in this chapter to explain the formulation of the EnICE approach is detailed in Fig. 2.1.

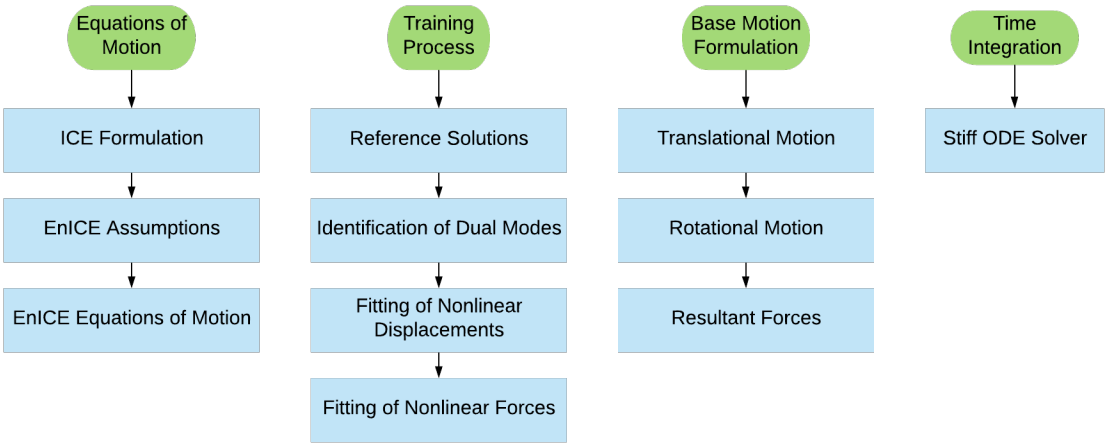

Figure 2.1: Various pieces of the formulation presented in Chapter 2.

2.1 Equations of Motion of the EnICE Method

2.1.1 Previous Formulation: Implicit Condensation and Expansion Method

Nonlinear displacements can be addressed using finite strain formulations to write the equations of motion of a structure. One example of finite strain suitable for such equations is the Green-Lagrange strain, which is conjugate to the Second Piola-Kirchhoff stress tensor. These strain and stress measures are objective, meaning that they do not change under rigid-body translations or rotations. Even assuming linear stress-strain relations, the equations of motion are nonlinear, due to the nonlinear strain-displacement relations. Discretizing the equations of motion and assuming displacements u as a linear combination of a basis of generalized displacements Z with amplitudes q, *i.e.*,

$$u = Zq \tag{2.1}$$

then the equations of motion are projected onto the basis Z in a Galerkin approach

are given by

$$M_{ij}\ddot{q}_j + K_{ij}^{(1)}q_j + K_{ijl}^{(2)}q_j q_l + K_{ijlp}^{(3)}q_j q_l q_p = f_i \tag{2.2}$$

where the terms M_{ij} are the entries of the reduced mass matrix, f_i are the modal components of the external force, and the terms $K_{ij}^{(1)}$, $K_{ijl}^{(2)}$ and $K_{ijlp}^{(3)}$ are the components of the reduced stiffness tensors. The analytical expression of these terms is related to the displacement basis functions and the constitutive relations for the material, as shown by Mignolet and Soize [34]. However, the explicit calculation of these coefficients is not practical for a built-up finite element structural model. For this reason, inference about the nonlinear terms from static solutions is desirable.

For a complete representation, Z should include displacement effects observed in both linear and nonlinear conditions. For a shell constrained on all sides, for example, the linear displacements would involve only transverse components, while the in-plane ones would be captured by additional basis vectors appropriate for nonlinear displacements.

A static condensation process reduces even further the degrees of freedom involved in Eq. 2.2 by splitting the displacements into bending and membrane ones. For shells constrained on all sides, this classification makes sense. Assuming that the membrane modes are functions of the bending displacements and forces along the membrane components, a static condensation is performed. A summary of the process starting from the nonlinear equations for all the degrees of freedom up to the nonlinear modal equations in condended form is presented in Fig. 2.2. In the end, only modal degrees of freedom related to the bending components are effectively used and the membrane displacements are implicitly included. More details about the static condensation process are found in Mignolet *et al.* [48] and Przekop *et al.* [95]. However, it is not useful to write down the equations relating membrane and bending modal amplitudes explicitly here. The assumptions of which particular terms can be neglected and which

ones cannot only introduce additional approximations. The goal is for the final modal equations to have quadratic and cubic nonlinearities in terms of bending modes only. The Implicit Condensation (IC) method introduced by McEwan *et al.* [39] includes the bending modes in the analyses, and all stiffness changes related to the couplings with membrane modes are implicitly included.

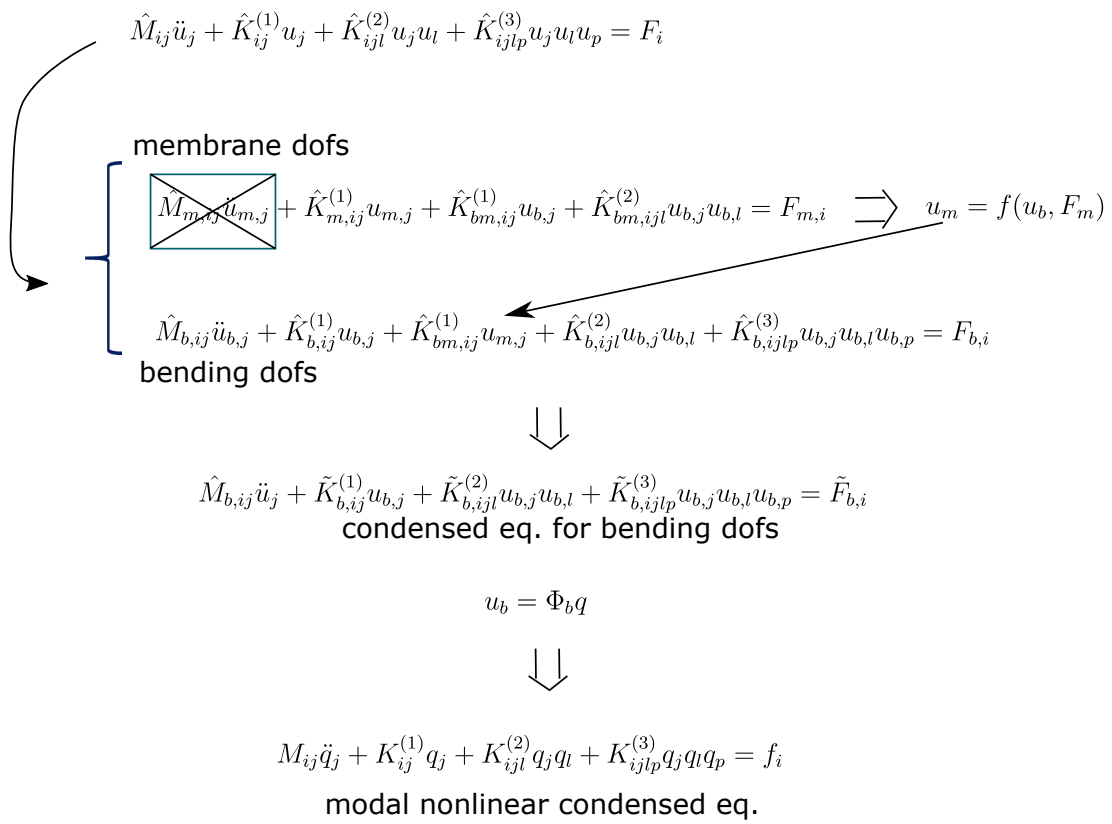

Figure 2.2: Static condensation process leading to nonlinear modal equations with bending modes only.

The IC method does not treat directly the membrane displacements, but these are naturally present when large distributed forces excite nonlinear displacements. The identification of nonlinear terms cannot be performed with enforced displacements, otherwise the membrane components will be restricted. Instead, forces in the shape of the first linear modes (bending degrees of freedom only) are applied to excite nonlinear static responses. The IC identifies the nonlinear terms $K^{(2)}_{ijl}$ and $K^{(3)}_{ijlp}$ using a seris of

static nonlinear results obtained from finite element solutions. This method is non-intrusive in the sense that only outputs are needed for identification of the governing equations. With the IC, only the first modes related to transverse displacements are included in the modal Eq. 2.2. If no static condensation was assumed, additional bases for displacements along the in-plane directions would have to be included for nonlinear computations.

Solving the equations of motion with the degrees of freedom related to the transverse modes only, the general displacements cannot be recovered. Hollkamp and Gordon [40] proposed the Implicit Condensation and Expansion (ICE) method to allow the complete recovery of the deformed shape. In this way, stresses can be calculated as well. Using a discretized finite element model, generalized displacements of all nodes are expressed in modal form as

$$u = \Phi q + \Psi r\,(q) \tag{2.3}$$

where u is a column matrix representing all the displacements and rotations of the nodes, Φ is a matrix with discretized shape functions along its columns to represent the linear contribution to displacements, q is a column matrix with the amplitudes related to the linear basis Φ, Ψ is a matrix with discretized shape functions along its columns to represent the nonlinear contribution to displacements, and r is a column matrix with amplitudes related to the nonlinear basis Ψ.

The approximation of Eq. 2.3 is equivalent to Eq. 2.1, with the basis Z explicitly split into linear components Φ and nonlinear components Ψ with its associated amplitudes r. From previous works [34, 96, 97], Ψ is called the set of dual modes.

The difference between the ICE method and the previous IC one is the separated fitting between the amplitudes of linear displacements q and nonlinear displacements r, which are the membrane modes in the case of shells constrained on all sides. For the ICE, the relation is a prescribed quadratic mapping given by

$$r_i = A_{ijl} q_j q_l \tag{2.4}$$

where the coefficients A_{ijl} are fitted using the same reference nonlinear static solutions used for identification of nonlinear forces.

The Implicit Condensation and Expansion is the initial point for the enhancement proposed in this dissertation. As discussed in the introduction, the ICE neglects the influence of nonlinear motion on the inertial loads, which is a reasonable assumption for shells. However, a modification is needed to apply the method to cantilevered structures.

2.1.2 Assumptions for Large Displacements

For the new Enhanced Implicit Condensation and Expansion method (EnICE), the basic representation of displacements is kept the same as Eq. 2.3. While this dissertation uses linear modes for the basis of linear displacements Φ, it is possible to use any set of admissible functions, which satisfy the geometrical boundary conditions of the system.

The nonlinear components of displacements are expressed using the basis Ψ, which also satisfies geometrical boundary conditions. It should be noticed that the shape functions represented by Ψ are not normal modes, since they are not free-vibration shapes.

A fundamental assumption of the model reduction method is that the amplitudes r of the dual modes are function of the amplitudes q of the linear modes. This approximation is derived from observations of nonlinear effects for plates constrained on all sides or beams constrained on both ends (*e.g.*, [41,98]), where the in-plane displacements are quadratic functions of the out-of-plane ones. Here, this assumption is extended to large-displacement conditions. The consequence of this assumption is

that the degrees of freedom of are only related to the amplitudes of the linear modes. The EnICE extends the static condensation already employed in the ICE method, applying it to large nonlinear displacements typical of cantilevered structures. However, this mapping is not assumed to be a quadratic function of the linear modal amplitudes anymore. In this way, particular simplifications of modal interactions can be avoided and there is flexibility to model more degrees of freedom without a significant increase in the number of coefficients to be fitted as in the case of polynomial fittings.

The approach of the EnICE for the nonlinear elastic modal forces is similar to the ICE, but again the nonlinear polynomial fitting is not restricted to the cubic polynomial as assumed in Eq. 2.2. The significant nonlinear displacements render the Galerkin approach inappropriate in a context of static condensation. A general nonlinear fitting as a neural network function is more adequate for the large-displacement condition.

2.1.3 Enhanced Implicit Condensation and Expansion (EnICE) Formulation

Since the nonlinear displacements are assumed to be function of the amplitude q of the linear modes (Eq. 2.3), these are the degrees of freedom of the system. With this limited set of degrees of freedom, the Euler-Lagrange equations that describe the dynamics of the system are given by

$$\frac{d}{dt}\left(\frac{\partial T}{\partial \dot{q}_i}\right) - \frac{\partial T}{\partial q_i} + \frac{\partial U}{\partial q_i} = F^T \frac{\partial u}{\partial q_i} \quad \text{for} \quad i = 1, ..., n \tag{2.5}$$

where T is the kinetic energy and U is the potential energy corresponding to the elastic strain energy of the system. F is the column matrix of applied loads, using the FE notation, where these loads may be forces and moments, conjugate to the

related nodal displacements u. The number of equations is equal to the number of degrees of freedom used to describe the displacements, given by n.

Starting from the representation of displacements (Eq. 2.3), it is possible to write the nodal velocities as

$$\dot{u} = \left[\Phi + \Psi \frac{\partial r}{\partial q}\right] \dot{q} \tag{2.6}$$

where the partial derivative of the dual-mode amplitudes with respect to the degrees of freedom q brings the contribution of the nonlinear displacements. This Jacobian is given by

$$\frac{\partial r}{\partial q} = \begin{bmatrix} \frac{\partial r_1}{\partial q_1} & \frac{\partial r_1}{\partial q_2} \cdots \frac{\partial r_1}{\partial q_n} \\ \frac{\partial r_2}{\partial q_1} & \frac{\partial r_2}{\partial q_2} \cdots \frac{\partial r_2}{\partial q_n} \\ & \vdots \\ \frac{\partial r_s}{\partial q_1} & \frac{\partial r_s}{\partial q_2} \cdots \frac{\partial r_s}{\partial q_n} \end{bmatrix} \tag{2.7}$$

where the subscript s represents the number of dual modes used to complete the description.

To calculate the kinetic energy, it is necessary to account for the system mass. The mass matrix M is extracted from the FE model for this calculation, and the kinetic energy is written as

$$T = \frac{1}{2} \dot{u}^T M \dot{u} \tag{2.8}$$

For large displacements and rotations, one can ague that the mass matrix could change. However, only the terms related to rotational degrees of freedom change. If the FEM is finely discretized, M changes only slightly with rotations. Throughout this thesis, it is assumed to be constant, an approximation that is usually valid even for moderately large displacements [22]. Often, the nonlinear dynamic simulations in

commercial FE codes preserve a constant mass matrix along the simulations, updating only the tangent stiffness matrix.

Using Eq. 2.6 into Eq. 2.8, the kinetic energy can be rewritten as

$$T = \frac{1}{2}\dot{q}^T \underbrace{\left(M_\Phi + 2M_X \frac{\partial r}{\partial q} + \frac{\partial r}{\partial q}^T M_\Psi \frac{\partial r}{\partial q} \right)}_{M'} \dot{q} \tag{2.9}$$

where the matrices M_Φ, M_X and M_Ψ represent the linear, coupled and dual-mode mass matrices, respectively. These are calculated using the modes and the mass matrix of the linear model, i.e.,

$$\Phi^T M \Phi := M_\Phi \tag{2.10}$$

$$\Phi^T M \Psi := M_X \tag{2.11}$$

$$\Psi^T M \Psi := M_\Psi \tag{2.12}$$

Usually the linear modes are mass-normalized such that the modal mass matrix is the identity matrix.

For the equations of motion (EOM), the modal elastic force represented by $\frac{\partial U}{\partial q_i}$ in Eq. 2.5 is split in linear and nonlinear components, given by

$$\frac{\partial U}{\partial q_i} = \Lambda_{ij} q_j + \frac{\partial U_{nl}}{\partial q_i} \tag{2.13}$$

where Λ is the linear modal stiffness matrix. If the basis for displacements is the set of linear modes, this matrix is diagonal and its entries are the eigenvalues related to the modes. The term $\frac{\partial U_{nl}}{\partial q_i}$ is the nonlinear component of the modal elastic force, and this is identified in the preparation of the model as a function of the linear modal amplitudes q.

Starting from the kinetic energy (Eq. 2.9), it is possible to develop the Euler-

Lagrange equations in matrix form. The first term to be developed is the partial derivative of the kinetic energy with relation to the time rates of the degrees of freedom, $\frac{\partial T}{\partial \dot{q}}$, which can be written in a column matrix as

$$\frac{\partial T}{\partial \dot{q}} = \left(M_\Phi + M_X \frac{\partial r}{\partial q} + \frac{\partial r}{\partial q}^T M_X^T + \frac{\partial r}{\partial q}^T M_\Psi \frac{\partial r}{\partial q} \right) \dot{q} \tag{2.14}$$

Taking the time derivative of Eq. 2.14, the first inertial term of the Euler-Lagrange equations is given by

$$\begin{aligned} \frac{d}{dt}\left(\frac{\partial T}{\partial \dot{q}}\right) = & \left(M_\Phi + M_X \tfrac{\partial r}{\partial q} + \tfrac{\partial r}{\partial q}^T M_X^T + \tfrac{\partial r}{\partial q}^T M_\Psi \tfrac{\partial r}{\partial q} \right) \ddot{q} + \\ & [M_X \tfrac{d}{dt}\tfrac{\partial r}{\partial q} + \tfrac{d}{dt}\tfrac{\partial r}{\partial q}^T M_X^T + \tfrac{d}{dt}\tfrac{\partial r}{\partial q}^T M_\Psi \tfrac{\partial r}{\partial q} + \tfrac{\partial r}{\partial q}^T M_\Psi \tfrac{d}{dt}\tfrac{\partial r}{\partial q}]\dot{q} \end{aligned} \tag{2.15}$$

To represent the time derivative of the Jacobian, $\frac{d}{dt}\frac{\partial r}{\partial q}$, one has

$$\frac{d}{dt}\frac{\partial r}{\partial q} = \left[\left(\frac{\partial^2 r}{\partial q^2} \right)_{sn \times n} \dot{q} \right]_{s \times n} \tag{2.16}$$

where reshaping of the matrices is used such that:

$$\left(\frac{\partial^2 r}{\partial q^2} \right)_{sn \times n} = \left[\left(\tfrac{\partial^2 r}{\partial q_1 \partial q} \right)_{sn \times 1} \left(\tfrac{\partial^2 r}{\partial q_2 \partial q} \right)_{sn \times 1} \cdots \left(\tfrac{\partial^2 r}{\partial q_n \partial q} \right)_{sn \times 1} \right] \tag{2.17}$$

In Eqs. 2.16 and 2.17, the sub-indexes indicate a reshaping from the original format of the matrices. In $\left(\frac{\partial^2 r}{\partial q_1 \partial q} \right)_{sn \times 1}$, for example, the matrix $\frac{\partial^2 r}{\partial q_1 \partial q}$ has originally the shape $s \times n$, since it is the partial derivative of the Jacobian $\frac{\partial r}{\partial q}$ with respect to the first degree of freedom q_1. However, the reshaping transforms it into a column matrix with sn rows. For this reshaping, the order of the elements along each column is followed, *i.e.*, $\left(\frac{\partial^2 r}{\partial q_1 \partial q} \right)_{sn \times 1}$ is a vertical stacking of the columns from $\frac{\partial^2 r}{\partial q_1 \partial q}$. The same order along columns is used for all shape changes.

The second term of inertia in the Euler-Lagrange equations is $\frac{\partial T}{\partial q}$. Taking the partial derivative of Eq. 2.9 with respect to the degrees of freedom q, yields:

$$\frac{\partial T}{\partial q} = \left[\dot{q}^T \left(M_X + \frac{\partial r}{\partial q}^T M_\Psi\right) \left(\frac{\partial^2 r}{\partial q^2}\right)_{s\times n^2}\right]^T_{n\times n} \dot{q} \tag{2.18}$$

where the second derivative of the dual-mode amplitudes $\left(\frac{\partial^2 r}{\partial q^2}\right)_{s\times n^2}$ is written as

$$\left(\frac{\partial^2 r}{\partial q^2}\right)_{s\times n^2} = \left[\frac{\partial^2 r}{\partial q_1 \partial q} \quad \frac{\partial^2 r}{\partial q_2 \partial q} \cdots \frac{\partial^2 r}{\partial q_n \partial q}\right] \tag{2.19}$$

with the n different derivatives of the $s \times n$ Jacobian $\frac{\partial r}{\partial q}$ stacked side-by-side.

In order to complete the development of the EOM, the modal forces $\frac{\partial u}{\partial q_i}^T F$ must be written in terms of linear and dual modes as

$$\frac{\partial u}{\partial q}^T F = \left(\Phi + \Psi \frac{\partial r}{\partial q}\right)^T F \tag{2.20}$$

Combining the results of Eqs. 2.13, 2.15, 2.18, and 2.20 into Eq. 2.5, one gets a set of n ordinary differential equations given by

$$\begin{aligned} \left(M_\Phi + M_X \frac{\partial r}{\partial q} + \frac{\partial r}{\partial q}^T M_X^T + \frac{\partial r}{\partial q}^T M_\Psi \frac{\partial r}{\partial q}\right) \ddot{q} + \\ \Big[M_X \frac{d}{dt}\frac{\partial r}{\partial q} + \frac{d}{dt}\frac{\partial r}{\partial q}^T M_X^T + \frac{d}{dt}\frac{\partial r}{\partial q}^T M_\Psi \frac{\partial r}{\partial q} + \frac{\partial r}{\partial q}^T M_\Psi \frac{d}{dt}\frac{\partial r}{\partial q} - \\ \left[\dot{q}^T \left(M_X + \frac{\partial r}{\partial q}^T M_\Psi\right) \left(\frac{\partial^2 r}{\partial q^2}\right)_{s\times n^2}\right]^T_{n\times n} \Big] \dot{q} \\ = \left(\Phi + \Psi \frac{\partial r}{\partial q}\right)^T F - \Lambda q - \frac{\partial U_{nl}}{\partial q} \end{aligned} \tag{2.21}$$

Equations 2.21 can be integrated in time to obtain the linear modes. With these, one can recover the magnitudes of the dual modes and obtain the complete state of

displacements, using Eq. 2.3.

The formulation discussed above is the backbone of the structural ROM. The next section discusses the training process followed to identify the dual modes Ψ and the nonlinear functions of displacements and forces.

2.2 Training Process

The training process for the development of structural ROMs starts with reference solutions. A database of nonlinear static responses is built to support the model identification. First, a set of dual modes is isolated. Then, amplitudes of the dual modes are fitted as functions of the linear modal amplitudes. Finally, nonlinear modal forces are also fitted as functions of the linear modal amplitudes. A flowchart of the training process from the estimation of loads for reference solutions until the fitting of neural networks for the nonlinear modal forces is presented in Fig. 2.3.

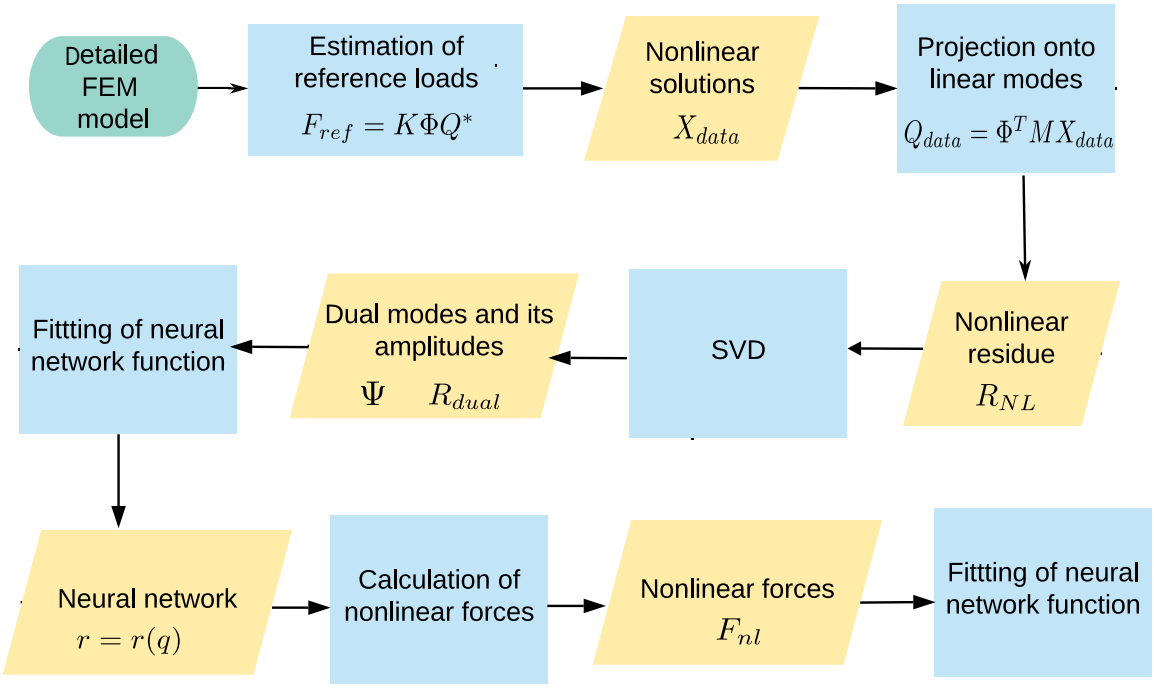

Figure 2.3: Training process for fitting of the nonlinear displacements and forces.

2.2.1 Reference Solutions

One of the key steps in the calculation of structural ROMs is the estimation of reference loads. It is necessary to excite the range of motion that will be encountered in future simulations with the ROM. Also, the distribution of loads along the degrees of freedom should resemble the expected simulation cases.

Previous studies [39, 43, 50] have suggested to use loads that would produce linear displacements and rotations in the shape of linear modes. In fact, these forces and moments are distributed and can approximately represent a great variety of conditions encountered in aeroelastic applications, for instance.

Most of the previous developments used contributions from up to three linear modes to compose the reference forces. In this work, each reference force considers contributions from all linear modes simultaneously. In this way, it is possible to cover more uniformly the range of loads using pseudo-random Halton sequences [99]. The reference loads are given by

$$F_{ref} = K\Phi Q^* \tag{2.22}$$

where F_{ref} is a matrix with each column of generalized loads (forces/moments) representing a different load case and Q^* is a matrix where each column contains the modal amplitudes for a load case. If the system were linear, the generalized displacements obtained from this series of loadings would be exactly the displacements ΦQ^*. However, due to nonlinearities, the actual results are different.

Selecting the amplitudes Q^* for the training loads requires some experimentation with the structure. If, at some point of the simulation, the linear modal amplitudes q are outside the training range for one or more of the components, then it may be an indication that the training cases need to be expanded. There is no way to know upfront what will be the expected loads, especially for dynamic simulations. For this

work, the first load estimates were calculated applying tip forces statically until the deformations achieved were in range expected for the simulations. For example, one can apply a tip vertical force until nonlinear static results for tip displacements higher than 30% of the semi-span are obtained. If the column matrix of generalized loads corresponding to this case is F, the modal amplitudes to be used as bounds for Q^* are given by

$$q^* = \left(\Phi^T K^T K \Phi\right)^{-1} \Phi^T K^T F \tag{2.23}$$

which comes from $K\Phi q^* \approx F$.

In order to establish the bounds for Q^*, different tip loads should be investigated. These include combinations of chordwise and vertical loads, as well as twist moments.

If the training loads are too high, convergence problems may be encountered with the nonlinear static finite element solution at some point of the training. In this case, the loads must be lowered for a proper training.

From the bounds established for each linear modal amplitude, the training cases are uniformly distributed and grouped in the matrix Q^*. It may happen that additional training cases are needed for more accurate simulations under certain loads. For example, it may be helpful to use a certain distribution of loads as a training case if this is an expected simulation condition, like in the case of distributed loading in aeroelastic analysis.

The responses of the training load cases are stored in the columns of a matrix of solutions X_{data}, i.e.,

$$X_{data} = [u_1 \quad u_2 \ldots u_m] \tag{2.24}$$

for a database of m training cases, where each column u_i represents a nonlinear displacement solution.

The nonlinear displacements obtained may not be written in terms of linear modes only. If these displacements are projected onto the basis of linear modes, it is possible to get the amplitudes that best represent them, but a non-negligible residue will remain. This projection onto the basis of linear modes is defined as

$$Q_{data} = \Phi^T M X_{data} \tag{2.25}$$

where the matrix Q_{data} contains the modal amplitudes that best approximate the training solutions. For this projection, the mass matrix is used because the linear modes are orthogonal with respect to the mass matrix.

The nonlinear residue for the displacements is represented by

$$R_{NL} = X_{data} - \Phi Q_{data} \tag{2.26}$$

where R_{NL} is the matrix of nonlinear residues.

2.2.2 Identification of Dual Modes

It is not possible to represent all the large displacements using only the basis of linear modes. For example, the tip of a beam will present a displacement component along its spanwise direction (Fig. 2.4) in order to approximately keep its original length. This kind of displacement is included in the modeling by means of dual modes.

The dual modes are extracted from the matrix of nonlinear residues. A singular value decomposition is performed on R_{NL}, i.e.,

$$R_{NL} = L \Sigma V^T \tag{2.27}$$

where L is the left-eigenvectors matrix, Σ is the diagonal matrix of principal values and V is the right-eigenvectors matrix. The dual modes are a subset of the left-

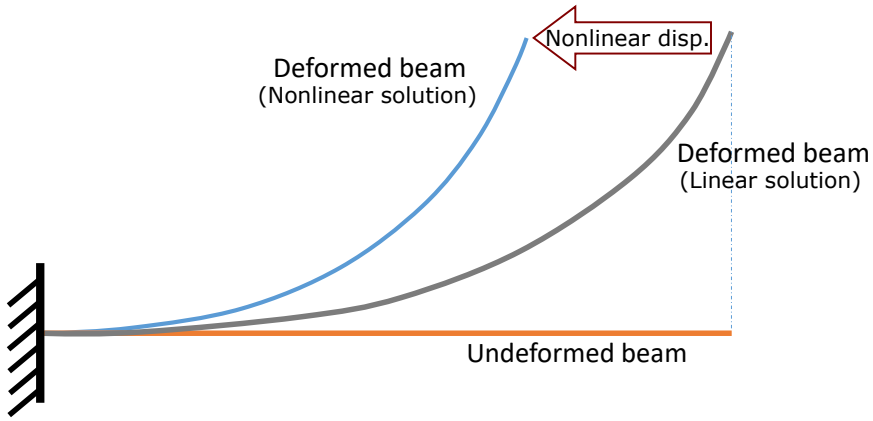

Figure 2.4: Representative nonlinear and linear solutions for a beam involving large displacements.

singular vectors, obtained through truncation.

Usually, an important quantity used to select the retained number of dual modes is the relative information content (RIC) defined by

$$RIC(d) := \frac{\sum_{j=1}^{d} \sigma_j}{\sum_{j=1}^{n} \sigma_j} \tag{2.28}$$

where n is the total number of singular values and d is the number of retained dual modes. The singular values σ_j are ordered in decreasing magnitude from $j = 1$ to $j = n$. Usually, the number d of dual modes is chosen so that the RIC is close to 1.

The set of dual modes Ψ is isolated by truncation of the left-singular vectors matrix L to the first d columns.

By truncating the right-singular vector matrix and the singular vectors matrix to the first d columns, the matrix of amplitudes of the dual modes are

$$R_{dual} = \Sigma_d V_d^T \tag{2.29}$$

where R_{dual} is the matrix with each column representing the dual-mode amplitudes

related to a particular reference solution, while Σ_d and V_d are the diagonal matrix of singular values and the right-singular matrix, respectively, each truncated to the first d columns.

Through the selection of the most important singular values, the nonlinear residue of displacements can be recovered effectively using the approximate solutions, i.e.,

$$R_{NL} \approx \Psi R_{dual} \tag{2.30}$$

The dual modes and their associated amplitudes for the reference solutions are the starting point for the fittings of nonlinear functions.

2.2.3 Fitting of Nonlinear Displacements

Having identified the dual modes and their corresponding amplitudes for the reference solutions, it is possible to relate those values to the linear modal amplitudes. As discussed before, one of the main assumption of the structural ROM is that the amplitudes of the dual modes are function of the amplitudes of linear modes, *i.e.*,

$$r = r(q) \tag{2.31}$$

In principle, any nonlinear fitting function could be used for this relation. Since dual modes are identified from nonlinear residue of displacements, there is no linear component. For this reason, and based on observation from mild deflections of plate structures, initial developments pointed to the use of quadratic functions for the fitting [48]. However, there are drawbacks related to polynomials. For example, the number of nonlinear terms grows quickly with the increase in degrees of freedom, and a strategy for selection of the most significant binomials is needed for a proper fitting, such as a cleaning of the model [45].

For this work, artificial neural networks (ANNs) were selected for the fitting of

nonlinear displacements and forces. The primary reasons for the choice were simplicity and accuracy when using a large data set for training and speed of computation, suitable for dynamic solutions.

The feedforward-kind of neural networks was chosen to represent the system. This kind of ANN does not have loops and is generically represented with layers of nodes, like in Fig. 2.5. The input layer receives the inputs, applies weights to each of them and delivers the scaled values to the hidden layer. In each node of this middle layer, the values received from the input layer are summed up and added to a bias. The resultant value is then input to a nonlinear activation function. Tangent Sigmoid activation functions are used in the hidden layer. If the response of the node is y and the input is x, the tangent Sigmoid function is

$$y = \frac{2}{1 + e^{-2x}} - 1 \tag{2.32}$$

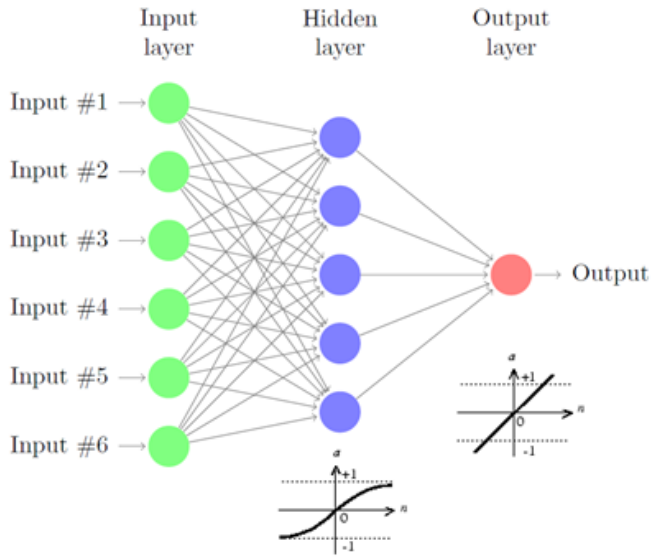

Figure 2.5: Feedforward neural network architecture with one hidden layer.

From the hidden layer, the outputs are passed to an output layer after another application of weights and bias. The output layer contains a single node with a linear

activation function.

Training an ANN is equivalent to identifying a set of weights and bias values that yield minimum error, comparing the outputs of the ANN and the reference solutions provided as samples. Training was performed using the Bayesian regularization approach, which prevents overfitting, compared to a Levenberg-Marquadt method. More details can be found in MacKay [100].

Minimization of errors generally leads to a local minimum due to nonlinear nature of the reference solution. For this reason, multiple trainings are performed with a given neural network and sample data, and the best result is selected. For the fitting of Eq. 2.31, the error was evaluated using the coefficient of determination R, with

$$R^2 = \frac{\sum_i (y_i - f_i)^2}{\sum_i (y_i - y_{avg})^2} \tag{2.33}$$

where y_i is the i^{th} sample output and f_i is the prediction of the ANN corresponding to that output, while y_{avg} is the mean of the sample results.

For each training, the set of samples available is divided into three subsets: training, validation, and testing subsets. The training data are used for minimization of the residue of the ANNs, while the validation data is used to estimate the generalization capabilities of the fitted function, in order to choose the best model. The testing subset is used for error evaluation, after training.

In this work, the error was minimized a few times for each fitting, each time with different initial weights and biases. The best solution was chosen based on the maximum coefficient of determination R evaluation of the testing subset of the samples.

The nonlinear displacements were fitted using the data from the linear modal amplitudes of the reference solutions, Q_{data}, and the amplitudes of the dual modes, R_{dual}.

For each reference solution, there are s amplitudes of dual modes. A neural

network was fitted for each one of these s amplitudes. In this way the output is only a scalar value, but each calculation of dual modes requires s function evaluations.

2.2.4 Fitting of Nonlinear Forces

The fitting of nonlinear forces is similar to the one of nonlinear displacements. The only difference is the reference data. The nonlinear forces are calculated after the fitting of nonlinear displacements, since the derivatives $\frac{\partial r}{\partial q}$ are used to calculate the nonlinear forces.

Looking at Eq. 2.21, the nonlinear forces are represented by $\frac{\partial U_{nl}}{\partial q}$. In a static condition, where the time derivatives $\dot{q}$ and $\ddot{q}$ are zero, the equilibrium is represented by

$$f_{nl} = \frac{\partial U_{nl}}{\partial q} = \left(\Phi + \Psi \frac{\partial r}{\partial q}\right)^T F - \Lambda q \tag{2.34}$$

Recalling the particular reference solutions F_{ref} prescribed in Eq. 2.22, the nonlinear modal reference forces are calculated for the i^{th} reference solution using Eq. 2.34, *i.e.*,

$$\begin{aligned} f_{nl,i} = &\quad \left(\Phi + \Psi \tfrac{\partial r}{\partial q}\right)^T K \Phi Q_i^* - \Lambda Q_{data,i} \\ = &\quad \Lambda \left(Q_i^* - Q_{data,i}\right) + \tfrac{\partial r^T}{\partial q} \Psi^T K \Phi Q_i^* \end{aligned} \tag{2.35}$$

where $f_{nl,i}$ is a column matrix with the nonlinear modal forces related to the i^{th} reference solution. It is important to notice two main components of the nonlinear force. The first one is related to the difference between the expected linear modal displacements Q_i^* and the obtained nonlinear solutions $Q_{data,i}$. The second component of the nonlinear forces is related to the contribution of the dual modes. For this second component, the partial derivative of the dual modes $\frac{\partial r}{\partial q}$ plays a fundamental role. For

each reference solution, this derivative is evaluated based on the previously fitted functions $r(q)$ evaluated at the point of the reference solution, *i.e.*, the i^{th} column of Q_{data}, or $Q_{data,i}$.

Equation 2.35 is the particular form of the nonlinear elastic modal forces when the training loads have the shape of linear modes (Eq. 2.22). However, the reference loads may take any shape more appropriate to the problem, and Eq. 2.34 is the general formulation of the nonlinear modal loads.

Grouping all the reference nonlinear forces in a single matrix, *i.e.*,

$$F_{nl} = \left[f_{nl,1} \quad f_{nl,2} \quad \dots \quad f_{nl,n} \right], \tag{2.36}$$

it is possible to fit an ANN for each row of F_{nl}, relating these data to the columns of Q_{data}, just as performed before for the fitting of nonlinear displacements.

2.3 Base Motion and Fictitious Loads

Even though this dissertation does not include a complete framework for aircraft flight dynamics simulation, the formulation of nonlinear structural ROMs can be extended to include inertia forces related to accelerated reference frames. This section explains how to include inertia forces related to translation and rotation of the reference frame in a modal formulation.

Imposing translation and rotation to a clamping point of a wing, it is possible to retrieve the displacements related to this kind of motion and also recover the loads that would be transmitted to the root of an aircraft equipped with such a wing. Since the modal formulation developed in the previous section is based on a fixed system of coordinates, the most straightforward approach to include base motion is the inclusion of modal inertial forces related accelerations of a reference point. For wing-like structures, this reference point is the point of attachment to the fuselage.

Recall the inertial loads for a single point mass m described by position vector $\vec{x}$ and velocity $\dot{\vec{x}}$ in an accelerated reference frame B. The reference frame B translates with acceleration $\vec{a}_B$ relative to the inertial frame, and it has an angular velocity $\vec{\omega}_B$ and angular acceleration $\dot{\vec{\omega}}_B$. In this scenario, the inertial force acting on the mass m in reference frame B is

$$\vec{F}_m = -m\left[\vec{a}_B + 2\vec{\omega}_B \times \dot{\vec{x}} + \vec{\omega}_B \times (\vec{\omega}_B \times \vec{x}) + \dot{\vec{\omega}}_B \times \vec{x}\right] \tag{2.37}$$

Derivation details for Eq. 2.37 can be found in mechanics books, *e.g.*, Taylor [101].

If there is a rigid rotating body instead of a point mass, there are additional inertial moments related to the angular acceleration of the reference frame B, *i.e.*,

$$\vec{M}_m = -\bar{\bar{I}}\dot{\vec{\omega}}_B + \ldots \tag{2.38}$$

where $\bar{\bar{I}}$ is the inertia tensor of the rigid body. There are other terms not represented in Eq. 2.38 related to the derivative of the inertia tensor as seen in the B frame as the body rotates. However, these terms are not included in the present analysis, an approximation compatible with the hypothesis of constant mass matrix for the FEM, as employed in Section 2.1.

Equations 2.37 and 2.38 are the basis for the calculation of fictitious loads, even for a complex model. In this case, all the linear and dual modes are described in the accelerated reference frame B with angular velocity $\vec{\omega}_B$ and acceleration $\vec{a}_B$, as illustrated in Fig. 2.6.

From the FEM, the mass matrix M is available. Also from the FEM, it is possible to recover the initial positions of all nodes, which are stacked in a column matrix x_0, with the entries corresponding to the related degrees of freedom (translations and/or rotations).

Using the mass matrix, the column matrix of initial positions, the modes and its

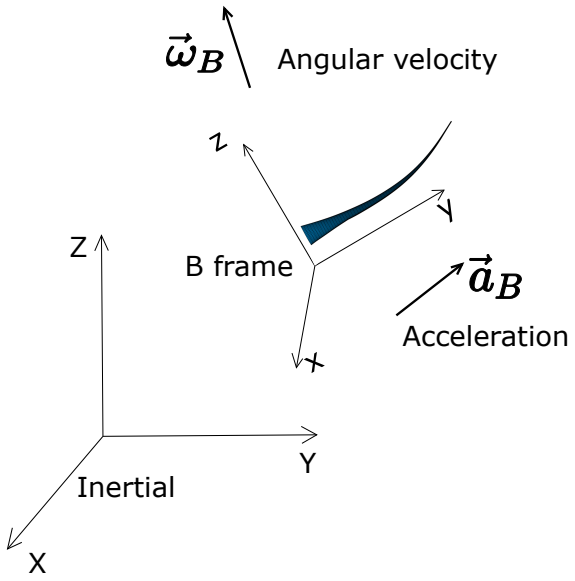

Figure 2.6: Description of accelerated frame B relative to the inertial frame.

amplitudes, it is possible to calculate the modal fictitious loads as it is going to be described next.

2.3.1 Translational Base Motion

If the frame B has an acceleration $\vec{a}_B$ relative to the inertial frame, the fictitious force on a particle with mass m is simply $-m\vec{a}_B$. For a complete FEM, this is equivalent to

$$F_{trans} = -M\tau_x a_x - M\tau_y a_y - M\tau_z a_z \tag{2.39}$$

where the scalars a_x, a_y and a_z are the components of the acceleration vector $\vec{a}_B$ of the reference frame B relative to the inertial frame, and τ_x, τ_y and τ_z are column matrices with 1 in the entries corresponding to the translational degrees of freedom of the FEM and 0 for all other entries. For example, τ_x has 1 for the degrees of freedom of translation in x and 0 for all other degrees of freedom. Similarly, the column matrices τ_y and τ_z indicate the degrees of freedom related to translations in

the y and z directions, respectively.

It is possible to condense Eq. 2.39, stacking the translation matrices τ_x, τ_y and τ_z horizontally in one single matrix indicative of the translational d.o.fs:

$$\Upsilon = [\tau_x \quad \tau_y \quad \tau_z] \tag{2.40}$$

and the column matrix of fictitious forces related to translation is rewritten as

$$F_{trans} = -M\Upsilon a_B \tag{2.41}$$

where a_B is a column matrix with the components of $\vec{a}_B$.

The load F_{trans} calculated in Eq. 2.41 is a column matrix with size corresponding to the number of d.o.fs of the complete FEM. However, in the modal formulation, it is computationally more efficient to pre-calculate all the terms that involve large matrices. For that, the fictitious modal forces related to translation are given by

$$\begin{aligned} f_{trans} =& \frac{\partial u}{\partial q}^T F_{trans} \\ =& -\left(\Phi + \Psi\frac{\partial r}{\partial q}\right)^T (M\Upsilon a_B) \\ =& -\left(\Phi^T M\Upsilon\right) a_B - \frac{\partial r}{\partial q}^T \left(\Psi^T M\Upsilon\right) a_B \end{aligned} \tag{2.42}$$

On the above equation, the terms $\left(\Phi^T M\Upsilon\right)$ and $\left(\Psi^T M\Upsilon\right)$ can be pre-calculated and stored for fast on-line computations.

2.3.2 Rotational Base Motion

The fictitious loads related to rotation are an extension of Eqs. 2.37 and 2.38 to the general FEM. In Eq. 2.37, there are cross products involving the angular velocity of the reference frame B relative to the inertial frame. For matrix computations,

the cross products are replaced by matrix multiplications using the skew-symmetric matrix of $\vec{\omega}_B$, *i.e.*,

$$\Theta = \begin{bmatrix} 0 & -\omega_z & \omega_y \\ \omega_z & 0 & -\omega_x \\ -\omega_y & \omega_x & 0 \end{bmatrix} \tag{2.43}$$

where the entries correspond to the components of the angular velocity $\vec{\omega}_B$ of B relative to the inertial frame, expressed in the B frame.

The cross products in the rotational portion of Eq. 2.37 are applied to the position and translational velocity of the point mass. For a complex FEM, it is possible to arrange the positions and orientations of all nodes in a single column matrix. The same can be done to the nodal velocities, comprising translational and rotational components. Then, assembling a sparse matrix with Θ as the basic unit, it is possible to perform the cross-product for the entire FEM in a single matrix multiplication. This sparse matrix has the dimensions of the total number of degrees of freedom of the FEM. The non-zero entries are related to translational degrees of freedom, following the rows of the matrix Θ in Eq. 2.43, with rows 1, 2 and 3 corresponding to translational d.o.fs in the x, y and z directions, respectively. This sparse matrix for cross product of $\vec{\omega}_B$ with the entire FEM positions or velocities are represented by Ω, given by

$$\Omega = \begin{bmatrix} \Theta & [0] \dots [0] \\ [0] & \Theta \dots [0] \\ & \vdots \\ [0] & [0] \dots \Theta \end{bmatrix} \tag{2.44}$$

where [0] is a matrix of zeros with same size of Θ. If not all translations and rotations are included in the FEM, the rows/columns corresponding to the missing degrees of

freedom are crossed out in Eq. 2.44. Joining the loads acting on the translational degrees of freedom from Eq. 2.37 and the loads on the rotational degrees of freedom from Eq. 2.38, it is possible to write the generalized fictitious loads related to rotation on the entire FEM as

$$F_{rot} = -M \left[2\Omega\dot{u} + \left(\Omega^2 + \frac{d\Omega}{dt} \right) p + \Xi\dot{\omega}_B \right] \tag{2.45}$$

where the column matrix p represents the positions (not displacements) of all the d.o.fs of the FEM, *i.e.*,

$$p = x_0 + \Phi q + \Psi r \tag{2.46}$$

and Ξ is a matrix with 3 columns indicating the rotational degrees of freedom in the x, y and z directions, respectively, analogous to the matrix Υ for translation in Eq. 2.40.

The sparse skew-symmetric matrix Ω in Eq. 2.45 has ω_x, ω_y and ω_z as the only non-zero entries. Therefore, it is possible to decompose it into three other matrices, Ω_1, Ω_2 and Ω_3, each composed only with entries 0 and 1, such that

$$\Omega = \Omega_1\omega_x + \Omega_2\omega_y + \Omega_3\omega_z \tag{2.47}$$

In computational terms, this allows a pre-calculation of all large matrix multiplications, such that the on-line solution is faster. Replacing Eqs. 2.46 and 2.47 into Eq. 2.45, the fictitious forces may be written in terms of pre-computed matrices and the three angular velocities and accelerations, analogous to Eq. 2.42.

Finally, fictitious modal loads related to rotation of the frame B can be written as

$$f_{rot} = -\left(\Phi + \Psi\frac{\partial r}{\partial q}\right)^T M\left[2\Omega\dot{u} + \left(\Omega^2 + \frac{d\Omega}{dt}\right)p + \Xi\dot{\omega}_B\right] \tag{2.48}$$

2.3.2.1 Complete Base Motion

The total fictitious modal loads acting on the general FEM due to a combination of linear and angular accelerations of the base motion are:

$$f_{fictitious} = f_{trans} + f_{rot} \tag{2.49}$$

where f_{trans} and f_{rot} are given by Eqs. 2.42 and 2.48, respectively. Online computations with large matrices could degrade significantly the ROM performance. In order to avoid that, it is necessary to pre-compute matrices for the inertia loads. This process is described in the Appendix D.

2.3.3 Resultants of Fictitious Forces

The previous subsections presented the modal components of the fictitious loads which should be included in the structural analysis if the frame of reference for the modal description of displacements is accelerated relative to an inertial one. In a flight dynamics computation, it would be important to also know the resultants acting over the flexible structure in terms of forces and moments.

Using the list of d.o.fs for the FEM, it is possible to get the resultant components from the loads F_{trans} and F_{rot} given in Eqs. 2.39 and 2.45. The x, y and z components of the fictitious resultant force on a wing analyzed with the EnICE method are calculated from

$$f_{xyz,B} = \Upsilon^T\left(F_{trans} + F_{rot}\right) \tag{2.50}$$

where Υ is the three-column matrix used for selection of the translational d.o.fs,

detailed in Eq. 2.40, $f_{xyz,B}$ is a column matrix with three entries corresponding to the components of the resultant fictitious load in the accelerated reference frame B. If these force components are needed in the inertial frame, a rotation should be applied.

For the calculation of the resultant moments about the origin of reference frame B, the positions of all the nodes should be considered. In this case, a sparse matrix should be prepared to replace the cross-product of the position and the point force for the FEM. This sparse matrix would be similar to the matrix Ω used in the calculation of fictitious loads.

2.4 Time Integration

For the structural ROM, the number of degrees of freedom considered in this work was always relatively small (< 20) when compared to the number of d.o.fs of the complete FEM. For this reason, the numerical integration methods for the modal equations of motion are not the ones typically employed in structural dynamics solutions, such as Newmark-β [102]0 or generalized-α [103] methods. Instead, algorithms available for first-order systems of ODEs were used. In fact, Eq. 2.21 can be rewritten in the form

$$\mathscr{M}(Q)\dot{Q} = F(t, Q) \tag{2.51}$$

where $\mathscr{M}$ here represents the mass matrix of the ODE system and Q is the state of the system, with modal amplitudes and velocities, *i.e.*,

$$Q = \begin{Bmatrix} q \\ \dot{q} \end{Bmatrix} \tag{2.52}$$

For most of the work, Numerical Differentiation Formulas (NDFs) were employed from available packages [104, 105]. These methods are especially efficient when used

with stiff systems of equations. Detailing the NDFs is beyond the scope of this work, but the reader is referred to Shampine and Reichelt [104] for more details. The particular implementation for the NDF algorithm has variable order and time step. Up to second order, the time integration is unconditionally stable. The time step and the order are varied according to the convergence rate of the problem. The Jacobians for Eq. 2.51 can be provided externally or estimated with finite differences. The method evaluates the Jacobian only as needed, improving the speed. In practice, any time integration scheme capable of dealing with semi-implicit ODEs like Eq. 2.51 could be used.

CHAPTER 3

Aerodynamic ROM Formulation

3.1 Motivation

This chapter presents the aerodynamic reduced order model employed in the dissertation: the Method of Segments (MoS) for steady solutions, with convolution and correction factor for nonlinear unsteady responses. The assumptions of the method are outlined, and the method is explained, detailing the off-line and on-line phases of the solution. Reference solutions obtained from the CFL3D code are described, and details such as splines for modal mesh deformation are explained.

The MoS with correction factor for unsteady responses has already been successfully tested at the Active Aeroelasticity and Structures Research Laboratory (A^2SRL) by Skujins and Cesnik [1, 21]. In those studies, nonlinear unsteady results were obtained with a correction factor applied over the linear convolved responses. Skujins and Cesnik analyzed an AGARD 445.6 wing from the subsonic to the supersonic regimes. Lift, drag and moments were evaluated, considering modal deformations of the first three elastic modes in unsteady conditions. However, as pointed out in [1], the AGARD 445.6 wing has a narrow transonic range around Mach 1.0. Nonlinear aerodynamic behavior in wider transonic range still had to be investigated using the MoS. Also, in the previous work, only integrated loads were used for error assessment. For aeroelastic analysis, the distribution of loads plays a fundamental role. Moreover,

for this work, the modal aerodynamic loads are needed.

3.2 Assumptions

The main objective of the aerodynamic ROM is to reduce the costs of the nonlinear simulations, using prediction of loads based on a small set of CFD reference results. For the structural ROM, the reference solutions are obtained at different deformation conditions. In the CFD context, it would be expensive to cover more than a few dimensions with steady computations at different modal shapes. The Method of Segments avoids these expensive simulations by partitioning the wing into segments and treating each one independently, while still capturing its 3D effects.

The main assumption in the Method of Segments is that the aerodynamic load at each chordwise segment along the wing is uniquely determined by its local (geometrical or effective) angle of attack (AoA) relative to the incoming flow. The MoS alone provides steady solutions. Unsteady computations are achieved with linear convolution of step responses to modal deformations. The ROM developed by Skujins and Cesnik assumed that a correction factor applied to the linear response corrects for nonlinear effects, an assumption that is valid in a limited neighborhood of the evaluation point. The correction factor is the ratio between steady results from the MoS and linear calculations.

The next sections details the MoS used for steady results and the instantaneous correction factor employed for unsteady computations.

3.3 Method of Segments

If all deformation conditions had to be explored to generate reference data, the amount of required upfront steady simulations would grow with the number of modes considered in the structural description of the structure. Since aerodynamic compu-

tations are orders of magnitude more time consuming than structural solutions, this strategy is not employed here. Instead, it was decided to use the Method of Segments, since it requires only a few steady nonlinear solutions for the training of the aerodynamic ROM. In fact, it needs only a single deformed state to get the forces on a number of segments parallel to the incoming flow, varying the angle of attack and the Mach number.

Skujins and Cesnik [1] did not investigate the effects of variations of the induced angle of attack according to the deformation state. Since this work is devoted to the analysis of large displacements conditions, including torsion, this effect is important. To model it in a simplified way, a lifting line approach was chosen to estimate the induced angle of attack.

3.3.1 Off-line Phase

The Method of Segments uses loads identified from a series of reference solutions. Obtaining the reference solutions and creating tables of loads for each segment according to the local angle of attack is the off-line phase of the MoS. This training cycle is summarized in the flowchart of Fig. 3.1. From a reference configuration, like the undeformed wing or, more appropriately, the 1-g flight shape, CFD solutions are obtained at different root angles of attack and Mach numbers. The wing is partitioned into segments, and the loads normalized by dynamic pressure and reference area are obtained for each one. At each flight condition, the loads distributed over the segments are used to estimate the effective AoA along the wing. This is performed using the circulation related to each segment and the lines of trailing vortices shed between segments.

An illustration of the vortex lines shed between segments is presented in Fig. 3.2. The wing partition into segments serves only for illustration purposes. Each segment has a control point located at its geometrical center. The loci of control points define

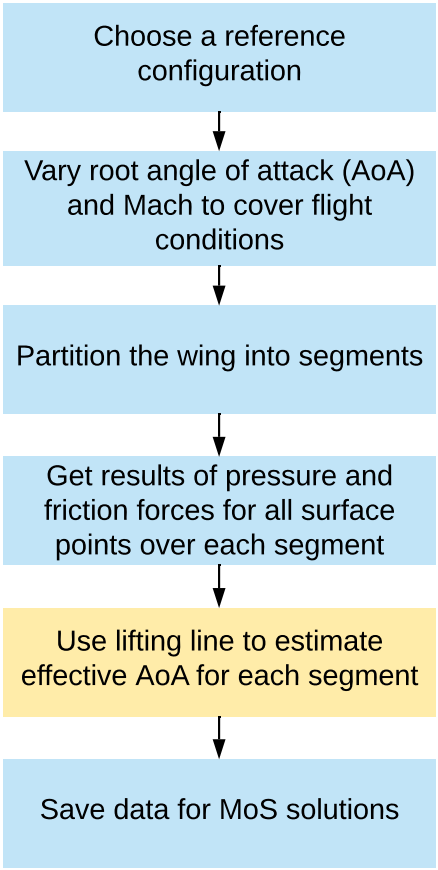

Figure 3.1: Flowchart describing the calculation of reference data for the Method of Segments (orange block indicates change to the original process represented by the blue blocks).

a reference line. The vortex lines are released from points over the reference line at the determined spanwise stations which delimit the segments. The illustration shows the position vector $\vec{p}_{ij}$ that goes from the initial point of the j^{th} vortex line to the i^{th} control point. The j^{th} vortex line has intensity $\vec{\Gamma}_j$.

Each vortex line induces velocity at a given control point. This induced velocity is given by the Biot-Savart law. Figure 3.3 illustrates a semi-infinite segment and a control point where the induced velocity is calculated. The induced velocity direction observes the right-hand rule and its magnitude is given by

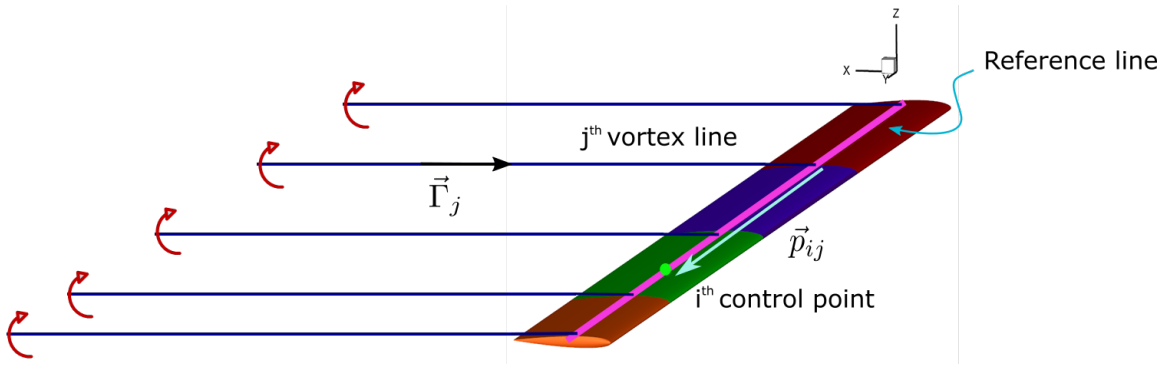

Figure 3.2: Illustration of vortex lines and the control points where the induced velocities are calculated.

$$|\vec{V}_i^j| = \frac{|\vec{\Gamma}_j^i|}{4\pi d_{ij}} (1 + \cos\theta_{ij}) \tag{3.1}$$

where $\vec{V}_i^j$ is the velocity induced by the j^{th} vortex line on the i^{th} control point, d_{ij} is the distance between the point and the vortex line, and θ_{ij} is the angle as indicated in Fig. 3.3. In practice, $\vec{V}_i^j$ can be written solely in terms of the vectors $\vec{\Gamma}_j$ and $\vec{p}_{ij}$, *i.e.*,

$$\vec{V}_i^j = \frac{1}{4\pi} \frac{\vec{\Gamma}_j^i \times \vec{p}_{ij}}{|\vec{\Gamma}_j \times \vec{p}_{ij}|^2} |\vec{\Gamma}_j|^2 \left(1 - \frac{\vec{\Gamma}_j \cdot \vec{p}_{ij}}{|\vec{\Gamma}_j \cdot \vec{p}_{ij}|}\right) \tag{3.2}$$

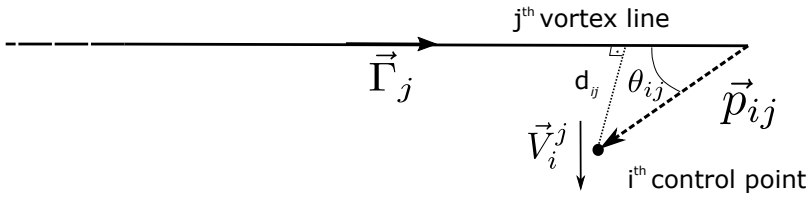

Figure 3.3: Semi-infinite vortex line and a control point with induced velocity.

From the induced velocities calculated from Eq. 3.2, the local AoA induced by the shed vortex lines are estimated for each segment of the wing.

A fundamental piece of information is the circulation released in each trailing vortex. That is related to the difference of bound circulation in adjacent segments,

as illustrated in Fig. 3.4. The i^{th} line vortex has magnitude given by

$$\Gamma_i = \Gamma_{b,i+1} - \Gamma_{b,i} \tag{3.3}$$

where $\Gamma_{b,i}$ represents the intensity of the vortex line at the i^{th} segment.

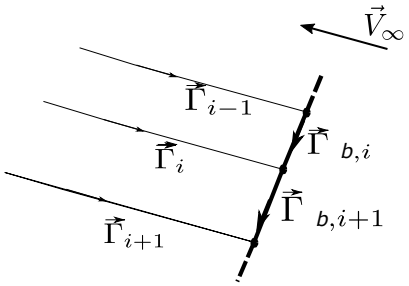

Figure 3.4: Emission of semi-infinite vortex lines from differences in bound circulation along span.

The bound circulation on each segment is calculated through the Kutta-Joukowski theorem extended to the wing that is

$$\vec{V}_\infty \times \vec{\Gamma}_{b,i} l_i = \vec{L}_i \tag{3.4}$$

where $\vec{V}_\infty$ is the undisturbed incoming flow, $\vec{\Gamma}_{b,i}$ is the bound circulation for to the i^{th} segment, oriented parallel to the segment, and l_i is the length of the i^{th} segment. The lift of the i^{th} segment is given by $\vec{L}_i$ and its direction is orthogonal to the direction of the i^{th} segment, $\hat{e}_{y,i}$, and $\vec{V}_\infty$, and it is given by

$$\hat{e}_{L,i} = \frac{\vec{V}_\infty \times \hat{e}_{y,i}}{|\vec{V}_\infty \times \hat{e}_{y,i}|} \tag{3.5}$$

In the training phase of the MoS, the lift on each segment is calculated from the total aerodynamic force on that segment $\vec{F}_{aero,i}$ projected onto the lift direction $\hat{e}_{L,i}$ of the segment, *i.e.*,

$$\vec{L}_i = \left(\vec{F}_{aero,i} \cdot \hat{e}_{L,i}\right) \hat{e}_{L,i} \tag{3.6}$$

With the lift calculated from the reference solution for each segment of the wing, and using Eq. 3.4, the circulation magnitude $\Gamma_{b,i}$ is calculated. From the bound vortex magnitudes of Eq. 3.3 and induced velocities of Eq. 3.2, the corresponding induced angle of attack $\alpha_{ind,i}$ for the i^{th} segment is calculated as

$$\alpha_{ind,i} = \arctan\left(\frac{\sum_j \vec{V}_i^j \cdot \hat{e}_{L,i}}{V_\infty}\right) \tag{3.7}$$

where induced velocities are summed up for each segment, considering the influences of all emitted vortex lines.

In practice, it may happen that the calculation of the aerodynamic loads from the CFD pressure distribution on each segment contains errors due to the discretization. If the borders between segments do not coincide with the CFD mesh, the mesh nodes will not be distributed correctly. This in turn will cause oscillations in the bound circulation distribution along the span, even though the average circulation is correct. However, these oscillations affect the strengths of the emitted vortices and the induced AoA, and they must be filtered out. Any fitting process may be used to calculate a smoother circulation distribution along the spanwise direction. For this work, a fifth-order polynomial was used to fit the bound circulation magnitudes according to the spanwise coordinate of the control points. The same fitting should be used for the training and simulation phases of the MoS.

The reference data for each segment is a list of aerodynamic forces at mesh points written in the aerodynamic frame as a function of the effective angle angle of attack $\alpha_{eff,i}$ of the segment. The effective angle of attack is the sum of the geometrical and induced angles of attack, *i.e.*,

$$\alpha_{eff,i} = \alpha_{geo,i} + \alpha_{ind,i} \tag{3.8}$$

where $\alpha_{geo,i}$ is the geometrical angle of attack at the i^{th} segment, explained in the next subsection, and $\alpha_{ind,i}$ is the induced angle of attack considering the influence of all the trailing vortices at the control point of the i^{th} segment.

For reference solutions using half-wing, usually a symmetry condition is imposed. The same symmetry boundary condition should be replicated when calculating the induced velocities. The modeled half-wing is reflected along the spanwise position, and the influence of the reflected image is taken into account for all induced velocities. This is an important detail that should be observed for both the reference solutions and during the on-line solution phase.

If unsteady simulations are desired, the training phase also requires calculation of unsteady responses to step modal deformations. These responses are needed for the linear convolution described in subsection 3.3.3. For aeroelastic simulations, the modal aerodynamic forces are usually the output of interest from the step responses. Experience showed that the step responses can vary significantly according to the initial deformation state. Therefore, these responses should be calculated close to the deformation state around which the simulations are to be performed, like a 1-g cruise condition. The modal forces are obtained for all the linear and dual modes, from each step deformation, as illustrated in Fig. 3.5.

The number of step simulations performed for each flight condition corresponds to the number of elastic degrees of freedom. The modal step deformations involve linear and dual modes, but the displacements are dominated by the linear modes. If the amplitude of the k^{th} step deformation is ϵ_k, the structural displacements for the step response are given by

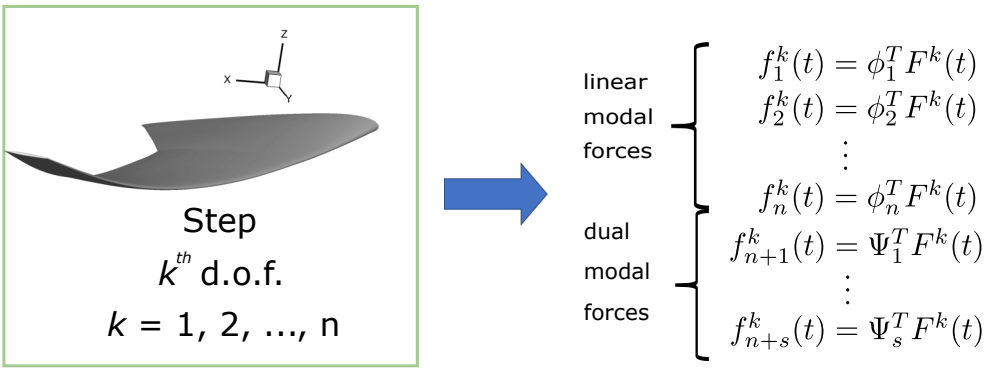

Figure 3.5: Step responses from each d.o.f and stored information on modal forces.

$$u_{st,k} = \left[\Phi + \Psi \frac{\partial r}{\partial q}(q)\right] \epsilon_k \tag{3.9}$$

where $\frac{\partial r}{\partial q}(q)$ is the Jacobian of the dual-mode amplitudes with respect to the linear-mode amplitudes q of the current deformation state. The amplitudes ϵ_k of the step deformations are small values chosen to avoid numerical problems with the CFD solution, while keeping the responses linear. If the amplitudes of the step responses are too small, the modal forces are not smooth. If the amplitudes of the step responses are too large, nonlinear responses are obtained. A practical approach to check the quality of the step responses is to compare results for different ϵ_k values and check for linear and smooth outputs. The structural displacements of Eq. 3.9 are related to the FEM. For the CFD mesh motion, the modal shapes must be interpolated to the aerodynamic mesh, in a process described in section 3.6.

3.3.2 On-line Phase

During the on-line phase of the solution, the modal amplitudes are used to determine the deformation of the wing. The geometric AoA of each segment is determined using a frame attached to the segment. The induced AoA is calculated iteratively, adjusting the loads on the segments until the changes in the induced AoA between

two iterations are below a certain tolerance for all segments. Using the converged effective AoA for each segment, the nodal forces are used to calculate modal loads. The process is illustrated in the flowchart of Fig. 3.6. This procedure is relative to the steady solution. If unsteady simulations are sought, a convolution is employed as well, but that is explained in the subsection 3.3.3.

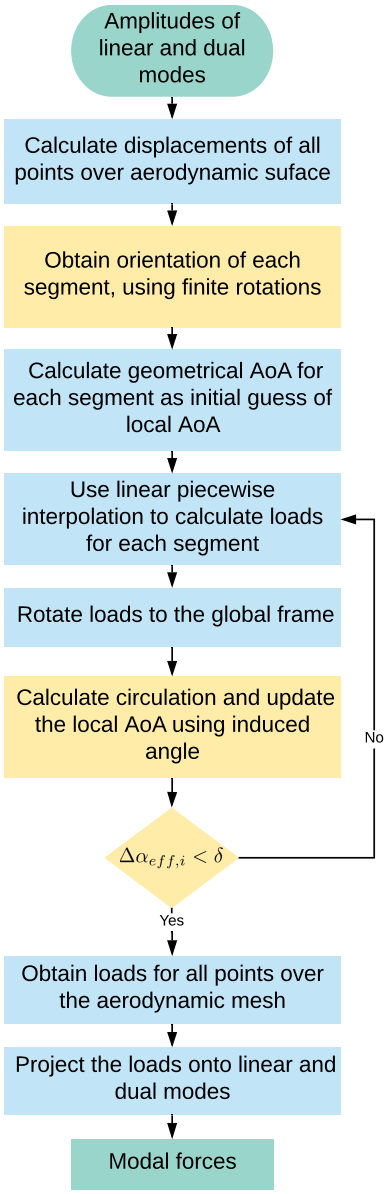

Figure 3.6: Process for the calculation of modal loads using the Method of Segments (orange blocks show changes to the original process of Skujins and Cesnik [1].

The geometrical AoA for each segment is calculated considering finite rotations. In a condition of small rotations, this angle may be determined by monitoring the displacements of a leading edge and a trailing edge points. Since this work is focused on large displacements, approximations of small angles are not valid in order to calculate the geometrical angle of attack of the segments. Instead, it is necessary to monitor the orientation of a system of coordinates attached to each segment of the wing. Figure 3.7 illustrates an example of coordinate system orientation change due to deformation of a particular segment over the wing.

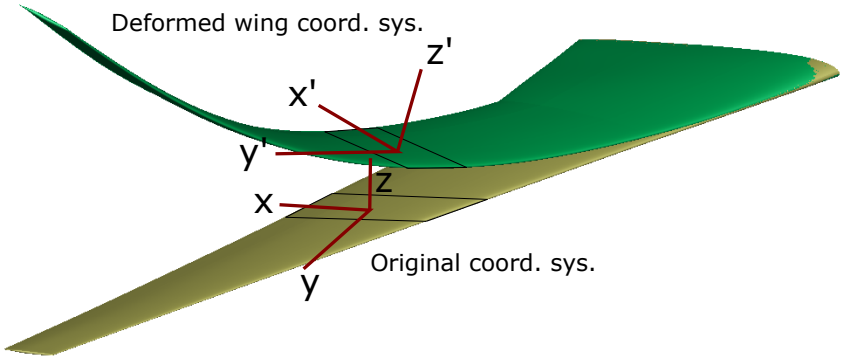

Figure 3.7: Wing segment finite rotation of local coordinate system.

The aerodynamic mesh is associated to the body coordinate system where the x-direction is chordwise, y-direction is spanwise and z-direction is vertical. The freestream velocity is defined in this system by its three components as

$$\vec{V}_\infty = \begin{Bmatrix} V_\infty \cos\beta \cos\alpha \\ V_\infty \sin\beta \\ V_\infty \cos\beta \sin\alpha \end{Bmatrix} \tag{3.10}$$

where β is the sideslip angle and α is the angle of attack. Initially, all the local frames attached to each segment of the wing are parallel to the body frame. As the structure is deformed, the local frames follow the segment orientation. Since the structure is

elastic even in the chordwise direction, it is only possible to calculate an average orientation of the points selected for a segment.

The average rotation matrix for a segment of the wing is calculated using the covariance matrix of the initial and displaced points of the segment. Given a segment of the wing with n points, a $3 \times n$ matrix P_0 stores the three coordinates of the initial positions of the points. These positions are all relative to the geometrical center of these points, such that the mean value along each row of P_0 is 0. Once the wing is deformed by an arbitrary displacement, a new matrix of displaced positions P_D is written, centered around the new geometrical center of the points, as illustrated in Fig. 3.8. The objective is to find the rotation matrix R_{ot} that transforms P_0 into P_D, such as

$$P_D = R_{ot} P_0 \tag{3.11}$$

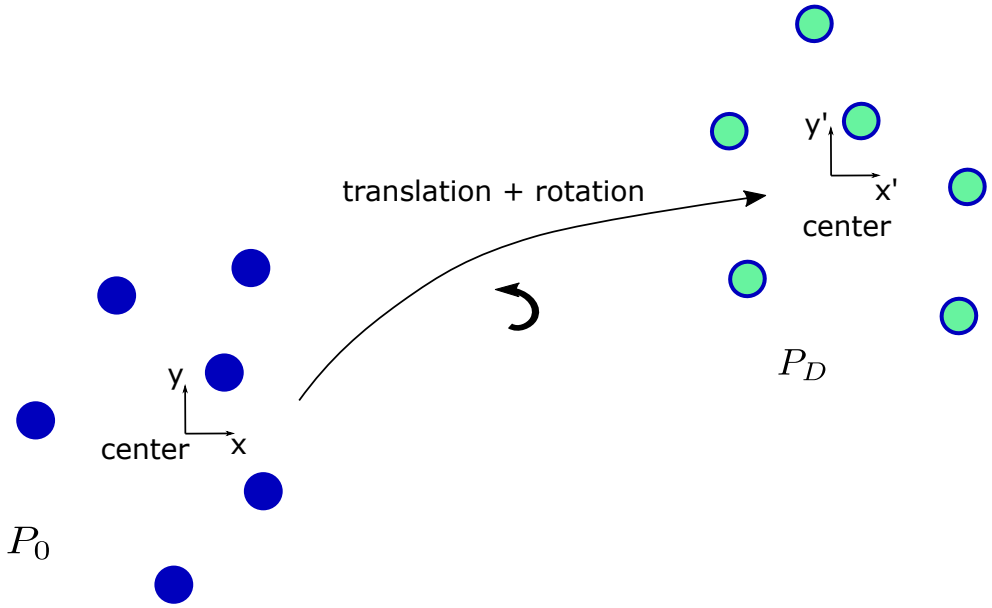

Figure 3.8: Example of translated and rotated points, with initial (P_0) and deformed (P_D) coordinate values.

A practical way to estimate such matrix is by applying singular value decomposi-

tion to the covariance matrix of the positions, *i.e.*,

$$H := P_0 P_D^T \tag{3.12}$$

$$H = USV^T \tag{3.13}$$

$$R_{ot} \cong VU^T \tag{3.14}$$

where H is the covariance matrix of positions, and U, S and V are the left-singular vectors, the matrix of singular values, and the right-singular vectors of H.

For each segment, the rotation matrix is applied to the initial coordinate system xyz to get the deformed-state coordinate system $x'y'z'$, just as depicted in Fig. 3.7.

To calculate the geometrical angle of attack for each segment of the wing at a deformed condition, the freestream flow of Eq. 3.10 is decomposed into the the deformed-state coordinate system. If the velocity components are V_x', V_y' and V_z', the local geometrical angle of attack is given by

$$\alpha_{geo} = \arctan\left(\frac{V_z'}{V_x'}\right) \tag{3.15}$$

Using Eqs. 3.15 and 3.7 into Eq. 3.8, the effective AoA can be calculated.

3.3.3 Unsteady Solution and Correction Factor

Linear convolution about steady responses is used to calculate the unsteady solution for a given reference condition. Due to nonlinearities, however, the linear convolution may fail to capture the correct lift and drag responses [1]. To reduce this error, Skujins and Cesnik [1] introduced a correction factor based on nonlinear steady responses at deformed condition.

Given an output of interest y, which can be a modal aerodynamic force or a global quantity such as the lift coefficient, the instantaneous correction factor [1] is applied to the linear convolved response of the system to get the nonlinear unsteady prediction, *i.e.*,

$$y_{NL,u} = f_c \quad y_{Lin,u} \tag{3.16}$$

where f_c is the correction factor applied to the linear convolved response $y_{Lin,u}$ and $y_{NL,u}$ is the prediction for the nonlinear unsteady output.

The linear convolved response at a time t is given by

$$y_{Lin,u}(t) = \sum_{j=1}^{n} \int_0^t \bar{y}_j(t-\tau)\dot{q}_j(\tau)d\tau \tag{3.17}$$

where $\bar{y}_j$ is the normalized step response of y due to a step input in the j^{th} linear mode, and $\dot{q}_j$ is the time derivative of the linear modal amplitude q_j of the system. All the linear modal amplitudes contribute to the convolution. In Eq. 3.17, no initial value is assumed. In practice, $y_{Lin,u}$ is an increment to be added to the initial value. The initial output is obtained from the MoS for the deformed condition before the unsteady excitation.

The correction factor is determined using steady nonlinear reference solutions. It is supposed that the ratio between nonlinear and linear unsteady response amplitudes can be approximated by the ratio of nonlinear and linear steady output amplitudes, considering a given flight condition and structural deformation. In Skujins and Cesnik [1], this hypothesis was shown to hold for several numerical examples.

The expression for the correction factor is [1]:

$$f_c = \frac{y_{NL,s}}{y_{Lin,s}} \tag{3.18}$$

where $y_{NL,s}$ is the steady output considering a nonlinear CFD solution, and $y_{Lin,s}$

is the steady linear response that can be obtained from the converged value of the response to the step excitation. As such, the correction factor is updated at each time step. Both the numerator and denominator in Eq. 3.18 are the output predictions after eliminating the initial value coming from a steady-state response based on the MoS.

During the simulation, it may happen that the linear convolved response crosses a zero. In this case, the expression of Eq. 3.18 is undefined. In order to circumvent this issue, Skujins and Cesnik [1] introduced a term in the correction factor so that it will approach 1 as the denominator goes to 0. The modified correction factor is given by

$$f_c = \frac{y_{NL,s} + \delta}{y_{Lin,s} + \delta} \tag{3.19}$$

where δ is a value large enough such that the denominator of Eq. 3.19 never crosses zero. In this case, the nonlinear unsteady output given in Eq. 3.16 becomes

$$y_{NL,u} = f_c \left(y_{Lin,u} + \delta \right) - \delta \tag{3.20}$$

In the context of this work, the nonlinear steady solution is calculated with the MoS approach. As is explained in Chapter 5, the correction factor did not lead to reasonable results in the transonic analysis conducted for the chosen numerical case. For that case, the linear convolution alone was used to approximate unsteady responses.

3.4 Reference Solutions

The highest-fidelity aerodynamic results employed in this work are RANS solutions. The computational tool chosen for generation of the reference data is the

CFL3D code [106], developed in the 80's at NASA. The addition of a linear aeroelastic modal solution to the latest versions of this code [107] made it especially useful for this work. Recently, the software has been made open source, and that was the most compelling reason for the selection of this mature tool.

3.4.1 CFL3D Environment

The CFL3D is a RANS solver for structured grids. The time-dependent conservation equations are solved with a finite-volume semi-discrete approach [106]. The convective and pressure terms are upwind-biased, while the shear and heat transfer terms are calculated with central differences.

3.4.1.1 Governing Equations

The governing equations solved by CFL3D in Cartesian coordinates are

$$\frac{\partial Q}{\partial t} + \frac{\partial \left(F - F_\nu\right)}{\partial x} + \frac{\partial \left(G - G_\nu\right)}{\partial y} + \frac{\partial \left(H - H_\nu\right)}{\partial z} = 0 \tag{3.21}$$

where Q is the column matrix of the conserved quantities, which are mass, momentum and internal energy. The fluxes are partitioned into inviscid terms (F, G and H) and viscous ones (F_ν, G_ν and H_ν). In practice, Eq. 3.21 is transformed to generalized coordinates, according to the structured mesh. Also, the quantities are all non-dimensionalized in terms of air density, speed of sound and free-stream molecular viscosity. For the boundary layer, the assumption of thin-layer is used, such that only the derivatives normal to the wall are considered in the shear stress and heat flux terms. The conserved quantities are all regarded as averages for the cell, and the fluxes are averages for the faces.

Many turbulence models are available in CFL3D. For this work, the Spalart-Allmaras model is used [108]. This turbulence model is simpler than the other option

and was used successfully in studies with one of the examples presented in this dissertation, the uCRM 13.5 wing (*e.g.*, [109]).

3.4.1.2 Mesh Deformation

Regarding the mesh deformation, there are two options already implemented in CFL3D: exponential decay combined with Trans-Finite Interpolation (TFI) of interior mesh points, and finite macro-element deformation combined with TFI. The first method considers an exponential decay of the displacement with the distance from the moving surface. The second method performs a finite element solution considering elements with stiffness decaying with distance from the aeroelastic surface. Finite macro-element deformation is significantly more time consuming, but it maintains a better mesh quality [110]. However, according to the experiences of this work for large displacements, the method of exponential decay performed better in terms of avoiding negative volumes close to wing tips. Consequently, the exponential decay was chosen for the analyses. The user may specify control points on the mesh where the formulation for mesh motion is applied. Inside the blocks delimited by the control points, a linear interpolation is carried out to determine the positions of the nodes.

The formulation for the displacements of the control points according to the exponential decay method is

$$\vec{r}_c^{\,n+1} - \vec{r}_c^{\,n} = D_{sc}\left(\vec{r}_s^{\,n+1} - \vec{r}_s^{\,n}\right) \tag{3.22}$$

where $\vec{r}_c$ defines the position of a control point, and the super index indicates the time step; $\vec{r}_s$ refers to the position of the nearest surface control point to the point C. The displacement of the point C is related to the displacement of the surface control point by an exponential decay with index D_{sc} given by

$$D_{sc} = min\left[1, e^{-\beta_{mesh}\left(\frac{|\delta\vec{r}_{sc}|}{\delta r_{max}} - \alpha_{mesh}\right)}\right] \tag{3.23}$$

In Eq. 3.23, r_{max} is the maximum distance from the surface control point to another control point in the computational domain. $\delta\vec{r}_{sc}$ is the vector from the surface point to the control point considered. The parameter β_{mesh} controls the displacement decay, while α_{mesh} establishes a distance up to which the surface displacement is transmitted with no decay.

An important point is that Eq. 3.23 does not consider possible rotations of the surface mesh, but only translations are transmitted to the volume points. This formulation imposes limitations on the maximum achievable deformations without negative volumes close to the wing tips.

Negative volumes may show up easily when large deformations are analysed in CFL3D. In order to mitigate this problem, the number of surface control points may be increased considerably. One particular configuration that showed success was selecting half of the surface mesh points as control points for the deformation, picking one point and skipping the next one.

3.4.2 Wing Partition into Segments

In the Method of Segments, the loads are calculated for each segment defined along the wing surface. An average geometric twist for a segment is calculated from the displacements of points contained in it. The partition is based on the spanwise coordinate of the aerodynamic nodes. A simple example of such a partition is presented in Fig. 3.9.

Care should be taken in order to avoid too wide segments. Since each segment is defined by a single orientation, the structure should not twist significantly along the spanwise direction of a segment. However, no parametric study was conducted to decide the ideal number of segments.

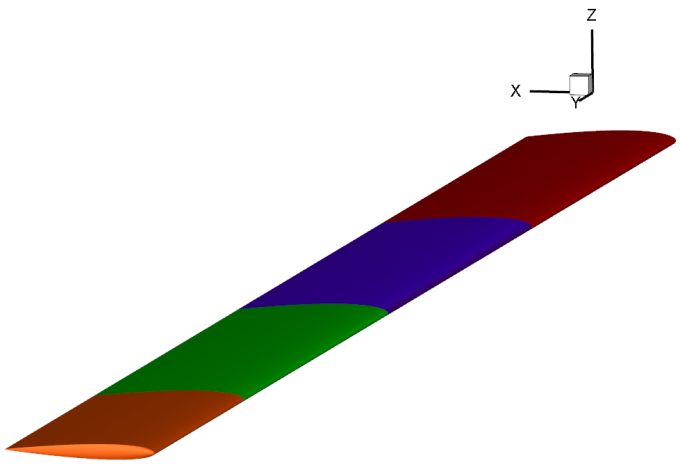

Figure 3.9: Example of a wing partitions into segments along the semi-span.

3.4.3 High-Fidelity Steady Simulations

A database of high-fidelity steady solutions is used to define the loads along each segment of the wing according to the flight conditions. For this work, the steady simulations are performed on the rigid wing on its undeformed geometry. The angle of attack is varied in a range wide enough to cover the possible deformations of the structure during simulations.

According to the range of flight conditions that the aerodynamic ROM should cover, the number of steady simulations may vary. The reference solutions should span the range of angles of attack, Mach and Reynolds numbers.

Each steady simulation is iterated until the norm of the residue has decreased a few orders of magnitude and the lift, drag and moment coefficients have converged. The results to be retrieved from each simulation are the pressure coefficients and friction force coefficients over the body surface.

Skujins and Cesnik [1] integrated the loads along each of the segments, for posterior use in unsteady predictions. This work follows a different strategy, storing the force distributed to each point of the surface mesh instead of the integrated quantities. The reason for the change was the high sensitivity of modal forces to the distribution

of loads over the surface. Using only the integrated forces and moments was not enough to achieve a high accuracy in terms of modal forces.

The pressure and friction coefficients are given for each quadrilateral element over the surface of the wing. The total aerodynamic force for that quadrilateral is then calculated using the normal vector and the area, and the resultant force is distributed equally to the 4 corner grid points, as illustrated in Fig. 3.10. Each corner point will receive 1/4 of the aerodynamic force from each quadrilateral it is part of. This is equivalent to the procedure adopted in the original CFL3D implementation for calculation of modal forces. For a refined mesh, moment errors around the centroid of the quadrilaterals should not be significant. For each steady solution, a column matrix is stored contained the three components of forces for each grid point over the surface of the wing.

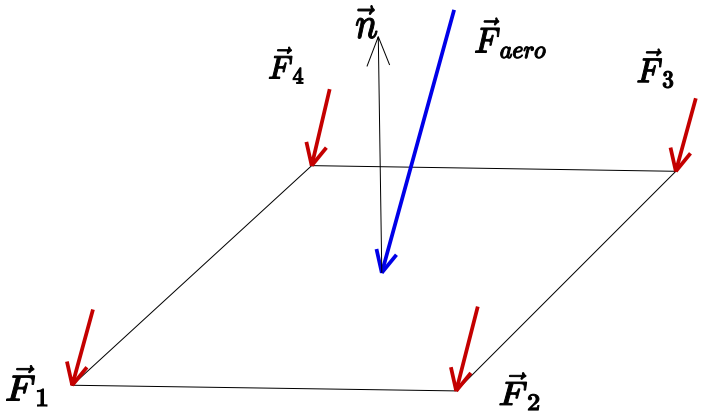

Figure 3.10: Distribution of aerodynamic forces to the four corner points of each quadrilateral of the CFD surface mesh.

In CFL3D, only the normal component of the aerodynamic force is considered for aeroelastic analyses. The developed aerodynamic ROM follows the same strategy in order to avoid differences with respect to the reference solution. This approximate calculation of aerodynamic loads is neglecting the friction forces, possibly reducing the accuracy of in-plane displacements, but the pressure forces are the dominant ones.

3.4.4 Small-Displacement Transient Solutions

In order to calculate the linear responses used in the aerodynamic ROM, Eqs. 3.16 and 3.18, it is necessary to have step transient responses as reference. These steps are small modal deformation applied to the originally undeformed wing. Since the CFD codes can only handle small steps, the step amplitudes must be sufficiently small so as to allow converged transient solutions.

From transient solutions, it is possible to record the history of lift, drag and moment coefficients, as well as modal forces. These step response simulations are performed until convergence is achieved.

There is no need to perform the transient solutions from different angles of attack. According to the hypothesis of linear solution, only the differences relative to the initial point are taken. The different Mach and Reynolds conditions, however, will affect the linear step response.

An example of time step response for a modal force related to mode 1 of the uCRM 13.5 wing [109] is presented in Fig. 3.11, as consequence of a deformation in the shape of mode 9 (torsion). The wing will be described in the results chapter. The step response presented serves only as an example. This step response is obtained for Mach 0.85, and it is normalized by the amplitude of the modal deformation used as input.

As noticed in Fig. 3.11, the response is high at the beginning due to the sudden deformation of the wing. In fact, the peak of the first time step is not even shown in the plot. This initially high response is due to the sudden velocity change due to the step deformation. The initial peak should not be neglected, because it contributes significantly to the convolved response.

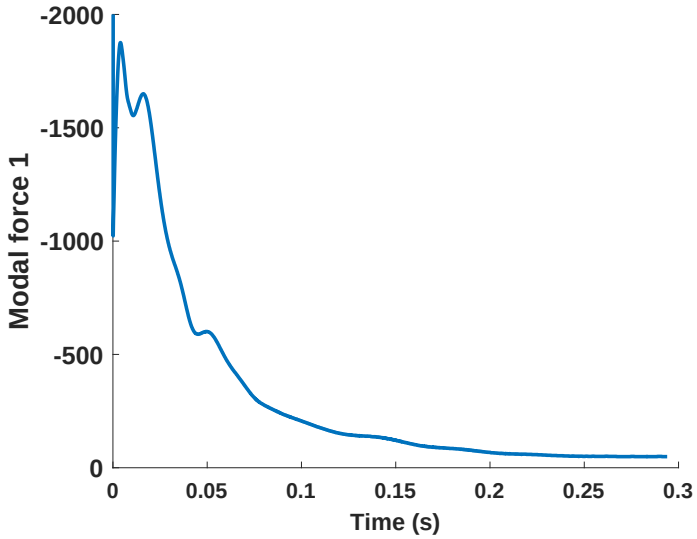

Figure 3.11: Step response of first bending modal force, related to a step on the first torsional mode.

3.5 Loads Interpolation for Flight Conditions

In this work, only the focus was not to cover multiple Mach conditions. The reference steady solutions and the step responses were obtained for Mach 0.85. In the case of steady solutions, different angles of attack were simulated to yield the loads on the wing segments. As explained, the forces were stored for each grid point over the wing. In order to get the loads for a wing segment at a geometrical angle of attack different from the one use in the reference simulations, a simple linear interpolation is used. Skujins and Cesnik [1] dealt with Mach and angle of attack variations, and used a Kriging interpolation to get solutions at non-simulated conditions. In this case, using linear interpolation is faster for the aerodynamic ROM, since not only the integrated loads were stored, but the all the loads for the aerodynamic surface grid.

Since linear interpolation is used for the steady loads as function of the angle of attack, it is important to check if the number of points obtained is sufficient to represent the load variations as a function of the angle of attack. In fact, the loads on each section may be highly nonlinear across the transonic region.

3.6 Splines for Modal Mesh Deformation

A fundamental aspect of any aeroelastic solution involving CFD is the interpolation of displacements from the structural mesh to the aerodynamic one. For the aeroelastic solution in the CFL3D environment, for example, one of the inputs is a file with the modal displacements for the aerodynamic mesh over the wing surface.

Initially, the linear and dual modes are calculated only for the structural mesh of the FEM. From that, an interpolation is calculated to transform the modes from the wing box to the aerodynamic mesh that covers the outer mold line of the wing. For the upper and lower surfaces of the wing box, thin-plane splines (TPS) were used to get the displacement at the aerodynamic grid points. TPS were recommended by Smith *et al.* [111] as a robust and accurate kind of spline. This kind of spline is calculated from a minimization of the integrated square of second derivatives along the domain, i.e.,

$$I\left[f(x,y)\right] = \int_{\mathbb{R}^2} \left[\left(\frac{\partial^2 f}{\partial x^2} \right)^2 + 2 \left(\frac{\partial^2 f}{\partial x \partial y} \right)^2 + \left(\frac{\partial^2 f}{\partial y^2} \right)^2 \right] \tag{3.24}$$

where $f(x,y)$ is a two-dimensional function that passes through the sample data. It was demonstrated by Duchon [112] that the function which minimizes Eq. 3.24 is a linear combination of radial basis functions centered on the data samples, with kernel $\phi(r) = r^2 ln(r)$. A linear system is solved for coefficients of the radial basis functions. This linear system is as large as the data set, and may be time-consuming to solve. However, since the interpolation is performed only once, in an off-line stage of the ROM modeling, cost of interpolation is not an issue.

It was mentioned that the TPS interpolation is performed only for the upper and lower surfaces of the wing box. It is noteworthy that the selection of the nodes corresponding to the different regions of the wing from the FEM set of points may not be obvious. There are many internal details in the structural model, but only

the exterior nodes are important for the aerodynamic analysis. In order to select the exterior nodes, a boundary set analysis is applied to the nodes of the FEM. The mathematical formulation of this boundary selection are the alpha shapes first described by Edelsbrunner *et al.* [113]. It is a generalization of the concept of convex hull to include incursions inside a cloud of points. Once the boundary points of the FEM are selected, a Delaunay triangulation allows to define faces and normals, from which the points can be classified for as pertaining to one of the spars or one of the upper or lower surfaces of the wing box. Figure 3.12 exemplifies the selection of points for a wing box, using an illustrative model of built-up FEM.

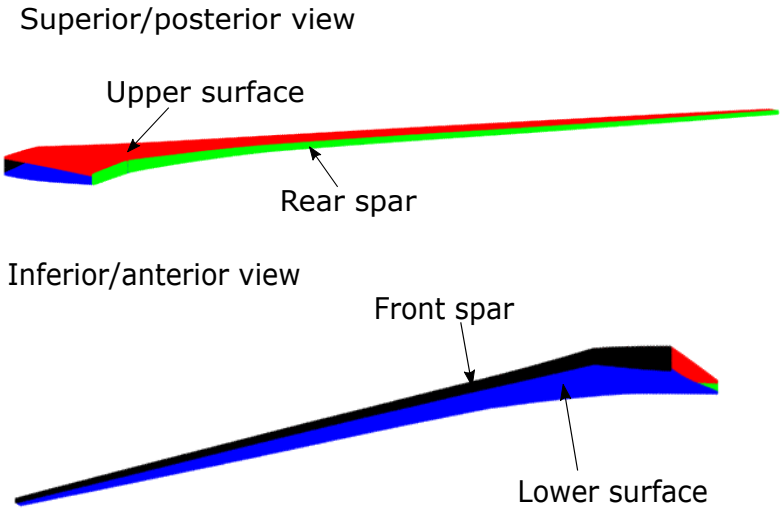

Figure 3.12: Wing box regions identified from structural nodes.

For the upper and lower surfaces of the wing box, a spline is calculated for each of the linear and dual modes identified in the structural ROM calculation. This process may take a while, but is performed only once and may be computed in parallel.

After the regions are identified for the FEM nodes, it is possible to classify each grid point of the aerodynamic surface mesh. For the points over the upper or lower aerodynamic surfaces, the splines calculated determine the displacements for each of the modes. If an aerodynamic grid point is located over the leading edge or the

trailing edge, the modal displacements of this point are related to the displacements of the closest points over the leading and the trailing edge. The idea is that the motion of the leading edge is related to the motion of the front spar, for example. Figure 3.13 illustrates the displacements from a point over the leading edge and a point over the upper surface. While the displacements of the upper surface points are determined from the spline of that surface, the points over the leading edge are displaced keeping the similarity of the green triangle from the undeformed to the deformed condition.

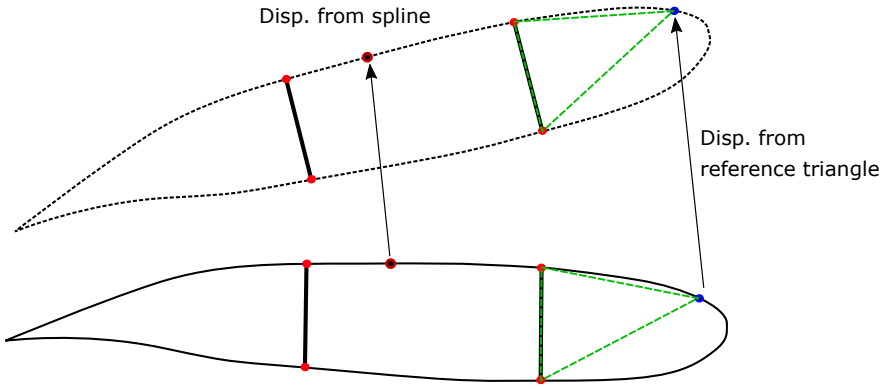

Figure 3.13: Interpolation of modal displacements according to the region of the wing box. The airfoil is illustrative only.

Ideally, the displacements from the leading and trailing edge points would be determined from a complete FEM, considering all the wing regions. The approximation discussed above is an alternative when there is no structural model for the leading or trailing edges, but only the wing box. In this approximation, all the forces applied to the leading edge are transmitted to the upper and lower points of the front spar, and similarly for the trailing edge.

An important note is that the linear and dual modal displacements are composed linearly to obtain the final displacements during the simulations. The procedure illustrated in Fig. 3.13 involves finite rotations for the leading and trailing edge points. In order to prevent these nonlinearities, the modal displacements are scaled down first,

then the small displacements are calculated for all the surface points of the aerodynamic grid, and finally the modal displacements are scaled up again to match the amplitudes of the corresponding structural modes. Finally, it is possible to calculate linear and dual modes with the three components of displacements for each point of the aerodynamic surface grid.

CHAPTER 4

Numerical Implementation of ROM Methods

This chapter explains the organization of the codes written to implement the structural and the aerodynamic ROMs. The goal is to describe in details the steps needed for the construction and for simulation of the models.

The structural ROM is described first, with details about the offline and online phases of the solution. Issues about parameter choices, number of degrees of freedom of the reduced model and sampling strategies are discussed. For the aerodynamic ROM, the integration of the nonlinear structural ROM with the CFL3D code is described first. This composition allowed exploration of aeroelastic phenomena related to large displacements and rotations in a CFD environment. Also, this development was a required step to evaluate the aerodynamic ROM. Finally, details of the aerodynamic ROM implementation developed with the Method of Segments and convolution for unsteady computations are described, involving the creation of the reference data and simulation phase of the solution.

4.1 Structural ROM

Developing a nonlinear structural ROM based on modal approach was the primary objective of this thesis. Although the formulation is general and may be implemented

in a variety of computational ways and languages, this section explains the particular implementation that was followed in terms of general processes involving reference solutions, model identification, and dynamic simulations. First, the overall organization of the structural ROM is presented, then each of the solution phases is detailed. As in any model reduction, there are parameters to be chosen that depend on the particular model and the required degree of accuracy. Those parameters choices are discussed.

4.1.1 Workflow of the EnICE Code

In general, the implementation of the nonlinear structural ROM, called Enhanced Implicit Condensation and Expansion (EnICE) method, follows three basic stages:

- Calculation of reference solutions;
- Model identification and preparation;
- Model simulation.

The calculation of reference nonlinear static solutions from a commercial solver (Nastran SOL 400) and the model preparation and identification are illustrated in Fig. 4.1.

Each stage of the EnICE requires code development. The general workflow is presented, such that the process can be replicated in any particular code development. However, there are particular aspects that should be highlighted to facilitate its development. Whenever possible, comments are made about such aspects.

The extraction of reference solutions begins with the FEM model to be processed. Initially, the linear modal solution is extracted. Also, the mass and stiffness matrices as well as the initial nodal positions are extracted from the FEM. With the modal shapes, trial solutions that excite large displacements are tested, and a set of training

loads is defined for nonlinear static solutions using the FEM solver. The information from these computations is stored for use in the identification of the nonlinear ROM.

For the model identification, the obtained reference solutions and the gathered model information are used. From the database of static solutions, the nonlinear displacement components are isolated and the dual modes are calculated using singular-value decomposition. From this decomposition, the dual-mode amplitudes are also calculated. The amplitudes of dual modes are fitted as nonlinear functions of the amplitudes of linear modes. In this work, the fitting is accomplished using artificial neural networks. Besides the fitted function, the first and second derivatives of the dual modes as function of the linear modes are also obtained. With the function for nonlinear displacements, the nonlinear forces are isolated and fitted as functions of the linear modal amplitudes as well. Again, ANNs are used for the fitting. From the dual modes, linear modes, mass matrix and initial nodal positions, the modal matrices to be used for gravity and fictitious forces (from base motion) are pre-calculated and stored. This makes possible to implement these loads in the online stage in an efficient way. Finally, the fitted functions, the pre-calculated matrices and the model data are stored for use in the ROM simulations.

The ultimate feature of the ROM is its fast simulation time in the online stage. To reduce computational time for simulations, multiplications of large matrices must be avoided during execution time. All matrices to be handled at that stage should have size compatible with the ROM d.o.f.s. A simulation preparation is performed before the actual execution to reduce all external loads to modal loads. This preparation also specifies details like gravity acceleration value and nature of the external loads, that is, if follower or fixed loads.

If $f_{ext}(t)$ is a column matrix of external loads applied to each of the FEM d.o.f.s and evolving in time, the linear and dual modal loads are pre-calculated, *i.e.*,

$$\Phi^T F_{ext}(t) = f_{lin}(t) \tag{4.1}$$

$$\Psi^T F_{ext}(t) = f_{dual}(t) \tag{4.2}$$

where $f_{lin}(t)$ and $f_{dual}(t)$ are the column matrices of the linear and dual loads, reduced to the size of linear modes and dual modes selected for the ROM. These matrices are stored as functions accessible during execution time.

After the execution, which is the time-integration of Eq. 2.51 or the solution of its static version, the output is saved in terms of modal amplitudes. From the modal amplitudes, the displacements of the entire FEM or a subset of it containing the d.o.f.s of interest can be recovered using Eq. 2.3.

4.1.2 Calculation of Reference Solutions

Training the ROM with reference solutions requires selection of external loads capable of representing the cases to be later simulated. In particular, the modal forces to be used during the training should be relatively close to the ones observed during the simulations.

There is no established objective metric to decide if the simulated reference solutions are sufficient for a desired level of ROM accuracy. It is possible to get error estimates for the fitted functions of nonlinear displacements and nonlinear forces, but the accuracy and stability of the ROM are not easily assessed. This is one of the points to be improved in this methodology.

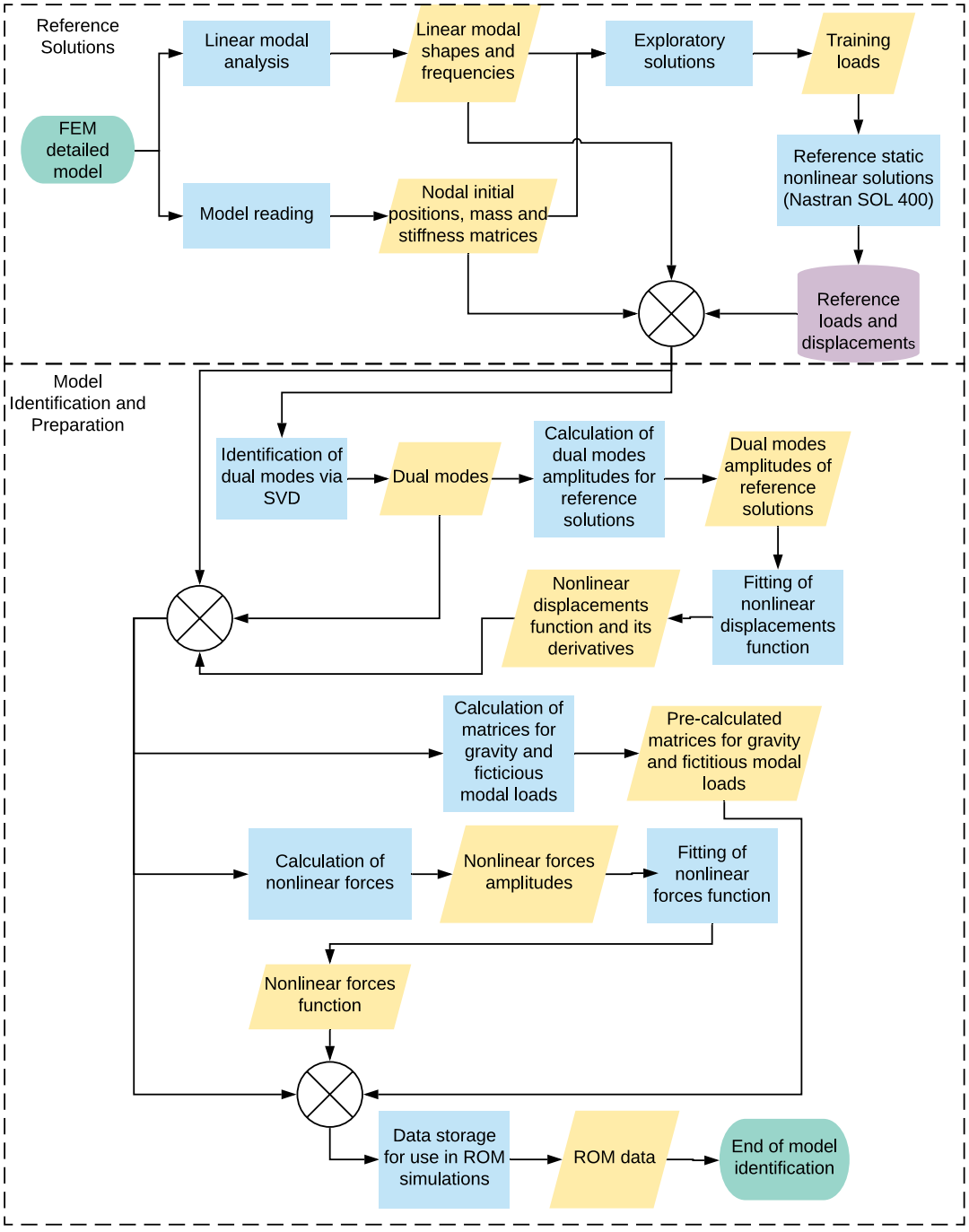

Figure 4.1: Model preparation and identification according to the EnICE methodology.

In aeroelastic applications, the loads are usually aerodynamic forces, distributed along the wing span, augmented by gravity loads and thrust. Even though there is no *a priori* knowledge about the exact shape of the loads to be simulated, a first generally valid approximation is to use loads in the shapes of linear modes, as discussed in section 2.2. These loads should be high enough to cover the range of displacements expected for the simulation phase of these very flexible structures. It is useful to test high amplitudes for the loads with static nonlinear solutions before sending a batch of simulations to the reference solver. In fact, there may be problems with the convergence of the static solutions for high loads within the commercial FEM as it is discussed in Chapter 5.

Knowing the positive and negative limits for the amplitudes of the simulation case of interest, the training points are distributed inside this hyperspace of amplitudes. One of the best sampling methods for uniform distribution in large dimensional spaces is the Halton sequences [114], and these are used to create reference loads exciting all the linear modes selected for the ROM.

As the reference solutions are generated from the finite element solver, the results are stored in a a data set to be later used in the model identification. Since built-up finite element models have a large number of degrees of freedom, usually on the order of 10^5 or 10^6, the memory requirements may be large. It is important to have the capability of storing the reference solution data in binary files, using formats like HDF5.

4.1.3 Model Identification and Preparation

The first stage in the model identification is a verification that the mass and stiffness matrices extracted from the FEM model are correct. This is performed by extracting the generalized eigenvalues using these matrices and comparing them with the values from the modal solution obtained directly from the commercial FE code.

It is important to notice that the mass and stiffness matrices have entries related to the active degrees of freedom only. Constrained d.o.f.s do not enter in the calculation of modal solutions, as expected.

After calculation of the nonlinear contribution to the displacements, according to section 2.2, the dual modes are identified. For the identification of dual modes, multiple procedures can be followed. As described in section 2.2, the singular-value decomposition is used to calculate the dual modes of nonlinear displacements (Eq. 2.27). However, if the model is too large, obtaining the SVD from the matrix of nonlinear residue R_{NL} may be impractical. A truncated SVD can be performed in this case to extract only the first dominant singular values and the related singular vectors. The method proposed by Liu *et al.* [115] can be used for an accelerated SVD.

Since the matrix of nonlinear residue has data from different degrees of freedom, including translations and rotations, it may happen that not all components are equally represented by the first dual modes, even if the coefficient of determination (Eq. 2.28) is high. For this reason, it is useful to check a few samples with large displacements from the reference solution and test if the linear and dual modes are able to represent the nonlinear displacements correctly for all the components at the wing tip or other representative locations. If it is found that the dual modes are not adequate for all translation and rotation components, an extraction of dual modes individually for each component may be needed.

Once dual modes are extracted, the dual-mode amplitudes $r(q)$ are fitted as functions of the linear mode amplitudes q. As discussed, this process could be performed with any fitting function, but in this work artificial neural networks were employed due to its speed and capability to deal with large amounts of data. Besides the fitting of nonlinear function, the first and second derivatives $\frac{\partial r}{\partial q}$ and $\frac{\partial^2 r}{\partial q^2}$ are also required for the equations of motion, as described in Chapter 2. It is more accurate to extract the derivatives directly from the fitted function, instead of using finite differences during

simulation time. However, depending on the complexity of the fitted function, it may require a long time to extract the derivatives. In this particular implementation, symbolic computations were used to get the derivatives from the fitted neural networks. Frequently, this is a slow process. Once the functions are calculated, however, the evaluation of those is quick and can be implemented in a language like C++. The main EnICE framework code of the is written in Matlab, but the functions of nonlinear displacements and forces that are called multiple times in the simulation are C++ MEX functions, which are C++ subroutines called from Matlab.

4.1.4 Static and Dynamic Solutions

Prior to the solution of the equations of motion (Eq. 2.21) or its static variant, all the simulation data must have been stored. These information include the points where the loads are applied and the linear and dual modal forces that are computed beforehand to save computational time.

In general, it is good practice to avoid computations with large matrices during simulation time. In other words, all quantities should be modal, written in terms of the modal degrees of freedom, like the gravity and fictitious loads discussed in section 2.3. Follower loads are particularly time-consuming, because a rotation matrix must be assembled for all the nodes receiving follower loads. For such reason, distributed follower loads may require much longer times to be simulated with this structural ROM, compared to dead forces.

Different ODE solution packages were used in the online phase: "ode115s" in the Matlab framework [104] and LSODI in the EnICE/CFL3D framework discussed in section 4.2.In particular, it was noticed that methods for stiff equation were more efficient. That cannot be generalized, though, because each solver may have its own characteristics, like frequency of Jacobian evaluations. A requirement for the dynamic solver is the capability to deal with non-constant mass matrix, in order to

solve systems like Eq. 2.51. For the Matlab framework, the solvers "ode45" (based on an explicit Runge-Kutta formula) and "ode15s" (variable-step, variable-order solver based on numerical differentiation formulas) were evaluated. It was found that solver "ode15s" was faster than solver "ode45."

If the fittings of nonlinear displacements and forces have high errors, or if the evaluated modal amplitudes are far from the training reference solutions, it can happen that the static and/or the dynamic solvers may not converge. For this reason, it is important to make sure that the solution stays within training bounds. If the evaluated loads exceed the initially planned range, it may be necessary to retrain the model after adding new reference solutions.

The total speedup obtained with the nonlinear structural ROM depends on the particular implementation used and the number of degrees of freedom kept in the ROM. In general, for complex wing problems, each second of physical time may be simulated with a few seconds of computational time, using Matlab for the main calculations with the heaviest fitted functions in C++.

4.1.5 Selection of Parameters

In the different phases of the model identification and simulation, parameters are chosen for the EnICE, ranging from the number of modal amplitudes for the reduced model to the parameters of the neural network fitting. This subsection discusses practices to choose these parameters in a meaningful way.

4.1.5.1 Number of DoFs

The number of degrees of freedom in the ROM is the number of equations being solved. In the EnICE methodology, it corresponds to the number of linear modes used to represent the displacements in Eq. 2.3. Even though the ROM is nonlinear, all the nonlinearities are expressed as functions of the amplitude of the linear modes.

If the chosen number of d.o.f.s is too low, the linear response to higher-frequency excitation will be inaccurate and the representation of displacements may be insufficient. On the other hand, if too many degrees of freedom are selected, the fitting of nonlinear displacements and forces may require an excessive number of samples. In this balance, it is important to consider the expected frequency content of the load cases to be analyzed with the ROM.

An approach commonly used in vibration analysis to decide for the number of significant linear modes is the analysis of modal effective mass [116]. This parameter is a measure of the response of each linear mode to a loading like a constant acceleration along each of the translation d.o.f.s (and analogously for each rotation). Along each translation (or rotation) direction, the cumulative sum of the modal effective masses of all modes is total mass of the system. For the i^{th} linear mode Φ_i, the effective modal mass in the x-direction is

$$M_{eff,i,x} = \frac{\left(\Phi_i^T M \bar{r}_x\right)^2}{\Phi_i^T M \Phi_i} \tag{4.3}$$

where $\bar{r}_x$ is a column matrix with displacement 1 for all the degrees of freedom related to the x-direction. It is analogous for the other translation directions as well as rotations.

There is no general agreement about what should be an acceptable effective modal mass, but cumulative values around 80% of the total mass in the most flexible direction are reasonable. The most flexible direction for a wing, for example, would the the vertical direction, which is usually related to the first bending mode.

Depending on the structure, the effective modal mass may be distributed to more linear modes or concentrated in the first few ones. For the models studied here, around 18 linear modes were needed to achieve 80% of the mass in the vertical direction.

Surely, the measure using effective modal mass is not an absolute way of deciding the number of degrees of freedom for the ROM. The frequency of the loading should

be taken into account as well. In the examples of this work, the loads had low frequency content and high amplitudes, but if higher frequencies are expected, it may be important to include linear modes compatible with those.

4.1.5.2 Number of Dual Modes

The number of dual modes is dependent on the desired accuracy in the representation of nonlinear displacements. The RIC (Eq. 2.28) is the measure usually used when determining the importance of the first singular values. However, as discussed before, it may be useful to check if all components of the nonlinear displacement are represented accurately with the selected dual modes. It may be helpful to create dual modes specific for certain rotation directions or in-plane displacements.

Including a very high number of dual modes is not a good practice. From the modeling experience, the fitting of higher dual modes may be inaccurate, suggesting that the limited set of degrees of freedom of the ROM may not be enough to determine their values. If the fitting errors are considerably higher for these dual modes, the solution loses accuracy. Monitoring the error of the fitting for nonlinear displacements helps in determining the number of dual modes.

4.1.5.3 Sampling Strategies

It was stated in the previous sections that Halton sequences [114] were employed to sample the loads for reference solutions. These are pseudo-random sequences that distribute points in a multi-dimensional space in a uniform manner, similar to Latin hypercube sampling [100]. However, depending on the particular application of the ROM, it may be interesting to enhance the samples with particular load cases different from the distributed loads in modal shapes (Eq. 2.22). For example, if tip forces are to be investigated, inclusion of tip forces in the reference static solutions will improve the accuracy of the ROM. Care should be exercised, however, to avoid

high concentration of points around specific areas of the sampling space.

4.1.5.4 ANN Fittings

The fitting with neural networks involves parameters related to complexity of the neural network, training process and overfitting avoidance.

A single hidden layer is generally used in fitting problems involving shallow neural networks. The number of neurons for this hidden layer determines the complexity of the ANN. If the number of neurons is too high, overfitting may be an issue. However, if the number of neurons is too low, the function may not have the flexibility required to fit accurately the reference data. From the models studied, with up to 18 degrees of freedom, a number up to 4 neurons is ideal for maximum accuracy in the predictions.

The training method of Bayesian regularization [117] takes longer to converge than the classical Levenberg-Marquardt algorithm [118], but it reduces the risk of overfitting. For all the training methods, there are criteria to stop the iterations. Usually, the training is completed when the error measure or its gradient falls below a specified threshold, when the maximum number of iterations allowed is achieved, or when the parameter μ exceeds a maximum value, whatever happens first. This parameter μ is used in the update of the weights and bias values, grouped in the column matrix w. The update of w from time step k to time step $k+1$ is performed as

$$w_{k+1} = w_k - [J^T J + \mu I]^{-1} J^T e \tag{4.4}$$

where J is the Jacobian of the error e with respect to the reference samples, and I is the identity matrix. If the parameter μ is zero, the error minimization is a quasi-Newton method [119], but a high μ turns the algorithm into a steepest descent minimization [120].

In particular, there are two parameters that were observed to impact the quality

of the training: the increase and decrease ratios of μ, represented by μ_{inc} and μ_{dec}, respectively. If the weight and bias update of Eq. 4.4 does not effectively reduce the error, the parameter μ is increased by the factor μ_{inc}. On the other hand, every succesful iteration reduces μ by μ_{dec}. Changing the default values of μ_{inc} and μ_{dec}, the velocity of convergence is impacted, but also the quality of the fitted function. For example, the default values of μ_{inc} and μ_{dec} are 10 and 0.1 in Matlab. By increasing μ_{dec} to a value of 0.6, the convergence is slower, but the fitting quality is better at the end. By decreasing μ_{inc} to a value of 1.2, an early training stop due to high μ is delayed. Playing with these parameters can be helpful in increasing the quality of the fittings. This is only an example of tuning for the training process. Depending on the minimization algorithm, other parameters may be available.

The minimization with ANNs is subject to the problem of being trapped in local minima. For this reason, it is recommended to repeat the minimization a few times. For this implementation, each minimization is repeated a number of times, and the fitting with minimum error evaluated over the test set is selected. The test set is a fraction of the samples chosen randomly and isolated from the reference solutions that are used in the training. Based on the numerical studies in Chapter 5, the error evaluated over the test set achieves its minimum value when repeating the training around 15 times.

4.2 EnICE/CFL3D Integration

Consider the integration of the developed structural ROM in the CFL3D aeroelastic framework. Using the formulation already tested separately for the structural ROM, the linear, modal-based aeroelastic analysis of CFL3D in incremented to include the EnICE nonlinear structural ROM. The objective was to enhance the capability of this high-fidelity tool and to create a framework for training and verification

of an aerodynamic ROM.

This section explains the modifications implemented into CFL3D to turn the linear structural solver into the nonlinear structural ROM.

4.2.1 Modifications Implemented into the CFL3D Code

The main modifications implemented to the CFL3D code are:

- Input file;
- Equations of motion for structural dynamics solution;
- Inclusion of fitted functions for nonlinear displacements and forces, as well as its derivatives.

In the modified version of the CFL3D code, the number of dual modes is included as one of the inputs. All the linear and dual modes are read by the code in the same form, for mesh deformation purposes, but the modal loads are treated differently inside the equations of motion. With the inclusion of the EnICE formulation, the equations of motion changed, requiring evaluations of the fitted nonlinear functions for dual-mode amplitudes and modal forces during simulation time. Including these functions as inputs was not practical for the first tests. Currently, these functions are part of the source code, and any change in the ROM model requires a new compilation of the modified CFL3D code.

4.2.2 Predictor-Corrector Time Integration Scheme

The time-integration for aeroelastic solutions inside CFL3D follows a predictor-corrector scheme [107], indicated in Fig. 4.2 and explained below. First, a predictor step uses the generalized aerodynamic forces calculated at the current and previous times, n and $n-1$, respectively, and extrapolates linearly to estimate the future forces

at the next time step, $n+1$. The displacement is advanced using an average between the predicted force at $n+1$ and the current force at n, *i.e.*,

$$\tilde{x}_{n+1} = \Theta x_n + 0.5\Gamma(3Q_n - Q_{n-1}) \tag{4.5}$$

where x_n is the state vector composed of modal amplitudes and velocities q and $\dot{q}$ at time step n, $\tilde{x}_{n+1}$ is the predicted state vector for time $n+1$, Θ is the state transition matrix and Γ accounts for the influence of the generalized aerodynamic force Q.

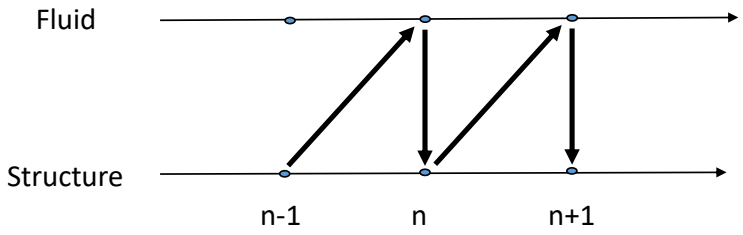

Figure 4.2: Fluid-structure staggered coupling scheme used in CFL3D.

After the mesh is deformed, the generalized aerodynamic forces are reevaluated, and a corrector step solves for the displacement using an average between the aerodynamic force at n and the aerodynamic force Q_{n+1} calculated with the predicted state $\tilde{x}_{n+1}$:

$$x_{n+1} = \Theta x_n + 0.5\Gamma(Q_{n+1} + Q_n) \tag{4.6}$$

Following this scheme, the generalized aerodynamic forces are calculated once per time step. The original method is described in Edwards *et al.* [121].

In this work, it was necessary to change the time-integration. In the original CFL3D implementation, a constant state transition matrix is used because the stiffness and mass matrices are constant. Θ and Γ calculated for the undeformed condition

are used throughout the simulation, since the time step is constant. For the EnICE approach, however, it is necessary to update the stiffness and mass matrices at each time step. Instead of using Eqs. 4.5 and 4.6 with the state transition matrix, the integration routine LSODI (Livermore Solver for Ordinary Differential Equations Implicit) [105] is used to perform the time marching of Eq. 2.21 with instantaneous mass and stiffness matrices. LSODI uses an implicit method with adjustable tolerances. So, it can be as accurate as desired. Replacing the previous time integration with this approach does not reduce the order of the fluid-structure coupling scheme. The procedure follows the same predictor-corrector scheme of Figure 4.2, and the same generalized forces of Eqs. 4.5 and 4.6 are used, summarized in Figure 4.3. The ODE solver LSODI uses the nonlinear force, nonlinear displacement, and the derivative matrices present in Eq. 2.21 and solves for the degrees of freedom corresponding to the number of linear modes.

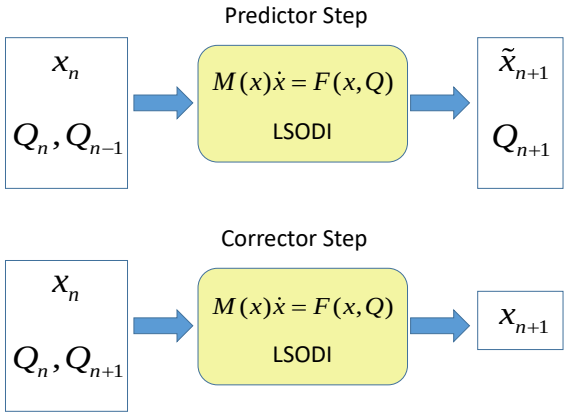

Figure 4.3: Predictor and corrector steps for the aeroelastic time marching using LSODI.

4.2.3 Mesh Deformation

The mesh deformation capabilities were already built in the CFL3D. Both finite macro-element models and exponential decay can be used. From the experience, large displacements can be adequately simulated with exponential decay. In this case, the parameters to be chosen are the offset α_{mesh} and the decay factor β_{mesh} already presented in Eq. 3.23. The values for these parameters are usually in the range of 0.005 to 0.05 for the offset and 1 to 10 for the decay factor. Both methods are used in this dissertation, but the later examples employ the exponential decay, because this method was observed to yield better deformations for large wing deflections, with less effort in adjusting parameters and/or mesh partitions. In the end, it is important to guarantee that no negative volumes will occur during simulation. CFL3D even has a tool for mesh deformation analysis that can be run beforehand to determine if the estimated amplitudes of motion are cleared from negative volumes.

4.3 Aerodynamic ROM

Compared to its structural counterpart, the aerodynamic ROM development was shorter, using procedures already developed and implemented by Skujins and Cesnik [21] and adapting them to very flexible structures. Eventually, the accuracy of the method was improved with the addition of a lifting-line correction for the effective angle of attack of the segments.

The preparation of the aerodynamic ROM involves mesh generation, calculation of reference solutions and processing of the data for posterior use in aeroelastic simulations. Figure 4.4 illustrates the preparation process in a flowchart.

From the geometry of the wing, the surface mesh is generated. This can be accomplished using a commercial code like Pointwise. In this work, the 3D mesh for the studied wings was obtained using the surface mesh and performing a normal

extrusion with the pyHyp code using its hyperbolic method [122].

Once the aerodynamic mesh is generated, the linear and dual modes obtained for the structure during the preparation of the structural ROM are used to interpolate modal displacements at each of the grid points over the aerodynamic surface. This method is described in section 3.6. These interpolated modes are needed for the input files of the CFD reference solutions.

The CFL3D simulations provide the output data, which are different for the steady and unsteady solutions. For the steady cases, a more detailed output is requested, comprising pressure and friction force coefficients. From the unsteady simulations, only the modal forces and lift coefficient are needed along the step response.

Using the pressure coefficient and possibly the friction force coefficients, aerodynamic forces are distributed to each grid point over the surface, for all the flight conditions of interest. In order to improve the accuracy of the method for cases where the load distribution is considerably different from the reference case of rigid wing, a correction with lifting-line is performed. Induced angle of attack calculations allow a more precise fitting of forces for later simulations.

The data from steady simulations are interpolated linearly in this work, as opposed to the Kriging method of Skujins and Cesnik [1]. Since the interpolation is performed in simulation time, there is no need to have a fitting step in the preparation phase.

After the finite step responses (FSR) are obtained from the unsteady simulations and the forces for the grid points are obtained from the steady reference simulations, these data are stored for use in the ROM simulations.

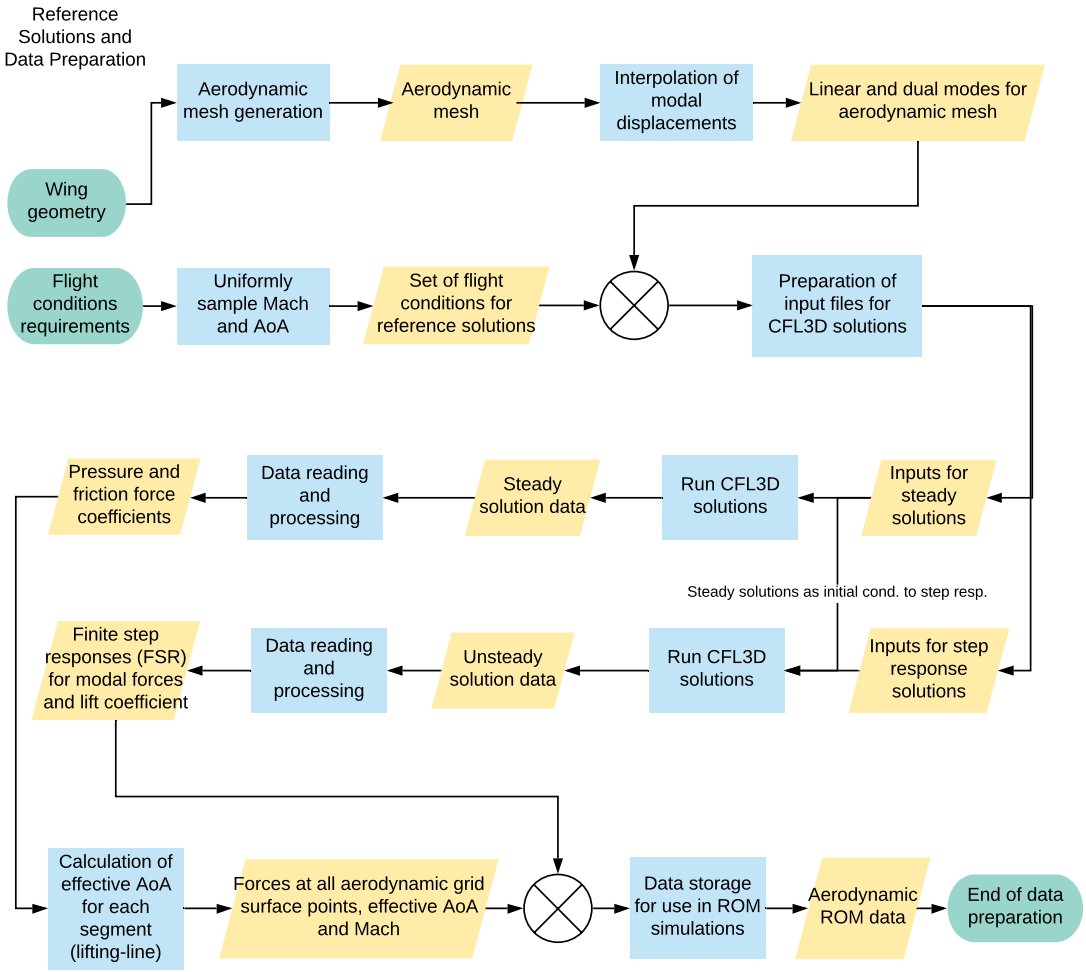

Figure 4.4: Reference solution calculation and data preparation for the aerodynamic ROM.

4.3.1 Reference Solutions

For each reference solution, proper convergence should be observed. This subsection discusses the parameters which are controlled in the reference solutions within the CFL3D environment.

4.3.1.1 Step Responses to Modal Perturbations

For the step response solutions, a single angle of attack is used in all reference cases. Since the unsteady response is used to compose only the linear portion of the solution in Eq. 3.16 (nonlinear effects are taken into account though the correction factor), the initial angle of attack is not influential. It should be small, though, to avoid excursion into the nonlinear regime.

The amplitude of the step responses is adjusted with trial and error to avoid numerical problems in running the solutions. In fact, large steps may cause convergence difficulties within CFL3D. On the other hand, the amplitudes should be high enough for a clear signal in the response.

Before the unsteady response is obtained, a converged steady solution is calculated as initial condition. However, since the step response can be so small due to the limited step amplitude, a reference solution with no step input is also obtained for the same initial condition. The step response becomes the difference between the unsteady solution within step input and the unsteady solution with no step input.

In the CFL3D framework, unsteady solutions can use multigrid and sub-iterations to improve accuracy. Convergence should be attained for every step, before advancing to the next one [110]. This can be checked by monitoring the lift coefficient throughout the sub-iterations within a step, as illustrated in Fig. 4.5. In this case, 20 sub-iterations are enough to obtain convergence for the first iteration, which involves the largest force variations due to the step input.

Another important requirement on the FSR is that enough simulation time should

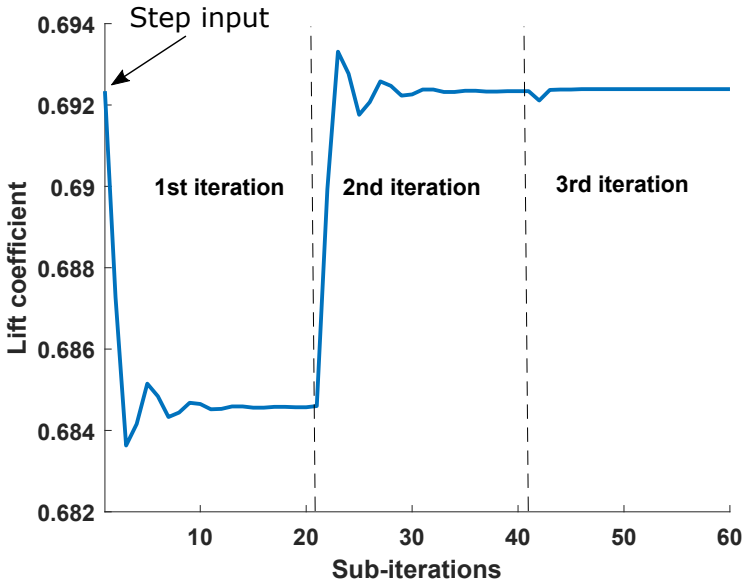

Figure 4.5: Sub-iterations in the response of lift coefficient right after step input in the shape of mode 1.

be recorded to guarantee that all unsteady response is captured. This is evaluated by checking the convergence of the modal force and the lift coefficient with time.

4.3.1.2 Steady Solutions with Rigid Wing

The steady simulations cover the entire range of angles of attack, Reynolds and Mach numbers designed for the simulations. Even large angles of attack in the non-linear regime can be included. These steady solutions provide the data reference data for the MoS predictions.

Since there is no mesh deformation in the steady reference solutions, the only detail that should be observed is the achievement of a proper convergence. This can be done in terms of the residue of the governing equations and convergence of the force coefficients. For example, it is expected a residue decrease of at least 3 to 4 orders of magnitude relative to its initial values.

The CFL3D aeroelastic solutions include only normal forces in the computation of modal loads. This way, friction forces are not included in the computations from the

original package. In order to verify ROM results against CFL3D simulations, only normal forces are obtained from reference steady results for MoS predictions.

In the implementation performed here, forces in the three global directions are obtained for each grid point of the aerodynamic surface. In the implementation by Skujins and Cesnik [1], the forces were calculated for each segment. However, in terms of modal forces it was observed that their approach led to high errors. Obtaining forces for each point is a way to reduce the ROM errors, even if that contributes to slower computation times, due to more data being analyzed. In order to reduce the costs related to a great amount of point forces, a simple linear interpolation of forces is used, as opposed to a fitting with Kriging or neural networks.

In order to improve the accuracy of force prediction for deformed shapes, a lifting-line approach is used to calculate the effective angle of attack for each segment along the wing, as explained in Chapter 2. The forces are then fitted as function of the effective-angle of attack. For that reason, the reference solutions with rigid wing should include calculation of the effective angle of attack for each segment. However, there is a detail that can complicate the calculation of effective angles of attack: rapid variations of circulation along the wing. If the wing is partitioned into a large number of segments, there will be inaccuracies in determining the circulation along the wing, and that may cause erroneous induced angles of attack. In terms of induced angle of attack distributions, it is more accurate to consider a smoothed lift distribution, using polynomial fittings for the circulation as function of the spanwise position of the segments. The number of segments and location of the segment boundaries were not explored in this dissertation.

4.3.2 Simulations with Linear Convolution

For aeroelastic ROM simulations, the aerodynamic ROM predictions are called from within the structural ROM. For steady simulations, only the fitting of forces is

performed as function of the local effective angle of attack and the freestream Mach number. The forces for each point are then rotated to the body reference frame and the linear and dual modal forces are calculated using the forces and the mode shapes for the aerodynamic grid points. However, if the simulation is unsteady, an additional procedure is needed: the convolution of the linear response since the beginning of the simulation time.

Convolution is the slowest computation for the aeroelastic ROM simulation, in the implemented framework. Considering that each linear modal shape deformation is related to profiles of FSR of modal forces for all linear and dual modes, the number of performed convolutions grows with the square of the degrees of freedom. Costs are high because each convolution is an inner product evaluated at every time step. The convolution for an output y is presented in Eq. 3.17 in continuous form. For a discrete computation, considering the unsteady output at time step N, the linear convolution is implemented in this work using the summation given by

$$y^N_{Lin,u} = \sum_{j=1}^{n} \sum_{i=0}^{N} \bar{y}^i_j \left(q^{N-i+1}_j - q^{N-i}_j \right) \tag{4.7}$$

where $\bar{y}^i_j$ is the normalized value of the FSR at time step i after a step deformation on the shape of the j^{th} linear mode. q^{N-i}_j is the amplitude of the j^{th} linear mode at the time step $N - i$. It is assumed that the deformation step occurs at the step time 0, and the total simulation has N time steps, with n linear modes. In Eq. 4.7, the summations are performed to cover all previous time steps and the deformation influence of deformation influence in the shape of all modes.

Since the FSR varies quickly in the beginning, the time steps for the unsteady response should be relatively short. That is the reason why the convolutions are approximated by relatively long array multiplications. Also, the short time step of the unsteady responses requires outputs of the structural ROM more frequently than a pure structural solution would.

There is space for improvement in the efficiency of the implemented convolution procedure for this aerodynamic ROM. Strategies for convolution acceleration are discussed by Pavel and David [123]. Given the decaying shapes of FSR, recursive filtering may be employed in the future for acceleration of the convolution.

Time integration for ROM aeroelastic predictions follow the same scheme of the structural ROM discussed in section 2.4.

CHAPTER 5

Structural and Aerodynamic ROM Numerical Studies

In this chapter, the methodologies for the nonlinear structural ROM and the aerodynamic ROM are illustrated with examples of structures showing increasing number of degrees of freedom. The first case is purely structural, resembling a multibody dynamics problem. The objective with such model is to gradually introduce the process of training and simulation with the EnICE method. The second problem is a 16-m half-wing model that has been used by other authors in studies of large displacements. It is a beam model, but the aerodynamics is modeled in the CFL3D framework and the first aeroelastic results are analyzed. Then, the wingbox of the University of Bristol Ultra-Green (BUG) Wing [11] is reduced and the results are compared against beam-based models in a benchmark study. Bend-twist coupling was introduced in the wing structure by defining anisotropic material properties in the skins. In this case, the built-up FEM is reduced with the EnICE structural ROM, but no aeroelastic analysis is performed. Finally, the built-up FEM of the wing of the undeflected Common Research Model (uCRM) with aspect ratio 13.5 wing introduced by Brooks *et al.* [109] is reduced for aeroelastic analyses. The model is simulated with a few degrees of freedom using the EnICE, preserving good accuracy for time-domain simulations involving large tip displacements. The aerodynamics involves transonic nonlinearities and large displacements. For this model, the aerodynamic ROM is coupled to the

structural ROM for aeroelastic analysis.

5.1 Example with Rods and Torsional Springs

This first example illustrates how large displacements can be modeled with a few degrees of freedom using an additional basis of dual modes. The model is a simple set of rods connected with torsional springs moving in a single plane.The reference solutions are obtained from the analytical equations for the purpose of training the ROM and verifying the results.

5.1.1 Model Description

The model consists of six rigid rods connected in series. The first rod is attached to a wall via a torsional spring, and each connection between two consecutive rods also has a torsional spring, as illustrated in Fig. 5.1. The spring attached to the wall is at an unstretched condition when the rod is perpendicular to the wall plane. The other springs are at their unstretched state when the connected rods are aligned with respect to each other.

All the rods have the same length of 1 m and have uniform density of 1 kg/m. All the torsional springs are linear, with restoring moment proportional to the misalignment angle between two adjacent rods, with a constant of 200 N.m/rad.

5.1.2 System Description

The motion of this relatively simple problem can be described using the angles of the rods relative to the horizontal as degrees of freedom, as illustrated in Fig. 5.2. The equations of motion for the rod governing this problem can be derived analytically.

For the structural ROM, the degrees of freedom are the amplitudes of the linear modes. However, the modes are represented by the displacements of all the nodes

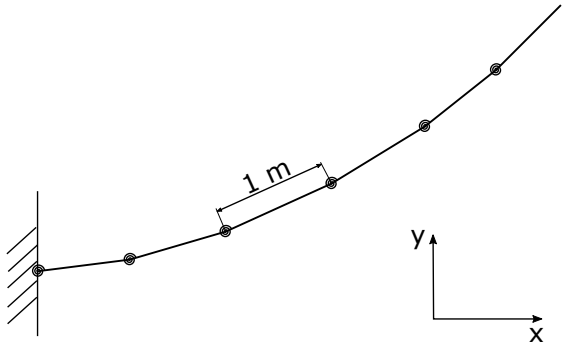

Figure 5.1: Rods connected with torsional springs

.

instead of angles. In this way, a basis of linear modes will never reproduce all the displacements achievable by the rod system. Therefore, a basis of dual modes is needed to obtain the displacements along the $x-$axis.

5.1.3 Training Loads

The training loads are selected to excite the system in the shape of the linear modes. Since the system has six degrees of freedom, there are only 6 linear modes. They are presented in Fig. 5.3 with amplitudes normalized by the mass matrix. Notice that only vertical displacements are represented with the linear modes.

The training loads could be forces or moments for this system. Without loss of generality, moments were selected for the ROM training. According to the number of degrees of freedom selected for the ROM, a Halton sequence was used to generate quasi-random amplitudes.

5.1.4 Selection of Dual Modes

The set of dual modes was selected from the residue of nonlinear static simulations. For the system of rods and torsional springs, the dual modes are needed to match displacements in the $x-$direction.

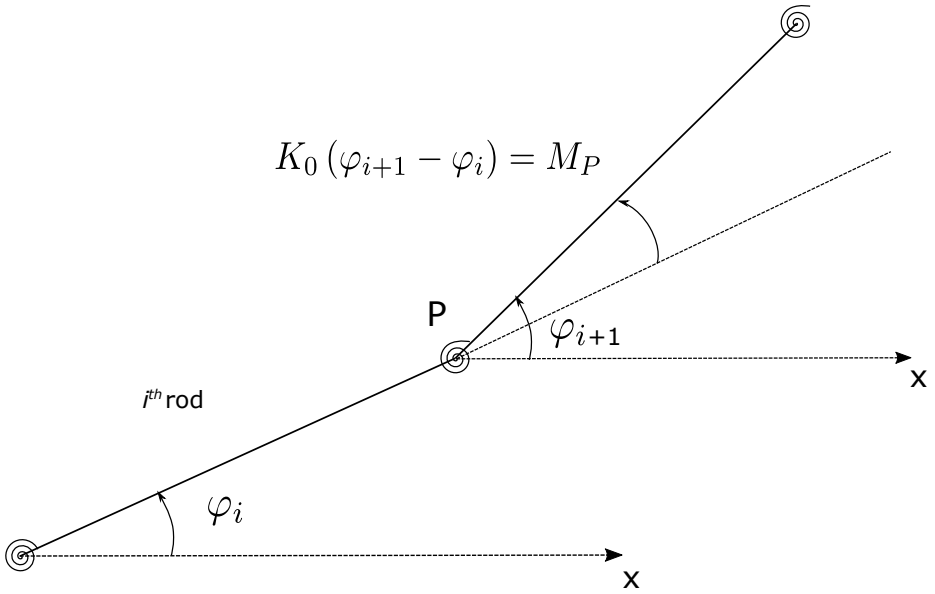

Figure 5.2: Angle used to describe the position of a rod.

For example, if one of the training cases is composed of large displacements, the components along the linear modes will imply large errors. However, as dual modes are added to the description, the final deformed state can be achieved, as shown in the progression on Fig. 5.4. Using only linear modes, the tip $x-$component is kept at the original position corresponding to the total length. With four dual modes, the rod-spring system practically matches the reference solution.

Taking the ROM case with two degrees of freedom and 1000 samples, the RIC of the residue matrix indicates an adequate number of dual modes (RIC ¿ 99%). Table 5.1 shows that the singular values of the first four dual modes are enough to reach a RIC of 99% for the residue matrix.

As discussed before, the RIC should not be taken as the only parameter for the determination of the number of dual modes. Observing the displacements for a few samples of nonlinear static solutions is useful to check if the set of dual modes is sufficient.

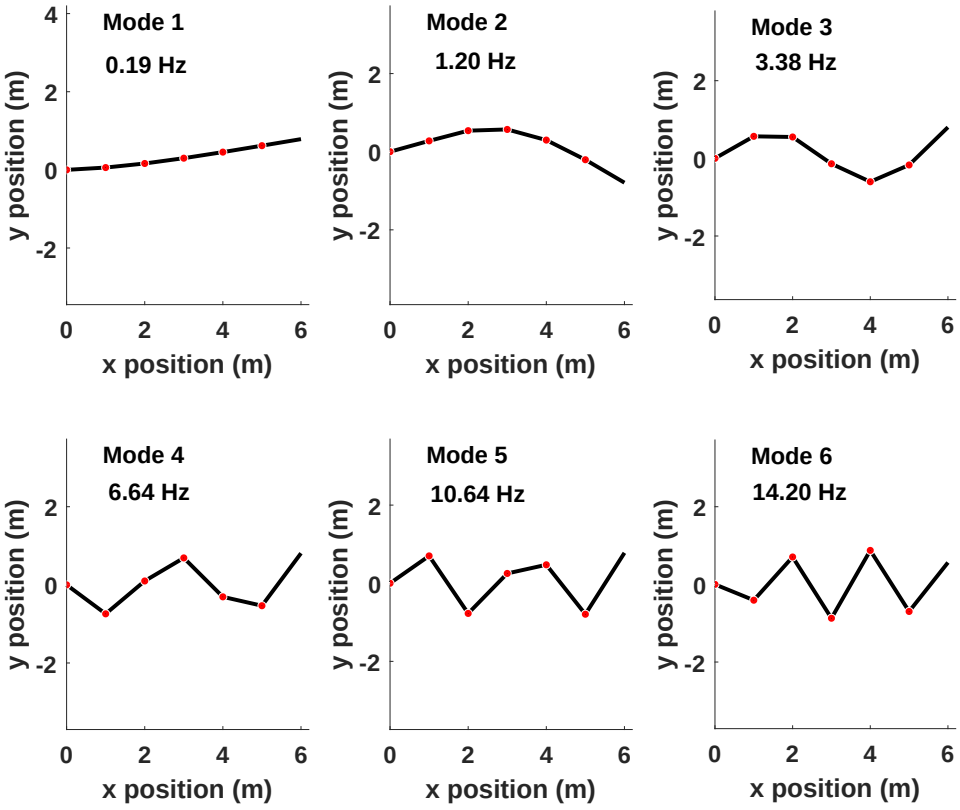

Figure 5.3: Natural frequencies of modes of the rod-spring system.

5.1.5 Fittings of Nonlinear Displacements

The number of selected dual modes influences the fitting complexity required to build the ROM. According to the hypotheses of the EnICE, the nonlinear functions depend solely on the amplitudes of the linear modes. Derivatives up to the second order are needed from the fitted functions of dual mode amplitudes, according to Eq. 2.21. These derivatives may be obtained analytically or through finite differences. In this case, since the number of degrees of freedom is relatively low (< 6), the derivatives are calculated analytically.

For a simple structure like the rod-spring system, the fitting of nonlinear amplitudes is achieved with great accuracy with four neurons in the hidden layer. The

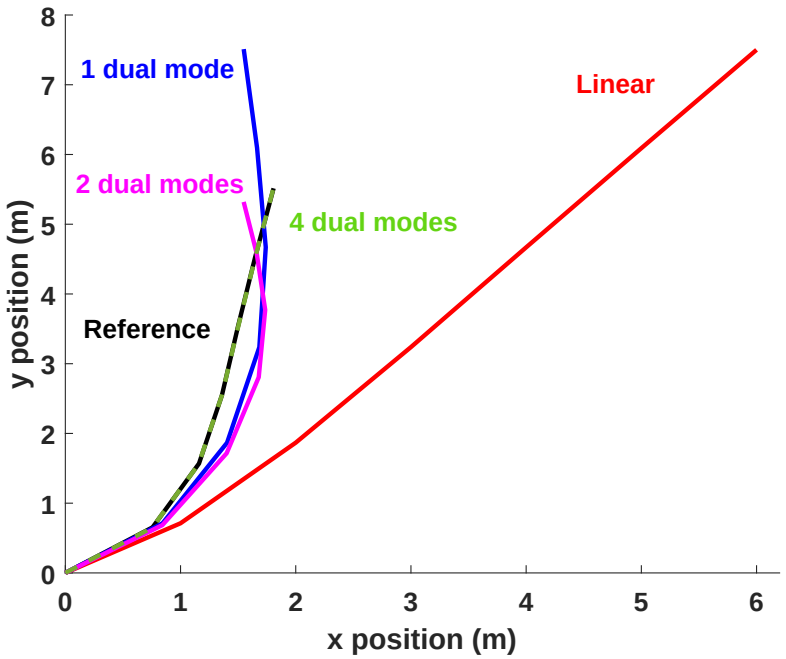

Figure 5.4: Displacement improvement with addition of dual modes.

coefficient of determination R described in section 2.2 is practically unity.

There are no fittings for nonlinear forces. In this case, the system is described by the angles depicted in Fig. 5.2. Since the torsional springs are linear, proportional to their angles, the moments depend linearly on the modal amplitudes. For this reason, only nonlinear fittings for displacements are meaningful in this context.

Table 5.1: Singular values of the residue matrix for ROM with two d.o.f.s.

Dual modes	Singular Value	RIC (%)
1	99.3	60.84
2	45.1	88.50
3	11.5	95.54
4	5.8	99.12
5	0.9	99.64
6	0.5	99.93

5.1.6 Time-Domain Responses

In dynamic responses, the errors on the tip displacement for high-aspect-ratio wings is a reasonable metric for evaluating the ROM accuracy. In fact, the wingtip is often the location with the highest discrepancies between reference solutions and approximations. For this simple system, the dynamic evaluations can also be performed based on the tip displacements.

For a vertical tip force of 8 N applied from $t = 0$, large displacements are obtained. For this example, the springs have proportional damping of 0.1%. Deflection on the order of 79% of the total length in the $y-$direction and 47% in the $x-$direction are observed in Figs. 5.5 and 5.6, respectively. With only two degrees of freedom representing the reduced system, an almost perfect match is observed between the ROM and the reference solution up to large displacements. The linear response shows the errors incurred when the system is linearized around the undeformed state and only the linear modes are used to recover displacements. All degrees of freedom are used for the linear response.

Consider now a sinusoidal tip vertical force of 80 N applied from $t = 0$ with frequency of 4 Hz. For this case, the ROM response is not accurate as in the previous case. Figure 5.7 shows the tip responses in the vertical and horizontal directions. Only the low frequency component of the response is captured correctly by the ROM. Since only two degrees of freedom were retained, an excitation beyond the frequency of the linear mode 3 is not represented correctly, as expected. Increasing the number of degrees of freedom accounted in the ROM would solve this issue.

5.1.7 Number of ROM degrees of freedom

When training the ROM, an increase in the number of degrees of freedom may improve the accuracy of the high-frequency response and the large-displacement representation by expanding the basis Φ in Eq. 2.3. However, the fitting becomes increas-

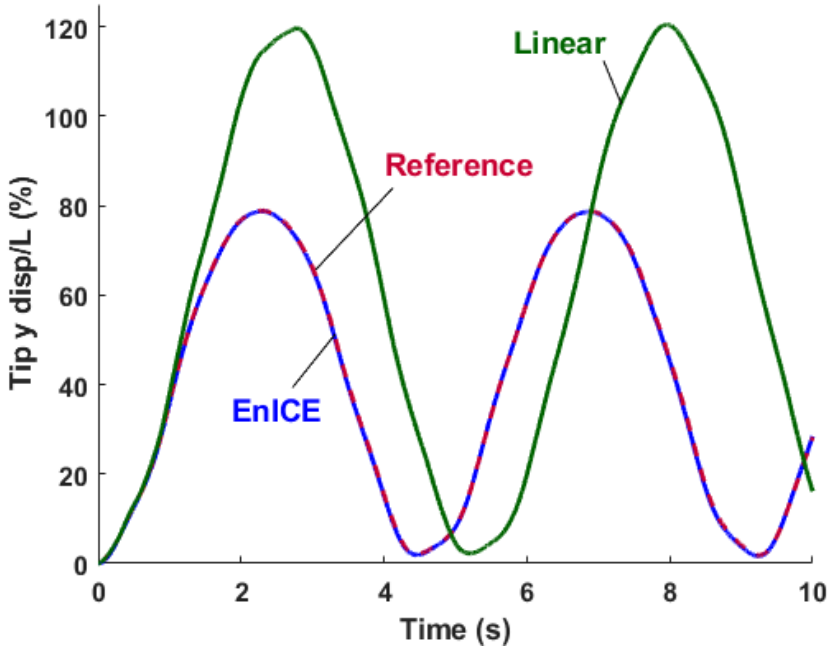

Figure 5.5: Tip vertical displacement after step force of 8 N.

ingly complex due to the additional dimensions. As a result, the prediction quality for a given excitation will increase initially until a minimum number of d.o.f.s is used, then increments of accuracy will be small or even negative.

For the load case of a step vertical tip force applied at $t = 0$ with 8-N magnitude , the response was evaluated by varying the number of degrees of freedom from 1 to 5. The metric used to evaluate accuracy is the average of the root mean square errors for all the translational degrees of freedom, considering all time steps for a 10-s simulation. This error metric is evaluated as

$$\text{Error} := \frac{1}{n_t} \sum_{i=1}^{n_t} \sqrt{\sum_{j=1}^{n_{dof}} \frac{1}{n_{dof}} \left(y_j^i - y_{j,ref}^i, \right)^2} \tag{5.1}$$

where y_j^i is the ROM output for the j^{th} degree of freedom at the i^{th} time step, normalized by the spring-rod total length (6 m), $y_{j,ref}^i$ is the reference solution, n_{dof} is the total number of degrees of freedom, and n_t is the total number of time steps

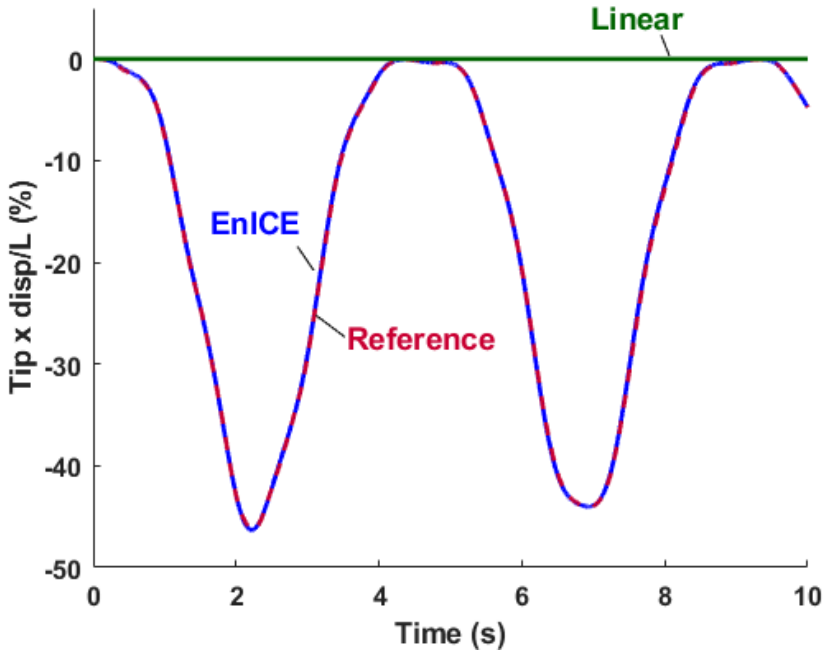

Figure 5.6: Tip horizontal displacement after step force of 8 N.

for the dynamic simulation.

Considering the increasing number of degrees of freedom, the evolution of the error metric is reported in Fig. 5.8. In this case, two degrees of freedom are enough for an accurate large-displacement low-frequency response. An increase in the number of degrees of freedom is not substantially beneficial. In fact, the increase from four to five degrees of freedom is associated to higher errors because the fitting quality may be worse with more degrees of freedom, if the number of reference solutions is kept constant.

5.1.8 Importance of Inertial Forces Related to Dual Modes

This subsection discusses the importance of accounting for the inertia forces related to dual modes in the equations of motion for this simple system of rods and torsional springs.

The inertia effects of dual modes depend on the excitation type and its magnitude.

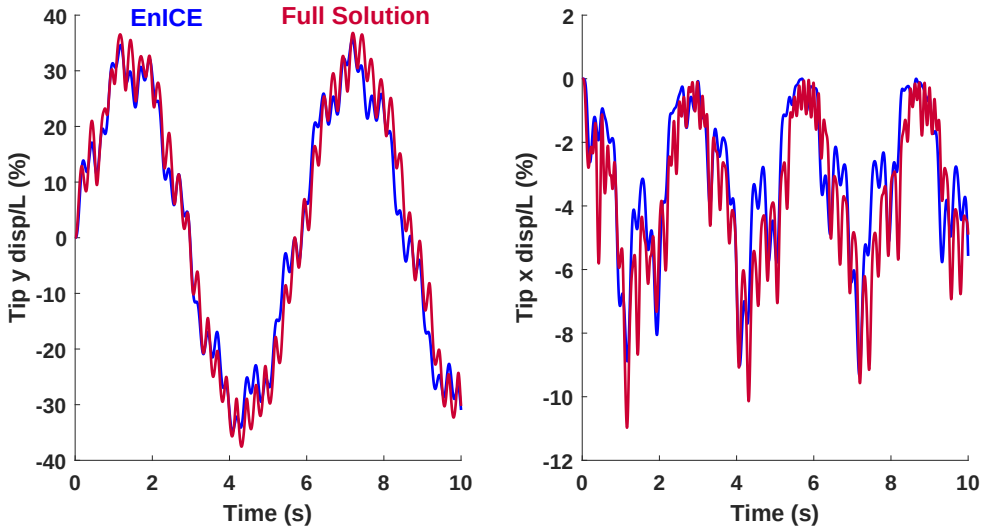

Figure 5.7: Tip vertical displacement after sinusoidal force of 80 N at 4 Hz.

For step forces like the one used in connection with the results in Figs. 5.5 and 5.6, the difference would be negligible. However, for sinusoidal loads, a significant difference is observed for simulations that include or exclude the inertia loads related to the dual modes.

Taking the example of a tip vertical load of 25 N applied with a sinusoidal profile from $t = 0$ at a frequency of 1 Hz, the responses are compared with and without consideration of the inertia loads related to the dual modes in Fig. 5.9. For this response, the EnICE solution has two degrees of freedom. The response with no dual-mode inertia forces is obtained by taking the mass matrix of Eq. 2.51 as identity, instead of the matrix calculated from the Euler-Lagrange equations.

As noted, the effects of dual modes in the dynamic response will depend on the loading. For small amplitude excitations, the responses will not be so different as the ones shown in Fig. 5.9. For larger amplitudes, the effects are more pronounced. For this reason, reduced order models for cantilevered structures cannot follow the static condensation procedure commonly used in the modeling of plates constrained on all edges.

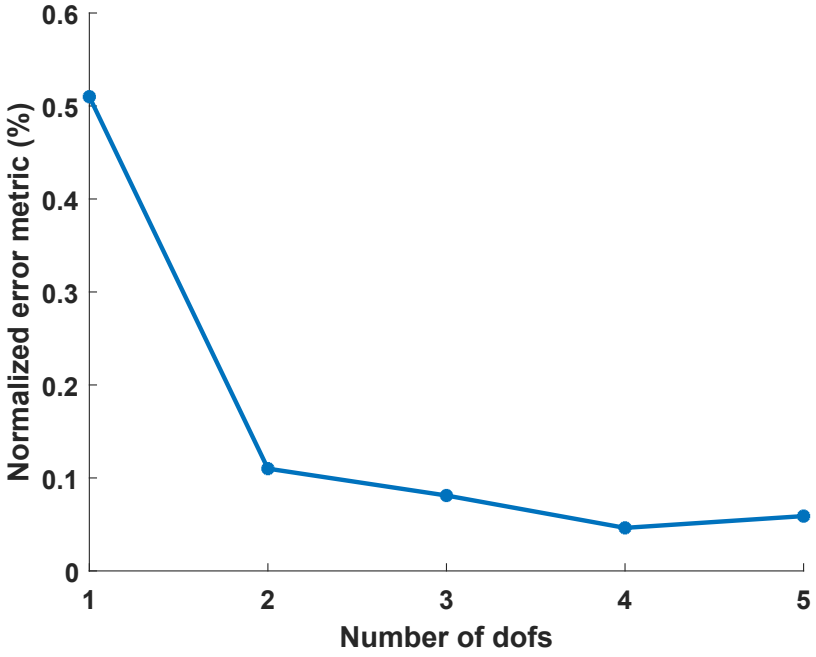

Figure 5.8: Error with the evolution of degrees of freedom considered for the ROM.

5.2 16-m Wing with Beam Model

The previous example showed that dual modes can enhance the displacement description for conditions of large deflections. This example explores a 16-m beam structure, representative of a slender cantilever wing. In this case, the reference solutions originate from the commercial code MSC Nastran. The ROM is integrated to the CFL3D code for aeroelastic analyses involving large displacements.

5.2.1 Model Description

The model is a straight 16-m beam, representing a high-aspect-ratio wing. This beam model is the same used by Ritter *et al.* [50,51]. It is a clamped-free model with 32 elements and concentrated masses along the span, as shown in Figure 5.10. This same structural model is used for the aeroelastic comparisons with a NACA 0012 constant profile of 1-m chord around the beam reference line.

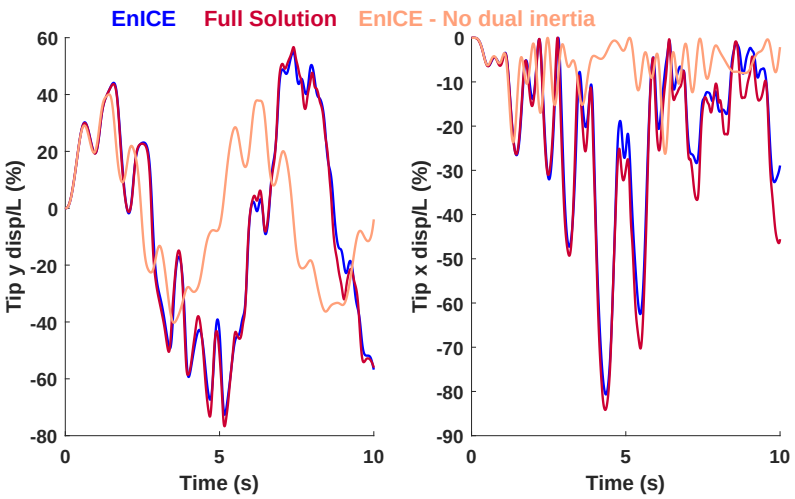

Figure 5.9: Tip responses with and without inertia forces of dual modes.

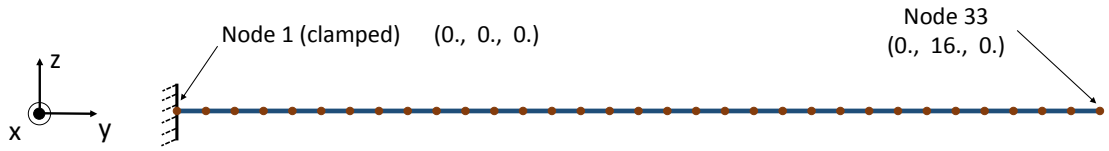

Figure 5.10: 16-m straight beam used for verification of the structural model.

5.2.2 Fitting of Nonlinear Displacements and Forces

For the structural reduced-order model, a total of 12 degrees of freedom was selected to represent the wing. The basic components of the model are the nonlinear elastic forces and the nonlinear displacements, represented by dual modes added to the modal representation. For this model, neural networks were used for both the nonlinear elastic forces and displacements. The identification used a total of 12,480 sample solutions with loads in the shape of the first 12 linear modes. Training amplitudes were established with reference tip loads, following the heuristics described in the Subsection 2.2.1, and the amplitudes are listed on Table 5.2.

Table 5.2: Linear modes amplitudes for training the 16-m beam EnICE model.

Modes	1	2	3	4	5	6
Amplitudes	70.00	4.50	3.00	0.30	0.30	0.18
cont'd						
Modes	7	8	9	10	11	12
Amplitudes	0.07	0.15	0.02	0.08	0.10	0.03

5.2.3 Structural Results

5.2.3.1 Step Response

The first check is the response of the beam model when a step force is applied at $t = 0$. The idea is to excite tip displacements on the order of 30% of the beam length. Two load cases are considered:

1. Tip vertical force of 2 kN (z direction)

2. Tip vertical force of 2 kN plus an in-plane force of 1 kN (x direction)

A stiffness-proportional damping of 2% is used. In both cases, the force is fixed to allow a clear comparison with the linear solution of MSC Nastran. However, the EnICE approach is suitable to both fixed and follower loads.

For the first load case, Figure 5.11 shows the comparison between the tip displacements obtained from the nonlinear Nastran solution, the linear Nastran solution, and the EnICE method. Going up to 30% of vertical tip displacement, it is possible to notice the geometric nonlinearity, and the linear solution is clearly different both in amplitude and phase.

Since the beam originally has no coupling between vertical and in-plane displacements/forces, no in-plane (x direction) displacement was expected after the vertical force is applied. The reason for the in-plane motion of the beam in the EnICE simulation is the residual error from the fitting of nonlinear displacements. However, this

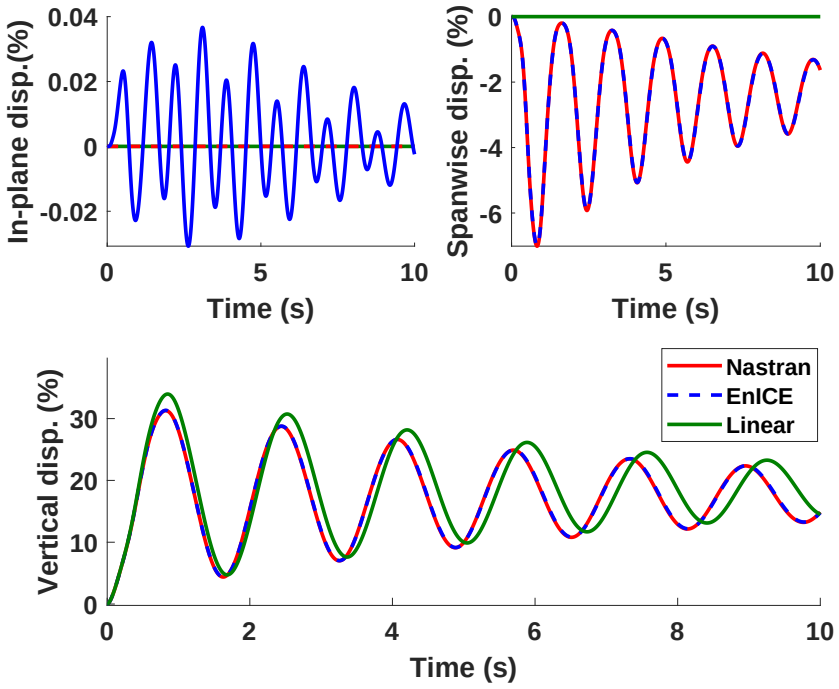

Figure 5.11: Tip displacement of the 16-m beam relative to the length of the beam for Load Case 1 (2kN z direction).

error is small compared to the beam length, and the resulting displacement is less than 0.04% of the beam length.

In the spanwise and vertical directions, the EnICE simulation matches the Nastran nonlinear simulation, while the linear motion shows the expected behavior of vertical displacement only, not preserving the beam length.

For the second load case, a tip force of 1 kN in the $x-$direction is applied together with the vertical force. This load excites displacement in the in-plane direction, besides the expected displacements in the vertical and spanwise directions. The results for the tip displacement are presented in Figure 5.12.

The in-plane displacement for Load Case 2 shows almost no difference between the nonlinear and the linear simulations. For this structure in particular, the torsional stiffness is high, limiting the nonlinear coupling between in-plane and torsion displacements. Even if the behavior in the in-plane direction is approximately linear,

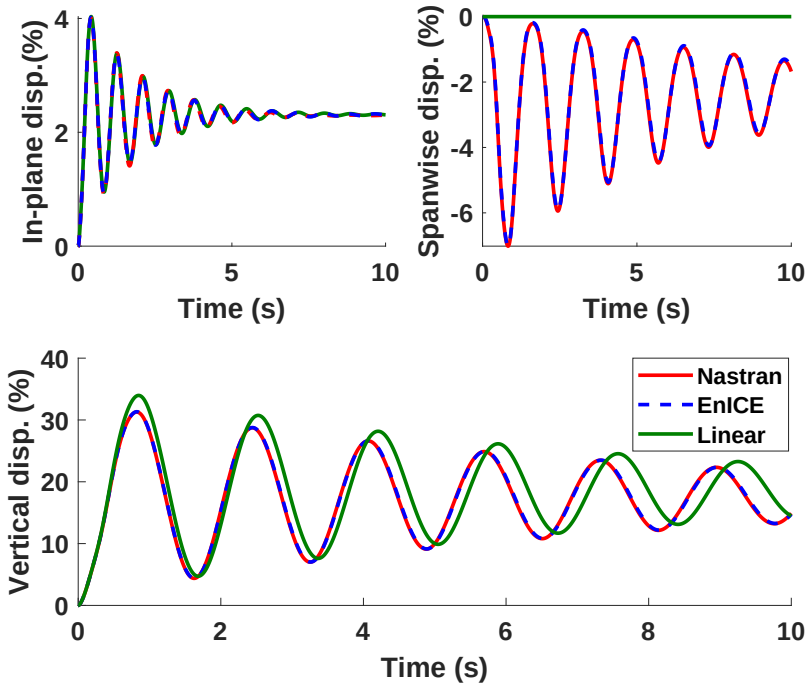

Figure 5.12: Tip displacement of the 16-m beam for Load Case 2 (2kN z direction, 1kN x direction) relative to the length of the beam.

the EnICE is predicting correctly the displacement in all directions and captures the beam shortening along the spanwise direction, something that the linear analysis is incapable of doing.

5.2.3.2 Harmonic Excitation

When exciting the displacement with a harmonic force, it is noticed an accumulation of phase error between the responses predicted with the linear and nonlinear simulations. Starting at time $t = 0$, a force is applied in both the vertical and in-plane directions, in phase and with amplitudes 3 kN and 1 kN, respectively, following a sinusoidal function with frequency 1 Hz. A good match between the EnICE and Nastran nonlinear solutions is observed for all three components as shown in Figure 5.13.

While this example does not completely capture the advantages of the EnICE

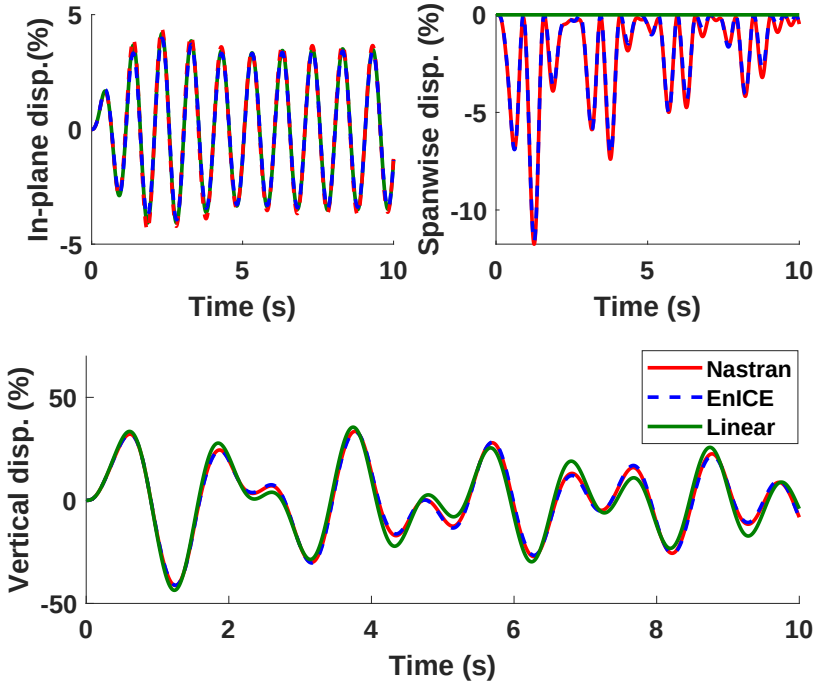

Figure 5.13: Tip displacement of the 16-m beam relative to the length of the beam for harmonic excitation.

reduced-order models in comparison to the direct nonlinear Nastran models, it does highlight the main features of the methodology. In fact, the original model has only 192 degrees of freedom. Even with a ROM reduced to 12 degrees of freedom, the benefit is not significant as in the case of a complex built-up structure, when the degrees of freedom are reduced from tens of thousands to less than 20. In this beam case, a 10-s run using time steps of 0.001 seconds takes around 9 minutes for the nonlinear Nastran SOL 400 and about 30 seconds using the EnICE method, both running in a Xeon E3 processor at 3.5 GHz.

5.2.3.3 Non-periodic Excitation

If the inertia loads related to dual modes are not included in the equations of motion, time-domain simulations can lead to significantly different results. In fact, response frequencies change due to these inertia loads. The effects are particularly

noticeable when the excitation is non-periodic, because in this case no steady-state response with same frequency of excitation is achieved.

For this example, a tip vertical load is applied from $t = 0$ with amplitude F_z given by

$$F_z = 3.5 \sin\left[\sin\left(6.6\pi t\right) + \sin\left(2\pi t\right)\right] \text{ N} \tag{5.2}$$

In this case, the tip displacement is plotted in Fig. 5.14. Also shown are the responses for a simulation where the inertia loads related to the dual modes are not included in the equations of motion. Notice that the Nastran SOL 400 and the EnICE responses are on top of each other for the spanwise and vertical displacements, while the response that ignores the effects of inertia related to dual modes accumulates a significant error. The inertia forces related to the dual modes also introduce a noise for the in-plane displacements, but that is relatively small if compared to the tip displacement magnitudes. This noise can be related to fitting errors. In all responses, a damping proportional to stiffness of 2% is used.

5.2.4 Aerodynamic Model Description

The next section compares aeroelastic results with the ones from Ritter *et al.* [50], which uses a Vortex Lattice approach for its aerodynamics. In order to have a good comparison, an inviscid solution is obtained first from the CFL3D/EnICE integrated code.

For the inviscid calculation, a coarse mesh was generated (shown at the top of Figure 5.15). With this mesh, however, it is possible to capture all the necessary details of the flow, and the lift coefficient in the undeformed configuration matches the one obtained with VLM. The mesh has only 243,200 hexahedron cells for relatively fast computations. For RANS solutions, it was necessary to create a finer mesh, with

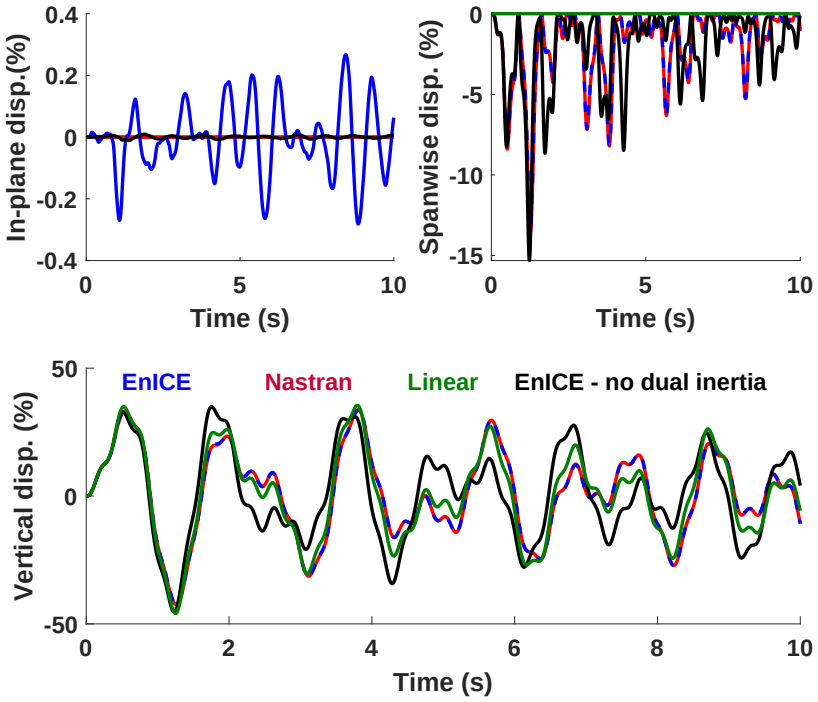

Figure 5.14: Tip displacement of the 16-m beam relative to the length of the beam for non-periodic excitation. Legend is color-based.

2,490,210 cells (shown at the bottom of Figure 5.15).

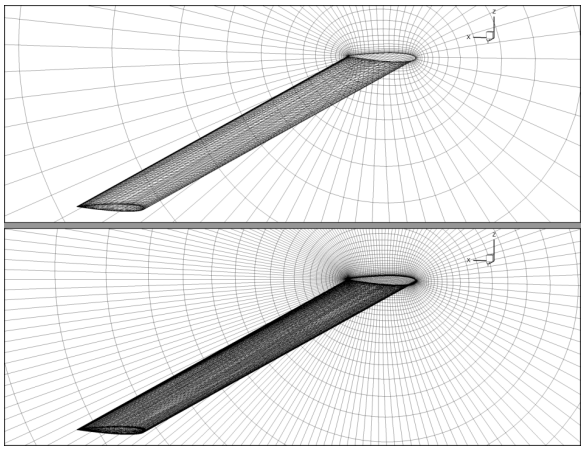

Figure 5.15: Coarse (top) and fine (bottom) meshes around the 16-m wing.

Using these meshes, it was possible to test the integration of EnICE inside the CFL3D code, including the effects of nonlinear stiffness and displacements following

dual modes. In order to perform mesh deformations, it is necessary to create a mapping between the mesh surface and each one of the modes. For a complex structure, usually a spline is the tool for such mapping. In the case of the beam, it is assumed that the NACA 0012 profile keeps a constant shape orthogonal to the reference axis located at 35% of its chord. From the translations and rotations along the beam, displacements are calculated at surface mesh points for a given mode. Since the number of spanwise sections of the aerodynamic mesh is greater than the number of structural nodes, a cubic spline allows the interpolation of modal translations and rotations along the span.

A fundamental issue regarding the aeroelastic calculations using CFD is the mesh deformation, especially for wings undergoing large amplitude motion. For this example, mesh deformation was carried out using macro-elements. For a case with relatively large deformation, it was observed that the mesh keeps its quality. Figure 5.16 shows the detail of the deformed mesh when the wing has a tip displacement around 20% of its semi-span. The deformation keeps the orthogonality of the fluid cells around the tip (in yellow), and the solution is not affected by mesh distortion.

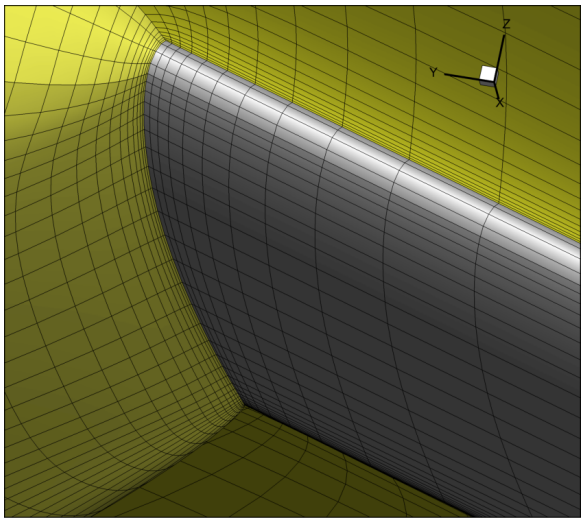

Figure 5.16: Mesh at the tip of the 16-m wing undergoing 20% tip deflection: fluid cells in yellow.

5.2.5 Static Aeroelastic Studies with the CFL3D/EnICE Framework

To obtain static aeroelastic results in CFL3D, it is necessary to run an unsteady solution with high structural damping. This procedure was followed and it was possible to obtain the converged steady-state solutions after approximately 3 seconds of physical time for the 16-m beam. An example of the deformed mesh is presented in Figure 5.17, with a vertical deflection of 3 m, corresponding to approximately 19% of the wing semi-span.

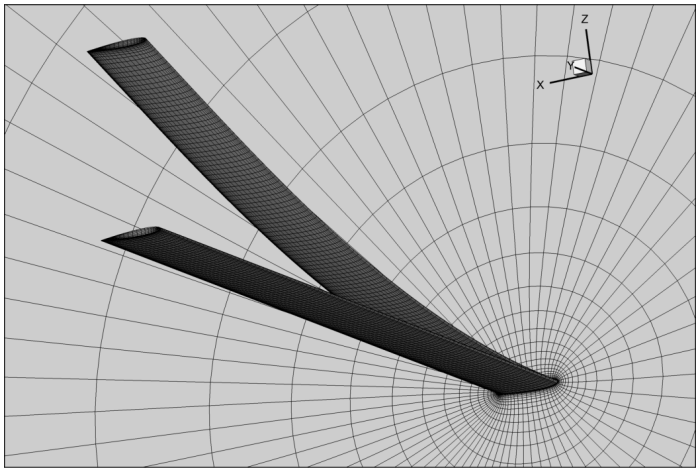

Figure 5.17: Deformed mesh from aeroelastic static solution at AoA = 5 deg and compared to the undeformed one.

Using the angle of attack of 5 degrees, an incoming flow of 40 m/s and an atmospheric density of 1.225 kg/m^3, the displacement was obtained with the CFL3D solution using the traditional linear modal aeroelastic solution and the newly implemented EnICE structural method. Figure 5.18 compares the wing reference line shapes for the static aeroelastic solutions using both approaches. The shapes are close to each other, however the beam length is only preserved for the nonlinear model. This is consistent with the steady structural solutions presented in Ritter *et al.* [51] for the same model. Static simulations usually lead to linear and nonlinear results

in close proximity, with the nonlinear displacement visibly truncated to preserve the beam length. In Figure 5.18, the nonlinear deformed structure is slightly more deflected at the tip compared to the linear one due to follower forces incorporated in the EnICE analysis, while the linear solution only considers the generalized forces acting on the linear modes.

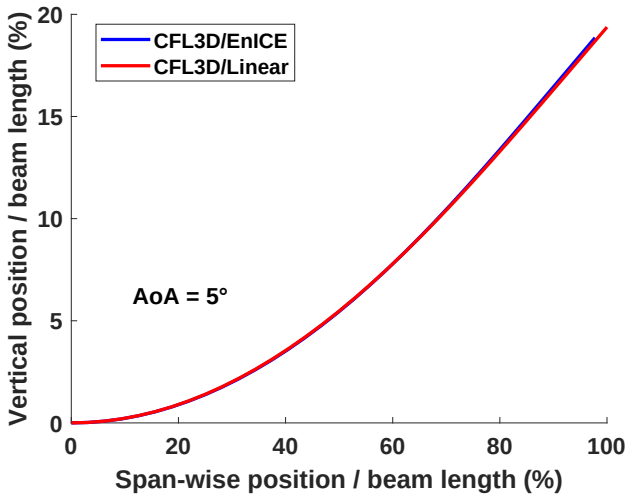

Figure 5.18: Comparison between the 16-m wing static aeroelastic solutions using linear and nonlinear structural models (40 m/s, 5-deg AoA, sea level).

Another comparison is made against the results of Ritter *et al.* [51] for the same wing case but now for angles of attack varying from 0 to 5 degrees. Figure 5.19 compares the solutions obtained with CFL3D using Euler solution and with the solvers from Ritter *et al.* [51] that uses VLM integrated with the Enhanced Modal Approach (EnMA), another reduced-order method for nonlinear structural modal representation. The solutions are similar, but there are differences in the magnitude of the vertical displacement that increase with angle of attack. Unfortunately the aerodynamic solutions are obtained with different methods and that by itself may contribute to the differences. While VLM treats the airfoil as a flat plate, the Euler solution considers the discretized surface. Also, the wake in the vortex lattice approach is not rolled-up as it is convected, while the CFD solution will automatically include this

effect. However, it is possible to say that the CFD inviscid solution is more sensitive to geometrical discontinuities and may have a higher error due to a blunt trailing edge. At 5-degree angle of attack, the differences between the CFL3D/EnICE and the VLM/EnMA solutions are particularly large. Since the response of CFL3D/EnICE at 5 degrees was below the one obtained with VLM/EnMA and considerably smaller than the previous increments, it raises a concern about the CFD inviscid solution for that particular setting.

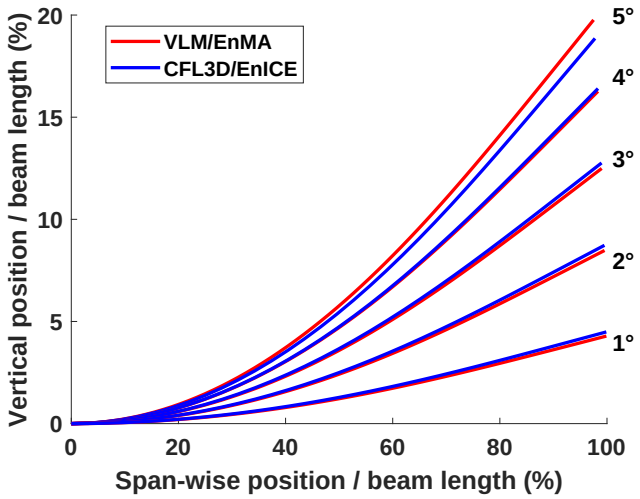

Figure 5.19: Comparison of 16-m wing static aeroelastic solutions obtained with different nonlinear methods varying AoA from 1 to 5 degrees, 40 m/s, sea level.

In order to have a more accurate CFD solution, a finer mesh was used, this time with a viscous solution (RANS, Spalart-Allmaras turbulence modeling [108]), at the angle of attack of 5 degrees. At this condition, a comparison with the Vortex Lattice solution is not possible because the effects of boundary layer are not included in that method. A better comparison is performed using the aeroelastic solver UM/NAST [18] developed at the University of Michigan. The structural solution in UM/NAST is strain-based and nonlinear, while the aerodynamic solution is based on strip theory, but accepts corrections to take into account the lift distribution along the span. The beam solution obtained with UM/NAST was also used in Ritter *et al.* [50] for

benchmarks, but in that case no viscous effects were included. For this comparison with a RANS solution, the table of aerodynamic coefficients obtained with the XFOIL solver considers viscous effects at a Reynolds number of 2.7 million.

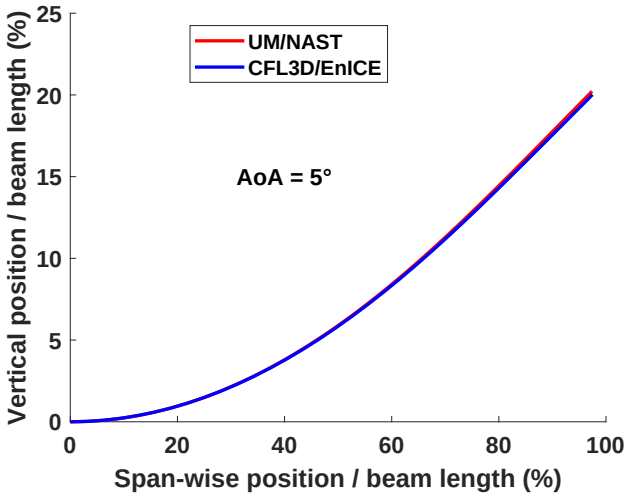

Figure 5.20: Wing deflections for the 16-m wing static aeroelastic solutions accounting for flow viscosity (40 m/s, 5-deg AoA, $Re = 2.7 \cdot 10^6$, sea level).

Figure 5.20 shows only a small difference between the UM/NAST solution and the static aeroelastic deflection obtained with CFL3D/EnICE. At the tip, the difference in the vertical displacement obtained with the two methods is 0.2% of the beam length. For this simulation, UM/NAST used the aerodynamic coefficients from the viscous 2D simulation in XFOIL [124] and the lift distribution correction along the semi-span due to tip effects was obtained from the CFL3D solution. This comparison finalizes the static aeroelastic investigations, and serves as starting point for a brief study on the dynamic evolution of the system, given external loads from the equilibrium point.

5.2.6 Dynamic Aeroelastic Studies with the CFL3D/EnICE Framework

From the aeroelastic static equilibrium position, external dynamic loads can be applied and the system evolution can be observed.

If a sinusoidal tip moment is applied in the y direction of the global frame, with amplitude of 10 kN.m and frequency of 27.1 Hz, which is the frequency of the first torsion mode, it is possible to compare the tip rotation angle for both the CFL3D/EnICE and the UM/NAST solvers. The result is presented in Figure 5.21, where amplitude and phase differences are observed. At the resonance frequency, the amplitude is limited by damping, both structural and aerodynamic. In a purely linear structural solution, the 2% proportional damping results in an amplitude of 4.5 degrees. With the aerodynamic damping, it is expected that the amplitude will be lower. From Figure 5.21, the UM/NAST solution achieves an amplitude of 4.4 degrees, while the CFL3D/EnICE solution shows a lower amplitude of 3.5 degrees.

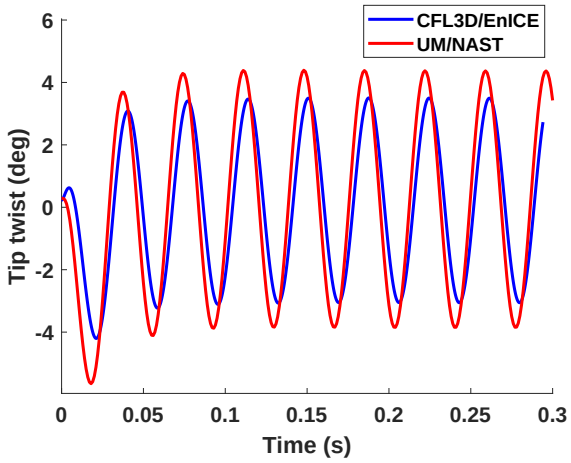

Figure 5.21: 16-m wing tip rotation angle under the effect of a prescribed tip torsion moment of amplitude 10 kN.m and frequency of 27.1 Hz (wing first torsion natural mode) at 40 m/s, 5-deg AoA, $Re = 2.7 \cdot 10^6$, sea level.

The difference observed in Figure 5.21 is not due to geometric nonlinearity, but it is related to the accuracy of the aerodynamic computation. The aerodynamic solution in UM/NAST considers viscous effects from XFOIL corrected coefficients. However, the spanwise lift distribution is adjusted to include the tip effects by only multiplying the strip theory results by the normalized distribution obtained at a reference condition. This approach does not cover torsion, even for small deflections,

since an induced angle of attack should be applied instead of a multiplicative factor along the span.

Comparing torsion results between the original CFL3D implementation with linear modal structural solution and the current implementation with EnICE for the structural analysis (Fig. 5.22), a slight difference is noticed for the tip angle. The applied load is a 7-kN.m sinusoidal moment at the tip and about the y direction (spanwise) with frequency of 27.1 Hz, as in the previous case. The difference relative to the previous case is that the excitation amplitude and damping are reduced, since the original implementation of CFL3D cannot handle damping levels higher than the critical value. For the torsion mode, Rayleigh damping of 2% was higher than the critical viscous damping in the linear case. Therefore, the Rayleigh damping was reduced to 1.2% in order to have a linear comparison from the original CFL3D implementation. Figure 5.22 shows small differences in the initial response, but apart from that there is only a small lag of the linear solution relative to the nonlinear one.

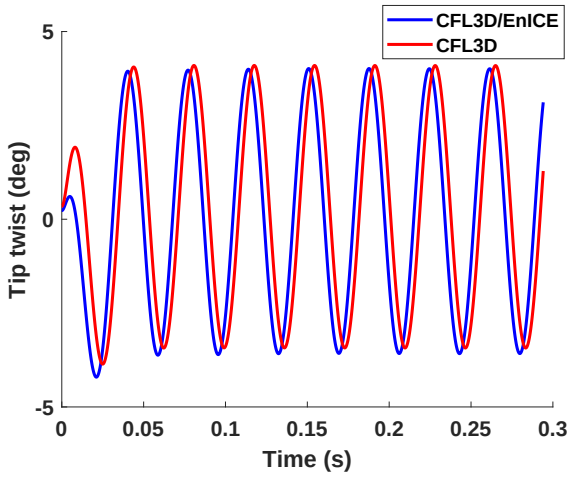

Figure 5.22: Wing tip rotation angle for the 16-m wing case with linear and nonlinear structural solutions coupled with CFL3D and under a prescribed tip torsion moment of amplitude 7 kN.m and frequency 27.1 Hz (first torsion mode) at 40 m/s, 5-deg AoA, $Re = 2.7 \cdot 10^6$, sea level.

Another test of dynamic response comparing the adapted CFL3D/EnICE code and the original CFL3D implementation uses a tip load of 2 kN in the vertical direction

and a force of 1 kN in the horizontal direction, parallel to the flow. These forces were applied suddenly at time $t = 0$, after the steady RANS solution for the angle of attack of 0 degree at 40 m/s was calculated. The response to this step excitation from different solvers are compared in Figure 5.23. This same loading was considered before (Figure 5.12), but without the incoming flow. Notice the amount of damping related to aerodynamic forces. In fact, the response obtained previously with the EnICE method showed sub-critical behavior, while the tip vertical response in Fig. 5.23 shows no oscillation on the way up to the steady condition. As expected, the linear solution shows no shortening of the horizontal projection of the wing. The vertical displacement presents small differences due to both the structural nonlinearity and the aerodynamic forces which are significant after deformation takes place.

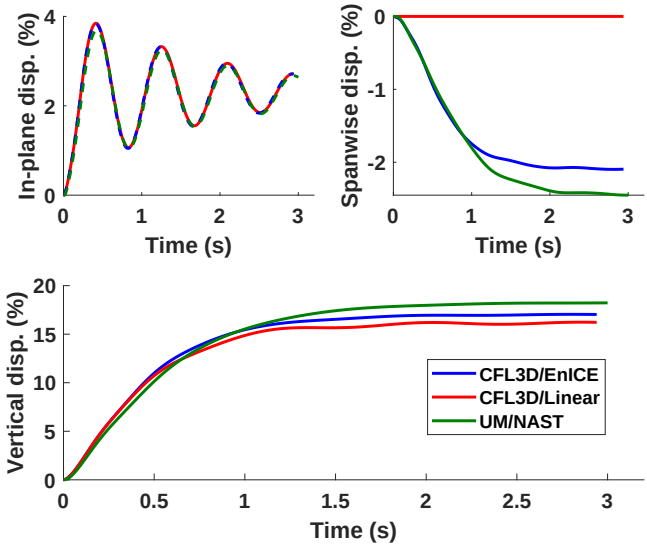

Figure 5.23: Tip displacements of the 16-m wing subject to a prescribed step tip force of 2 kN in the vertical and 1 kN in the horizontal directions at 40 m/s, 5-deg AoA, $Re = 2.7 \cdot 10^6$, sea level.

Bringing the results of UM/NAST with corrected strip theory into this comparison, it is possible to see differences relative to the solution with CFL3D/EnICE. UM/NAST accurately predicts the aerodynamic damping for low frequency motion, and the transient response shows a good match. A nonlinear effect shared by both

UM/NAST and CFL3D/EnICE nonlinear structural solutions is the torsion excited by the in-plane force when in a deflected configuration. This effect can be observed from the tip twist angle plotted in Figure 5.24. In this case, the linear modal solution of CFL3D is not able to capture the increase in the twist angle. Since the 16-m wing is relatively stiff in torsion, this effect is small, but depending on the model this coupling can significantly affect the aerodynamic forces.

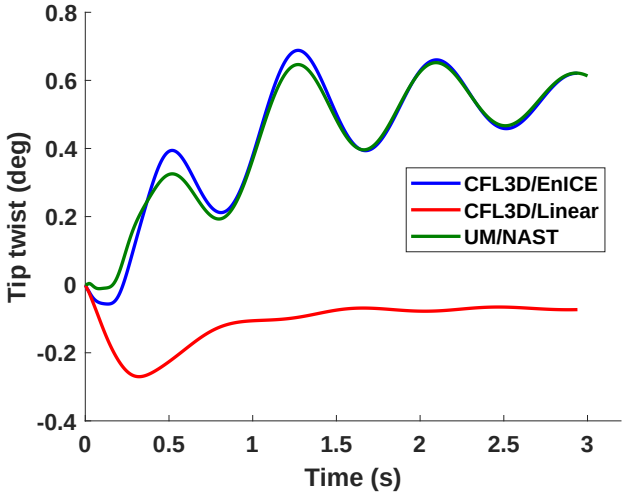

Figure 5.24: Tip rotation angle of the 16-m wing under a step tip force of 2 kN in the vertical and 1 kN in the horizontal direction at 40 m/s, 5-deg AoA, $Re = 2.7 \cdot 10^6$, sea level.

5.2.7 Aeroelastic Results with the MoS/EnICE Framework

This subsection outlines the main results obtained with the MoS/EnICE framework where the method of segments provides the aerodynamic loads for the structural solution obtained using the ROM. For the MoS, reference steady solutions were obtained with angles of attack up to 15 degrees, past the stall angle, and the step responses were obtained for small perturbations in the shape of the first 12 linear modes, the same ones considered for the structural ROM.

At the stage when these results were produced, no correction for induced angles

of attack had been implemented to improve the MoS predictions when high twist affects the load distribution significantly. Later, for the final example considering a built-up wing, the MoS employs the correction based on lifting-line which is described in Section 3.3. Another procedure different for this example is the calculation of local angles of attack. Instead of using the average finite rotation of the mesh points of each segment, as described in Chapter 3, local coordinate systems are employed using the rotational degrees of freedom of the beam nodes.

At this point, it is assumed that the structural model was properly verified against Nastran nonlinear solutions. Therefore, all comparisons have the objective of verifying the aerodynamic solution considering the CFL3D/EnICE as the reference one.

5.2.7.1 Static Aeroelastic Comparisons

The first aeroelastic comparison set is for static cases. The wing is subjected to a freestream flow with speed 40 m/s and two different root angles of attack, one to excite a small deflection and the other a high deflection with nonlinear effects.

Figure 5.25 compares the final deformation obtained using the MoS/EnICE framework and the reference solution calculated with CFL3D/EnICE. Looking at the vertical and span-wise displacements, there is a good agreement between the predictions. In absolute numbers, the errors are higher for the large deflection condition. This decreasing accuracy was expected because the reference deformation used for the calculation of the aerodynamic loads at each segment was the straight undeformed wing. This reference condition may be adjusted according to the range of application of the analysis.

Table 5.3 compares the tip translations and rotations for the two angles of attack simulated. The translations are expressed as % of semi-span, while rotations are in degrees.

The tip vertical displacement shows good comparison between the MoS/EnICE

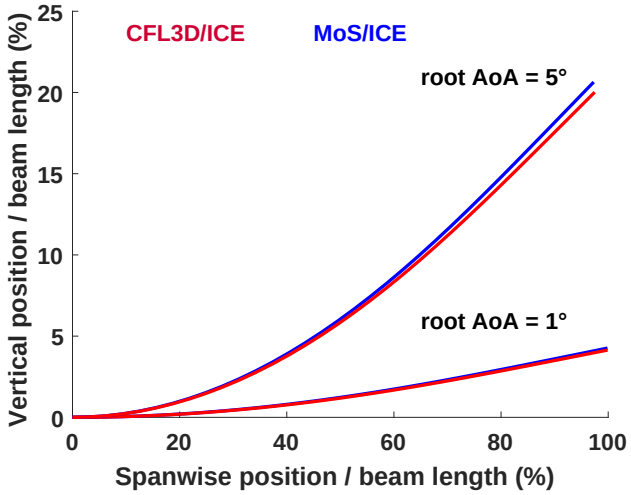

Figure 5.25: Aeroelastic static results for the 16-m wing at 40 m/s and two different root angles of attack.

Table 5.3: Comparison of tip displacements and rotations for the 16-m wing aeroelastic static solution at 40 m/s and different root angles of attack.

Root AoA (deg)	1		5	
Method	CFD	MoS	CFD	MoS
In-plane disp. (%)	0.0	1.5	-0.4	0.8
Spanwise disp. (%)	-0.1	-0.1	-2.5	-2.7
Vertical disp. (%)	4.1	4.3	20.0	20.6
Rotation x (deg)	3.7	3.8	18.3	18.9
Torsion angle (deg)	0.0	0.2	0.2	0.7
Rotation z (deg)	0.0	-1.7	0.4	-1.1

and the CFL3D/EnICE results with highest error lower than 0.6% of the wing semi-span. However, the in-plane displacements (in the x direction) and the in-plane rotation (around the z axis) have errors of 1.5% relative to the semi-span and 1.7 deg, respectively. Calculation of drag forces is key for comparison of these in-plane displacements and rotations. Additional investigations are needed to evaluate the drag calculated with the MoS for each segment.

5.2.7.2 Dynamic Aeroelastic Comparisons

The dynamic aeroelastic test for the MoS/EnICE framework is to compare the unsteady large-displacement motion of the wing against a solution obtained with the CFL3D/EnICE code. For this, a harmonic tip moment is applied about the y direction (torsion moment), inducing an angle of attack capable of generating lift for a large deflection simulation. The solution starts from the steady condition at 0-deg root AoA and the wingtip performs an oscillatory motion. This condition represents a typical low-frequency excitation for such high-aspect-ratio wings. The moment applied at the tip has amplitude of 6 kNm and the profile is a "$1 - \cos$" function with frequency of 0.5 Hz. The freestream velocity is 40 m/s, as in the steady cases, and the structure has a proportional damping of 2%. The tip displacements are presented in Fig. 5.26. In this case, the vertical component achieves a maximum value around 24% of the semi-span at the first peak. The simulation time of the reference CFL3D/EnICE solution is 1.9 s. Although short, the agreement between the high-fidelity aerodynamic solution and the ones from the MoS was reasonable for this initial motion considering all three displacement components. If only small disturbances relative to a given configuration are desired, it is possible to adopt a deformed reference condition. That will increase the quality of the predictions for large displacements.

Comparing the tip twist angle in Fig. 5.27, there is good agreement between the MoS/EnICE prediction and the solution obtained with the CFL3D/EnICE framework. The twist angle goes up to approximately 14 degrees, indicating that nonlinear phenomena are already playing a role in the aeroelastic solution. In fact, the tip twist angle obtained from the MoS with pure convolution without any correction factor is at a lower level and has higher frequency when compared to its nonlinear counterparts. This result also shows that using a linear solution for aeroelastic analysis involving large displacements may not be a conservative approach in terms of loads

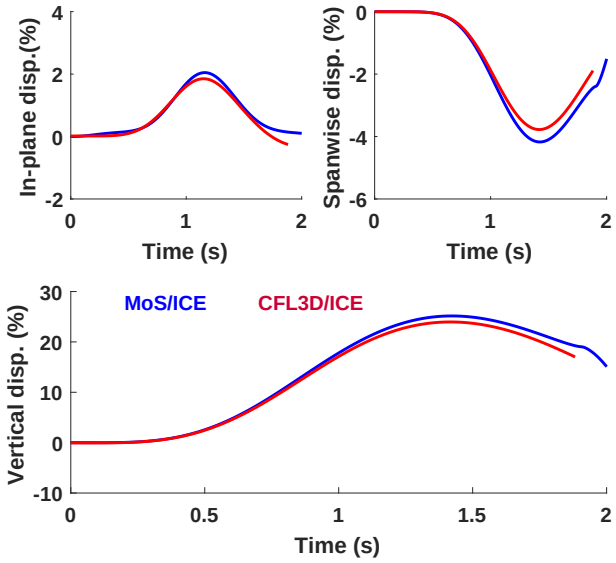

Figure 5.26: Tip displacement of the 16-m wing following the application of a harmonic torsion moment of 6 kNm and 0.5 Hz.

and angle-of-attack predictions.

The main benefit from the MoS is the decreased computational cost compared to the CFD solution. Running the high-fidelity solution with an adequate time step for only 1.9 s using 45 cores takes 27 hours, while the same solution using the MoS/EnICE framework in Matlab takes 7 minutes. For a reduced order model, 7 min. is a relatively long time, but there is potential to decrease this time significantly by selecting suitable samples for the time step responses used in the convolution. In fact, the convolution is the most time-consuming task in the MoS calculation.

5.3 Bristol Ultra-Green Wing

This analysis is part of an effort to assess the predictive capabilities of different ROM methodologies [2]. No aerodynamic model was developed for the BUG wing, but structural comparisons with this wingbox allowed a first glimpse on the difficulties of reducing a complex FEM with the EnICE.

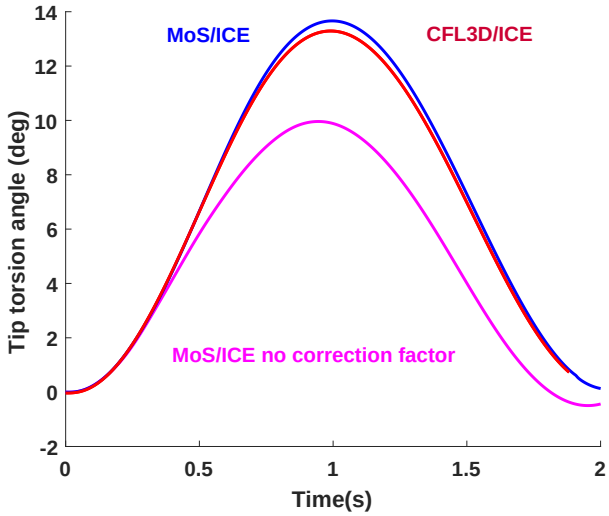

Figure 5.27: Tip twist angle for the 16-m wing following the application of an harmonic torsion moment of 6 kNm and 0.5 Hz.

As discussed in the introduction, a common method for structural reduction of large-aspect-ratio wings is condensation to an equivalent beam. These ROMs are based on property identification (material constitutive law) of the linear responses of the undeformed model. Using a nonlinear beam model with the properties calculated from the undeformed case, good predictions are generally obtained for large deflections. However, if pre-stress effects are present, the stiffness changes are not typically captured by beam models.

5.3.1 Model Decription

5.3.1.1 Wing Box Model

The structure used for all comparisons is a wing box built out of graphite/epoxy composites modeled in MSC NASTRAN with 48,750 degrees of freedom, using CQUAD4 and CTRIA3 (shells) and CBEAM (beam) elements, besides concentrated masses and rigid connectors. Due to large displacements conditions, nonlinear properties were introduced for the shell elements using the PSHLN1 card.

The wing box corresponds to a high-winged design, the University of Bristol Ultra-Green (BUG) wing, which is derived from the truss-braced high aspect-ratio wing of the SUGAR Volt aircraft [125]. This wing has negative dihedral and the fiber orientation is designed to allow bending-torsion coupling. The semi-span of the wing box is 25.9 m. A general view of the model is presented in Fig. 5.28.

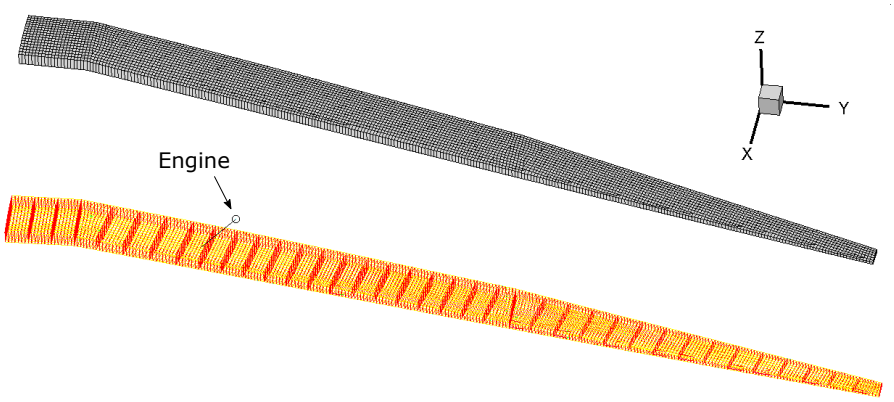

Figure 5.28: BUG wing mesh (top) and geometry for wing ribs and engine (bottom).

The boundary conditions are compatible with a high-wing design. The root nodes of the wing are constrained with symmetry conditions: no span-wise translations (y-direction) and no rotations along the x and z directions. Besides that, the nodes on the section connected to the fuselage are constrained in translation along the x and z directions.

The quality of the reduced-order models for small displacements depends on how well the first linear modes are reproduced. With this set of constraints, the first free-vibration mode has a frequency of 1.30 Hz. The first three modes are shown in Fig. 5.29, but engine displacement is not displayed along with the wing box. The first mode is a bending one with a relatively low frequency, characteristic of high aspect-ratio wings. The second mode is an in-plane mode, while the third one shows some torsion towards the wingtip.

The mass of the wing is mostly lumped. Points connected to neighboring nodes on

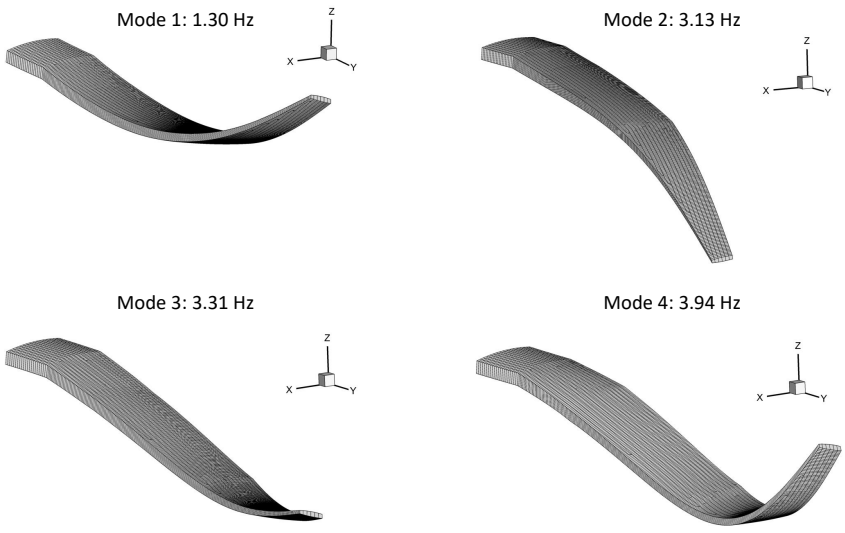

Figure 5.29: First three free-vibration modes of the BUG wing box.

the structure via RBE3 rigid connections are used to transfer inertia forces. Through this kind of connection, the point that receives the load moves as a weighted average of the neighboring nodes. Unlike the RBE2, the RBE3s do not make the section stiffer. These same points with lumped masses are also used to apply external loads and obtain a reference solution for the dynamic load case investigated later.

5.3.1.2 Beam Model

As discussed in the introduction, multiple approaches may be followed to compute a representative beam for a built-up wing. Depending on the kind of beam solution sought, different parameters may be calculated. For the results used for comparison[1], an automated method that calculates an equivalent Timoshenko beam from the 6×6 flexibility matrix was used [11]. The extraction of the flexibility matrix follows the procedure outlined by Malcolm and Laird [126]. A reference line is proposed and reference points are selected, defining the beam elements. Forces and moments

[1]Beam model results for this comparison were generated by Olivia Stodieck, University of Bristol [2].

are then applied at the nodes along the reference line and the results in terms of displacements and rotations are used to construct the flexibility matrix C.

Once the flexibility matrix is determined, the following Timoshenko beam properties are calculated analytically from its entries:

- section offsets of the shear center with respect to the element end nodes;
- torsion and bending stiffness constants $\bar{J}$, k_1, k_2 and k_{12};
- section centroid offsets from the elastic axis;
- section area
- Timoshenko shear corrections

For details about the properties calculations, refer to Stodieck *et al.* [11]. Using the properties of a Timoshenko beam, the parameters of the beam elements are defined for the FE analysis. For this work, the NASTRAN SOL 400 [127] sequence was selected, but any other nonlinear FE code could have been used.

In order to evaluate the beam model that reproduces the wing box, it is necessary to first compare frequencies and mode shapes of the linear free-vibration problem. A reference line was chosen to represent the wing box, comprised of 30 distributed nodes. The reference line and points are shown in Fig. 5.30. It was chosen to pass approximately through the geometric center of the wing box. The method used to reduced the box to a beam allows for disparities between the elastic axis and the reference line. This approach allows for a better representation of the element stiffness properties. The elastic axes of the individual elements are represented in red in Fig. 5.30. The mass related to the elements close to each reference point are concentrated at their center of gravity, which may have an offset with respect to the corresponding reference point. This offset is especially significant at the node closest to the engine mass, as shown in Fig. 5.31.

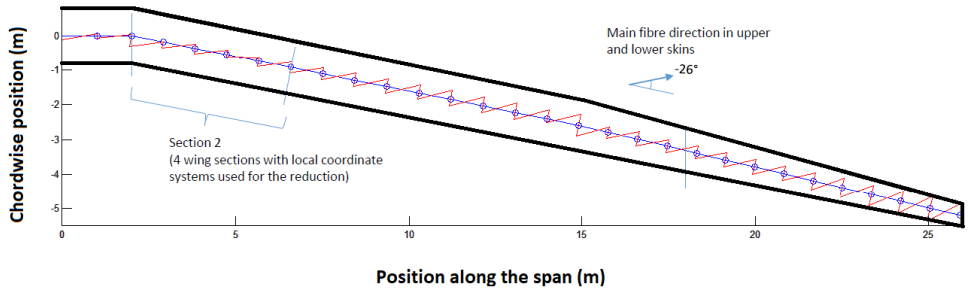

Figure 5.30: Reference line and points selected to represent the wing box structure [2].

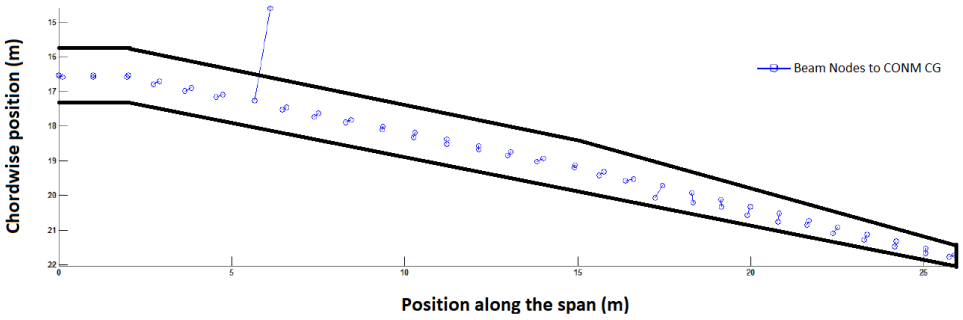

Figure 5.31: Point masses and its offsets relative to the reference points [2].

From the beam reduction process, an equivalent beam model was generated with match in frequencies with the complete wing box model within 1% up to the seventh mode. Table 5.4 compares the frequencies of the two models. In general, the matching is better for the lowest modes. For the higher modes, some discrepancy happens due to local effects.

In terms of mode shapes, the Modal Assurance Criterion (MAC) was used to compare displacements for the points of the equivalent beam and the corresponding points connected to the wing box neighboring nodes via RBE3 connections. Table 5.5 compares the beam modes and the wing box modes. The MAC is an approximate comparison between two mode shapes. It disregards the mass in the process, but it will be 1.0 if two mode shapes are identical. For this table, the degrees of freedom considered are the three translations and the rotation along the y-direction. The formula of the MAC is

Table 5.4: Comparison of modal frequencies for the wing box and the equivalent beam model [2].

Mode	Eq. beam freq. (Hz)	Wing box freq. (Hz)	Error (%)
1	1.29	1.30	-0.4
2	3.14	3.13	0.4
3	3.31	3.31	0.1
4	3.95	3.94	0.4
5	7.20	7.16	0.6
6	9.70	9.63	0.7
7	12.0	12.1	-0.4
8	14.9	13.5	10
9	17.5	15.3	15
10	18.5	17.4	6.2
11	22.6	21.6	4.9
12	27.3	26.5	2.7
13	28.0	27.4	2.4

$$MAC = \frac{\left(\Phi_1^T \Phi_2\right)^2}{\left(\Phi_1^T \Phi_1\right)\left(\Phi_2^T \Phi_2\right)} \tag{5.3}$$

where Φ_1 and Φ_2 are two modal shapes being compared. For the example shown in Table 5.5, all the MAC values in the diagonal are 1 until mode 7, while there are discrepancies for mode 8 onward, just like in the frequency comparison. Even though the diagonal terms in the MAC matrix are not all ones, it can be said that the agreement in low-frequency response is very good. Obtaining a beam with that level of agreement is only possible by tuning different parameters in the NASTRAN modeling, including the position of the shear center.

It is interesting to note that mode 8 on the GFEM corresponds to a local box cross section deformation mode. That occurs at the location where the engine inertia forces are being transferred into the wing through four discrete nodes on the wing section. Clearly, this local mode cannot be captured by the beam model. The mode mismatch also appears in the results of Table 5.5, where the MAC between the beam mode 8 and the GFEM mode 9 is equal to one, indicating that the GFEM mode 8

Table 5.5: Modal Assurance Criterion comparison of modal shapes for the equivalent beam along rows and the wing box along columns [2].

	1	2	3	4	5	6	7	8	9	10	11	12	13
1	1.0	0.5	0.1	0.5	0.1	0.0	0.0	0.0	0.0	0.0	0.0	0.0	0.0
2	0.5	1.0	0.0	0.5	0.5	0.0	0.2	0.1	0.0	0.0	0.1	0.0	0.0
3	0.1	0.0	1.0	0.5	0.0	0.6	0.0	0.1	0.0	0.1	0.1	0.0	0.0
4	0.5	0.4	0.5	1.0	0.3	0.3	0.2	0.0	0.0	0.2	0.0	0.0	0.0
5	0.1	0.5	0.0	0.3	1.0	0.0	0.5	0.3	0.1	0.1	0.1	0.1	0.0
6	0.0	0.0	0.6	0.3	0.0	1.0	0.0	0.2	0.0	0.4	0.1	0.1	0.0
7	0.1	0.2	0.0	0.2	0.5	0.0	1.0	0.1	0.0	0.3	0.4	0.0	0.0
8	0.0	0.0	0.0	0.0	0.2	0.0	0.0	0.6	1.0	0.0	0.0	0.5	0.6
9	0.0	0.0	0.2	0.2	0.1	0.5	0.2	0.0	0.1	1.0	0.0	0.2	0.0
10	0.0	0.0	0.1	0.0	0.0	0.2	0.3	0.0	0.4	0.0	0.6	0.2	0.3
11	0.0	0.1	0.0	0.0	0.2	0.0	0.4	0.2	0.1	0.2	0.8	0.3	0.0
12	0.0	0.0	0.0	0.0	0.0	0.0	0.0	0.3	0.7	0.0	0.0	0.7	0.9
13	0.1	0.0	0.0	0.1	0.0	0.1	0.1	0.0	0.0	0.5	0.1	0.2	0.2

was skipped. The GFEM in Stodieck *et al.* [11] was modified compared to the model used in this study, by connecting the discrete engine mass to a larger number of nodes on the wing cross section. Using this updated GFEM, it was verified that the beam and GFEM normal modes up to 20 Hz were indeed closely correlated (2% maximum frequency error).

5.3.1.3 EnICE Model

The EnICE model of the BUG wing is based on 18 degrees of freedom, corresponding to the amplitudes of the first 18 linear modes. The nonlinear displacements and elastic forces are fitted with artificial neural networks composed of 4 neurons in one hidden layer.

For the training of the EnICE model, a total of 11,480 nonlinear static solutions were obtained. Loads in the shape of linear modes excited large amplitudes for extraction of nonlinear displacements and nonlinear forces. The heuristics for choosing the amplitudes of the reference loads is a trial-and-error process to achieve expected displacements and twist angles, explained in the Subsection 2.2.1. The maximum of

the amplitudes of Q^* used for the 18 d.o.f.s considered is listed on Table 5.6. The nonlinear displacements were represented as combinations of 10 dual modes.

Table 5.6: Linear modes amplitudes for training the BUG EnICE model.

Modes	1	2	3	4	5	6	7	8	9
Amplitudes	120.0	20.0	15.0	20.0	8.0	5.5	5.5	3.5	3.5
cont'd									
Modes	10	11	12	13	14	15	16	17	18
Amplitudes	3.5	3.5	2.4	2.4	1.8	1.8	1.2	1.2	1.0

5.3.2 Comparison of Results

Different load cases were used to analyze the accuracy of the proposed reduced-order models. The benchmark comparisons were performed to 1) check each ROM with different load excitation and conditions, and 2) compare the accuracy of each ROM against the other ones and the full model whenever possible.

This section compares dynamic and static results obtained for different load cases. Tip displacement was used to evaluate the differences among the investigated models.

One aspect of practical utility regarding GFEM solution undergoing large displacements in MSC Nastran SOL 400 is that the presence of rigid connections may lead to convergence problems. Taking the BUG wing as an example, dynamic solutions cannot be obtained easily for tip displacements beyond 16% of the semi-span if sufficiently small time steps are adopted. If the rigid connections are removed, however, then larger displacements can be calculated.

5.3.2.1 Load cases for the Benchmark Comparisons

Load cases were selected to explore different input profiles, as well as the effects of inclusion of follower forces. Solutions were obtained for the ROMs and the full model. For higher loads, the dynamic nonlinear solution with the GFEM was not possible

to be obtained anymore despite the numerous attempts to achieve convergence with different parameters sets. In order to explore larger displacements, only static loads were used.

While Case 1 is the application of a step load input at two different points along the wing, Case 2 explores a sinusoidal load with frequency of 0.125 Hz. Case 3 is a comparison of static results considering larger deflections. Table 5.7 summarizes the definition of the three load cases considered.

Table 5.7: Load cases for benchmark comparisons

Case	**Type**	**Damping (%)**	**Amplitude**	**Direction/ Profile**	**Applic. Point**	**Follower Force**
1	Dynamic	0.5	15 kN 45 kN	z-direction step	Node 30 Node 17	Yes
2	Dynamic	0.5	15 kN 45 kN	z-direction sinusoidal	Node 30 Node 17	Yes
3	Static	-	$\leq$ 70 kN	z-direction	Node 30	No

5.3.2.2 Responses from Different Methods

This subsection details the results obtained from the load cases given in Table 5.7. Time-domain tip responses were selected to compare the behavior of the different ROMs. The out-of-plane displacement is particularly important to indicate the degree of nonlinearity. Tip displacements around 15% of the semi-span will generally be associated to a mild nonlinearity.

Cases 1 and 2 represent dynamic loads. The amplitudes were chosen with smaller values to make the comparison with GFEM results possible. For Case 1, the out-of-plane tip displacement is shown in Fig. 5.32. Since the displacements are kept below 15% for this case, the nonlinearity is not strong and the differences between the full solution and the linear one are relatively small. From Fig. 5.33, one can better see the differences, where the linear solution has the highest error among the ROMs and the beam-based approach showing relatively small errors. The EnICE results achieved a

good accuracy for this level of displacements, because the linear behavior matches the first 12 modes and the light nonlinearity is well-captured by the fitted functions. The span-wise displacements are compared in Fig. 5.34. As expected, the linear solution does not present an accurate span-wise displacement, since the shortening along this direction is a typical nonlinear effect. The wing still shows a small linear response due to its negative dihedral. The nonlinearity dominates the span-wise direction and all nonlinear ROM models are able to capture it.

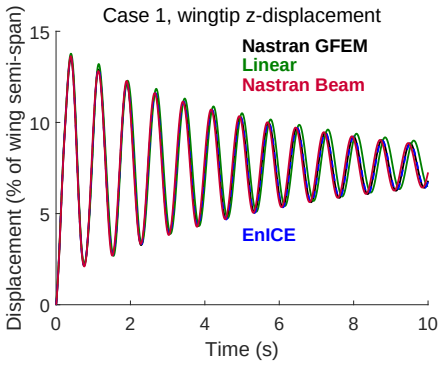

Figure 5.32: Out-of-plane displacements for Case 1.

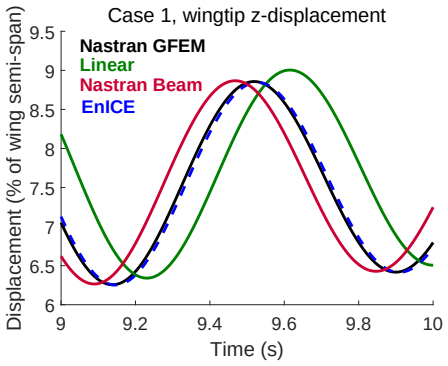

Figure 5.33: Zoom at the out-of-plane displacements.

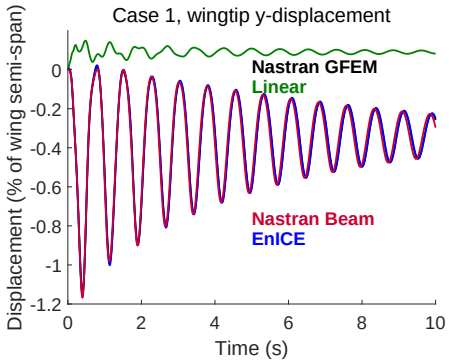

Figure 5.34: Tip spanwise displacements for Case 1.

In Case 2, the excitation has the same amplitude as Case 1 but it is sinusoidal with frequency of 0.125 Hz. This case turned out to have small amplitude response, as shown in Fig. 5.35. In a long simulation of 100 s, all the solutions remained accurate, and there was no phase error accumulated. The only differences are visible with a

zoom into the peaks, as shown in Fig. 5.36. There it can be noticed a small error of the linear solution, while the nonlinear solutions remained very close to the GFEM reference one. For forced excitation, it was expected that no phase error accumulation would happen because the response is driven by the applied load away from the initial transient response.

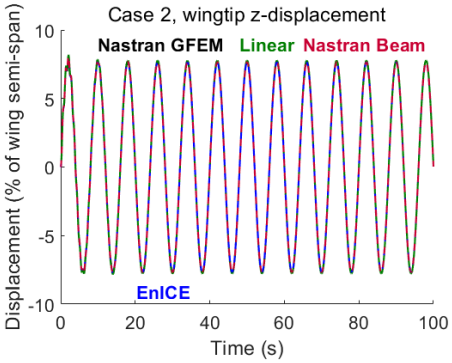

Figure 5.35: Out-of-plane displacements for Case 2.

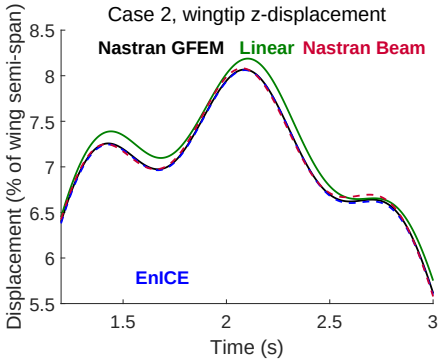

Figure 5.36: Zoom at the out-of-plane displacements.

As explained above, GFEM dynamic results could not be obtained for large displacements due to lack of convergence with the rigid elements included in the model. However, it is possible to remove the rigid elements together with the concentrated masses and obtain static results up to very large displacements. This is the reason for Case 3.

For this case, a tip vertical load was applied statically and the results for tip displacements predicted by the the different ROM methods were compared to the GFEM reference up to a tip vertical force of 70 kN. Since this loading corresponds to a tip force, a high stress is generated at the outboard region of the wing, resulting in local buckling and deformation of the cross section.

Figures 5.37 and 5.38 show the out-of-plane and span-wise tip displacements as the load is increased. Until 60% of the maximum load, the agreement between all models is very good, comparing both the vertical and the span-wise displacements. When the tip vertical displacement achieves values higher than 15% of the semi-span,

however, a significant difference is observed between the GFEM solution and the beam-based model, while the EnICE predictions remain close to the reference.

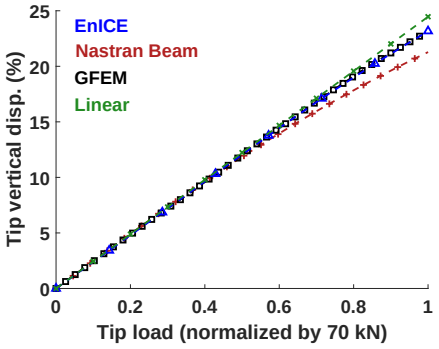

Figure 5.37: Out-of-plane displacements for static loading.

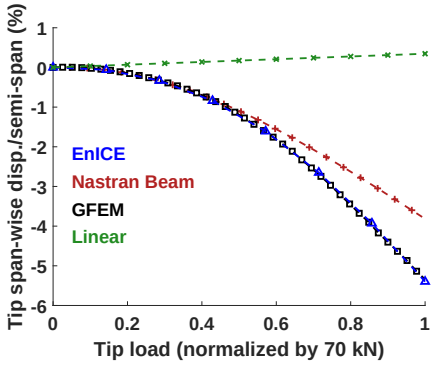

Figure 5.38: Span-wise displacements for static loading.

Finally, another interesting aspect of the ROM solution is the possibility to capture local effects with an enrichment of the basis of dual modes considered in the nonlinear displacements. These are purely nonlinear features accessible to modal ROM predictions. In order to analyze this capability, the cross section of the minimum principal strain was selected for this study. For an applied tip load, this cross section is the one indicated in Fig. 5.39.

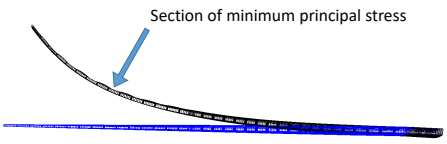

Figure 5.39: Position of cross section selected for analysis.

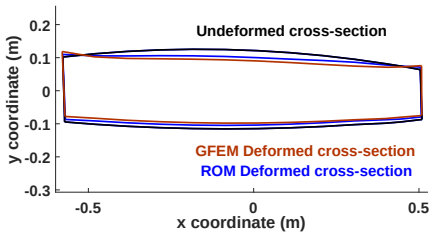

Figure 5.40: cross section deformation after tip load.

In order to capture the local effects of the cross section deformation, it was necessary to introduce additional dual modes specific for the nodes on the selected cross section. With an additional set of 15 dual modes, a result was obtained for the cross section shape that indicates both the local buckling of the upper surface and the

crushing of the cross section due to the Brazier effect [128]. The comparison of cross section geometries for the reference and the ROM solutions is presented in Fig. 5.40, along with the undeformed cross section. Besides the increase in the accuracy of the EnICE solution, this approach shows that local effects can be captured with ROM models enriched with nonlinear features on the spot of interest.

5.3.2.3 Discussion of Results

From the tip responses of dynamic load cases, a good agreement was observed between the solutions of two different nonlinear ROMs considered. The step response pointed out to accumulation of phase errors between the beam solution and the modal approach. However, for the harmonic excitation, excellent matching was observed. Due to the large deformations, the linearized GFEM failed to accurately capture the correct response for span-wise components.

When higher tip deflections are achieved, the beam solution is not able to represent phenomena like local buckling and Brazier effect, as expected. Therefore, softening due to the deformation of the cross section is not properly modeled using these approaches. The load cases investigated tip loads, which are associated to a high curvature in the outboard region of the wing. Since this region is not designed for such high loads, local buckling is observed. Figure 5.41 shows a qualitative comparison of minimum principal strain distributions when the load applied is a concentrated tip force and when it is a distributed load in the shape of the first bending mode. In the first case, the loads are concentrated at the tip, and there is local buckling. In the second case, the tip displacement is similar, but the strain is more uniformly distributed and there is no buckling.

The EnICE is able to capture effects of pre-stress cross section deformation, which explains the matching between tip displacements obtained with the EnICE and the GFEM solutions for static solutions. In terms of torsion, the EnCE prediction is also

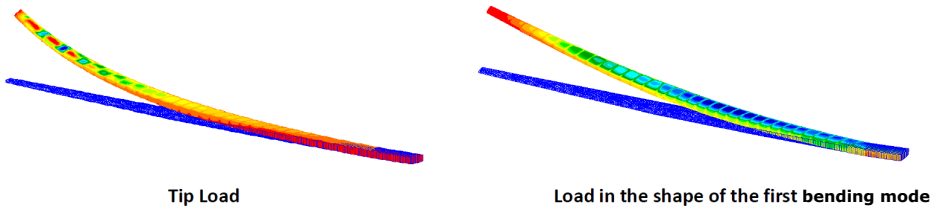

Figure 5.41: Minimum principal strain distributions for two different loading conditions.

matching the reference. Figure 5.42 shows the geometry of the tip section of the deformed wing under the tip vertical load of 70 kN, comparing the reference solution with the EnICE prediction. This view emphasizes the ROM errors relative to the cross section dimensions and the torsion discrepancies. The torsion angle is -21.8 degrees for the GFEM reference and -22.4 degrees for the ROM prediction.

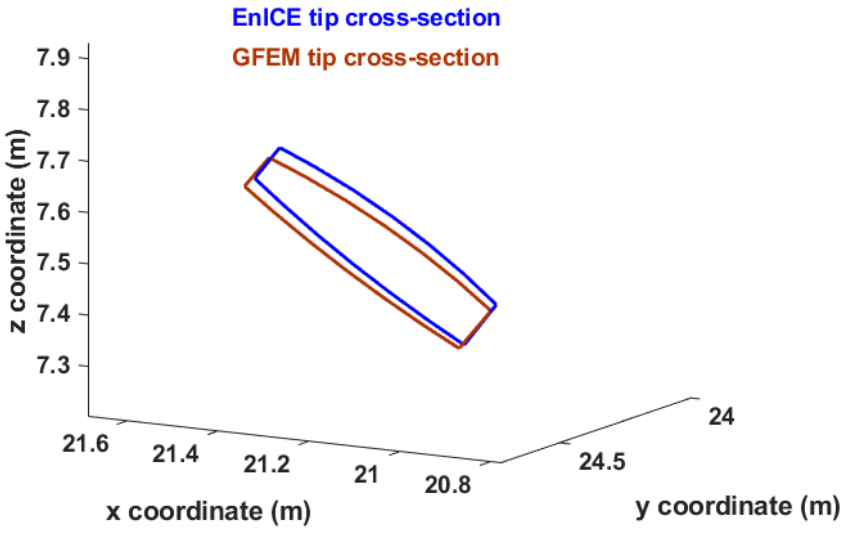

Figure 5.42: Tip cross section of deformed wing under 70 kN tip force.

It was not possible to obtain the GFEM reference for dynamic cases in large displacements, but from the results of lower amplitudes and high amplitudes under static loads, it is expected that the ROM predictions would be accurate for large amplitude dynamic solutions. In this case, the ROM in dynamic conditions has

the versatility of predicting a response when the GFEM solution shows convergence difficulties.

In terms of computational efficiency and model preparation, the EnICE approach is the less automated in the off-line phase, requiring considerable effort to reason the appropriate set of training loads for the identification of nonlinear stiffness and displacements. The calculation of reference solutions takes approximately 37 hours in a Xeon E3 processor. However, the reference solutions may be calculated in parallel. The extraction of equivalent beam properties is based on GFEM linear static solutions that are much faster to obtain. The number of degrees of freedom considered is also different. The EnICE method deals with fewer degrees of freedom due to its modal nature, while the beam method will usually include more than 100 degrees of freedom. Even though the modal solution has less dependent variables involved, the computational efficiency is not as high as the classical modal approach due to the complexity of the nonlinear functions and its derivatives, which are neural networks. Table 5.8 presents an approximate comparison of computational times required from each method to simulate 1 s of dynamic response.

Table 5.8: Computational time comparisons for 1 s of physical time simulation

Model	**Time (s)**	**DoF**	**Max. time step**
GFEM	14,270.6	48,750	1 ms
FE beam	23.6	174	1 ms
EnICE	5.4	18	1 ms

5.4 uCRM 13.5 Wing

The last application is a wing design developed by Brooks *et al.* [109] based on the NASA Common Research Model (CRM) [129]. This design, called uCRM 13.5, is an extended elastic version derived from the CRM, with aspect ratio of 13.5. The

main purpose of the uCRM 13.5 is to serve as a benchmark for aeroelastic investigations concerning designs of higher aspect-ratio wings that can be employed in next-generation transonic transport aircraft.

5.4.1 Model Description

The uCRM 13.5 model was optimized around the nominal cruise condition of Mach 0.85 at the flight altitude of 37,000 ft. The model has a total span of 72 m, and the geometry of the wing is shown in Fig. 5.43. The wingbox was estimated from public drawings of the Boeing 777-200. It is an aluminum structure, with optimized thickness distribution along the span. Different constraints were taken into account, such as transonic buffet and yield stress in maneuvers with accelerations of -1 g and 2.5 g, as well as a gust condition around cruise [109].

The different finite element models and the aerodynamic meshes were made available by Brooks *et al.* [109] and used in this work. In this case, the focus is on the wing along. No fuselage portion is included in the analysis. Only the coarser FE model and aerodynamic mesh data were evaluated in order to reduce computational costs for this study.

The FEM that represents the wingbox is composed of 23,399 shell elements. Only half wing is represented. The boundary conditions are symmetry at $y = 0$ (symmetry plane) and restriction of displacement in the vertical plane for the wing-fuselage junction. There are concentrated masses in many points representing fuel, engine and actuators and other peripheral structures. The ribs closer to the root are parallel to the fuselage, while the other ones are perpendicular to the leading edge except the wingtip rib. The FEM of the wingbox for the undeformed condition is shown in Fig. 5.44. All the structural analyses were performed using the MSC Nastran SOL 400.

The aerodynamic mesh is based on the mesh made available by Brooks *et al.* [109].

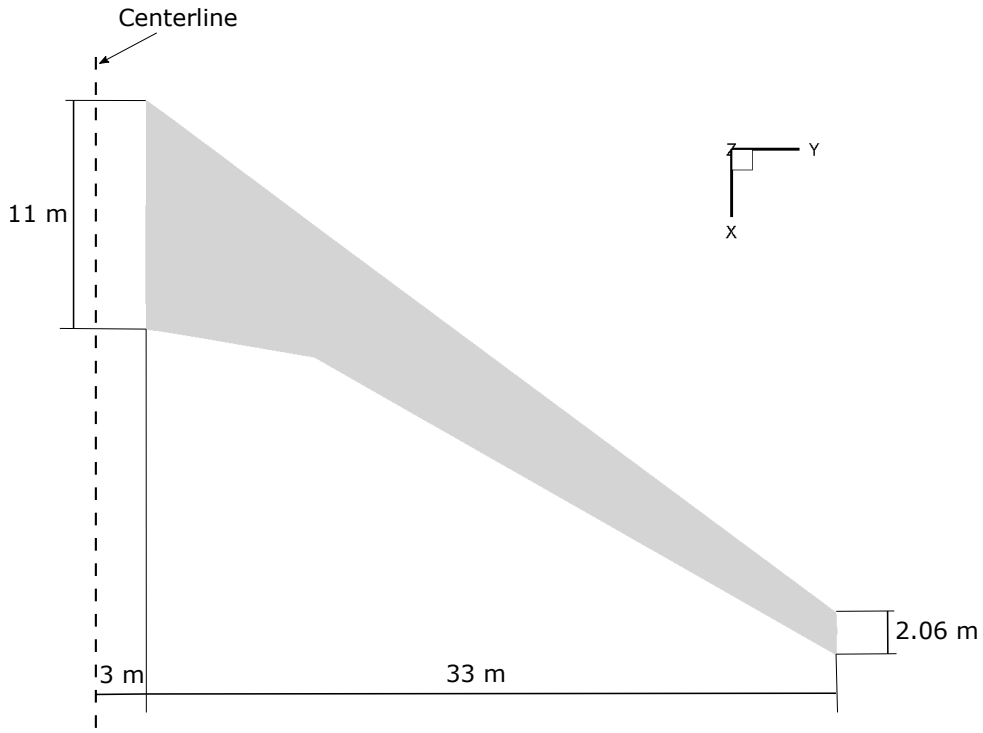

Figure 5.43: Planform of the uCRM 13.5 wing.

However, since only the half wing was desired for this study and the CFD solver had specific sensitivities and requirements for the mesh, it was redesigned from the CAD geometry. A symmetry plane is considered from the wing-fuselage intersection. In total, it has 532,480 volume cells with 6,656 quadrilaterals over the semi-wing surface and 80 layers from the normal extrusion. The surface mesh and a few layers over the symmetry plane are shown in Fig. 5.45.

All aerodynamic analyses were performed using the CFL3D RANS solver, with Spalart-Allmaras turbulence model. No transition model was coupled to the solver, and the equations have turbulence terms since the leading edge. For mesh deformation, the exponential decay method was used.

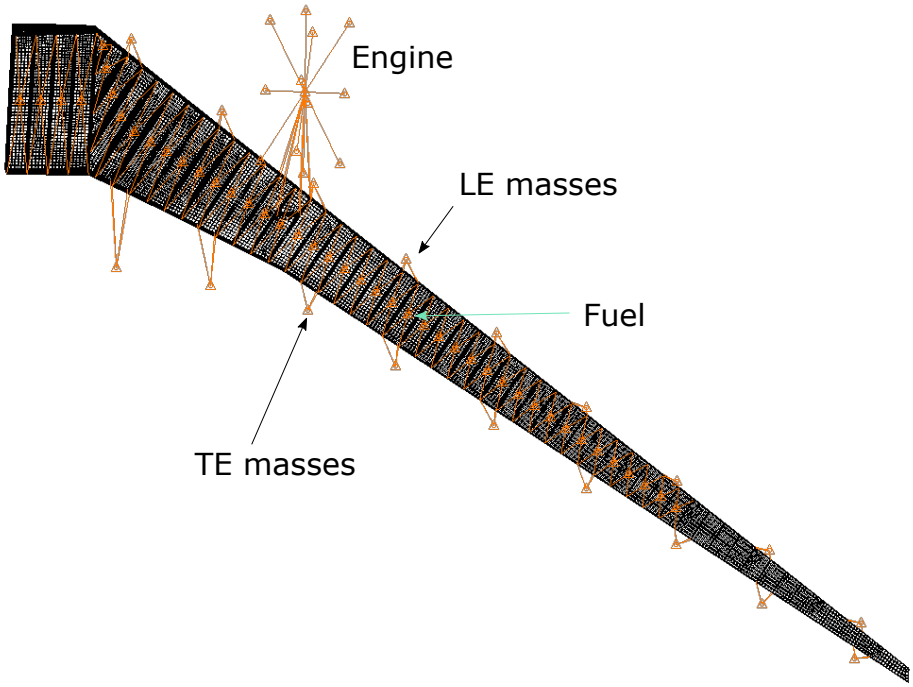

Figure 5.44: FEM of the wingbox of uCRM 13.5.

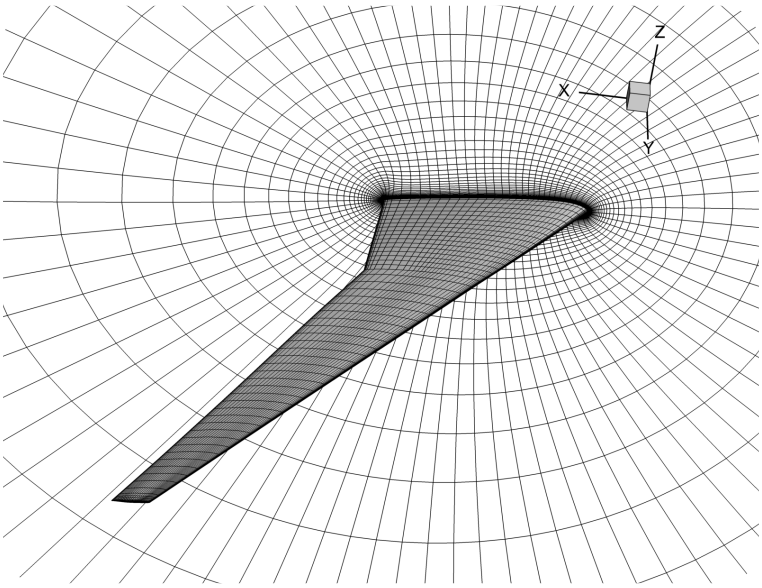

Figure 5.45: Structured mesh for the uCRM 13.5.

5.4.2 Fitting of Nonlinear Displacements and Forces

For the identification of the structural ROM, nonlinear static solutions using Nastran SOL 400 were used as reference. In total, 542 solutions were obtained, each with 20 load levels, summing up for 10,840 reference points, with linear modes training amplitudes reported on Table 5.9. The 20 levels are obtained to save computational time, since each Nastran SOL 400 is performed at increasing load magnitudes. However, the loads for the 542 solutions are obtained with Halton sequences, considering the range of amplitudes of Table 5.9. At the end, 18 degrees of freedom were retained for the ROM. Since the model is more complex, reference solutions are more expensive to obtain. Each solution for large-displacements took an average of 50 minutes in a Xeon E3 processor.

Table 5.9: Linear modes amplitudes for training the uCRM EnICE model.

Modes	1	2	3	4	5	6	7	8	9
Amplitudes	129.87	35.26	1.08	10.41	1.44	3.71	1.65	0.54	0.07
cont'd									
Modes	10	11	12	13	14	15	16	17	18
Amplitudes	0.84	0.52	0.11	0.26	0.17	0.21	0.15	0.05	0.05

The fittings for nonlinear displacements and forces were both performed using neural networks with 3 neurons in the hidden layer. Fifteen dual modes were employed to represent the displacements. A technique to isolate different components of displacements in different dual modes was applied. This way, it is guaranteed that each component of displacements/rotations is represented adequately. From the matrix of nonlinear residue R_{NL}, the procedure of Subsection 2.2.2 is performed for each component separately and sequentially, creating bases of dual modes with components along one single direction and zero entries for the other directions. The number of dual modes for each component and the sequence of identification are presented on Table 5.10. The number of dual modes chosen for each component is different,

according to the accuracy desired, and the sequence is also related to a qualitative importance for each component.

Table 5.10: Table of sequential identification of dual modes for the uCRM wing.

Sequence of ID	Component	Dual modes
1	z translation	3
2	y translation	2
3	y rotation	4
4	x translation	2
5	x rotation	2
6	z rotation	2

For example, the z-displacements are represented with the first three dual modes. This procedure allows a better representation of displacements for more complex structures, separating different magnitudes.

In general, the coefficients of determination R obtained from the fittings of the nonlinear displacements and forces for complex structures are smaller than the ones related to fittings for models like beams. The displacements still achieve a high quality fitting, with R higher than 0.98, but the nonlinear forces are fitted with R around 0.90 and one of the components reaching only 0.6. One of the possible explanations for that is that large rotations are not always accounted for correctly in the Nastran SOL 400 solutions. That deteriorates the quality of fittings for these complex models. Anyway, in general the predictions follow closely the reference results as reported next.

The model used for fitting was the wingbox only, with no additional masses such as engine, fuel or other systems. For the aeroelastic analyses, the mass matrix is modified to take into account the additional masses.

5.4.3 Structural Results

For verification of the EnICE ROM, dynamic responses were calculated using Nastran SOL 400 solutions and ROM predictions.

The verification case is a distributed dead load of 600 kN in the vertical direction. In order to make it a realistic load, a distribution was adopted decaying from the root to the tip according to Fig. 5.46. From the GFEM, the nodes of the exterior surfaces were selected excluding the ribs. The semi-span was then partitioned into 50 strips and the nodes within the y range of strip shared uniformly the vertical load related to that strip according to the distribution of Fig. 5.46.

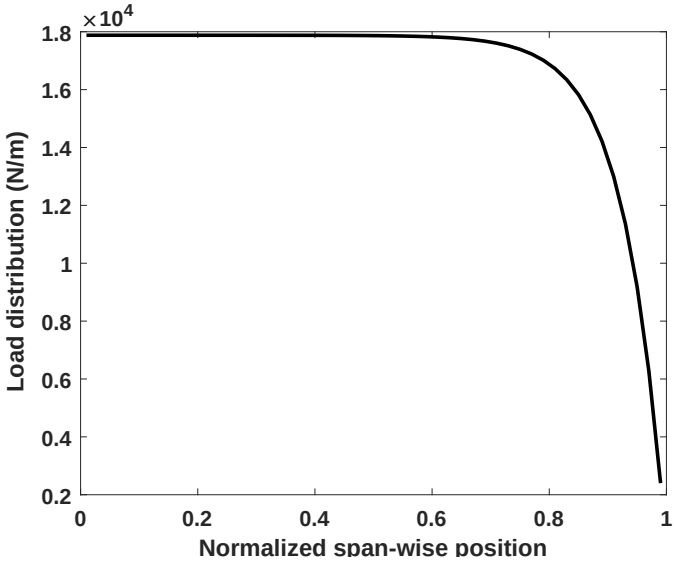

Figure 5.46: Load distribution along the semi-span of the uCRM 13.5 wing.

The distributed load of 600 kN in the vertical direction was applied as a step from $t = 0$. There is a proportional damping of 0.2% applied to both the EnICE model and the reference GFEM (Nastran SOL 400) reference model. Additionally, a linear solution was obtained using the same GFEM model in Nastran SOL 112 sequence. Comparisons of tip vertical displacements and tip torsion are plotted in Fig. 5.47. The tip displacements were measured as an average displacement from the nodes at

the wingbox tip cross-section (closing rib).

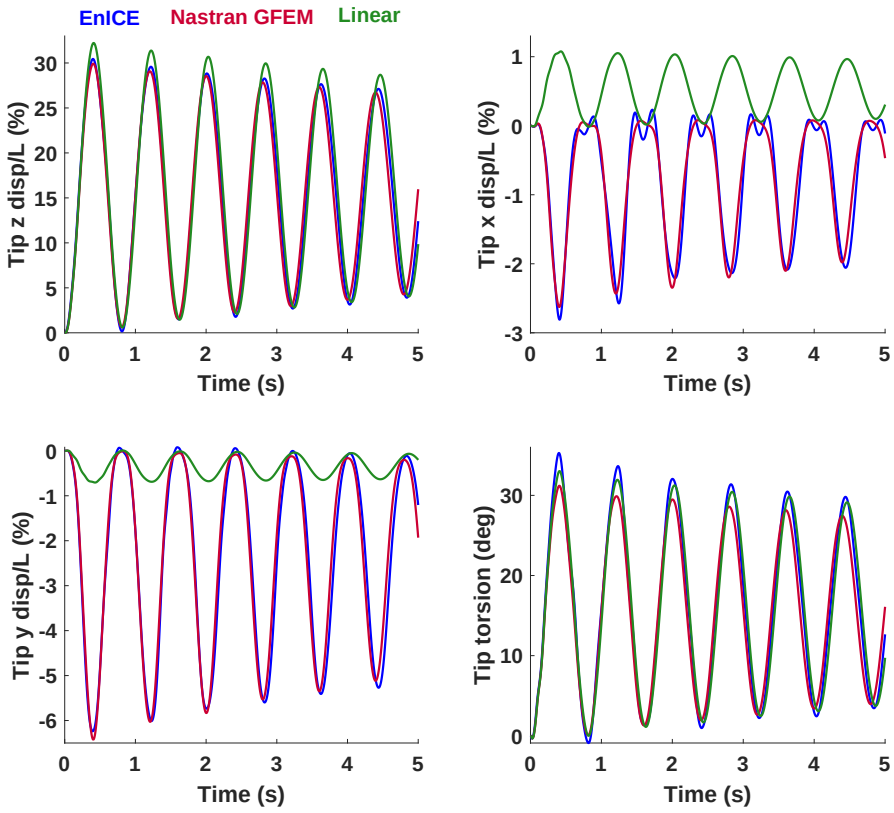

Figure 5.47: Tip displacement response for distributed vertical dead load of 600 kN applied as a step at $t = 0$.

From this result, the EnICE prediction was better for displacements. The peaks of vertical displacement are predicted with errors of 0.5% of the semi-span, while the linear solution over-predicts the maximum vertical response in 2.4% of the semi-span. The span-wise displacements (y-direction) are generally captured by the ROM. The EnICE also predicts chord-wise displacements (x-direction), but it introduces additional oscillations close to the peaks. The major errors from ROM predictions are in the rotations, where the linear prediction seems to perform better. The solutions are calculated for a relatively short time of 5 seconds. However, it is already noticeable an accumulation of phase errors. The phase of the ROM predictions are closer to the reference when compared to the linear solutions, but these errors indicate that EnICE

predictions will not be reliable for long simulation times.

Comparing this response to the ones obtained for the previous cases, it is clear the fittings of this ROM were not so well-suited as the ones for simpler structures. In terms of short-term responses, though, it still has very good performance for displacements. The torsion results shown in Fig. 5.47 are from the degrees of freedom of rotation in the y-direction. However, only displacements are used for mesh motion via splines in the aeroelastic framework, and these predictions of rotation d.o.f.s should not affect the results.

5.4.4 Identification of Aerodynamic ROM

For identification of the aerodynamic ROM, the splines for linear and dual modes were calculated from the structural model using the procedure of splines described in Section 3.6. Steady RANS solutions were obtained for the undeformed wing varying the root angle of attack from -11 degrees to 15 degrees, at nominal flight conditions of Mach 0.85 at 37,000 ft. For this study, the focus is not the robustness to varied flight conditions. For this reason, only this condition is explored.

A database was built with aerodynamic forces obtained for the grid points with different angles of attack. According to the Method of Segments (MoS), the wing is partitioned along the span-wise direction, and the steady reference solutions are calculated for each segment. In this case, a total of 17 segments were selected along the semi-span and they are shown in Fig. 5.48 by grid points pertaining to different segments in distinct colors.

For each steady solution, the effective angle of attack of each segment is approximated using the lifting-line approach. These angles are stored in the database for the fitting of loads.

Besides the steady data, step responses are also obtained from small perturbations in the shape of all linear modes considered. These constitute a database for linear

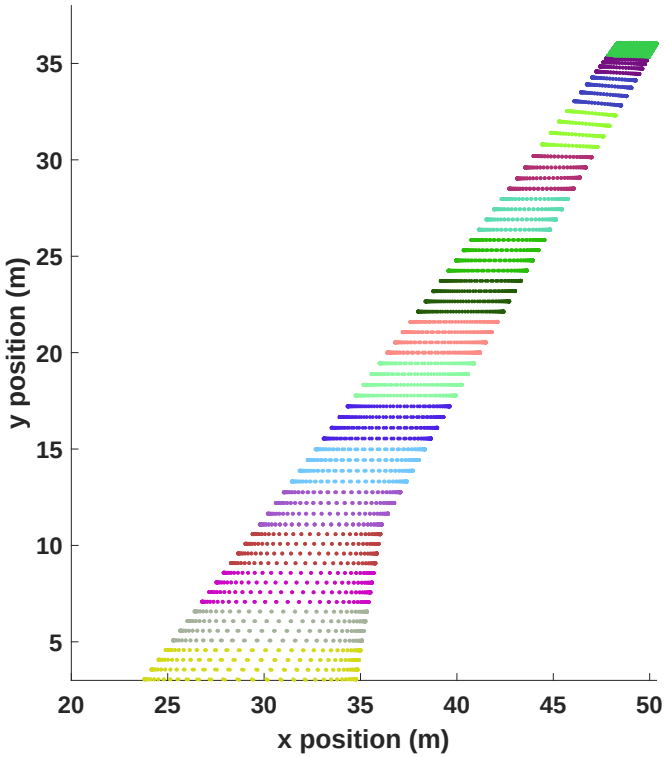

Figure 5.48: Partition of 17 segments for the uCRM 13.5 semi-wing.

convolutions in the unsteady predictions.

5.4.5 Static Aeroelastic Results

From the EnICE ROM and the reference data from steady solutions, predictions using the aerodynamic ROM are compared with CFL3D solutions. For the nominal condition of Mach 0.85, air density of 0.348 kg/m^3, root angle of attack of 2.59 degrees and considering the gravity of 9.81 m/s^2, and fuel level of 20%, the reference and the ROM solutions are compared. Figure 5.49 shows the deformed wing for the reference solution (EnICE/CFL3D) and the aerodynamic ROM solution (EnICE/MoS). Table 5.11 shows a comparison of tip displacements from the two solutions.

The EnICE/MoS solution provides an approximation with errors around 1% for

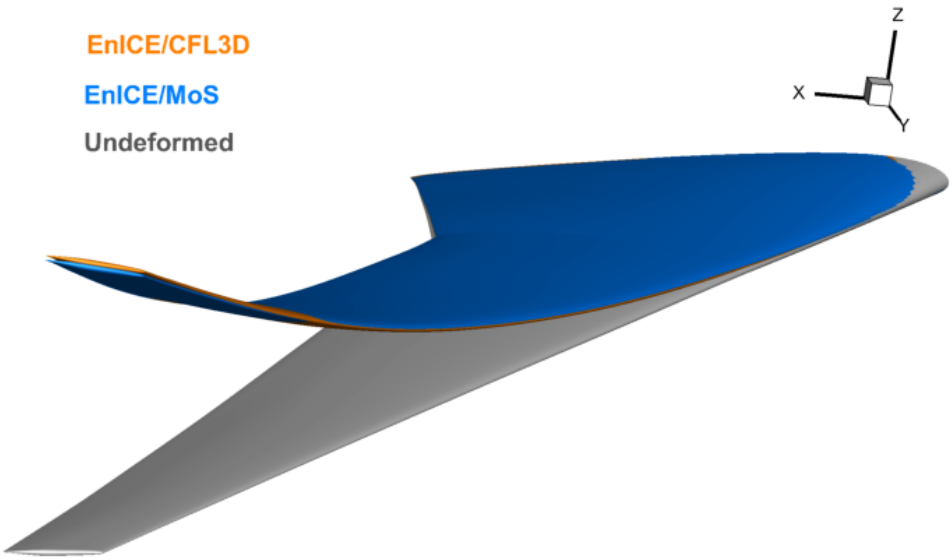

Figure 5.49: Comparison of static aeroelastic displacements obtained with the EnICE/CFL3D framework and the EnICE/MoS ROM.

Table 5.11: Comparison for tip displacements in the static aeroelastic equilibrium of the uCRM 13.5 wing at cruise (1 g) condition, M=0.85, AoA = 2.59 deg, altitude 37,000 ft.

	EnICE/CFL3D	EnICE/MoS	Error (%)
X disp. (m)	−0.149	−0.130	−13
Y disp. (m)	−0.711	−0.675	−5
Z disp. (m)	5.828	5.747	−1

the tip vertical displacements. The error is higher in the other directions, but their absolute magnitudes are much smaller. A lifting-line approach with discrete vortex filaments for the calculation of induced angles of attack contributes to such reduced errors compared to a case with no corrections. Looking at the wingtip in Fig. 5.49, the torsion observed is similar for the EnICE/CFL3D and the EnICE/MoS results. In such a scenario with transonic flow, obtaining static deformations is non-trivial, especially because not only the resultant force should match but also the modal forces. In summary, the distribution of loads predicted by the MoS must match as well the reference solution.

Computational savings are significant for the MoS solution. While the static aeroelastic solution in the EnICE/CFL3D framework requires a steady solution and a dynamic aeroelastic response with high damping (there is no steady aeroelastic solution in CFL3D) in a process that takes more than 6 hours, the same ROM solution is achieved in less than 30 seconds.

A load case corresponding to a 2.5-g condition was also analyzed. In order to obtain a higher lift, both the root angle of attack is increased from 2.59 to 5.40 degrees and the dynamic pressure increased by 120% relative to the cruise condition. The Mach number of 0.85 is kept.

In this case, the comparison between the static aeroelastic equilibrium deformations achieved with the EnICE/CFL3D framework and the reduced order combination EnICE/MoS is presented in Fig. 5.50. The error of displacements in the vertical direction is 3% of the reference value obtained in the EnICE/CFL3D framework, as presented in Table 5.12.

For the 1-g equilibrium, the tip vertical displacement relative to the undeformed condition is around 16% of the semi-span, while in the 2.5-g equilibrium the displacement is around 28% of the semi-span. For such conditions, the nonlinearities may play an important role, coupling twisting and torsion and affecting the flutter behavior.

Not only displacements are important, but also the distribution of loads. For the uCRM 13.5 wing in the 1-g equilibrium, the tip is twisted 9 degrees relative to its undeformed orientation, reducing the local angle of attack and changing the distribution of loads. This redistribution of loads is responsible for inducing different local angles of attack relative to the undeformed configuration used for reference solutions. In this context, taking the induced angles of attack into account is required to keep the accuracy of the MoS.

The load distribution was evaluated with and without the correction for induced

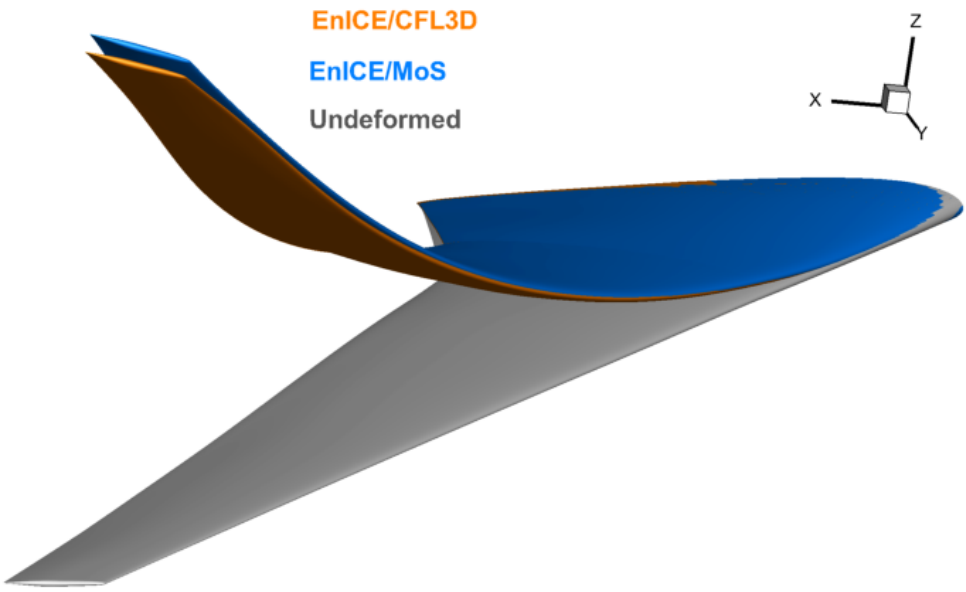

Figure 5.50: Comparison of static aeroelastic displacements obtained with the EnICE/CFL3D framework and the EnICE/MoS ROM at a load factor of 2.5 g.

angle of attack, and compared to the distribution obtained from the EnICE/CFL3D framework. The lift was evaluated for each segment. The purpose of this comparison is to understand the relative importance of the change in induced angles of attack when the wing deforms, particularly when there is torsion involved. The lift of each segment is plotted in Fig. 5.51 as a function of the spanwise position of the segment's geometric center. For this plot, the EnICE/MoS lift values were calculated with the wing deformed in the shape of the aeroelastic static equilibrium obtained for the

Table 5.12: Comparison for tip displacements in the static aeroelastic equilibrium of the uCRM 13.5 wing at 2.5-g condition, Mach=0.85, AoA = 5.40 deg, altitude 15,000 ft.

	EnICE/CFL3D	EnICE/MoS	Error (%)
X disp. (m)	−0.505	−0.559	11
Y disp. (m)	−1.839	−1.897	3
Z disp. (m)	10.168	10.500	3

1-g cruise condition (root AoA of 2.59 deg) with induced angles of attack. That deformation is close to the equilibrium of the EnICE/CFL3D framework, as shown in Fig. 5.49 and Table 5.11. The lift values for the EnICE/CFL3D were calculated at the equilibrium condition. Redistribution of loads due to the elastic wing torsion changes the local induced angles of attack significantly in its outboard portion. If only the geometric angle of attack is used to calculate the forces on each segment for both training and simulation phases, then the lift in the outer segments is under-predicted for given root AoA and wing shape. In total, the lack of induced AoA correction decreases the lift by 30% as shown in Fig. 5.51. When a lifting-line approximation corrects the induced angle of attack, the lift distribution resembles the one obtained in the CFD calculation.

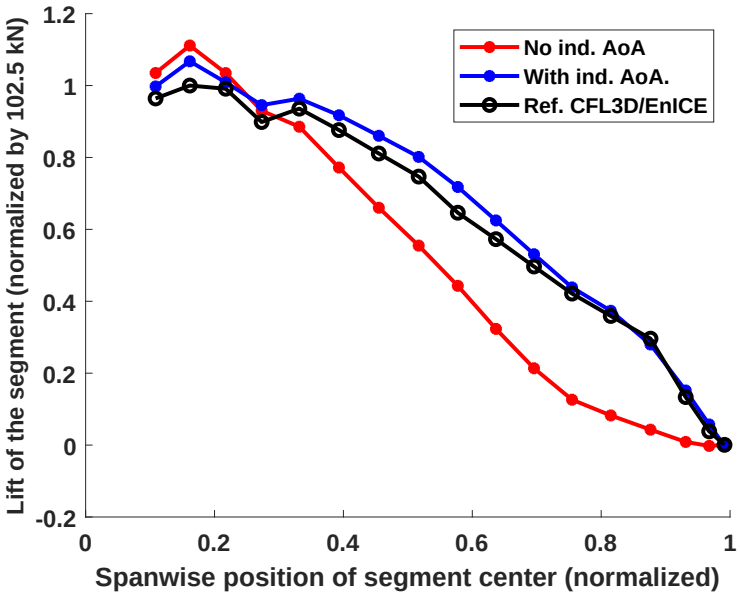

Figure 5.51: Lift along the segments of the uCRM 13.5 wing

If the aeroelastic static calculations are performed without correction for induced angle of attack, the equilibrium achieved for the cruise condition is very different from the one observed with the EnICE/CFL3D reference. Figure 5.52 shows this comparison, where the error in the tip vertical displacement is 25%.

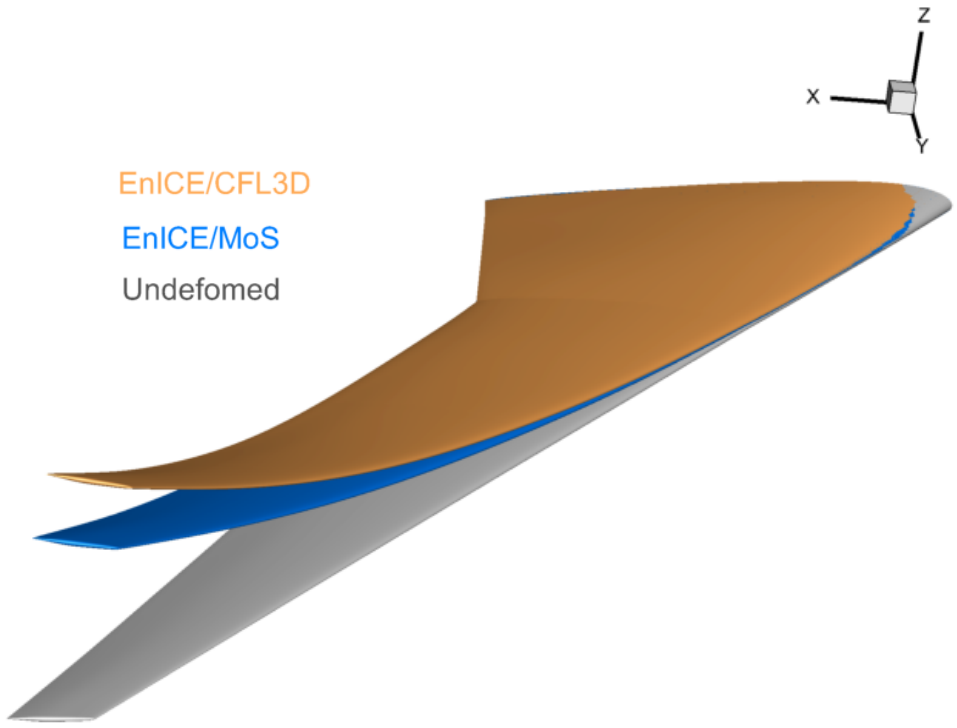

Figure 5.52: Static aeroelastic displacements obtained from EnICE/CFL3D [3] and EnICE/MoS, without correction of induced angles of attack.

5.4.6 Dynamic Aeroelastic Results

Starting from the equilibrium position achieved for the 1-g flight configuration in the EnICE/MoS framework, modal step responses were obtained. Modal forces along the linear and dual modes were recorded after step deformations in the shapes dominated by linear modes, as described in Section 3.3, for a 0.2-s window of unsteady simulations. These responses were used for calculation of the unsteady modal forces in the EnICE/MoS framework. Using the correction factor for nonlinearities discussed in Chapter 3 did not yield good results, as will be shown in Figs. 5.53 and 5.54. Therefore, linear convolution alone with no correction factor is the best method for this example.

The cases of aeroelastic response analyzed are solutions to a step load perturbation

along the first degree of freedom. In other words, a load is applied suddenly in the shape of the first mode, *i.e.*,

$$f_{1,u} = f_{1,eq} + \delta_f \tag{5.4}$$

where $f_{1,u}$ is the unsteady modal force related to the first degree of freedom, $f_{1,eq}$ is the equilibrium load for the cruise condition and δ_f is the step increment used to excite the unsteady response.

Using a step load of amplitude $\delta_f = 3,600$ N·m, which corresponds to 50% of $f_{1,eq}$, the tip response obtained with EnICE/MoS with convolution of step responses is compared against the reference solution of the high-fidelity EnICE/CFL3D framework and the EnICE/MOS solution with convolution and the correction factor using $\delta = 10^5$ (explained in Subsection 3.3.3) in Fig. 5.53. Even though the step load is large when compared to the $f_{1,eq}$, the tip vertical displacement only achieves 4% of of the semi-span. This moderate deformation is due to the step load being applied to the first degree of freedom only. Predicting the unsteady solution involves errors from the identification of the step responses, the convolution calculation, and from the nonlinearities that arise even for small deformations in transonic conditions. In this case, the amplitude and damping of the response is well-captured by the response with convolution, in the vertical and spanwise directions. However, there is a phase error accumulation for all components.

Considering a larger step load in the shape of the first mode with amplitude of $\delta_f = 1.46 f_{1,eq}$. For this case the response is more pronounced, but the errors of the EnICE/MoS framework with linear convolution are also larger as seen in Fig. 5.54. The increased displacements are related to a more nonlinear response not captured by the linear convolution. The damping for the vertical displacement is well captured. At the end, both levels of excitation lead to similar response and error level from the EnICE/MoS approach with convolution. The correction factor

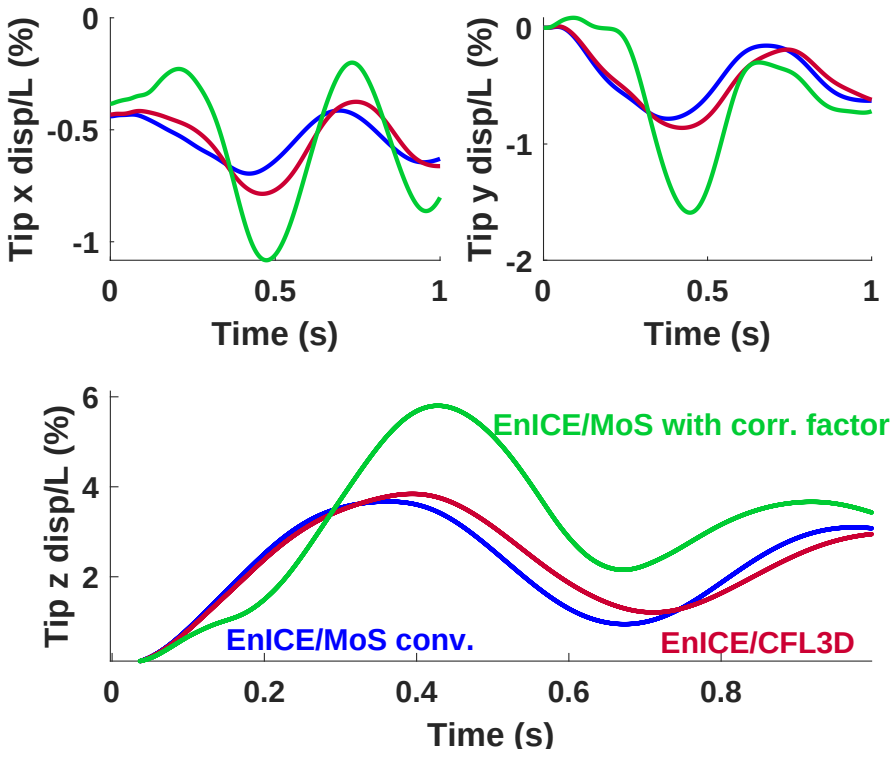

Figure 5.53: Moderate tip response after moderate step load excitation ($\delta_f = 0.5 f_{1,eq}$).

Both dynamic simulations correspond to 1 s of response after the step load is applied. The computational cost of those in an office desktop (Xeon E3) is around 6 minutes. The implemented linear convolution implemented is computationally expensive for 18 degrees of freedom. Different convolution calculation techniques may reduce this cost. Even so, the high-fidelity reference solution of 1 s obtained in EnICE/CFL3D takes around 13 hours in a parallel computer using 17 processors. The ROM certainly represents a significant time reduction.

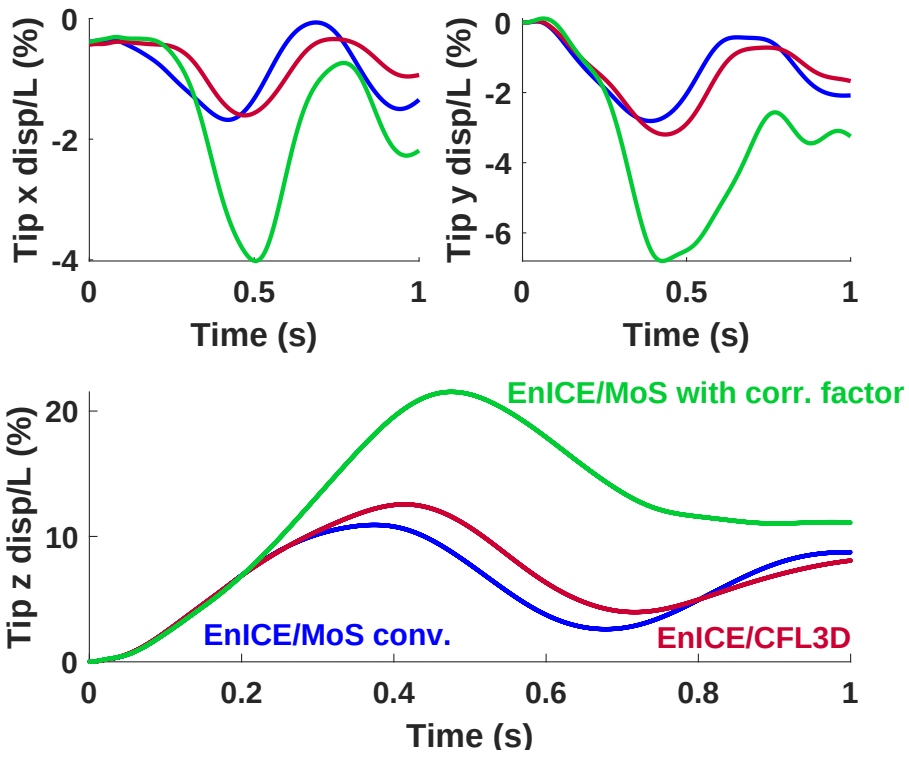

Figure 5.54: Large tip responses after step load excitation ($\delta_f = 1.46 f_{1,eq}$).

CHAPTER 6

Concluding Remarks

This chapter presents a summary of the developments, main conclusion, key contributions, and recommendations for future work.

6.1 Summary

The dissertation presents a new computational aeroelastic framework to capture geometrically nonlinear effects in slender wings. The structure is represented with a nonlinear modal reduced order model (ROM), the Enhanced Implicit Condensation and Expansion (EnICE), integrated with a Computational Fluid Dynamics (CFD) solver, the CFL3D, and with an aerodynamic ROM, the Method of Segments (MoS).

The EnICE is based on a description of large displacements using linear modes and a supplementary set of dual modes. These shapes are identified specifically to address the large displacements not covered by the linear modes.

Using static nonlinear reference solutions obtained from a commercial FEM (MSC Nastran SOL 400), both the nonlinear modal stiffness terms and the amplitudes of dual modes are calculated and fitted as functions of the modal degrees of freedom related to linear modes. Euler-Lagrange equations considering the kinetic energy of dual modes compose the system dynamics.

Examples are shown to illustrate the structural model-order reduction with increasingly complex structural models. Using a system of 6 degrees of freedom com-

posed of rigid rods connected with torsional springs, the method and choice of parameters are detailed. Then, the EnICE is applied to a 16-m wing, and two built-up finite element models: BUG wing and uCRM 13.5 wing. For the BUG wing, it is shown that nonlinear effects related to deformation of the cross section cannot be captured with conventional beam models and the EnICE predicts accurately the nonlinear displacements.

The EnICE was integrated into the code CFL3D for high-fidelity aeroelastic analyses. Due to its modal formulation, the EnICE is easily linked to tools with existing linear modal solutions. Modifications to the time-integration methods and equations of motion are the main steps for this enhancement. Comparisons with another solver using the 16-m wing provide verification for the CFL3D/EnICE framework in steady and unsteady conditions.

A reduced-order aerodynamic model was developed using reference results from RANS computations in the CFL3D code. This aerodynamic ROM is suitable for steady and unsteady computations involving large displacements. For steady results, the Method of Segments (MoS) with corrections for the effective angle of attack is used. The wing is divided in segments and the aerodynamic forces are fitted for the nodes of each segment using the local angle of attack corrected with induced AoA. For the unsteady solutions, a linear convolution is performed using the finite step response due to each modal deformation. The nonlinearities may be accounted for by means of a correction factor. This factor is calculated during the time simulations using the ratio between steady computations with MoS and a linear steady solution.

Steady results for the uCRM 13.5 wing show a good match between predictions using the EnICE/CFL3D framework and the EnICE/MoS ROM. Unsteady simulations show higher errors, and the correction factor does not yield accurate results in this case.

In general, the ROMs represent significant time savings relative to the high-fidelity

structural and aerodynamic solutions. Table 6.1 shows time comparisons for the structural ROMs discussed, detailing preparation and simulation costs. Note that the comparisons of simulation costs for the EnICE models were not performed under same conditions, with differences in loads, presence of gravity and type of force (dead or follower), but all were computed with a Xeon E3 processor. Also, the code evolved in time, and a feature for acceleration (MEX functions) was not present in the evaluation of the 16-m wing model. In general, the costs will depend on the number of d.o.f.s considered and the cost of evaluating the fitting functions, such that models with more neurons in the hidden layer will be more expensive. However, for all EnICE simulations performed, the cost of 1 s of physical simulation is only a few seconds. For the aeroelastic computations, the time for preparation of the aerodynamic ROM involves calculation of static solutions and step responses. Those may vary significantly with the model and the refinement desired. In the example analyzed of the uCRM 13.5 wing, the training cost was around 1 day, using a cluster with 128 cores. The simulation costs are higher, compared to the structural ROM. Each 1 s of physical simulation takes approximately 5 minutes in a Xeon E3 computer, but it takes 13 hours in a CFD solver with aeroelastic capabilities.

Table 6.1: Comparison of times for structural ROMs training and simulation.

Wing Model	16-m wing	BUG Wing	uCRM 13.5
DoFs	192	48,750	132,684
# Ref. Sols.	12,480	11,480	10,760
Ref. Sols. Time	20 min	239 h	448 h
ROM DoFs	12	18	18
Cost 1 s (EnICE)	2.4 s	5.4 s	1.6 s
Cost 1 s (Nastran)	55 s	4 h	1.5 h

6.2 Conclusions

These are the main conclusions of this dissertation, regarding the identification and simulation with structural ROMs:

- Reduced order models with a few degrees of freedom based on linear modes amplitudes can successfully represent built-up structures undergoing low-frequency, large-displacement motion. These nonlinear ROMs reduce in orders of magnitude the costs associated to dynamic simulations;

- Dynamic simulations of built-up wing structures undergoing large-displacement motion are expensive and non-robust. From the examples analyzed, convergence problems are frequent for large tip displacements. In those cases, the structural ROM is valuable for quick and robust analysis;

- The number of nonlinear sample static solutions required for accurate fittings of nonlinear displacements and forces grows with the number of degrees of freedom of the ROM. The examples studied considered up to 18 degrees of freedom. For such cases, some fittings of nonlinear forces did not achieve a coefficient of determination R greater than 0.9, indicating that more samples could be beneficial for fitting accuracy. That said, generation of the structural ROMs may require significant amounts of sample solutions;

- For large models, with hundreds of thousands of d.o.f.s, the EnICE ROM generation can take significant effort in sampling generation. However, the ROMs developed are specially useful in those cases, because the nonlinear dynamic solutions with the built-up FEM are expensive. For a certain time length of dynamic computations, the effort required to create the ROM is compensated by the fastor computations obtained. For the uCRM 13.5 wing, for example, 460 hours of a (single-processor) Xeon E3 were used for the obtention of sample

solutions, while each second of a nonlinear Nastran SOL 400 simulation with the built-up FEM takes more than 1.5 hours. Thus, a break-even point is achieved when more than 270 s of dynamic simulations are required. For other models, different costs of preparation and simulation are obtained;

- When high tip displacements are observed, nonlinear effects related to the softening of the structure due to deformation of the cross-section could be captured with the EnICE model, for the example of the BUG wing. In that case, an equivalent nonlinear beam model could not predict correct displacements, and the dynamic solution with the built-up FEM had convergence problems for tip vertical displacements higher than 15 % of the semi-span.

The conclusions regarding identification and simulation with the Method of Segments and correction factor for unsteady nonlinear computations as aerodynamic ROM are:

- Transonic flow is associated with nonlinearities in the aerodynamic response, making aeroelastic computations expensive when different flight conditions are involved and the wing deformation is significant. The MoS ROM is capable of quickly predicting aerodynamic steady loads for wings undergoing large deformations in such conditions. The time savings compared to CFD computations for steady solutions are around three orders of magnitude;

- Induced angles of attack are important in transonic conditions. To correct for those when the wing undergoes large twist/displacements, shedding of semi-infinite vortex lines in a lifting-line approach proved to be an essential tool for aeroelastic static computations. With this corrections, results of vertical tip displacement accurate up to 1% of the wing semi-span were obtained for the uCRM 13.5 wing;

- The unsteady aeroelastic response obtained with a correction factor for nonlinearities was more challenging than the aeroelastic static analysis. For the transonic case of the uCRM 13.5 wing, the linear convolution without correction factor was more accurate than the results with it. Further investigations are required to clarify the reasons for the inaccuracies and a possible range of applicability of the nonlinear correction factor.

6.3 Key Contributions

The key contributions from the studies reported in this dissertation are

- Development of a formulation for nonlinear modal-based structural ROMs accounting for the kinetic energy related to nonlinear displacements. Previous static condensation approaches neglected the contribution of nonlinear displacements to inertia forces. This dissertations shows that a full representation of the kinetic energy may be essential for the accuracy of time-domain simulations.

- Generalization of the nonlinear forces and displacements in the structural ROM equations. Previously, only polynomials had been used to fit these terms, but this work shows that general nonlinear fittings in the form of neural networks are better approach. This approach avoids the scaling limitations and problems with selecting the meaningful polynomial terms in fittings with many variables.

- Development and demonstration of the integration of the nonlinear structural modal ROM into a CFD code for simulations considering large displacements.

- Benchmarks with other nonlinear beam-based ROMs for a complex wing box. Comparisons performed showed that the EnICE produces more accurate results for conditions of large displacements and can capture pre-stress and significant cross-section deformation effects.

- Extension of the Method of Segments for conditions of large displacements and rotations. Due to significant departures from the undeformed condition, the steady solutions using Method of Segments can be corrected for induced angles of attack with a lifting-line approach.

6.4 Recommendations for Future Work

In the course of this study, it has become clear that some topics need further attention:

- It was noticed that commercial FE packages may account for large rotations incorrectly. In order to avoid contamination of the reference solutions in these cases, it would be useful to test training cases with no moments. Only nodal forces would be included. That can improve the quality of fittings for complex structures.

- Cross-section deformation may represent a departure from beam assumptions, and that is one of the reasons why nonlinear EnICE may be so useful. It would be interesting to investigate with more details the conditions where equivalent beam models can be used successfully to represent complex wing box structures.

- The fitting of nonlinear forces with neural networks does not guarantee a symmetric stiffness matrix using EnICE. Even though the dynamic responses were not significantly affected by this issue, an alternative path is to employ different degrees of freedom. Instead of using amplitudes of linear modes, it is possible to employ modal forces as degrees of freedom. In this case, amplitudes of linear and dual modes should be fitted as function of the modal forces for description of the displacements.

- Fittings are difficult for more than 10 degrees of freedom. Since the number

of reference static solutions is limited, alternatives for dimension reduction like POD should be considered. More investigations should be conducted to create solid guidelines for this process of fitting.

BIBLIOGRAPHY

[1] Skujins, T. and Cesnik, C. E. S., "Reduced-Order Modeling of Unsteady Aerodynamics Across Multiple Mach Regimes," *Journal of Aircraft*, Vol. 51, No. 6, sep 2014, pp. 1681–1704.

[2] Medeiros, R. M., Cesnik, C. E. S., Stodieck, O., E., C. D., E., C. J., and Coetzee, E. B., "Comparison of Structural Model Reduction Methods Applied to a Large-Deformation Wing Box," *6th Aircraft Structural Design Conference*, Bristol, 9-11 October 2018.

[3] Medeiros, R. R., Cesnik, C. E. S., and Coetzee, E. B., "Nonlinear Computational Aeroelasticity Using Structural Modal Coordinates," *2018 AIAA/ASCE/AHS/ASC Structures, Structural Dynamics, and Materials Conference*, AIAA SciTech Forum, American Institute of Aeronautics and Astronautics, jan 2018.

[4] Anon., "Global Market Forecast 2018 - 2037," Tech. rep., Airbus, 2018.

[5] Anon., "Commercial Market Outlook 2019 - 2038," Tech. rep., The Boeing Company, 2019.

[6] Afonso, F., Vale, J., Oliveira, É., Lau, F., and Suleman, A., "A Review on Non-Linear Aeroelasticity of High Aspect-Ratio Wings," *Progress in Aerospace Sciences*, Vol. 89, 2017, pp. 40–57.

[7] Noll, T. E., Brown, J. M., Perez-Davis, M. E., Ishmael, S. D., Tiffany, G. C., and Gaier, M., "Investigation of the Helios Prototype Aircraft Mishap," Tech. Rep. Volume I - Mishap Report, NASA, January 2004.

[8] Anon., "National Transportation Safety Board Aviation Accident Final Report," Accident number: dca16ca197, National Transportation Safety Board, Washington, DC, 2016.

[9] S. Cesnik, C. E., Senatore, P. J., Su, W., Atkins, E. M., and Shearer, C. M., "X-HALE: A Very Flexible Unmanned Aerial Vehicle for Nonlinear Aeroelastic Tests," *AIAA Journal*, Vol. 50, No. 12, 2012, pp. 2820–2833.

[10] Jones, J. R. and Cesnik, C. E. S., "Preliminary Flight Test Correlations of the X-HALE Aeroelastic Experiment," *The Aeronautical Journal*, Vol. 119, No. 1217, 2015, pp. 855–870.

[11] Stodieck, O., Cooper, J. E., Neild, S. A., Lowenberg, M. H., and Iorga, L., "Slender-Wing Beam Reduction Method for Gradient-Based Aeroelastic Design Optimization," *AIAA Journal*, Vol. 56, No. 11, oct 2018, pp. 4529–4545.

[12] Cesnik, C. and Su, W., "Nonlinear Aeroelastic Simulation of X-HALE: a Very Flexible UAV," *49th AIAA Aerospace Sciences Meeting including the New Horizons Forum and Aerospace Exposition*, Aerospace Sciences Meetings, American Institute of Aeronautics and Astronautics, jan 2011.

[13] Hodges, D. H., Lee, B. W., and Atilgan, A. R., "Application of the Variational-Asymptotical Method to Laminated Composite Plates," *AIAA Journal*, Vol. 31, No. 9, 1993, pp. 1674–1683.

[14] Hodges, D., Shang, X., and Cesnik, C., "Finite Element Solution of Nonlinear Intrinsic Equations for Curved Composite Beams," *36th Structures, Structural Dynamics and Materials Conference*, Structures, Structural Dynamics, and Materials and Co-located Conferences, American Institute of Aeronautics and Astronautics, apr 1995.

[15] Palacios, R. and Cesnik, C., "Structural Models for Flight Dynamic Analysis of Very Flexible Aircraft," *50th AIAA/ASME/ASCE/AHS/ASC Structures, Structural Dynamics, and Materials Conference*, Structures, Structural Dynamics, and Materials and Co-located Conferences, American Institute of Aeronautics and Astronautics, may 2009.

[16] Palacios, R. and Cea, A., "Nonlinear Modal Condensation of Large Finite Element Models: Application of Hodges?s Intrinsic Theory," *AIAA Journal*, Vol. 0, No. 0, 0, pp. 1–14.

[17] Brazier, L. G. and Southwell, R. V., "On the Flexure of Thin Cylindrical Shells and Other "Thin" Sections," *Proceedings of the Royal Society of London. Series A, Containing Papers of a Mathematical and Physical Character*, Vol. 116, No. 773, 1927, pp. 104–114.

[18] Shearer, C. M. and Cesnik, C. E. S., "Nonlinear Flight Dynamics of Very Flexible Aircraft," *Journal of Aircraft*, Vol. 44, No. 5, 2007, pp. 1528–1545.

[19] Thompson, P. M., Klyde, D. H., Farhat, C., and Harris, C., "Aeroservoelastic Predictive Analysis Capability," *AIAA Atmospheric Flight Mechanics Conference and Exhibit, Guidance, Navigation, and Control and Co-located Conferences*, 2007, Hilton Head, South Carolina, 20-23 August 2007. AIAA 2007-6716, 10.2514/6.2007-6716.

[20] Ritter, M., Teixeira, P., and Cesnik, C. E. S., "Comparison of Nonlinear Aeroelastic Methods for Maneuver Simulation of Very Flexible Aircraft," *2018 AIAA/ASCE/AHS/ASC Structures, Structural Dynamics, and Materials Conference*, AIAA SciTech Forum, American Institute of Aeronautics and Astronautics, jan 2018.

[21] Skujins, T. and Cesnik, C. E. S., "Toward an Unsteady Aerodynamic ROM for Multiple Mach Regimes," *53rd AIAA/ASME/ASCE/AHS/ASC Structures, Structural Dynamics and Materials Conference*, American Institute of Aeronautics and Astronautics, April 2012.

[22] Pai, P., *Highly Flexible Structures: Modeling, Computation, and Experimentation*, American Institute of Aeronautics and Astronautics, Reston ,VA, 2007.

[23] Bathe, K.-J., *Finite Element Procedures*, K. J. Bathe, Watertown, MA, 2014.

[24] Palazotto, A. N. and Dennis, S. T., *Nonlinear Analysis of Shell Structures*, American Institute of Aeronautics and Astronautics, Reston ,VA, 1992.

[25] Pai, P. F. and Nayfeh, A. H., "A New Method for the Modeling of Geometric Nonlinearities in Structures," *Computers & Structures*, Vol. 53, No. 4, 1994, pp. 877 – 895.

[26] Felippa, C. A. and Haugen, B., "A Unified Formulation of Small-Strain Corotational Finite Elements: I. Theory," *Computer Methods in Applied Mechanics and Engineering*, Vol. 194, No. 21, 2005, pp. 2285–2335.

[27] Yang, J. and Xia, P., "Corotational Nonlinear Dynamic Analysis of Thin-Shell Structures with Finite Rotations," *AIAA Journal*, Vol. 53, No. 3, 2015, pp. 663–677.

[28] Stoker, J. J., *Nonlinear Vibrations in Mechanical and Electrical Systems*, Interscience, New York, 1950.

[29] Nayfeh, A. H. and Mook, D. T., *Nonlinear Oscillations*, Wiley-Interscience, New York, 1979.

[30] Nayfeh, A. H., *Perturbation Methods*, Wiley-VCH, Weinheim, 2000.

[31] "Experiences with Nonlinear Modeling and Acoustic Fatigue," *Journal of Sound and Vibration*, Vol. 437, 2018, pp. 437 – 446.

[32] Blevins, R. D., Holehouse, I., and Wentz, K. R., "Thermoacoustic Loads and Fatigue of Hypersonic Vehicle Skin Panels," *Journal of Aircraft*, Vol. 30, No. 6, 1993, pp. 971–978.

[33] Shi, Y. and Mei, C., "A Finite Element Time Domain Modal Formulation for Large Amplitude Free Vibrations of Beams and Plates," *Journal of Sound and Vibration*, Vol. 193, No. 2, jun 1996, pp. 453–464.

[34] Mignolet, M. P. and Soize, C., "Stochastic Reduced Order Models for Uncertain Geometrically Nonlinear Dynamical Systems," *Computer Methods in Applied Mechanics and Engineering*, Vol. 197, 2008, pp. 3951–3963.

[35] Segalman, D. J. and Dohrmann, C. R., "A Method for Calculating the Dynamics of Rotating Flexible Structures, Part 1: Derivation," *Journal of Vibration and Acoustics*, Vol. 118, No. 3, jul 1996, pp. 313–317.

[36] Segalman, D. J., Dohrmann, C. R., and Slavin, A. M., "A Method for Calculating the Dynamics of Rotating Flexible Structures, Part 2: Example Calculations," *Journal of Vibration and Acoustics*, Vol. 118, No. 3, jul 1996, pp. 318–322.

[37] Muravyov A.A., T. T. L. R. J. H. and Rizzi, S. A., "A New Stochastic Equivalent Linearization Implementation for Prediction of Geometrically Nonlinear Vibrations," *40th AIAA/ASME/ASCE/AHS/ASC Structures, Structural Dynamics and Materials Conference*, AIAA, apr 1999.

[38] Muravyov, A. A. and Rizzi, S. A., "Determination of Nonlinear Stiffness with Application to Random Vibration of Geometrically Nonlinear Structures," *Computers & Structures*, Vol. 81, No. 15, 2003, pp. 1513 – 1523.

[39] McEwan, M. I., Wright, J. R., Cooper, J. E., and Leung, A. Y. T., "A Combined Modal/Finite Element Analysis Technique for the Dynamic Response of a Non-linear Beam to Harmonic Excitation," *Journal of Sound and Vibration*, Vol. 243, No. 4, 2001, pp. 601–624.

[40] Hollkamp, J. J. and Gordon, R. W., "Reduced-order Models for Nonlinear Response Prediction: Implicit Condensation and Expansion," *Journal of Sound and Vibration*, Vol. 318, No. 4, 2008, pp. 1139–1153.

[41] Kim, K., Radu, A. G., Wang, X., and Mignolet, M. P., "Nonlinear Reduced Order Modeling of Isotropic and Functionally Graded Plates," *International Journal of Non-Linear Mechanics*, Vol. 49, mar 2013, pp. 100–110.

[42] Gordon, R. and Hollkamp, J., "Reduced-Order Modeling of Random Response of Curved Beams Using Implicit Condensation," *47th AIAA/ASME/ASCE/AHS/ASC Structures, Structural Dynamics, and Materials Conference*, Structures, Structural Dynamics, and Materials and Co-located Conferences, American Institute of Aeronautics and Astronautics, may 2006.

[43] Kuether, R. J., Deaner, B. J., Hollkamp, J. J., and Allen, M. S., "Evaluation of Geometrically Nonlinear Reduced-Order Models with Nonlinear Normal Modes," *AIAA Journal*, Vol. 53, No. 11, 2015, pp. 3273–3285.

[44] Kuether, R. J. and Allen, M. S., "A Numerical Approach to Directly Compute Nonlinear Normal Modes of Geometrically Nonlinear Finite Element Models," *Mechanical Systems and Signal Processing*, Vol. 46, No. 1, may 2014, pp. 1–15.

[45] Wang, X. Q., Perez, R. A., and Mignolet, M. P., "Nonlinear Reduced Order Modeling of Complex Wing Models," *54th AIAA/ASME/ASCE/AHS/ASC Structures, Structural Dynamics and Materials Conference*, AIAA, apr 2013.

[46] Przekop, A., Guo, X., and Rizzi, S. A., "Alternative Modal Basis Selection Procedures for Reduced-Order Nonlinear Random Response Simulation," *Journal of Sound and Vibration*, Vol. 331, No. 17, aug 2012, pp. 4005–4024.

[47] Wang, X. Q., O'Hara, P. J., Mignolet, M. P., and Hollkamp, J. J., "Reduced Order Modeling with Local Enrichment for the Nonlinear Geometric Response of a Cracked Panel," *AIAA Journal*, Vol. 57, No. 1, oct 2018, pp. 421–436.

[48] Mignolet, M. P., Przekop, A., Rizzi, S. A., and Spottswood, S. M., "A Review of Indirect/Non-intrusive Reduced Order Modeling of Nonlinear Geometric Structures," *Journal of Sound and Vibration*, Vol. 332, No. 10, 2013, pp. 2437–2460.

[49] Kim, K., Khanna, V., Wang, X. Q., and Mignolet, M. P., "Nonlinear Reduced Order Modeling of Flat Cantilevered Structures," *50th AIAA/ASME/ASCE/AHS/ASC Structures, Structural Dynamics, and Materials Conference, Structures, Structural Dynamics, and Materials and Co-located Conferences*, 2009.

[50] Ritter, M., Cesnik, C. E. S., and Krüger, W. R., "An Enhanced Modal Approach for Large Deformation Modeling of Wing-Like Structures," *AIAA Science and Technology Forum and Exposition (SciTech2015), 56th AIAA/ASCE/AHS/ASC Structures, Structural Dynamics, and Materials Conference*, 2015, Kissimmee, Florida, 5-9 January 2015. AIAA 2015-0176, 10.2514/6.2015-0176.

[51] Ritter, M. and Cesnik, C. E. S., "Large Deformation Modeling of a Beam Type Structure and a 3D Wingbox using an Enhanced Modal Approach," *57th AIAA/ASCE/AHS/ASC Structures, Structural Dynamics, and Materials Conference*, AIAA SciTech Forum, American Institute of Aeronautics and Astronautics, January 2016.

[52] Ritter, M., Jones, J., and Cesnik, C. E. S., "Enhanced Modal Approach for Free-flight Nonlinear Aeroelastic Simulation of Very Flexible Aircraft," *15th Dynamics Specialists Conference*, AIAA SciTech Forum, American Institute of Aeronautics and Astronautics, jan 2016.

[53] Medeiros, R. M., Cesnik, C. E. S., and Coetzee, E. B., "Modal Formulation for Geometrically Nonlinear Structural Dynamics," *International Forum on Aeroelasticity and Structural Dynamics (IFASD)*, Como, Italy, 25-28 June 2017.

[54] Kuether, R. J., Allen, M. S., and Hollkamp, J. J., "Modal Substructuring of Geometrically Nonlinear Finite Element Models with Interface Reduction," *AIAA Journal*, Vol. 55, No. 5, apr 2017, pp. 1695–1706.

[55] Wu, L., Tiso, P., and van Keulen, F., "Interface Reduction with Multilevel Craig-Bampton Substructuring for Component Mode Synthesis," *AIAA Journal*, Vol. 56, No. 5, apr 2018, pp. 2030–2044.

[56] Krattiger, D., Wu, L., Zacharczuk, M., Buck, M., Kuether, R. J., Allen, M. S., Tiso, P., and Brake, M. R., "Interface Reduction for Hurty/Craig-Bampton Substructured Models: Review and Improvements," *Mechanical Systems and Signal Processing*, Vol. 114, jan 2019, pp. 579–603.

[57] Zhao, Z. and Ren, G., "Multibody Dynamic Approach of Flight Dynamics and Nonlinear Aeroelasticity of Flexible Aircraft," *AIAA Journal*, Vol. 49, No. 1, jan 2011, pp. 41–54.

[58] Castellani, M., Cooper, J. E., and Lemmens, Y., "Nonlinear Static Aeroelasticity of High-Aspect-Ratio-Wing Aircraft by Finite Element and Multibody Methods," *Journal of Aircraft*, Vol. 54, No. 2, nov 2016, pp. 548–560.

[59] Leishman, J. G. and Beddoes, T. S., "A Semi-Empirical Model for Dynamic Stall," *Journal of the American Helicopter Society*, Vol. 34, No. 3, 1989, pp. 3–17.

[60] McAlister, K., Lambert, O., and Petot, D., "Application of the ONERA Model of Dynamic Stall," Tech. Rep. NASA-TP-2399, NASA Ames Research Center, Moffett Field, CA, United States, 1984.

[61] Lucia, D. J., Beran, P. S., and Silva, W. A., "Reduced-Order Modeling: New Approaches for Computational Physics," *Progress in Aerospace Sciences*, Vol. 40, No. 1, 2004, pp. 51 – 117.

[62] Taira, K., Brunton, S. L., Dawson, S. T. M., Rowley, C. W., Colonius, T., McKeon, B. J., Schmidt, O. T., Gordeyev, S., Theofilis, V., and Ukeiley, L. S., "Modal Analysis of Fluid Flows: An Overview," *AIAA Journal*, oct 2017, pp. 1–29.

[63] Quarteroni, A. and Rozza, G., editors, *Reduced Order Methods for Modeling and Computational Reduction*, Springer International Publishing, Cham, 2014.

[64] Hesthaven, J. S., Rozza, G., and Stamm, B., *Certified Reduced Basis Methods for Parametrized Partial Differential Equations*, Springer, 2016.

[65] Benner, P., Cohen, A., Ohlberger, M., and Willcox, K., *Model Reduction and Approximation : Theory and Algorithms*, Society for Industrial and Applied Mathematics, Philadelphia, PA, 2017.

[66] Forrester, A. I. J., Sbester, A., and Keane, A. J., *Engineering Design via Surrogate Modelling*, J. Wiley, Chichester, 2008.

[67] Silva, W. A., "Recent Enhancements to the Development of CFD-Based Aeroelastic Reduced-Order Models," *48th AIAA/ASME/ASCE/AHS/ASC Structures, Structural Dynamics, and Materials Conference*, Structures, Structural Dynamics, and Materials and Co-located Conferences, American Institute of Aeronautics and Astronautics, apr 2007.

[68] Silva, W. A., "AEROM: NASA's Unsteady Aerodynamic and Aeroelastic Reduced-Order Modeling Software," *International Forum on Aeroelasticity and Structural Dynamics*, Como, Italy, 25-28 June 2017.

[69] Juang, J.-N. and Pappa, R. S., "An Eigensystem Realization Algorithm for Modal Parameter Identification and Model Reduction," *Journal of Guidance, Control, and Dynamics*, Vol. 8, No. 5, sep 1985, pp. 620–627.

[70] Silva, W. A., "Simultaneous Excitation of Multiple-Input/Multiple-Output CFD-Based Unsteady Aerodynamic Systems," *Journal of Aircraft*, Vol. 45, No. 4, jul 2008, pp. 1267–1274.

[71] Lee-Rausch, E. M. and Batina, J. T., "Wing Flutter Boundary Prediction Using Unsteady Euler Aerodynamic Method," *Journal of Aircraft*, Vol. 32, No. 2, mar 1995, pp. 416–422.

[72] Raveh, D. E., "Identification of Computational-Fluid-Dynamics Based Unsteady Aerodynamic Models for Aeroelastic Analysis," *Journal of Aircraft*, Vol. 41, No. 3, may 2004, pp. 620–632.

[73] Klock, R. and Cesnik, C. E. S., "Rapid Simulation of a Hypersonic Vehicle Through Singular Value Decomposition," *58th AIAA/ASCE/AHS/ASC Structures, Structural Dynamics, and Materials Conference*, AIAA SciTech Forum, American Institute of Aeronautics and Astronautics, jan 2017.

[74] Raveh, D., "Reduced-Order Models for Nonlinear Unsteady Aerodynamics," *AIAA Journal*, Vol. 39, No. 8, August 2001, pp. 1417–1429.

[75] Balajewicz, M. and Dowell, E., "Reduced-Order Modeling of Flutter and Limit-Cycle Oscillations Using the Sparse Volterra Series," *Journal of Aircraft*, Vol. 49, No. 6, nov 2012, pp. 1803–1812.

[76] Skujins, T. and Cesnik, C. E. S., "Reduced-Order Modeling of Hypersonic Vehicle Unsteady Aerodynamics," *AIAA Atmospheric Flight Mechanics Conference*, Guidance, Navigation, and Control and Co-located Conferences, American Institute of Aeronautics and Astronautics, aug 2010.

[77] Skujins, T. and Cesnik, C. E. S., "Reduced-Order Modeling of Hypersonic Unsteady Aerodynamics Due to Multi-Modal Oscillations," *17th AIAA International Space Planes and Hypersonic Systems and Technologies Conference*, International Space Planes and Hypersonic Systems and Technologies Conferences, American Institute of Aeronautics and Astronautics, apr 2011.

[78] Faller, W. E. and Schreck, S. J., "Unsteady Fluid Mechanics Applications of Neural Networks," *Journal of Aircraft*, Vol. 34, No. 1, jan 1997, pp. 48–55.

[79] Marques, F. D. and Anderson, J., "Identification and Prediction of Unsteady Transonic Aerodynamic Loads by Multi-Layer Functionals," *Journal of Fluids and Structures*, Vol. 15, No. 1, 2001, pp. 83–106.

[80] Huang, R., Hu, H., and Zhao, Y., "Nonlinear Reduced-Order Modeling for Multiple-Input/Multiple-Output Aerodynamic Systems," *AIAA Journal*, Vol. 52, No. 6, apr 2014, pp. 1219–1231.

[81] Isogai, K., "Transonic Dip Mechanism of Flutter of a Sweptback Wing: Part II," *AIAA Journal*, Vol. 19, No. 9, sep 1981, pp. 1240–1242.

[82] Winter, M. and Breitsamter, C., "Neurofuzzy-Model-Based Unsteady Aerodynamic Computations Across Varying Freestream Conditions," *AIAA Journal*, Vol. 54, No. 9, jun 2016, pp. 2705–2720.

[83] Winter, M. and Breisamter, C., "Application of Unsteady Aerodynamic Reduced-Order Modeling Techniques to a Complex Configuration," *International Forum on Aeroelasticity and Structural Dynamics*, Como, Italy, 25-28 June 2017.

[84] Wang, Q., Medeiros, R. R., Cesnik, C. E., Fidkowski, K., Brezillon, J., and Bleecke, H. M., *Techniques for Improving Neural Network-based Aerodynamics Reduced-order Models*.

[85] Willcox, K. and Peraire, J., "Balanced Model Reduction via the Proper Orthogonal Decomposition," *AIAA Journal*, Vol. 40, No. 11, nov 2002, pp. 2323–2330.

[86] Hesse, H. and Palacios, R., "Reduced-Order Aeroelastic Models for Dynamics of Maneuvering Flexible Aircraft," *AIAA Journal*, Vol. 52, No. 8, mar 2014, pp. 1717–1732.

[87] Ma, Z., Ahuja, S., and Rowley, C. W., "Reduced-Order Models for Control of Fluids Using the Eigensystem Realization Algorithm," *Theoretical and Computational Fluid Dynamics*, Vol. 25, No. 1, 2011, pp. 233–247.

[88] Walton, S., Hassan, O., and Morgan, K., "Reduced Order Modelling for Unsteady Fluid Flow Using Proper Orthogonal Decomposition and Radial Basis Functions," *Applied Mathematical Modelling*, Vol. 37, No. 20, 2013, pp. 8930 – 8945.

[89] Sevart, F. D., "Development of Active Flutter Supression Wind Tunnel Testing Technology," Tech. rep., The Boeing Company, Wichita, Kansas, 1974.

[90] Dum, H. J., "An Analytical Technique for Approximating Unsteady Aerodynamics in the Time Domain. NASA Technical Paper 1738." Tech. rep., Langley Research Center, Hampton, Virginia, 1980.

[91] Liu, L., Padthe, A. K., Friedmann, P. P., Quon, E., and Smith, M. J., "Unsteady Aerodynamics of an Airfoil/Flap Combination on a Helicopter Rotor Using Computational Fluid Dynamics and Approximate Methods," *Journal of the American Helicopter Society*, Vol. 56, No. 3, 2011, pp. 1–13.

[92] Liu, L., Padthe, A. K., and Friedmann, P. P., "Computational Study of Microflaps with Application to Vibration Reduction in Helicopter Rotors," *AIAA Journal*, Vol. 49, No. 7, jul 2011, pp. 1450–1465.

[93] Friedmann, P. P., "On-Blade Control of Rotor Vibration, Noise, and Performance: Just Around the Corner? The 33rd Alexander Nikolsky Honorary Lecture," *Journal of the American Helicopter Society*, Vol. 59, oct 2014.

[94] Myrtle, T. F. and Friedmann, P. P., "Application of a New Compressible Time Domain Aerodynamic Model to Vibration Reduction in Helicopters Using an Actively Controlled Flap," *Journal of the American Helicopter Society*, Vol. 46, No. 1, 2001, pp. 32–43.

[95] Przekop, A., Azzouz, M. S., Guo, X., Mei, C., and Azrar, L., "Finite Element Multiple-Mode Approach to Nonlinear Free Vibrations of Shallow Shells," *AIAA Journal*, Vol. 42, No. 11, 2004, pp. 2373–2381.

[96] Mignolet, M. P., Radu, A. G., and Gao, X., "Validation of Reduced Order Modeling for the Prediction of the Response and Fatigue Life of Panels Subjected to Thermo-Acoustic Effects," *VIII International Conference on Recent Advances in Structural Dynamics*, Southhampton, UK, 14-16 July 2003.

[97] Hollkamp, J. J., Gordon, R. W., and Spottswood, S. M., "Nonlinear Modal Models for Sonic Fatigue Response Prediction: A Comparison of Methods," *Journal of Sound and Vibration*, Vol. 284, No. 3, 2005, pp. 1145 – 1163.

[98] Perez, R., Wang, X. Q., and Mignolet, M. P., "Nonintrusive Structural Dynamic Reduced Order Modeling for Large Deformations: Enhancements for Complex Structures," *Journal of Computational and Nonlinear Dynamics*, Vol. 9, No. 3, feb 2014, pp. 31008–31012.

[99] Halton, J. H., "On The Efficiency of Certain Quasi-Random Sequences of Points in Evaluating Multi-Dimensional Integrals," *Numerische Mathematik*, Vol. 2, No. 1, Dec 1960, pp. 84–90.

[100] MacKay, D. J. C., "Bayesian Interpolation," *Neural Computation*, Vol. 4, No. 3, may 1992, pp. 415–447.

[101] Taylor, J. R., *Classical Mechanics*, University Science Books, 2005.

[102] Newmark, N. M., "A Method of Computation for Structural Dynamics," *Journal of the Engineering Mechanics Division*, Vol. 85, No. 3, 1959, pp. 67–94.

[103] Chung, J. and Hulbert, G. M., "A Time Integration Algorithm for Structural Dynamics With Improved Numerical Dissipation: The Generalized- Method," *Journal of Applied Mechanics*, Vol. 60, No. 2, 06 1993, pp. 371–375.

[104] Shampine, L. F. and Reichelt, M. W., "The MATLAB ODE suite," *SIAM Journal on Scientific Computing*, Vol. 18, No. 1, 1997, pp. 1–22.

[105] Hindmarsh, A. C., "ODEPACK, A Systematized Collection of ODE Solvers," *IMACS Transactions on Scientific Computation*, Vol. 1, 1983, pp. 55–64.

[106] Bartels, R. E., Rumsey, C. L., and Biedron, R. T., "CFL3D Version 6.4-General Usage and Aeroelastic Analysis," Tech. Rep. NASA/TM-2006-214301, NASA Langley Research Center, 2006.

[107] Silva, W. A. and Bartels, R. E., "Development of Reduced-Order Models for Aeroelastic Analysis and Flutter Prediction Using the CFL3Dv6.0 Code," *Journal of Fluids and Structures*, Vol. 19, No. 6, 2004, pp. 729–745.

[108] Spalart, P. and Allmaras, S., "A One-Equation Turbulence Model for Aerodynamic Flows," *30th Aerospace Sciences Meeting and Exhibit*, Aerospace Sciences Meetings, American Institute of Aeronautics and Astronautics, jan 1992.

[109] Brooks, T. R., Kenway, G. K. W., and Martins, J. R. R. A., "Benchmark Aerostructural Models for the Study of Transonic Aircraft Wings," *AIAA Journal*, Vol. 56, No. 7, 2018, pp. 2840–2855.

[110] Bartels, R. E., "Finite Macro-Element Mesh Deformation in a Structured Multi-Block Navier-Stokes Code," Tech. Rep. NASA/TM-2005-213789, NASA Langley Research Center, 2005.

[111] Smith, M. J., Hodges, D. H., and Cesnik, C. E. S., "An Evaluation of Computational Algorithms to Interface Between CFD and CSD Methodologies," Tech. Rep. WL-TR-96-3055, Wright Laboratory, Wright-Patterson AFB, Ohio, 1995.

[112] Duchon, J., "Interpolation des Fonctions de Deux Variables Suivant le Principe de la Flexion des Plaques Minces," *ESAIM: Mathematical Modelling and Numerical Analysis - Modélisation Mathématique et Analyse Numérique*, Vol. 10, No. R3, 1976, pp. 5–12.

[113] Edelsbrunner, H., Kirkpatrick, D., and Seidel, R., "On the Shape of a Set of Points in the Plane," *IEEE Transactions on Information Theory*, Vol. 29, No. 4, July 1983, pp. 551–559.

[114] Halton, J. H., "Algorithm 247: Radical-inverse Quasi-random Point Sequence," *Communications of the ACM*, Vol. 7, No. 12, Dec. 1964, pp. 701–702.

[115] Liu, X., Wen, Z., and Zhang, Y., "Limited Memory Block Krylov Subspace Optimization for Computing Dominant Singular Value Decompositions," *SIAM Journal on Scientific Computing*, Vol. 35, No. 3, jan 2013, pp. A1641–A1668.

[116] Wijker, J. J., *Spacecraft Structures*, Springer, Berlin, Heidelberg, 2008.

[117] Burden, F. and Winkler, D., "Bayesian Regularization of Neural Networks," *Artificial Neural Networks: Methods and Applications*, edited by D. Livingstone, chap. 3, Humana Press, Totowa, NJ, 2009, pp. 23–42.

[118] Marquardt, D., "An Algorithm for Least-Squares Estimation of Nonlinear Parameters," *Journal of the Society for Industrial and Applied Mathematics*, Vol. 11, No. 2, 1963, pp. 431–441.

[119] Nocedal, J. and Wright, S. J., "Quasi-Newton Methods," *Numerical Optimization*, chap. 8, Springer, New York, 1999, pp. 192–221.

[120] Nocedal, J. and Wright, S. J., "Line Search Methods," *Numerical Optimization*, chap. 3, Springer, New York, 1999, pp. 30–65.

[121] Edwards, J., Bennett, R., Whitlow W., J. R., and Seidel, D., "Time-Marching Transonic Flutter Solutions Including Angle-of-Attack Effects," *23rd Structures, Structural Dynamics and Materials Conference*, Structures, Structural Dynamics, and Materials and Co-located Conferences, American Institute of Aeronautics and Astronautics, May 1982.

[122] Chan, W. M. and Steger, J. L., "Enhancements of a Three-Dimensional Hyperbolic Grid Generation Scheme," *Applied Mathematics and Computation*, Vol. 51, No. 2-3, oct 1992, pp. 181–205.

[123] Pavel, K. and S., D., "Algorithms for Efficient Computation of Convolution," *Deisgn and Architectures for Digital Signal Processing*, edited by G. Ruiz and J. A. Michell, chap. 8, IntechOpen, London, 2013, pp. 179–203.

[124] Drela, M., "XFOIL: An Analysis and Design System for Low Reynolds Number Airfoils," *Low Reynolds Number Aerodynamics: Proceedings of the Conference Notre Dame, Indiana, USA, 5-7 June 1989*, Lecture Notes in Engineering, Springer-Verlag Berlin, Heidelberg, 1989.

[125] Bradley, M. K., Allen, T. J., and Droney, C. K., "Subsonic Ultra Green Aircraft Research: Phase II Volume III Truss Braced Wing Design Exploration," NASA/CR-2015-218704/VOL1, NF1676L-19776, NASA Langley Research Center, Hampton, VA, April 2015.

[126] Malcolm, D. J. and Laird, D. L., "Extraction of Equivalent Beam Properties from Blade Models," *Wind Energy*, Vol. 10, No. 2, dec 2006, pp. 135–157.

[127] "MSC/NASTRAN Nonlinear User's Guide SOL 400," 2014, MSC Software Corporation.

[128] Cecchini, L. S. and Weaver, P. M., "Brazier Effect in Multibay Airfoil Sections," *AIAA Journal*, Vol. 43, No. 10, oct 2005, pp. 2252–2258.

[129] Vassberg, J., Dehaan, M., Rivers, M., and Wahls, R., "Development of a Common Research Model for Applied CFD Validation Studies," *26th AIAA Applied Aerodynamics Conference*, Guidance, Navigation, and Control and Co-located Conferences, American Institute of Aeronautics and Astronautics, aug 2008.

[130] Cooper, J. E., Cook, R. G., F. G., de la Torre, O., Neild, S. A., Lowenberg, M. H., Alexander, S. S., Coetzee, E. B., and Evans, M., "Wind Tunnel Testing of a High Aspect Ratio Wing Model," *International Forum on Aeroelasticity and Structural Dynamics (IFASD)*, Savannah, Georgia, USA, 9-13 June 2019.

[131] Bruha, J., "N4SID Algorithm as System Identification Tool," *Bulletin of the Czech Econometric Society*, Vol. 5, No. 7, 1998.

[132] Teixeira, P. C. and Cesnik, C. E. S., "Propeller Influence on the Stability of HALE Aircraft," *31st Congress of the International Council of the Aeronautical Sciences (ICAS 2018)*, 2018, Belo Horizonte, Brazil, 9-14 September 2018.

APPENDIX A

Selection of ROM Parameters

Both the structural and the aerodynamic ROMs involve parameters for their various processes leading to the model reduction and simulation. This appendix describes the parameters that must be selected for both the Enhance Implicit Condensation and Expansion (EnICE) and the Method of Segments (MoS) approaches of model reduction.

Table A.1 details the parameters for the structural ROM used in the off-line phase, during preparation of the ROM. The parameters for the the online phase are listed on Table A.2.

Table A.3 details the parameters for the Method of Segments during the off-line phase. The parameters used in the online phase are listed on Table A.4.

The recommendations are presented only as general guidelines and examples of strategies that worked in the studied cases. Not all parameters were studied to verify if the chosen values lead to the best responses. For example, there was no parametric study with the number of segments for the MoS. Other parameters are largely dependent on the problem analysed, like the number of neurons in the hidden layer of the neural networks. In this case, only an expected range can be given.

Table A.1: Parameters for the EnICE ROM in the off-line phase.

Parameters for EnICE	**Recommendation**
Number of linear modes	Assure at least 80% of modal effective mass in the direction of out-of-plane displacement.
Amplitude of training loads	Compatible with the expected loads for simulations. Use a few nonlinear results with representative extreme loads for maximum amplitudes.
Number of training points	Start with first guess compatible with number of dimensions. From the fitting errors, the number of samples may need to be increased.
Number of dual modes	Aim for at least 99% of Relative Information Content in the residue of nonlinear displacements. Perform checks with sample cases.
Number of neurons in the hidden layer	3 to 5 neurons.
Number of training repetitions for the neural networks	10 to 15 repetitions.
μ_{inc} and μ_{dec} for the Bayesian regularization training of the neural networks	Around 1.2 for μ_{inc} and 0.6 for μ_{dec}
Sizes of training, validation and testing sets	70% for training, 25% for validation, and 5% for testing.

Table A.2: Parameters for the EnICE ROM in the online phase.

Parameters for EnICE	**Recommendation**
Max. time step	1 ms for the cases studied.
ODE solver and tolerances	ode 15s (Matlab) or LSODI (Fortran).

Table A.3: Parameters for the MoS ROM.

Parameters for MoS	**Recommendation**
Range of flight conditions	Use expected flight condition range.
Sampling of flight conditions	1 deg in AoA, did not study Mach or Reynolds.
Deformation state for steady reference solutions	Used undeformed, but 1-g flight deformed state should lead to more accurate predictions.
Number and distribution of wing segments	Not studied. Used 17 segments for uCRM 13.5 wing and 32 segments for 16-m wing.
Fitting type for the forces on aerodynamic mesh points of each segment	Piece-wise linear, for time savings.
Smoothing for circulation along the spanwise direction	5 $^{\text{th}}$ degree Polynomial.
Amplitude of deformation steps for step responses	Should be individually analyzed for converged, linear and smooth response.
Length of step responses	Time for freestream to traverse 15 chords.

Table A.4: Parameters for the MoS ROM in the online phase.

Parameters for MoS	**Recommendation**
Tolerance for iterations on induced AoA	Not studied. Used 0.1 deg.
Smoothing for circulation along the spanwise direction (same from off-line)	5^{th}-degree polynomial, same as off-line phase

APPENDIX B

Properties of the 16-m Wing

The properties of the 16-m wing model used in this work and introduced in Chapter 5 are given here as a reference. The data provided is related to a representation of the wing with 32 elements of equal lengths. Table B.1 presents data for the stiffness distribution, with values given as an average for each element. Similarly, Table B.2 presents data for the mass distribution. The values of inertia are provided for the beginning and ending sections of each element. Table B.3 details information about the lumped masses positioned at the nodes. Table B.4 presents relevant information for aerodynamic modeling.

Table B.1: Stiffness data for 16-m wing model. Values are an average for each element.

Element	EA [N/m^2]	GJ [N.m^2]	EI_y [N.m^2]	EI_z [N.m^2]
1	5.68×10^8	2.88×10^6	1.91×10^6	7.65×10^6
2	5.68×10^8	2.70×10^6	1.80×10^6	7.19×10^6
3	5.68×10^8	2.54×10^6	1.69×10^6	6.74×10^6
4	5.68×10^8	2.37×10^6	1.58×10^6	6.31×10^6
5	5.68×10^8	2.22×10^6	1.47×10^6	5.90×10^6
6	5.68×10^8	2.07×10^6	1.37×10^6	5.50×10^6
7	5.68×10^8	1.92×10^6	1.28×10^6	5.12×10^6
8	5.68×10^8	1.79×10^6	1.19×10^6	4.75×10^6
9	5.68×10^8	1.65×10^6	1.10×10^6	4.40×10^6
10	5.68×10^8	1.53×10^6	1.02×10^6	4.06×10^6
11	5.68×10^8	1.41×10^6	9.36×10^5	3.74×10^6
12	5.68×10^8	1.29×10^6	8.60×10^5	3.44×10^6
13	5.68×10^8	1.18×10^6	7.88×10^5	3.15×10^6
14	5.68×10^8	1.08×10^6	7.19×10^5	2.88×10^6
15	5.68×10^8	9.86×10^5	6.55×10^5	2.62×10^6
16	5.68×10^8	8.95×10^5	5.95×10^5	2.38×10^6
17	5.68×10^8	8.10×10^5	5.39×10^5	2.15×10^6
18	5.68×10^8	7.32×10^5	4.86×10^5	1.95×10^6
19	5.68×10^8	6.59×10^5	4.38×10^5	1.75×10^6
20	5.68×10^8	5.92×10^5	3.93×10^5	1.57×10^6
21	5.68×10^8	5.31×10^5	3.53×10^5	1.41×10^6
22	5.68×10^8	4.76×10^5	3.16×10^5	1.27×10^6
23	5.68×10^8	4.27×10^5	2.84×10^5	1.13×10^6
24	5.68×10^8	3.84×10^5	2.55×10^5	1.02×10^6
25	5.68×10^8	3.46×10^5	2.30×10^5	9.21×10^5
26	5.68×10^8	3.15×10^5	2.09×10^5	8.37×10^5
27	5.68×10^8	2.90×10^5	1.92×10^5	7.70×10^5
28	5.68×10^8	2.70×10^5	1.80×10^5	7.18×10^5
29	5.68×10^8	2.57×10^5	1.71×10^5	6.82×10^5
30	5.68×10^8	2.49×10^5	1.65×10^5	6.62×10^5
31	5.68×10^8	2.47×10^5	1.64×10^5	6.57×10^5
32	5.68×10^8	2.51×10^5	1.67×10^5	6.69×10^5

Table B.2: Mass distribution for the 16-m wing model. Inertia values are related to the starting and ending sections of each element.

Element [-]	Mass [kg/m]	I_{xx} (start) [kgm]	I_{xx} (end) [kgm]	I_{yy} (start) [kgm]	I_{yy} (end) [kgm]	I_{zz} (start) [m]	I_{zz} (end) [m]
1	6.4	8.88×10^{2}	8.36×10^{2}	2.22×10^{2}	2.09×10^{2}	8.88×10^{2}	8.36×10^{2}
2	6.4	8.36×10^{2}	7.84×10^{2}	2.09×10^{2}	1.96×10^{2}	8.36×10^{2}	7.84×10^{2}
3	6.4	7.84×10^{2}	7.35×10^{2}	1.96×10^{2}	1.84×10^{2}	7.84×10^{2}	7.35×10^{2}
4	6.4	7.35×10^{2}	6.87×10^{2}	1.84×10^{2}	1.72×10^{2}	7.35×10^{2}	6.87×10^{2}
5	6.4	6.87×10^{2}	6.42×10^{2}	1.72×10^{2}	1.60×10^{2}	6.87×10^{2}	6.42×10^{2}
6	6.4	6.42×10^{2}	5.98×10^{2}	1.60×10^{2}	1.49×10^{2}	6.42×10^{2}	5.98×10^{2}
7	6.4	5.98×10^{2}	5.55×10^{2}	1.49×10^{2}	1.39×10^{2}	5.98×10^{2}	5.55×10^{2}
8	6.4	5.55×10^{2}	5.15×10^{2}	1.39×10^{2}	1.29×10^{2}	5.55×10^{2}	5.15×10^{2}
9	6.4	5.15×10^{2}	4.76×10^{2}	1.29×10^{2}	1.19×10^{2}	5.15×10^{2}	4.76×10^{2}
10	6.4	4.76×10^{2}	4.39×10^{2}	1.19×10^{2}	1.10×10^{2}	4.76×10^{2}	4.39×10^{2}
11	6.4	4.39×10^{2}	4.04×10^{2}	1.10×10^{2}	1.01×10^{2}	4.39×10^{2}	4.04×10^{2}
12	6.4	4.04×10^{2}	3.71×10^{2}	1.01×10^{2}	9.27×10^{3}	4.04×10^{2}	3.71×10^{2}
13	6.4	3.71×10^{2}	3.39×10^{2}	9.27×10^{3}	8.48×10^{3}	3.71×10^{2}	3.39×10^{2}
14	6.4	3.39×10^{2}	3.09×10^{2}	8.48×10^{3}	7.73×10^{3}	3.39×10^{2}	3.09×10^{2}
15	6.4	3.09×10^{2}	2.81×10^{2}	7.73×10^{3}	7.03×10^{3}	3.09×10^{2}	2.81×10^{2}
16	6.4	2.81×10^{2}	2.55×10^{2}	7.03×10^{3}	6.38×10^{3}	2.81×10^{2}	2.55×10^{2}
17	6.4	2.55×10^{2}	2.31×10^{2}	6.38×10^{3}	5.76×10^{3}	2.55×10^{2}	2.31×10^{2}
18	6.4	2.31×10^{2}	2.08×10^{2}	5.76×10^{3}	5.20×10^{3}	2.31×10^{2}	2.08×10^{2}
19	6.4	2.08×10^{2}	1.87×10^{2}	5.20×10^{3}	4.67×10^{3}	2.08×10^{2}	1.87×10^{2}
20	6.4	1.87×10^{2}	1.68×10^{2}	4.67×10^{3}	4.19×10^{3}	1.87×10^{2}	1.68×10^{2}
21	6.4	1.68×10^{2}	1.50×10^{2}	4.19×10^{3}	3.76×10^{3}	1.68×10^{2}	1.50×10^{2}
22	6.4	1.50×10^{2}	1.35×10^{2}	3.76×10^{3}	3.37×10^{3}	1.50×10^{2}	1.35×10^{2}
23	6.4	1.35×10^{2}	1.21×10^{2}	3.37×10^{3}	3.02×10^{3}	1.35×10^{2}	1.21×10^{2}
24	6.4	1.21×10^{2}	1.09×10^{2}	3.02×10^{3}	2.72×10^{3}	1.21×10^{2}	1.09×10^{2}
25	6.4	1.09×10^{2}	9.86×10^{3}	2.72×10^{3}	2.47×10^{3}	1.09×10^{2}	9.86×10^{3}
26	6.4	9.86×10^{3}	9.01×10^{3}	2.47×10^{3}	2.25×10^{3}	9.86×10^{3}	9.01×10^{3}
27	6.4	9.01×10^{3}	8.34×10^{3}	2.25×10^{3}	2.08×10^{3}	9.01×10^{3}	8.34×10^{3}
28	6.4	8.34×10^{3}	7.84×10^{3}	2.08×10^{3}	1.96×10^{3}	8.34×10^{3}	7.84×10^{3}
29	6.4	7.84×10^{3}	7.53×10^{3}	1.96×10^{3}	1.88×10^{3}	7.84×10^{3}	7.53×10^{3}
30	6.4	7.53×10^{3}	7.39×10^{3}	1.88×10^{3}	1.85×10^{3}	7.53×10^{3}	7.39×10^{3}
31	6.4	7.39×10^{3}	7.43×10^{3}	1.85×10^{3}	1.86×10^{3}	7.39×10^{3}	7.43×10^{3}
32	6.4	7.43×10^{3}	7.64×10^{3}	1.86×10^{3}	1.91×10^{3}	7.43×10^{3}	7.64×10^{3}

Table B.3: Lumped masses located at the structural nodes

Node	Mass [kg]	I_{xx} [kgm^2]
2	5.000	0.200
3	4.970	0.199
4	4.939	0.198
5	4.909	0.196
6	4.879	0.195
7	4.848	0.194
8	4.818	0.193
9	4.788	0.192
10	4.758	0.190
11	4.727	0.189
12	4.697	0.188
13	4.667	0.187
14	4.636	0.185
15	4.606	0.184
16	4.576	0.183
17	4.545	0.182
18	4.515	0.181
19	4.485	0.179
20	4.455	0.178
21	4.424	0.177
22	4.394	0.176
23	4.364	0.175
24	4.333	0.173
25	4.303	0.172
26	4.273	0.171
27	4.242	0.170
28	4.212	0.168
29	4.182	0.167
30	4.152	0.166
31	4.121	0.165
32	4.091	0.164
33	4.061	0.162

Table B.4: 16-m wing aerodynamic model description.

Span	Chord	E. Axis	Dihedral	Incidence	Airfoil
[m]	[m]	[% chord]	[deg]	[deg]	[-]
16	1	35	0	0	NACA 0012

APPENDIX C

Studies with the Bristol Experimental Wing

Introduction

This appendix reports a work developed in support to wind tunnel tests held at University of Bristol and intended to explore the nonlinear behavior of a high-aspect-ratio wing at conditions of dynamic instability [130]. A nonlinear structural reduced order model (ROM) for this wing was developed at the University of Michigan. This structural ROM based on the Enhanced Implicit Condensation and Expansion (EnICE) methodology was later integrated with the computational fluid dynamics code CFL3D [106], resulting in an aeroelastic framework with high-fidelity aerodynamic analysis coupled to a structural solver capable of modeling large displacements as detailed in Chapter 4.

The model presented here is not intended to represent the as-built wind tunnel model reported by Cooper *et al.* [130]. The stiffness and mass distribution are representative and have been normalized since there is no intention to correlate with the results from the tests.

The first part of this appendix introduces the geometry of the wing, conditions analyzed, structural model and the verification of the structural ROM against ref-

erence solutions obtained with the Nastran SOL400 solver. The second part shows the predictions from the CFL3D/EnICE framework, such as static deflections and responses to small perturbations at different speeds.

Problem Description and Tools Verification

Wing Geometry

The basic model geometric features are:

- half-model clamped at the root;
- wing semi-span of 2.4 m;
- profile NACA 0012;
- taper ratio of 0.5;
- no mid-chord sweep angle;
- presence of tip mass for flutter studies.

The wing planform is shown in Fig. C.1, along with main dimensions in millimeters.

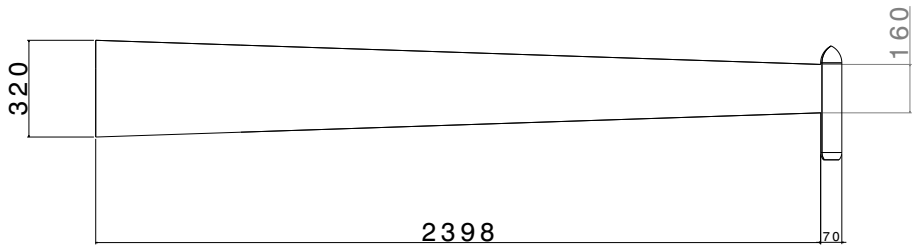

Figure C.1: Wing model with surface mesh and no tip mass. Dimensions in millimeters.

For simplicity, the mesh was obtained from a geometry with no tip mass, like the one showed in Fig. C.2, where it is possible to see a surface mesh including a rounded tip.

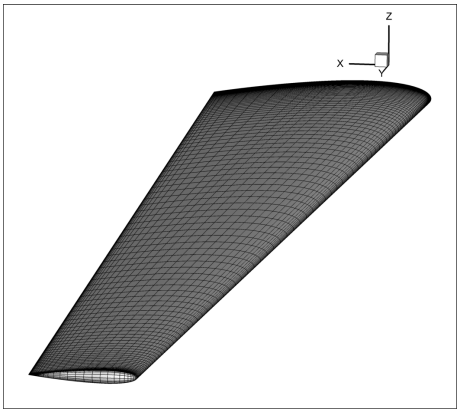

Figure C.2: Wing model with surface mesh and no tip mass.

Structural Model

Concentrated masses account for the wing inertia, instead of distributed ones. The structure is modeled with CBEAM elements defined in the Nastran file, with a total of 120 elements representing the complete beam. Since the beam represents primarily the main spar of the wing, it is slightly swept backwards, corresponding to the 40% chord-line along the semi-span of the wing. The beam properties are defined in tables at the end of this appendix. Table C.1 defines the positions of the nodes in the representative beam. Table C.2 presents the normalized stiffness properties along the beam. The cross-section area is normalized by the area at the root. EA is normalized by the root value, EA_{root}. The values for EI_{zz} and EI_{xx} and GJ are normalized by $EA_{\text{root}}c_{\text{root}}^2$, where c_{root} is the root chord. Table C.3 details the normalized properties of the concentrated masses attached to the nodes of the beam. X_{cg}, Y_{cg} and Z_{cg} are the offsets of the concentrated masses relative to its respective reference nodes, normalized by c_{root}. The inertia components I_{xx}, I_{xy}, I_{yy} and I_{zz} are

all normalized by $m_{\text{wing}}c_{\text{root}}^2$, where m_{wing} is the wing mass, not considering the tip removable mass. I_{xz} and I_{yz} are negligible compared to the other presented inertia components.

From the modal solution extracted using Nastran and the beam model, displacements and rotations were interpolated to the mesh points assuming rigid cross-sections. This process was developed to provide modal displacement data to the aeroelastic framework, but it also helps with the visualization of the beam linear modes. Figure C.3 shows the first 10 modal shapes along with their corresponding frequencies for the last structural model used in the aeroelastic analysis, the one with a tip mass. The factor number that accompanies the frequencies is the scaling used for that particular visualization. For the calculation of these modes, no gravity load was applied.

The first linear motion is pure out-of-plane bending. The second already involves certain amount of twist close to the tip. The third mode is the first in-plane one and the fourth definitely introduces torsion towards the tip.

For a good representation of inertia characteristics from a linear point of view, the modal effective mass in the z-direction was considered. The modal effective mass is related to the response of structure when excited as a base motion in a given direction. Usually, there are recommendations for spacecraft structures regarding the minimum modal effective mass that should be considered in the structural analysis. Even though there are no mandatory regulations regarding this analysis effort, including a modal effective mass around 85% in the out-of-plane direction seems reasonable to guarantee a good match in the small displacement application. With this objective, the modal effective mass was calculated, and a cumulative value of 85% was achieved with 15 modes. However, since modes 17 and 18 included significant torsion close to the tip, it was decided to include a total of 18 linear modes for the computation of the linear response.

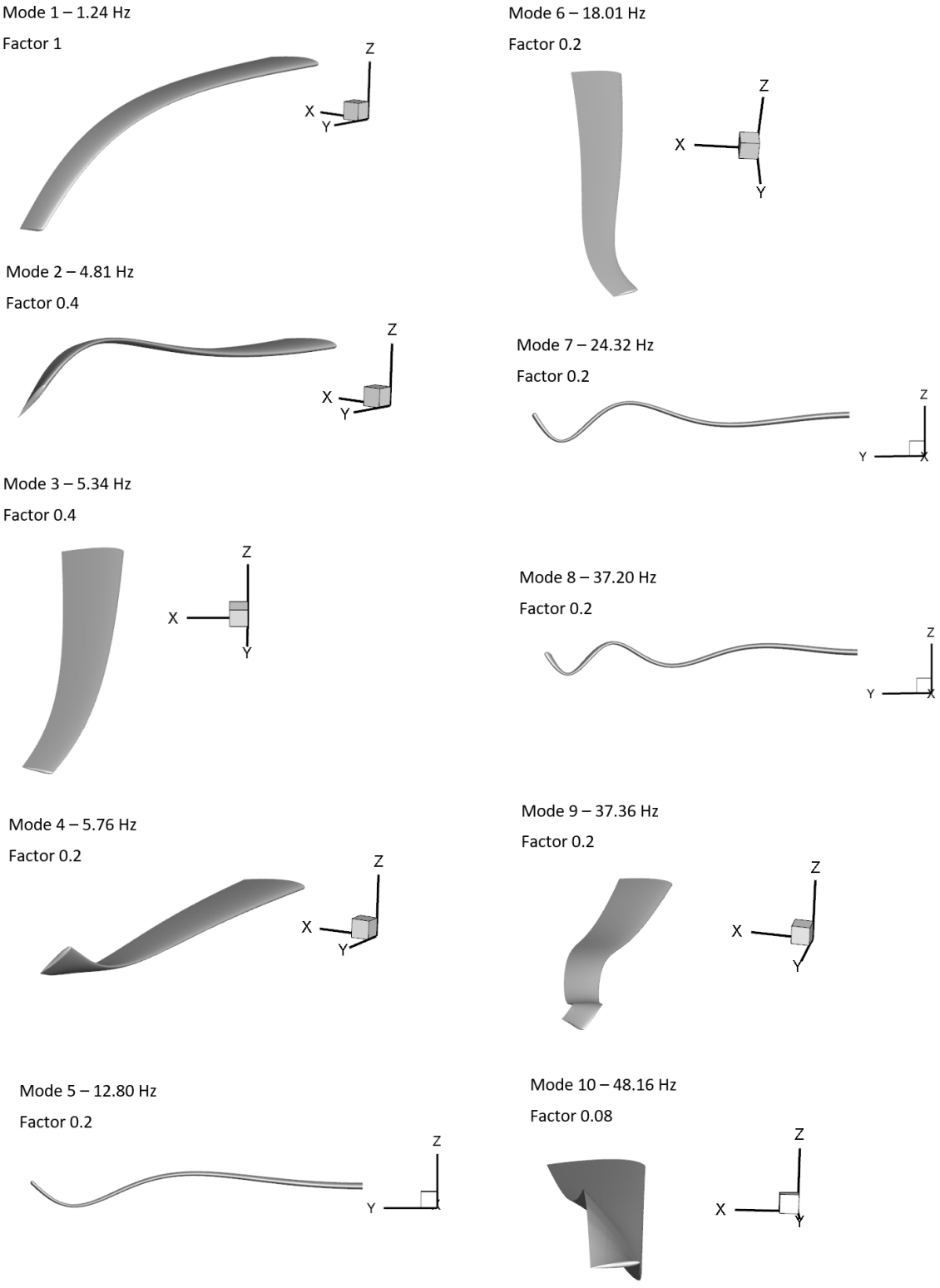

Figure C.3: Wing mode shapes with no tip mass.

Structural Reduced Order Model

The structural ROM was defined using the EnICE approach, which considers the degrees of freedom as the amplitudes of the observed displacements along the linear modes included in the analysis.

For the structural ROM of this model, with tip mass, a total of 200 static nonlinear Nastran SOL 400 solutions were used in the training phase. This results in a total of $4,000$ nonlinear reference solutions, since each Nastran case results in 20 levels of the applied force. This process is relatively fast, taking 23 minutes for the computation of the 200 cases with a Xeon E3 processor.

A total of four dual modes were included to achieve a good representation of nonlinear displacements, and the neural networks for each amplitude of the dual modes were fitted with three neurons in the hidden layer. These fitting were performed using only the displacement amplitudes related to the first four linear modes. The fitting of nonlinear forces, however, needed 6 neurons in the hidden layer, and the fittings were performed using the amplitudes of the first seven linear modes as independent variables.

Different from previous analyses, it was not straightforward to obtain quality predictions. The only difference observed that could explain this difficulty was the presence of a tip mass for this wing. Its effect on the inertia forces was larger than the normally observed in the models studied previously, requiring an estimate of linear modes amplitudes using pseudo-inversion, instead of the mass-based projection explained in Eq. 2.25. The linear modes amplitudes are calculated from the reference solutions X_{data} using

$$Q_{data} = \left(\Phi^T \Phi\right)^{-1} \Phi X_{data} \tag{C.1}$$

where Q_{data} are the linear modes amplitudes and Φ are the mass-normalized linear

modes. Another modification for this case was the removal of the orthogonalization procedure (based on the mass matrix) for the dual modes. Later, this change was incorporated into the method and all the models created after this one used dual modes non-orthogonal according to the mass matrix. These two modifications in the procedure resulted in a better displacement representation with linear and dual modes. In the end, out-of-plane displacements were captured correctly.

In order to test the structural ROM in a dynamic condition, tip forces of 50 N and 100 N were applied in the x and z directions, respectively, from the time $t = 0$ s, and the motion predicted by the structural ROM was compared to the reference solution calculated with Nastran SOL 400. In addition to the tip forces, gravity was applied in the span-wise direction. A proportional damping of 2% was also considered for this evaluation. The comparison is presented in Fig. C.4 for the tip displacement and in Fig. C.5 for the tip rotation. The linear results from Nastran SOL 112 are also presented for the purpose of observing the large errors that would happen if a linear approximation was adopted.

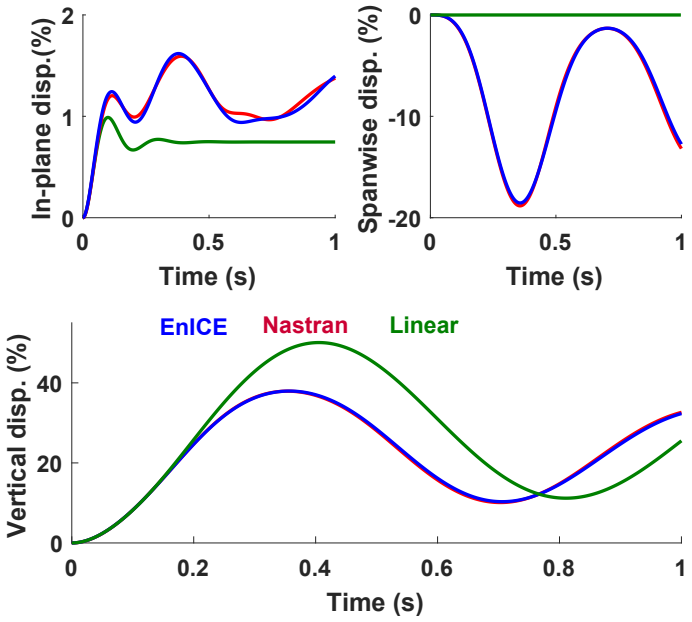

Figure C.4: Tip displacements comparison for the structural ROM obtained after the application of 50 N in the $x-$direction and 100 N in the $z-$direction.

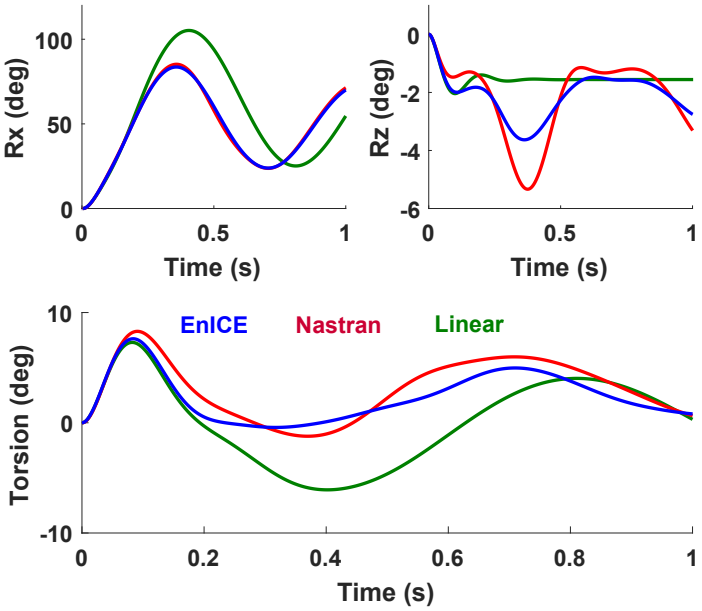

Figure C.5: Tip rotation comparison for the structural ROM obtained after the application of 50 N in the $x-$direction and 100 N in the $z-$direction.

Even though there are errors in the rotation components, especially the torsion, the trends are matching and the results from the nonlinear model are in much closer agreement than the linear approximation. The nonlinear functions of the EnICE model were then saved and used in the CFL3D/ICE framework for aeroelastic computations.

CFD Solution with the CFL3D

For the CFD solution, a convergence study was performed to decide for the adequate mesh refinement. After searching up to a fine level, it was decided for a coarser mesh with 419,840 hexahedron elements that was able to achieve a lift coefficient within 3% compared to a more refined design, as shown in Fig. C.6. The advantage is a reduced computational cost, while the error is still small if compared to the overall uncertainty of the modeling process.

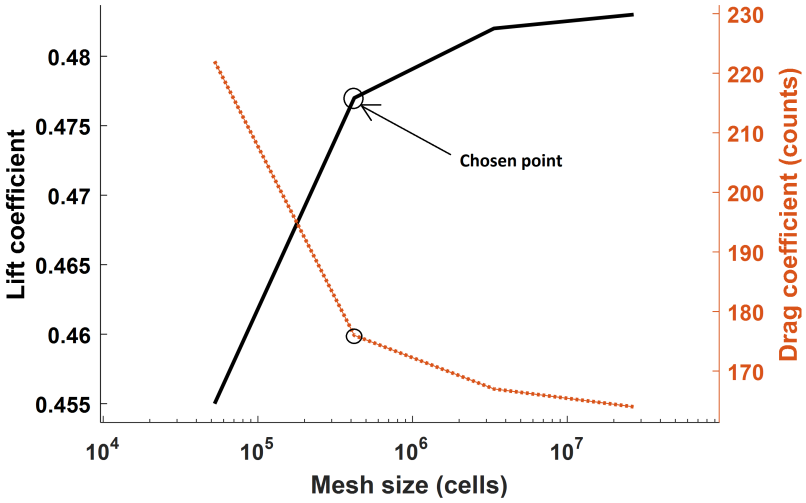

Figure C.6: Evolution of lift and drag as function of mesh refinement.

Aeroelastic Results

Aeroelastic Analyses

Using the aeroelastic tool described in the previous section, predictions were calculated for aeroelastic static displacements and instability onset speeds.

The test conditions were angle of attack of 5 degrees and speeds up to 90 m/s, with the wing in the vertical position.

Since the CFL3D/EnICE framework performs time-marching solution, the instability onset is determined by observing its time history. This process takes longer than the classical solution of an eigenvalue problem, but since parallel computation can be used, time is not a limiting factor.

For static aeroelastic solutions, the CFL3D code time marches with a high damping value for the structure. In a matter of a couple seconds of simulation, the converged condition is achieved if critical damping is used. This procedure was employed using a range of freestream velocities in order to get the states which are initial conditions for the dynamic perturbation analyses.

After the static equilibrium is achieved, the amplitudes of modal displacements q are saved and the perturbed values are used to restart the dynamic solution, with no initial velocity. The magnitudes of the initial perturbation are 0.1% of the amplitudes.

As in the previous assessments of instability onset, a range of speeds was investigated in order to identify the dynamic instability. For this structural model, an estimate of the range was $50 - 65$ m/s. Initially, the tested speeds were concentrated on the lower bound, but since the damping was still relatively high, the upper bound had also to be tested. In total, 12 different speeds were investigated.

Figure C.7 presents the out-of-plane tip displacement for the static aeroelastic solution as a function of freestream speed. It is important to notice that the range of displacements already points to nonlinearities. The wing deformation condition for

the speed of 65 m/s is presented in Fig. C.8. The out-of-plane tip displacement is approximately 28% of the wing length.

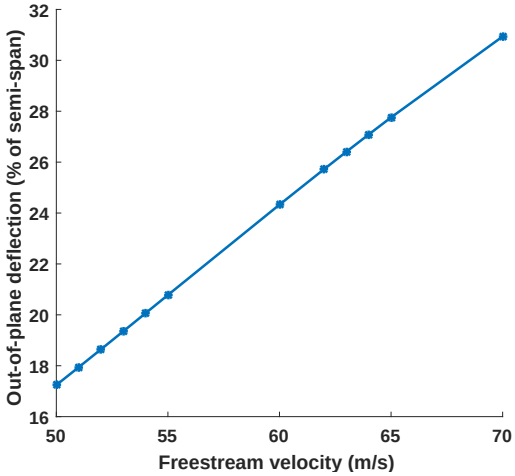

Figure C.7: Aeroelastic static out-of-plane tip displacements as function of airspeed.

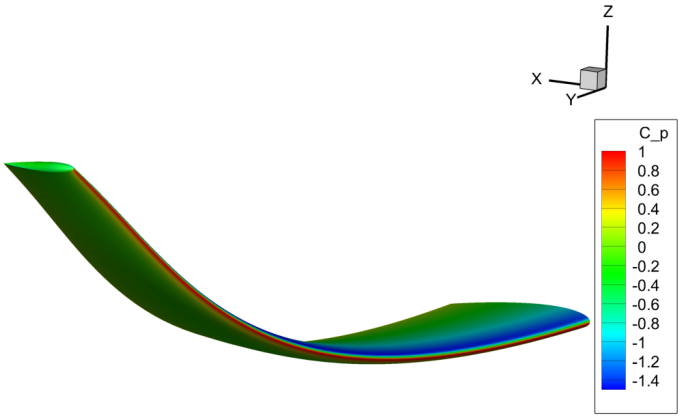

Figure C.8: Aeroelastic static condition at 65 m/s.

From the perturbed solutions, it was possible to identify stable and unstable solutions. Finally, direct dynamic instability was verified between 63 and 64 m/s. Figure C.9 presents the time history of the mode 1 amplitude for those two speeds. It is possible to see clearly the onset of instability.

In addition to the time histories, it is possible to compute the structural damping using system identification tools like the N4SID [131], which has an implementation in

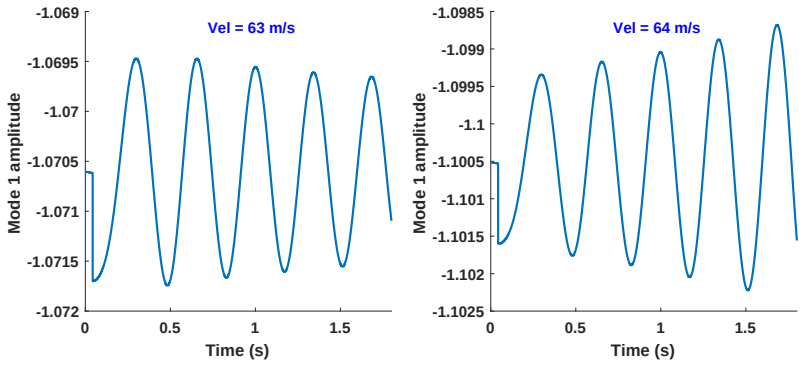

Figure C.9: Mode 1 amplitude after perturbation at 63 and 64 m/s.

Matlab. The particular procedure employed here was the same system identification of Teixeira and Cesnik [132].

Using the N4SID tool, the frequency and damping values for the aeroelastic modes were identified and plotted as functions of the airspeed in Fig. C.10 for the 12 different points analyzed. The mode tracking was done based on the modal assurance criterion (MAC) values for most of the points, but for some cases the MAC was not indicating clearly the matches and it is possible that the matches of the last point are not accurate due to the large jump from 65 to 70 m/s. However, it is clear the interaction between the first two modes for the instability. The second mode brings the torsion component to interact with the first bending mode.

From the unstable mode identified at 64 m/s, the eigenvector was calculated and plotted in Fig. C.11. The shape resembles the second mode, as expected.

Computational Effort

The heaviest computations were the dynamic CFD simulations. Each static aeroelastic computation took about 5.5 hours in a cluster using 37 cores (36 partitions of the volume mesh and one processor for tasks coordination). Once the damped solutions were obtained, each perturbed dynamic run with no structural damping and approximately 2 seconds of physical time took 11 hours of simulation in the same

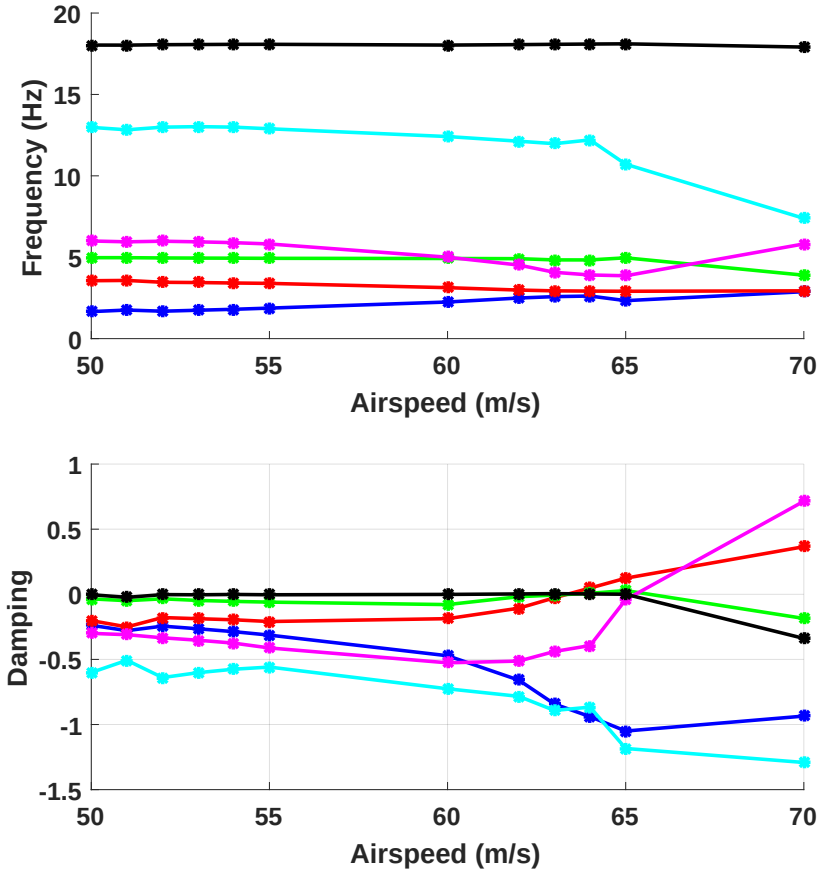

Figure C.10: Modal frequencies and damping evolving as airspeed increases.

cluster.

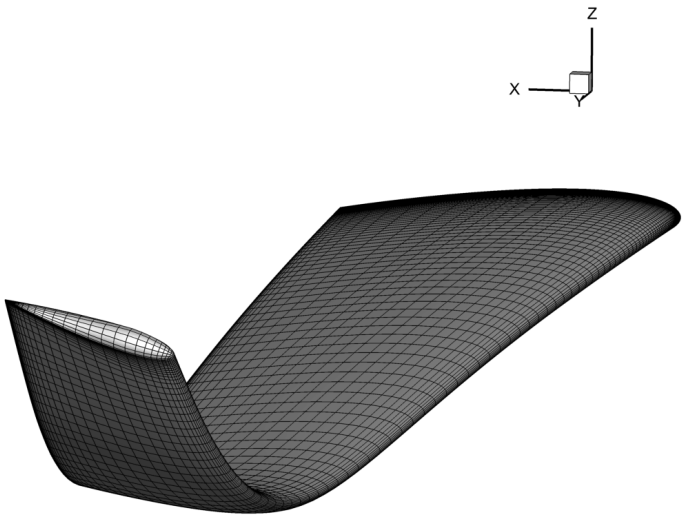

Figure C.11: Shape of the unstable mode predicted at 64 m/s.

Table C.1: Node positions for the representative beam

Node [-]	X [m]	Y [m]	Node [-]	X [m]	Y [m]	Node [-]	X [m]	Y [m]
500	1.0422	-0.040	47	1.0477	0.780	96	1.0532	1.600
501	1.0424	-0.020	48	1.0478	0.800	98	1.0533	1.620
1	1.0425	0.000	50	1.0480	0.820	99	1.0534	1.640
2	1.0426	0.020	51	1.0481	0.840	100	1.0536	1.660
3	1.0428	0.040	52	1.0482	0.860	101	1.0537	1.680
4	1.0429	0.060	53	1.0484	0.880	102	1.0538	1.700
5	1.0430	0.080	54	1.0485	0.900	104	1.0540	1.720
6	1.0432	0.100	56	1.0486	0.920	105	1.0541	1.740
8	1.0433	0.120	57	1.0488	0.940	106	1.0542	1.760
9	1.0434	0.140	58	1.0489	0.960	107	1.0544	1.780
10	1.0436	0.160	59	1.0490	0.980	108	1.0545	1.800
11	1.0437	0.180	60	1.0492	1.000	110	1.0546	1.820
12	1.0438	0.200	62	1.0493	1.020	111	1.0548	1.840
14	1.0440	0.220	63	1.0494	1.040	112	1.0549	1.860
15	1.0441	0.240	64	1.0496	1.060	113	1.0550	1.880
16	1.0442	0.260	65	1.0497	1.080	114	1.0552	1.900
17	1.0444	0.280	66	1.0498	1.100	116	1.0553	1.920
18	1.0445	0.300	68	1.0500	1.120	117	1.0554	1.940
20	1.0446	0.320	69	1.0501	1.140	118	1.0556	1.960
21	1.0448	0.340	70	1.0502	1.160	119	1.0557	1.980
22	1.0449	0.360	71	1.0504	1.180	120	1.0558	2.000
23	1.0450	0.380	72	1.0505	1.200	122	1.0560	2.020
24	1.0452	0.400	74	1.0506	1.220	123	1.0561	2.040
26	1.0453	0.420	75	1.0508	1.240	124	1.0562	2.060
27	1.0454	0.440	76	1.0509	1.260	125	1.0564	2.080
28	1.0456	0.460	77	1.0510	1.280	126	1.0565	2.100
29	1.0457	0.480	78	1.0512	1.300	128	1.0566	2.120
30	1.0458	0.500	80	1.0513	1.320	129	1.0568	2.140
32	1.0460	0.520	81	1.0514	1.340	130	1.0569	2.160
33	1.0461	0.540	82	1.0516	1.360	131	1.0570	2.180
34	1.0462	0.560	83	1.0517	1.380	132	1.0572	2.200
35	1.0464	0.580	84	1.0518	1.400	134	1.0573	2.220
36	1.0465	0.600	86	1.0520	1.420	135	1.0574	2.240
38	1.0466	0.620	87	1.0521	1.440	136	1.0576	2.260
39	1.0468	0.640	88	1.0522	1.460	137	1.0577	2.280
40	1.0469	0.660	89	1.0524	1.480	138	1.0578	2.300
41	1.0470	0.680	90	1.0525	1.500	140	1.0580	2.320
42	1.0472	0.700	92	1.0526	1.520	141	1.0581	2.340
44	1.0473	0.720	93	1.0528	1.540	142	1.0582	2.360
45	1.0474	0.740	94	1.0529	1.560	143	1.0584	2.380
46	1.0476	0.760	95	1.0530	1.580	144	1.0585	2.400

Table C.2: Normalized stiffness properties.

Element	Node 1	Node 2	EA	EI_{zz}	EI_{xx}	GJ
1	1	2	1.000	5.6×10^{-3}	4.7×10^{-4}	6.3×10^{-4}
2	2	3	1.000	5.6×10^{-3}	4.7×10^{-4}	6.3×10^{-4}
3	3	4	1.000	5.6×10^{-3}	4.7×10^{-4}	6.3×10^{-4}
4	4	5	1.000	5.6×10^{-3}	4.7×10^{-4}	6.3×10^{-4}
5	5	6	1.000	5.6×10^{-3}	4.7×10^{-4}	6.3×10^{-4}
6	6	8	0.857	4.4×10^{-3}	3.5×10^{-4}	4.3×10^{-4}
7	8	9	0.857	4.4×10^{-3}	3.5×10^{-4}	4.3×10^{-4}
8	9	10	0.857	4.4×10^{-3}	3.5×10^{-4}	4.3×10^{-4}
9	10	11	0.857	4.4×10^{-3}	3.5×10^{-4}	4.3×10^{-4}
10	11	12	0.857	4.4×10^{-3}	3.5×10^{-4}	4.3×10^{-4}
11	12	14	0.789	3.8×10^{-3}	2.9×10^{-4}	3.6×10^{-4}
12	14	15	0.789	3.8×10^{-3}	2.9×10^{-4}	3.6×10^{-4}
13	15	16	0.789	3.8×10^{-3}	2.9×10^{-4}	3.6×10^{-4}
14	16	17	0.789	3.8×10^{-3}	2.9×10^{-4}	3.6×10^{-4}
15	17	18	0.789	3.8×10^{-3}	2.9×10^{-4}	3.6×10^{-4}
16	18	20	0.714	3.2×10^{-3}	2.3×10^{-4}	2.9×10^{-4}
17	20	21	0.714	3.2×10^{-3}	2.3×10^{-4}	2.9×10^{-4}
18	21	22	0.714	3.2×10^{-3}	2.3×10^{-4}	2.9×10^{-4}
19	22	23	0.714	3.2×10^{-3}	2.3×10^{-4}	2.9×10^{-4}
20	23	24	0.714	3.2×10^{-3}	2.3×10^{-4}	2.9×10^{-4}
21	24	26	0.655	2.7×10^{-3}	1.9×10^{-4}	2.4×10^{-4}
22	26	27	0.655	2.7×10^{-3}	1.9×10^{-4}	2.4×10^{-4}
23	27	28	0.655	2.7×10^{-3}	1.9×10^{-4}	2.4×10^{-4}
24	28	29	0.655	2.7×10^{-3}	1.9×10^{-4}	2.4×10^{-4}
25	29	30	0.655	2.7×10^{-3}	1.9×10^{-4}	2.4×10^{-4}
26	30	32	0.590	2.2×10^{-3}	1.5×10^{-4}	1.9×10^{-4}
27	32	33	0.590	2.2×10^{-3}	1.5×10^{-4}	1.9×10^{-4}
28	33	34	0.590	2.2×10^{-3}	1.5×10^{-4}	1.9×10^{-4}
29	34	35	0.590	2.2×10^{-3}	1.5×10^{-4}	1.9×10^{-4}
30	35	36	0.590	2.2×10^{-3}	1.5×10^{-4}	1.9×10^{-4}
31	36	38	0.531	1.8×10^{-3}	1.2×10^{-4}	1.5×10^{-4}
32	38	39	0.531	1.8×10^{-3}	1.2×10^{-4}	1.5×10^{-4}
33	39	40	0.531	1.8×10^{-3}	1.2×10^{-4}	1.5×10^{-4}
34	40	41	0.531	1.8×10^{-3}	1.2×10^{-4}	1.5×10^{-4}
35	41	42	0.531	1.8×10^{-3}	1.2×10^{-4}	1.5×10^{-4}
36	42	44	0.474	1.5×10^{-3}	9.3×10^{-5}	1.2×10^{-4}
37	44	45	0.474	1.5×10^{-3}	9.3×10^{-5}	1.2×10^{-4}
38	45	46	0.474	1.5×10^{-3}	9.3×10^{-5}	1.2×10^{-4}
39	46	47	0.474	1.5×10^{-3}	9.3×10^{-5}	1.2×10^{-4}
40	47	48	0.474	1.5×10^{-3}	9.3×10^{-5}	1.2×10^{-4}
41	48	50	0.425	1.2×10^{-3}	7.2×10^{-5}	9.1×10^{-5}
42	50	51	0.425	1.2×10^{-3}	7.2×10^{-5}	9.1×10^{-5}
43	51	52	0.425	1.2×10^{-3}	7.2×10^{-5}	9.1×10^{-5}
44	52	53	0.425	1.2×10^{-3}	7.2×10^{-5}	9.1×10^{-5}
45	53	54	0.425	1.2×10^{-3}	7.2×10^{-5}	9.1×10^{-5}
46	54	56	0.376	9.9×10^{-4}	5.5×10^{-5}	6.9×10^{-5}

Continued on next page

Table C.2 – *Continued from previous page*

Element	Node 1	Node 2	EA	EI_{zz}	EI_{xx}	GJ
47	56	57	0.376	9.9×10^{-4}	5.5×10^{-5}	6.9×10^{-5}
48	57	58	0.376	9.9×10^{-4}	5.5×10^{-5}	6.9×10^{-5}
49	58	59	0.376	9.9×10^{-4}	5.5×10^{-5}	6.9×10^{-5}
50	59	60	0.376	9.9×10^{-4}	5.5×10^{-5}	6.9×10^{-5}
51	60	62	0.328	7.8×10^{-4}	4.1×10^{-5}	5.2×10^{-5}
52	62	63	0.328	7.8×10^{-4}	4.1×10^{-5}	5.2×10^{-5}
53	63	64	0.328	7.8×10^{-4}	4.1×10^{-5}	5.2×10^{-5}
54	64	65	0.328	7.8×10^{-4}	4.1×10^{-5}	5.2×10^{-5}
55	65	66	0.328	7.8×10^{-4}	4.1×10^{-5}	5.2×10^{-5}
56	66	68	0.290	6.2×10^{-4}	3.1×10^{-5}	4.0×10^{-5}
57	68	69	0.290	6.2×10^{-4}	3.1×10^{-5}	4.0×10^{-5}
58	69	70	0.290	6.2×10^{-4}	3.1×10^{-5}	4.0×10^{-5}
59	70	71	0.290	6.2×10^{-4}	3.1×10^{-5}	4.0×10^{-5}
60	71	72	0.290	6.2×10^{-4}	3.1×10^{-5}	4.0×10^{-5}
61	72	74	0.256	4.9×10^{-4}	2.4×10^{-5}	3.1×10^{-5}
62	74	75	0.256	4.9×10^{-4}	2.4×10^{-5}	3.1×10^{-5}
63	75	76	0.256	4.9×10^{-4}	2.4×10^{-5}	3.1×10^{-5}
64	76	77	0.256	4.9×10^{-4}	2.4×10^{-5}	3.1×10^{-5}
65	77	78	0.256	4.9×10^{-4}	2.4×10^{-5}	3.1×10^{-5}
66	78	80	0.224	3.8×10^{-4}	1.8×10^{-5}	2.3×10^{-5}
67	80	81	0.224	3.8×10^{-4}	1.8×10^{-5}	2.3×10^{-5}
68	81	82	0.224	3.8×10^{-4}	1.8×10^{-5}	2.3×10^{-5}
69	82	83	0.224	3.8×10^{-4}	1.8×10^{-5}	2.3×10^{-5}
70	83	84	0.224	3.8×10^{-4}	1.8×10^{-5}	2.3×10^{-5}
71	84	86	0.196	3.0×10^{-4}	1.4×10^{-5}	1.8×10^{-5}
72	86	87	0.196	3.0×10^{-4}	1.4×10^{-5}	1.8×10^{-5}
73	87	88	0.196	3.0×10^{-4}	1.4×10^{-5}	1.8×10^{-5}
74	88	89	0.196	3.0×10^{-4}	1.4×10^{-5}	1.8×10^{-5}
75	89	90	0.196	3.0×10^{-4}	1.4×10^{-5}	1.8×10^{-5}
76	90	92	0.170	2.2×10^{-4}	1.0×10^{-5}	1.3×10^{-5}
77	92	93	0.170	2.2×10^{-4}	1.0×10^{-5}	1.3×10^{-5}
78	93	94	0.170	2.2×10^{-4}	1.0×10^{-5}	1.3×10^{-5}
79	94	95	0.170	2.2×10^{-4}	1.0×10^{-5}	1.3×10^{-5}
80	95	96	0.170	2.2×10^{-4}	1.0×10^{-5}	1.3×10^{-5}
81	96	98	0.145	1.7×10^{-4}	7.6×10^{-6}	9.9×10^{-6}
82	98	99	0.145	1.7×10^{-4}	7.6×10^{-6}	9.9×10^{-6}
83	99	100	0.145	1.7×10^{-4}	7.6×10^{-6}	9.9×10^{-6}
84	100	101	0.145	1.7×10^{-4}	7.6×10^{-6}	9.9×10^{-6}
85	101	102	0.145	1.7×10^{-4}	7.6×10^{-6}	9.9×10^{-6}
86	102	104	0.124	1.2×10^{-4}	5.4×10^{-6}	7.1×10^{-6}
87	104	105	0.124	1.2×10^{-4}	5.4×10^{-6}	7.1×10^{-6}
88	105	106	0.124	1.2×10^{-4}	5.4×10^{-6}	7.1×10^{-6}
89	106	107	0.124	1.2×10^{-4}	5.4×10^{-6}	7.1×10^{-6}
90	107	108	0.124	1.2×10^{-4}	5.4×10^{-6}	7.1×10^{-6}
91	108	110	0.103	8.8×10^{-5}	3.9×10^{-6}	5.2×10^{-6}
92	110	111	0.103	8.8×10^{-5}	3.9×10^{-6}	5.2×10^{-6}
93	111	112	0.103	8.8×10^{-5}	3.9×10^{-6}	5.2×10^{-6}

Continued on next page

Table C.2 – *Continued from previous page*

Element	Node 1	Node 2	EA	EI_{zz}	EI_{xx}	GJ
94	112	113	0.103	8.8×10^{-5}	3.9×10^{-6}	5.2×10^{-6}
95	113	114	0.103	8.8×10^{-5}	3.9×10^{-6}	5.2×10^{-6}
96	114	116	0.087	6.1×10^{-5}	2.7×10^{-6}	3.6×10^{-6}
97	116	117	0.087	6.1×10^{-5}	2.7×10^{-6}	3.6×10^{-6}
98	117	118	0.087	6.1×10^{-5}	2.7×10^{-6}	3.6×10^{-6}
99	118	119	0.087	6.1×10^{-5}	2.7×10^{-6}	3.6×10^{-6}
100	119	120	0.087	6.1×10^{-5}	2.7×10^{-6}	3.6×10^{-6}
101	120	122	0.071	4.2×10^{-5}	1.9×10^{-6}	2.5×10^{-6}
102	122	123	0.071	4.2×10^{-5}	1.9×10^{-6}	2.5×10^{-6}
103	123	124	0.071	4.2×10^{-5}	1.9×10^{-6}	2.5×10^{-6}
104	124	125	0.071	4.2×10^{-5}	1.9×10^{-6}	2.5×10^{-6}
105	125	126	0.071	4.2×10^{-5}	1.9×10^{-6}	2.5×10^{-6}
106	126	128	0.059	2.7×10^{-5}	1.3×10^{-6}	1.7×10^{-6}
107	128	129	0.059	2.7×10^{-5}	1.3×10^{-6}	1.7×10^{-6}
108	129	130	0.059	2.7×10^{-5}	1.3×10^{-6}	1.7×10^{-6}
109	130	131	0.059	2.7×10^{-5}	1.3×10^{-6}	1.7×10^{-6}
110	131	132	0.059	2.7×10^{-5}	1.3×10^{-6}	1.7×10^{-6}
111	132	134	0.045	1.7×10^{-5}	8.6×10^{-7}	1.1×10^{-6}
112	134	135	0.045	1.7×10^{-5}	8.6×10^{-7}	1.1×10^{-6}
113	135	136	0.045	1.7×10^{-5}	8.6×10^{-7}	1.1×10^{-6}
114	136	137	0.045	1.7×10^{-5}	8.6×10^{-7}	1.1×10^{-6}
115	137	138	0.045	1.7×10^{-5}	8.6×10^{-7}	1.1×10^{-6}
116	138	140	0.047	1.7×10^{-5}	9.1×10^{-7}	1.3×10^{-6}
117	140	141	0.047	1.7×10^{-5}	9.1×10^{-7}	1.3×10^{-6}
118	141	142	0.047	1.7×10^{-5}	9.1×10^{-7}	1.3×10^{-6}
119	142	143	0.047	1.7×10^{-5}	9.1×10^{-7}	1.3×10^{-6}
120	143	144	0.047	1.7×10^{-5}	9.1×10^{-7}	1.3×10^{-6}

Table C.3: Normalized inertias.

Node	Mass	X_{cg}	Y_{cg}	Z_{cg}	I_{xx}	I_{xy}	I_{yy}	I_{zz}
1	0.0112	-0.002	0.002	0.000	9.5×10^{-6}	1.1×10^{-6}	7.4×10^{-5}	7.3×10^{-5}
2	0.0101	0.004	0.002	0.001	8.0×10^{-6}	-1.8×10^{-7}	6.2×10^{-5}	6.1×10^{-5}
3	0.0104	0.001	0.001	-0.001	8.3×10^{-6}	-1.4×10^{-6}	6.5×10^{-5}	6.4×10^{-5}
4	0.0102	0.000	0.001	0.000	8.1×10^{-6}	-1.5×10^{-6}	6.2×10^{-5}	6.1×10^{-5}
5	0.0098	-0.002	0.001	0.000	7.4×10^{-6}	-7.0×10^{-7}	5.7×10^{-5}	5.6×10^{-5}
6	0.0620	-0.006	-0.008	-0.024	2.3×10^{-3}	2.1×10^{-5}	3.5×10^{-3}	5.6×10^{-3}
6	0.0133	0.011	0.000	0.000	8.8×10^{-6}	2.5×10^{-7}	2.1×10^{-4}	2.1×10^{-4}
8	0.0104	0.001	0.002	0.000	8.7×10^{-6}	9.8×10^{-8}	6.1×10^{-5}	6.1×10^{-5}
9	0.0088	-0.001	0.002	-0.001	6.5×10^{-6}	5.4×10^{-8}	5.4×10^{-5}	5.3×10^{-5}
10	0.0096	0.002	0.001	0.000	7.4×10^{-6}	-4.9×10^{-7}	5.3×10^{-5}	5.3×10^{-5}
11	0.0093	0.000	0.003	0.000	6.9×10^{-6}	-1.0×10^{-6}	5.1×10^{-5}	5.1×10^{-5}
12	0.0086	-0.003	0.002	0.000	6.1×10^{-6}	-2.9×10^{-8}	4.8×10^{-5}	4.7×10^{-5}
14	0.0090	0.001	0.002	0.000	6.5×10^{-6}	2.8×10^{-7}	4.8×10^{-5}	4.8×10^{-5}
15	0.0089	0.000	0.004	0.000	6.8×10^{-6}	7.3×10^{-8}	5.0×10^{-5}	5.0×10^{-5}
16	0.0085	0.002	0.004	0.000	6.1×10^{-6}	-7.7×10^{-7}	4.2×10^{-5}	4.2×10^{-5}
17	0.0081	-0.003	0.003	0.000	5.6×10^{-6}	-2.8×10^{-7}	4.1×10^{-5}	4.1×10^{-5}
18	0.0553	-0.010	-0.002	-0.023	1.9×10^{-3}	-7.8×10^{-6}	2.8×10^{-3}	4.6×10^{-3}
18	0.0115	0.011	0.001	0.000	6.7×10^{-6}	2.3×10^{-7}	1.7×10^{-4}	1.7×10^{-4}
20	0.0082	-0.001	0.001	0.000	5.6×10^{-6}	2.4×10^{-8}	4.2×10^{-5}	4.2×10^{-5}
21	0.0081	0.001	0.002	0.000	5.3×10^{-6}	-7.6×10^{-8}	4.0×10^{-5}	4.0×10^{-5}
22	0.0079	-0.002	0.003	0.000	5.2×10^{-6}	1.9×10^{-7}	3.8×10^{-5}	3.9×10^{-5}
23	0.0074	0.002	0.003	0.000	4.7×10^{-6}	2.5×10^{-7}	3.5×10^{-5}	3.5×10^{-5}
24	0.0073	0.001	0.002	0.000	4.6×10^{-6}	-3.3×10^{-7}	3.5×10^{-5}	3.5×10^{-5}
26	0.0073	0.000	0.002	0.000	4.6×10^{-6}	-5.2×10^{-7}	3.4×10^{-5}	3.4×10^{-5}
27	0.0071	0.000	0.002	0.000	4.5×10^{-6}	-5.4×10^{-7}	3.3×10^{-5}	3.3×10^{-5}
28	0.0072	-0.003	0.003	0.000	4.6×10^{-6}	-6.0×10^{-8}	3.2×10^{-5}	3.3×10^{-5}
29	0.0066	0.001	0.003	0.000	3.9×10^{-6}	4.2×10^{-7}	2.9×10^{-5}	2.9×10^{-5}
30	0.0478	-0.020	-0.005	-0.019	1.6×10^{-3}	-1.6×10^{-6}	2.2×10^{-3}	3.6×10^{-3}
30	0.0101	0.008	0.001	0.000	5.3×10^{-6}	4.1×10^{-7}	1.4×10^{-4}	1.4×10^{-4}
32	0.0068	0.001	0.002	0.000	4.1×10^{-6}	8.0×10^{-8}	3.0×10^{-5}	3.1×10^{-5}
33	0.0066	-0.002	0.003	0.000	4.1×10^{-6}	2.6×10^{-7}	2.8×10^{-5}	2.9×10^{-5}
34	0.0063	-0.001	0.003	0.000	3.7×10^{-6}	7.8×10^{-7}	2.5×10^{-5}	2.5×10^{-5}
35	0.0062	0.001	0.003	0.000	3.6×10^{-6}	8.0×10^{-7}	2.5×10^{-5}	2.6×10^{-5}
36	0.0061	0.003	0.003	0.000	3.5×10^{-6}	7.2×10^{-8}	2.4×10^{-5}	2.5×10^{-5}
38	0.0062	0.001	0.005	0.000	3.7×10^{-6}	-6.1×10^{-7}	2.5×10^{-5}	2.6×10^{-5}
39	0.0057	-0.001	0.005	0.000	3.2×10^{-6}	-5.2×10^{-7}	2.1×10^{-5}	2.2×10^{-5}
40	0.0055	-0.002	0.004	0.000	3.0×10^{-6}	-5.7×10^{-8}	2.0×10^{-5}	2.1×10^{-5}
41	0.0054	0.001	0.002	0.000	2.9×10^{-6}	1.9×10^{-8}	2.0×10^{-5}	2.1×10^{-5}
42	0.0452	-0.015	-0.005	-0.023	1.5×10^{-3}	-1.6×10^{-6}	1.9×10^{-3}	3.3×10^{-3}
42	0.0087	0.005	0.001	0.000	4.2×10^{-6}	-2.0×10^{-7}	1.2×10^{-4}	1.2×10^{-4}
44	0.0055	0.000	0.002	0.000	3.2×10^{-6}	-3.2×10^{-7}	2.0×10^{-5}	2.1×10^{-5}
45	0.0052	-0.001	0.003	0.000	2.7×10^{-6}	-2.3×10^{-7}	1.9×10^{-5}	2.0×10^{-5}
46	0.0053	-0.001	0.004	0.000	2.9×10^{-6}	9.2×10^{-8}	1.8×10^{-5}	1.9×10^{-5}
47	0.0051	-0.001	0.006	0.000	2.8×10^{-6}	4.2×10^{-7}	1.8×10^{-5}	1.9×10^{-5}
48	0.0049	0.000	0.007	0.000	2.5×10^{-6}	4.9×10^{-7}	1.6×10^{-5}	1.7×10^{-5}
50	0.0047	0.000	0.007	0.000	2.5×10^{-6}	4.9×10^{-7}	1.6×10^{-5}	1.6×10^{-5}
51	0.0044	0.002	0.005	0.000	2.2×10^{-6}	2.1×10^{-7}	1.4×10^{-5}	1.5×10^{-5}
52	0.0044	0.001	0.004	0.000	2.2×10^{-6}	-1.1×10^{-7}	1.4×10^{-5}	1.4×10^{-5}
53	0.0042	-0.001	0.002	0.000	2.0×10^{-6}	-8.3×10^{-8}	1.3×10^{-5}	1.4×10^{-5}
54	0.0432	-0.024	-0.004	-0.021	1.5×10^{-3}	-6.3×10^{-6}	1.6×10^{-3}	3.0×10^{-3}
54	0.0063	0.001	0.000	0.000	2.6×10^{-6}	9.4×10^{-8}	6.4×10^{-5}	6.5×10^{-5}
56	0.0041	-0.001	0.000	0.000	2.0×10^{-6}	1.9×10^{-7}	1.3×10^{-5}	1.3×10^{-5}
57	0.0042	0.003	0.001	0.000	2.1×10^{-6}	-2.1×10^{-7}	1.2×10^{-5}	1.3×10^{-5}
58	0.0039	-0.002	0.001	0.000	1.9×10^{-6}	-3.7×10^{-7}	1.1×10^{-5}	1.2×10^{-5}

Continued on next page

Table C.3 – *Continued from previous page*

Node	Mass	X_{cg}	Y_{cg}	Z_{cg}	I_{xx}	I_{xy}	I_{yy}	I_{zz}
59	0.0040	-0.002	0.002	0.000	2.0×10^{-6}	-2.8×10^{-8}	1.1×10^{-5}	1.2×10^{-5}
60	0.0039	0.000	0.005	0.000	2.0×10^{-6}	2.2×10^{-7}	1.1×10^{-5}	1.2×10^{-5}
62	0.0037	0.001	0.005	0.000	1.7×10^{-6}	8.8×10^{-8}	9.6×10^{-6}	1.0×10^{-5}
63	0.0037	-0.001	0.006	0.000	1.7×10^{-6}	1.2×10^{-7}	9.7×10^{-6}	1.1×10^{-5}
64	0.0033	0.000	0.004	0.000	1.4×10^{-6}	1.5×10^{-7}	8.2×10^{-6}	8.8×10^{-6}
65	0.0033	0.001	0.000	0.000	1.4×10^{-6}	1.7×10^{-8}	8.6×10^{-6}	9.1×10^{-6}
66	0.0410	-0.024	-0.004	-0.020	1.4×10^{-3}	-7.8×10^{-6}	1.3×10^{-3}	2.6×10^{-3}
66	0.0054	-0.003	-0.001	0.000	2.0×10^{-6}	-4.4×10^{-8}	5.2×10^{-5}	5.3×10^{-5}
68	0.0034	0.000	0.000	0.000	1.6×10^{-6}	-2.8×10^{-8}	8.3×10^{-6}	9.1×10^{-6}
69	0.0033	0.000	0.002	0.000	1.6×10^{-6}	-6.6×10^{-8}	8.0×10^{-6}	8.9×10^{-6}
70	0.0033	-0.001	0.005	0.000	1.5×10^{-6}	6.3×10^{-8}	7.3×10^{-6}	8.1×10^{-6}
71	0.0031	0.000	0.007	0.000	1.4×10^{-6}	1.8×10^{-7}	7.0×10^{-6}	7.8×10^{-6}
72	0.0028	0.001	0.007	0.000	1.2×10^{-6}	5.8×10^{-8}	6.2×10^{-6}	6.8×10^{-6}
74	0.0029	0.001	0.006	0.000	1.3×10^{-6}	-1.3×10^{-7}	6.4×10^{-6}	7.2×10^{-6}
75	0.0028	0.000	0.007	0.000	1.2×10^{-6}	-2.2×10^{-7}	5.9×10^{-6}	6.6×10^{-6}
76	0.0025	-0.001	0.004	0.000	9.6×10^{-7}	-1.4×10^{-7}	5.3×10^{-6}	5.8×10^{-6}
77	0.0025	-0.001	0.000	0.000	1.0×10^{-6}	-3.4×10^{-8}	5.0×10^{-6}	5.6×10^{-6}
78	0.0367	-0.027	-0.004	-0.020	1.2×10^{-3}	-6.9×10^{-6}	1.0×10^{-3}	2.2×10^{-3}
78	0.0045	-0.006	0.000	0.000	1.5×10^{-6}	1.9×10^{-8}	4.2×10^{-5}	4.3×10^{-5}
80	0.0027	0.001	0.002	0.000	1.3×10^{-6}	-9.0×10^{-8}	5.3×10^{-6}	6.1×10^{-6}
81	0.0024	-0.001	0.003	0.000	9.6×10^{-7}	-6.9×10^{-8}	4.4×10^{-6}	5.0×10^{-6}
82	0.0024	0.001	0.003	0.000	1.1×10^{-6}	-4.7×10^{-8}	4.6×10^{-6}	5.3×10^{-6}
83	0.0023	0.000	0.004	0.000	9.6×10^{-7}	-9.2×10^{-8}	4.1×10^{-6}	4.7×10^{-6}
84	0.0023	0.000	0.004	0.000	9.1×10^{-7}	-1.1×10^{-7}	3.9×10^{-6}	4.5×10^{-6}
86	0.0022	-0.001	0.003	0.000	8.7×10^{-7}	-9.5×10^{-8}	3.6×10^{-6}	4.2×10^{-6}
87	0.0023	-0.001	0.003	0.000	9.3×10^{-7}	2.3×10^{-8}	3.8×10^{-6}	4.4×10^{-6}
88	0.0021	0.002	0.003	0.000	8.0×10^{-7}	-5.2×10^{-8}	3.2×10^{-6}	3.8×10^{-6}
89	0.0020	-0.002	0.001	0.000	7.3×10^{-7}	-9.3×10^{-8}	3.0×10^{-6}	3.5×10^{-6}
90	0.0345	-0.032	-0.002	-0.019	1.1×10^{-3}	-7.7×10^{-6}	8.4×10^{-4}	1.9×10^{-3}
90	0.0038	-0.011	0.000	0.000	1.2×10^{-6}	2.8×10^{-9}	3.3×10^{-5}	3.3×10^{-5}
92	0.0022	0.000	0.003	0.000	1.0×10^{-6}	-4.6×10^{-9}	3.2×10^{-6}	4.0×10^{-6}
93	0.0019	0.001	0.007	0.000	7.7×10^{-7}	-6.8×10^{-8}	2.9×10^{-6}	3.4×10^{-6}
94	0.0018	0.000	0.006	0.000	6.8×10^{-7}	-1.3×10^{-7}	2.5×10^{-6}	3.0×10^{-6}
95	0.0017	-0.001	0.003	0.000	6.1×10^{-7}	-7.1×10^{-8}	2.1×10^{-6}	2.6×10^{-6}
96	0.0018	0.001	0.003	0.000	7.5×10^{-7}	-1.4×10^{-7}	2.4×10^{-6}	3.0×10^{-6}
98	0.0016	-0.003	0.003	0.000	6.4×10^{-7}	-8.1×10^{-8}	2.0×10^{-6}	2.5×10^{-6}
99	0.0016	0.001	0.003	0.000	6.4×10^{-7}	-1.5×10^{-8}	2.1×10^{-6}	2.5×10^{-6}
100	0.0016	-0.001	0.004	0.000	6.3×10^{-7}	-1.8×10^{-9}	2.0×10^{-6}	2.4×10^{-6}
101	0.0014	0.000	0.002	0.000	4.8×10^{-7}	1.7×10^{-8}	1.6×10^{-6}	2.0×10^{-6}
102	0.0329	-0.034	-0.004	-0.017	1.6×10^{-3}	-6.1×10^{-6}	7.0×10^{-4}	1.7×10^{-3}
102	0.0023	-0.010	0.000	0.000	6.7×10^{-7}	-1.8×10^{-9}	1.5×10^{-5}	1.5×10^{-5}
104	0.0016	0.001	0.003	0.000	7.1×10^{-7}	-8.2×10^{-8}	1.8×10^{-6}	2.4×10^{-6}
105	0.0013	-0.002	0.004	0.000	4.8×10^{-7}	-3.2×10^{-8}	1.4×10^{-6}	1.7×10^{-6}
106	0.0013	0.000	0.002	0.000	4.8×10^{-7}	4.2×10^{-8}	1.4×10^{-6}	1.8×10^{-6}
107	0.0014	0.000	0.004	0.000	6.2×10^{-7}	7.0×10^{-8}	1.3×10^{-6}	1.8×10^{-6}
108	0.0012	0.000	0.004	0.001	4.6×10^{-7}	5.0×10^{-8}	1.2×10^{-6}	1.6×10^{-6}
110	0.0011	0.000	0.002	0.000	4.2×10^{-7}	2.4×10^{-8}	1.1×10^{-6}	1.5×10^{-6}
111	0.0012	0.000	0.003	0.000	4.9×10^{-7}	2.8×10^{-8}	1.1×10^{-6}	1.5×10^{-6}
112	0.0010	0.002	0.002	0.000	3.8×10^{-7}	-5.2×10^{-8}	9.5×10^{-7}	1.3×10^{-6}
113	0.0010	-0.002	0.000	0.000	3.8×10^{-7}	-5.5×10^{-8}	8.7×10^{-7}	1.2×10^{-6}
114	0.0595	-0.014	-0.010	0.000	1.9×10^{-3}	-3.1×10^{-6}	1.7×10^{-3}	3.6×10^{-3}
114	0.0020	-0.017	0.000	0.000	5.1×10^{-7}	-3.7×10^{-9}	1.1×10^{-5}	1.2×10^{-5}
116	0.0010	0.000	-0.001	0.000	3.6×10^{-7}	-3.6×10^{-8}	8.1×10^{-7}	1.1×10^{-6}
117	0.0010	0.000	0.001	0.000	4.3×10^{-7}	-6.6×10^{-8}	7.8×10^{-7}	1.1×10^{-6}
118	0.0010	-0.003	0.006	0.000	4.5×10^{-7}	2.2×10^{-8}	7.8×10^{-7}	1.2×10^{-6}
119	0.0008	0.003	0.006	0.000	2.8×10^{-7}	2.1×10^{-8}	5.4×10^{-7}	7.7×10^{-7}

Continued on next page

Table C.3 – *Continued from previous page*

Node	Mass	X_{cg}	Y_{cg}	Z_{cg}	I_{xx}	I_{xy}	I_{yy}	I_{zz}
120	0.0008	0.000	0.004	0.000	3.1×10^{-7}	-4.0×10^{-8}	5.9×10^{-7}	8.6×10^{-7}
122	0.0008	0.000	0.004	0.000	3.0×10^{-7}	-4.1×10^{-8}	5.4×10^{-7}	8.0×10^{-7}
123	0.0008	-0.002	0.005	0.000	3.3×10^{-7}	-4.6×10^{-9}	5.4×10^{-7}	8.3×10^{-7}
124	0.0008	0.000	0.008	0.000	3.2×10^{-7}	3.8×10^{-8}	4.9×10^{-7}	7.7×10^{-7}
125	0.0007	0.001	0.004	0.000	1.7×10^{-7}	9.2×10^{-9}	3.4×10^{-7}	4.8×10^{-7}
126	0.0238	-0.044	-0.006	-0.015	7.8×10^{-4}	-5.4×10^{-6}	3.8×10^{-4}	1.1×10^{-3}
126	0.0016	-0.022	0.000	0.000	3.8×10^{-7}	-5.5×10^{-9}	8.7×10^{-6}	9.0×10^{-6}
128	0.0008	0.002	0.002	0.000	3.1×10^{-7}	-6.7×10^{-8}	4.1×10^{-7}	6.8×10^{-7}
129	0.0008	-0.001	0.006	0.000	3.4×10^{-7}	-7.0×10^{-8}	3.5×10^{-7}	6.6×10^{-7}
130	0.0006	-0.002	0.008	0.000	2.0×10^{-7}	-1.0×10^{-8}	2.7×10^{-7}	4.4×10^{-7}
131	0.0006	0.000	0.006	0.000	2.1×10^{-7}	1.2×10^{-8}	2.7×10^{-7}	4.6×10^{-7}
132	0.0006	0.000	0.006	0.000	2.1×10^{-7}	1.0×10^{-8}	2.5×10^{-7}	4.3×10^{-7}
134	0.0006	0.000	0.006	0.000	1.9×10^{-7}	8.3×10^{-9}	2.3×10^{-7}	4.0×10^{-7}
135	0.0006	0.000	0.005	0.000	1.8×10^{-7}	1.2×10^{-8}	2.0×10^{-7}	3.7×10^{-7}
136	0.0006	0.002	0.007	0.000	2.3×10^{-7}	-2.1×10^{-8}	2.2×10^{-7}	4.3×10^{-7}
137	0.0004	-0.002	0.003	0.000	1.2×10^{-7}	-1.9×10^{-8}	1.2×10^{-7}	2.3×10^{-7}
138	0.0202	-0.037	-0.016	-0.013	6.4×10^{-4}	-3.9×10^{-6}	2.8×10^{-4}	9.2×10^{-4}
138	0.0013	-0.029	0.000	0.000	2.7×10^{-7}	1.7×10^{-8}	6.8×10^{-6}	7.0×10^{-6}
140	0.0005	-0.002	0.002	0.000	2.2×10^{-7}	2.7×10^{-8}	1.6×10^{-7}	3.6×10^{-7}
141	0.0005	0.001	0.006	0.000	1.7×10^{-7}	2.2×10^{-8}	1.3×10^{-7}	2.9×10^{-7}
142	0.0006	0.001	0.010	0.000	1.5×10^{-7}	-1.0×10^{-8}	3.0×10^{-7}	4.3×10^{-7}
143	0.0036	-0.023	0.000	0.000	1.4×10^{-6}	-5.0×10^{-8}	2.1×10^{-5}	2.2×10^{-5}
144	0.0018	-0.024	-0.016	0.000	2.4×10^{-7}	-1.1×10^{-8}	1.0×10^{-5}	1.0×10^{-5}
144	0.1611	0.206	0.086	0.000	8.6×10^{-4}	1.8×10^{-5}	3.1×10^{-2}	3.1×10^{-2}
500	0.1983	0.000	-0.268	0.000	5.9×10^{-3}	4.1×10^{-6}	4.2×10^{-3}	9.9×10^{-3}
501	0.0107	0.000	0.002	0.000	8.5×10^{-6}	1.0×10^{-7}	8.3×10^{-5}	8.1×10^{-5}

APPENDIX D

Fictitious Loads from Base Motion

The objective of this appendix is to detail the formulation of fictitious forces when there is base motion for a built-up structure. Specifically, the matrices that can be pre-calculated to save time during online calculations are presented.

This formulation is a continuation of Section 2.3. The same notation used there is adopted and expanded in this appendix.

As explained in Section 2.3, the modal fictitious loads due to base motion are the sum of the loads due to translation and rotation of the base, with the total modal forces given by

$$\begin{aligned} f_{fictitious} = &- \left(\Phi + \Psi\frac{\partial r}{\partial q}\right)^T (M\Upsilon a_B) \\ &- \left(\Phi + \Psi\frac{\partial r}{\partial q}\right)^T M\left[2\Omega\dot{u} + \left(\Omega^2 + \frac{d\Omega}{dt}\right)p + \Xi\dot{\omega}_B\right] \end{aligned} \tag{D.1}$$

The expression of Eq. D.1 can be expanded in terms of pre-calculated matrices multiplied by the the accelerations a_B, angular velocity components ω_x, ω_y and ω_z and angular acceleration $\dot{\omega}_B$ and its components $\dot{\omega}_x$, $\dot{\omega}_y$ and $\dot{\omega}_z$, as well as modal amplitudes q and modal velocities $\dot{q}$.

In the following, the matrices that can be pre-calculated are defined, and then the expression of modal fictitious loads in terms of these matrices is written.

The pre-calculated matrices all have modal dimensions, *i.e.*, number of rows and columns on the same order as the number of the degrees of freedom or dual modes of the EnICE model. As such, these matrices do not consume significant memory resources. Having them pre-calculated speeds up the online phase significantly.

$$A_1 := -\Phi^T M \Upsilon \tag{D.2}$$

$$A_2 := -\Psi^T M \Upsilon \tag{D.3}$$

$$A_3 := -\Phi^T M \Xi \tag{D.4}$$

$$A_4 := -\Psi^T M \Xi \tag{D.5}$$

$$B_1 := -2\Phi' M \Omega_1 \Phi \tag{D.6}$$

$$B_2 := -2\Phi' M \Omega_1 \Psi \tag{D.7}$$

$$B_3 := -2\Psi' M \Omega_1 \Phi \tag{D.8}$$

$$B_4 := -2\Psi' M \Omega_1 \Psi \tag{D.9}$$

$$B_5 := -2\Phi' M \Omega_2 \Phi \tag{D.10}$$

$$B_6 := -2\Phi' M \Omega_2 \Psi \tag{D.11}$$

$$B_7 := -2\Psi' M \Omega_2 \Phi \tag{D.12}$$

$$B_8 := -2\Psi' M \Omega_2 \Psi \tag{D.13}$$

$$B_9 := -2\Phi' M \Omega_3 \Phi \tag{D.14}$$

$$B_{10} := -2\Phi' M \Omega_3 \Psi \tag{D.15}$$

$$B_{11} := -2\Psi' M \Omega_3 \Phi \tag{D.16}$$

$$B_{12} := -2\Psi' M \Omega_3 \Psi \tag{D.17}$$

$$C_1 := -\Phi' M \Omega_1^2 x_0 \tag{D.18}$$

$$C_2 := -\Phi' M \Omega_2^2 x_0 \tag{D.19}$$

$$C_3 := -\Phi' M \Omega_3^2 x_0 \tag{D.20}$$

$$C_4 := -\Phi' M \left(\Omega_1 \Omega_2 + \Omega_2 \Omega_1\right) x_0 \tag{D.21}$$

$$C_5 := -\Phi' M \left(\Omega_1 \Omega_3 + \Omega_3 \Omega_1\right) x_0 \tag{D.22}$$

$$C_6 := -\Phi' M \left(\Omega_2 \Omega_3 + \Omega_3 \Omega_2\right) x_0 \tag{D.23}$$

$$C_7 := -\Psi' M \Omega_1^2 x_0 \tag{D.24}$$

$$C_8 := -\Psi' M \Omega_2^2 x_0 \tag{D.25}$$

$$C_9 := -\Psi' M \Omega_3^2 x_0 \tag{D.26}$$

$$C_{10} := -\Psi' M \left(\Omega_1 \Omega_2 + \Omega_2 \Omega_1\right) x_0 \tag{D.27}$$

$$C_{11} := -\Psi' M \left(\Omega_1 \Omega_3 + \Omega_3 \Omega_1\right) x_0 \tag{D.28}$$

$$C_{12} := -\Psi' M \left(\Omega_2 \Omega_3 + \Omega_3 \Omega_2\right) x_0 \tag{D.29}$$

$$\tag{D.30}$$

$$C_1' := -\Phi' M \Omega_1 x_0 \tag{D.31}$$

$$C_2' := -\Phi' M \Omega_2 x_0 \tag{D.32}$$

$$C_3' := -\Phi' M \Omega_3 x_0 \tag{D.33}$$

$$C_4' := -\Psi' M \Omega_1 x_0 \tag{D.34}$$

$$C_5' := -\Psi' M \Omega_2 x_0 \tag{D.35}$$

$$C_6' := -\Psi' M \Omega_3 x_0 \tag{D.36}$$

$$D_1 := -\Phi' M \Omega_1^2 \Phi \tag{D.37}$$

$$D_2 := -\Phi' M \Omega_2^2 \Phi \tag{D.38}$$

$$D_3 := -\Phi' M \Omega_3^2 \Phi \tag{D.39}$$

$$D_4 := -\Phi' M \left(\Omega_1 \Omega_2 + \Omega_2 \Omega_1\right) \Phi \tag{D.40}$$

$$D_5 := -\Phi' M \left(\Omega_1 \Omega_3 + \Omega_3 \Omega_1\right) \Phi \tag{D.41}$$

$$D_6 := -\Phi' M \left(\Omega_2 \Omega_3 + \Omega_3 \Omega_2\right) \Phi \tag{D.42}$$

$$D_7 := -\Psi' M \Omega_1^2 \Phi \tag{D.43}$$

$$D_8 := -\Psi' M \Omega_2^2 \Phi \tag{D.44}$$

$$D_9 := -\Psi' M \Omega_3^2 \Phi \tag{D.45}$$

$$D_{10} := -\Psi' M \left(\Omega_1 \Omega_2 + \Omega_2 \Omega_1\right) \Phi \tag{D.46}$$

$$D_{11} := -\Psi' M \left(\Omega_1 \Omega_3 + \Omega_3 \Omega_1\right) \Phi \tag{D.47}$$

$$D_{12} := -\Psi' M \left(\Omega_2 \Omega_3 + \Omega_3 \Omega_2\right) \Phi \tag{D.48}$$

$$D'_1 := -\Phi' M \Omega_1 \Phi \tag{D.49}$$

$$D'_2 := -\Phi' M \Omega_2 \Phi \tag{D.50}$$

$$D'_3 := -\Phi' M \Omega_3 \Phi \tag{D.51}$$

$$D'_4 := -\Psi' M \Omega_1 \Phi \tag{D.52}$$

$$D'_5 := -\Psi' M \Omega_2 \Phi \tag{D.53}$$

$$D'_6 := -\Psi' M \Omega_3 \Phi \tag{D.54}$$

$$E_1 := -\Phi' M \Omega_1^2 \Psi \tag{D.55}$$

$$E_2 := -\Phi' M \Omega_2^2 \Psi \tag{D.56}$$

$$E_3 := -\Phi' M \Omega_3^2 \Psi \tag{D.57}$$

$$E_4 := -\Phi' M \left(\Omega_1 \Omega_2 + \Omega_2 \Omega_1\right) \Psi \tag{D.58}$$

$$E_5 := -\Phi' M \left(\Omega_1 \Omega_3 + \Omega_3 \Omega_1\right) \Psi \tag{D.59}$$

$$E_6 := -\Phi' M \left(\Omega_2 \Omega_3 + \Omega_3 \Omega_2\right) \Psi \tag{D.60}$$

$$E_7 := -\Psi' M \Omega_1^2 \Psi \tag{D.61}$$

$$E_8 := -\Psi' M \Omega_2^2 \Psi \tag{D.62}$$

$$E_9 := -\Psi' M \Omega_3^2 \Psi \tag{D.63}$$

$$E_{10} := -\Psi' M \left(\Omega_1 \Omega_2 + \Omega_2 \Omega_1\right) \Psi \tag{D.64}$$

$$E_{11} := -\Psi' M \left(\Omega_1 \Omega_3 + \Omega_3 \Omega_1\right) \Psi \tag{D.65}$$

$$E_{12} := -\Psi' M \left(\Omega_2 \Omega_3 + \Omega_3 \Omega_2\right) \Psi \tag{D.66}$$

$$E_1' := -\Phi' M \Omega_1 \Psi \tag{D.67}$$

$$E_2' := -\Phi' M \Omega_2 \Psi \tag{D.68}$$

$$E_3' := -\Phi' M \Omega_3 \Psi \tag{D.69}$$

$$E_4' := -\Psi' M \Omega_1 \Psi \tag{D.70}$$

$$E_5' := -\Psi' M \Omega_2 \Psi \tag{D.71}$$

$$E_6' := -\Psi' M \Omega_3 \Psi \tag{D.72}$$

With the pre-calculated matrices, the modal fictitious forces are calculated by

$$
\begin{aligned}
f_{fictitious} = & \left(A_1 + \frac{\partial r}{\partial q}^T A_2 \right) a_B + \left(A_3 + \frac{\partial r}{\partial q}^T A_4 \right) \dot{\omega}_B \\
& \left[\left(B_1 + B_2 \frac{\partial r}{\partial q} + \frac{\partial r}{\partial q}^T B_3 + \frac{\partial r}{\partial q}^T B_4 \frac{\partial r}{\partial q} \right) \omega_x \right. \\
& \left(B_5 + B_6 \frac{\partial r}{\partial q} + \frac{\partial r}{\partial q}^T B_7 + \frac{\partial r}{\partial q}^T B_8 \frac{\partial r}{\partial q} \right) \omega_y \\
& \left. \left(B_9 + B_{10} \frac{\partial r}{\partial q} + \frac{\partial r}{\partial q}^T B_{11} + \frac{\partial r}{\partial q}^T B_{12} \frac{\partial r}{\partial q} \right) \omega_z \right] \dot{q} \\
& + (C_1 + \frac{\partial r^T}{\partial q} C_7)\omega_x^2 + (C_2 + \frac{\partial r^T}{\partial q} C_8)\omega_y^2 + (C_3 + \frac{\partial r^T}{\partial q} C_9)\omega_z^2 \\
& + (C_4 + \frac{\partial r^T}{\partial q} C_{10})2\omega_x\omega_y + (C_5 + \frac{\partial r^T}{\partial q} C_{11})2\omega_x\omega_z + (C_6 + \frac{\partial r^T}{\partial q} C_{12})2\omega_y\omega_z \\
& + (C_1' + \frac{\partial r^T}{\partial q} C_4'\dot{\omega}_x + (C_2' + \frac{\partial r^T}{\partial q} C_5')\dot{\omega}_y + (C_3' + \frac{\partial r^T}{\partial q} C_8')\dot{\omega}_z \\
& + q \left[(D_1 + \frac{\partial r^T}{\partial q} D_7)\omega_x^2 + (D_2 + \frac{\partial r^T}{\partial q} D_8)\omega_y^2 + (D_3 + \frac{\partial r^T}{\partial q} D_9)\omega_z^2 \right. \\
& + (D_4 + \frac{\partial r^T}{\partial q} D_{10})2\omega_x\omega_y + (D_5 + \frac{\partial r^T}{\partial q} D_{11})2\omega_x\omega_z + (D_6 + \frac{\partial r^T}{\partial q} D_{12})2\omega_y\omega_z \\
& \left. + (D_1' + \frac{\partial r^T}{\partial q} D_4'\dot{\omega}_x + (D_2' + \frac{\partial r^T}{\partial q} D_5')\dot{\omega}_y + (D_3' + \frac{\partial r^T}{\partial q} D_8')\dot{\omega}_z \right] \\
& + r \left[(E_1 + \frac{\partial r^T}{\partial q} E_7)\omega_x^2 + (E_2 + \frac{\partial r^T}{\partial q} E_8)\omega_y^2 + (E_3 + \frac{\partial r^T}{\partial q} E_9)\omega_z^2 \right. \\
& + (E_4 + \frac{\partial r^T}{\partial q} E_{10})2\omega_x\omega_y + (E_5 + \frac{\partial r^T}{\partial q} E_{11})2\omega_x\omega_z + (E_6 + \frac{\partial r^T}{\partial q} E_{12})2\omega_y\omega_z \\
& \left. + (E_1' + \frac{\partial r^T}{\partial q} E_4'\dot{\omega}_x + (E_2' + \frac{\partial r^T}{\partial q} E_5')\dot{\omega}_y + (E_3' + \frac{\partial r^T}{\partial q} E_8')\dot{\omega}_z \right]
\end{aligned}
\tag{D.73}
$$